Spectroscopic and Electrochemical Studies Towards Understanding the Activation of C-H and O-H Bonds by High-valent Metal Oxo Intermediates

Thesis Submitted to AcSIR for the Award of
the Degree of
DOCTOR OF PHILOSOPHY
In Chemical Sciences

AcSIR

By
Santanu Pattanayak
(10CC12A26026)

Under the guidance of
Dr. Kumar Vanka (supervisor)
and
Dr. Sayam Sen Gupta (co-supervisor)

CSIR-National Chemical Laboratory, Pune(India)

Certificate

This is to certify that the work incorporated in this Ph.D. thesis entitled **"Spectroscopic and Electrochemical Studies Towards Understanding the Activation of C-H and O-H Bonds by High-valent Metal Oxo Intermediates"** submitted by **Mr. Santanu Pattanayak** to **Academy of Scientific and Innovative Research (AcSIR)** in fulfillment of the requirements for the award of the Degree of Doctor of Philosophy, embodies original research work under my supervision. I further certify that this work has not been submitted to any other University or Institution in part or full for the award of any degree or diploma. Research material obtained from other sources has been duly acknowledged in the thesis. Any text, illustration, table etc., used in the thesis from other sources, have been duly cited and acknowledged.

Santanu Pattanayak

(Student)

Reg. No. 10CC12A26026

Dr. Kumar Vanka

(Supervisor)

Dr. Sayam Sen Gupta

(Co-supervisor)

Date: 29/11/17

Place: Pune

DECLARATION

I hereby declare that the thesis entitled "**Spectroscopic and Electrochemical Studies Towards Understanding the Activation of C-H and O-H Bonds by High-valent Metal Oxo Intermediates**" submitted to **Academy of Scientific & Innovative Research (AcSIR)** for Award of the **Degree of Philosophy in Chemistry**, has been carried out by me at CSIR-National Chemical Laboratory, Pune-411008, India, under the guidance of Dr. Sayam Sen Gupta (co-supervisor) and Dr. Kumar Vanka (supervisor). The work is original and has not been submitted in part or full by me for any other degree or diploma to this or any other University.

Pune

November 2017

Santanu Pattanayak

To my Parents

Acknowledgement

First and foremost, I would like to express my gratitude to my supervisors, Dr. Sayam Sen Gupta and Dr. kumar Vanka, for their guidance, scientific surroundings, and supports throughout my years. They have also created an indispensable environment for me to conduct my research work. I could not have imagined having a better advisor and mentor for my Ph.D study. They have given me the freedom to explore new opportunities as well as welcoming me when I seek help.

I also need to thank my doctoral advisory committee Dr. Selvaraj Kaliaperumal (Chairman), Dr. Akkattu Biju and Dr. Sayan Bagchi for scientific discussions during my whole research study at NCL. I would like to thank the University Grants Commission, New Delhi, India, for the award of a research fellowship. I am thankful to Dr. S. Pal, Ex-Director, and Prof. Ashwini Nangia, Director, CSIR-National Chemical Laboratory, Pune, for extending all possible infrastructural facilities to complete my research work.

I would like to express my heartfelt thanks to all the scientific members of CSIR-NCL. I need to express my thanks to the support group and all the staff members, especially Mr. Raheja for his valuable cooperation and help to process all the official work. I acknowledge all the staffs and in charge of the central facility (NMR, and J wing's instrument room of PAML building).

I sincerely thank Dr. Amitava Das and his research group for sharing lab work space during my whole electrochemistry work. I feel blessed to get the opportunity to interact with Dr. Abhisek Dey (IACS-Kolkata). I thank Atanu Rana (IACS-Kokata) and their whole research group for a friendly environment all the time when I visited IACS. My special thanks to Atanu Rana and Biswajit Mondal from IACS for helping me to learn various aspects of electrochemistry, resonance Raman and theoretical calculations. It was unforgettable to work with Prof. Lawrence Que Jr. (University of Minnesota, USA) for his immense help during EXAFS, rRaman measurement analysis. I learn many things about writing a good paper with proper scientific discussions. I am aslo thankful to Prof. Michael P Hendrich (CMU, USA) for Mossbauer analysis. I am very much thankful to Bikash Garai (NCL, Pune) for his help in X-ray crystallography, Dr. Ajit Singh for mass spectrometry (Venture Centre,

Santanu

Table of Contents

Particulars			Page
Acknowledgements			
List of Figures			vi
List of Schemes			xii
List of Tables			xiii
List of Abbreviations			xiv
Abstract of the Thesis			xvii

List of Figures

List of Schemes

List of Tables

List of Abbreviations

*m*CPBA	*meta*-chloroperbenzoic acid
DMCY	Dimethylcyclohexane
DMB	2,3-Dimethylbutane
His	Histidine
MMO	Methane monooxygenase
NADPH	Nicotinamide adenine dinucleotide (phosphate)
EXAFS	X-ray absorption fine structure
EWG	Electron withdrawing group
Cpd I	Compound I
HRP	Horseradish peroxidase
FOWA	Foot of the Wave Analysis
TON	Turnover number
UV-vis	Ultraviolet-visible
EPR	Electron paramagnetic resonance
ESI-MS	Electron spray ionization mass spectrometry
TMP	*meso*-Tetramesityl porphyrin
TPPS	*meso*-tetrakis(4-sulfonatophenyl) porphyrin
TPFPP	*meso*-tetrakis(pentaflurophenyl) porphyrin
TDFPP	*meso*-tetrakis(2,6-difluorophenyl)porphyrin
TDCPP	*meso*-tetrakis(2,6-dichlorophenyl)porphyrin
Br_8TDCPP	*meso*-tetrakis(2,6-diclorophenyl)-β-octabromoporphyrin
Cl_8TDCPP	*meso*-tetrakis(2,6-dichlorophenyl)-β-octachloroporphyrin
Br_8TMP	*meso*-tetramesityl(2,6-dichlorophenyl)-β-octachloroporphyrin
TCP	Trichloro phenol
rds	Rate determining step
RT	Room temperature
RC	Retention of configuration
UV-vis	Ultraviolet-visible
NMR	Nuclear magnetic resonance
GC	Gas chromatography
GC-MS	Gas chromatography mass spectrometry
HRMS	High resolution mass spectrometry
TPA	Tris(2-pyridylmethyl)amine
TACN	1,4,7-Triazacyclononane
PyTACN	1-(2´-pyridylmethyl)-4,7-dimethyl-1,4,7-triazacyclononane
N_4Py	1,1-di(pyridine-2-yl)-N,N-bis(pyridine-2-ylmethyl)methanamine
TMC	1,4,8,11-tetramethyl-1,4,8,11-tetraazacyclotetradecane
BBP	2,6-bis(N-methylbenzimidazol-2-yl)pyridine
BPMEN	N,N´-*bis*-(2-pyridylmethyl)-ethane-1,2-diamine

Bn-tpen	N-benzyl-N,N,N′,N′-tris(2-pyridylmethyl)-1,2-diaminoethane
BQEN	Bis(quinolyl)-diamine
TAPH	1,4,8,12-tetraazacyclopentadecane
PdP	N-N′-*bis*-(2-pyridylmethyl)2,2′-bipyridine
BPMCN	N,N′-*bis*-(2-pyridylmethyl)-N,N′-dimethyl-trans-1,2-diaminocyclohexane
TPEN	N,N,N,N-tetrakis(2-pyridylmethyl)- N,N′-dimethyl-trans-1,2-diaminocyclohexane
TAML	Tetraamido macrocyclic ligand
Cyclam	1,4,8,11-tetraazacyclotetradecane
DPAQ	2-[bis(pyridine-2-ylmethyl)]amino-N-quinolin-8yl-acetamidate
MCPP	N,N′-dimethyl-N,N′-bis(((R)-4,5pinenepyridin-2-yl)methyl)cyclohexane-1,2-diamine
OTf	Trifluoromethanesulfonate anion
TBDPS	Tert-butyldiphenylsilyl ether
Triflate	Trifluoromethanesulfonate
OAc	Acetate
MHz	Megahertz
ppm	Parts per million
ee	Enantiomeric excess
CV	Cyclic voltammetry
THF	Tetrahydrofuran
Et_3N	Triethylamine
EtOAc	Ethyl acetate
CH_3CN	Acetonitrile
CD_3OD	Methanol-d4
MeOH	Methanol
DMSO	Dimethyl sulfoxide
n-BuLi	n-Butyl lithium
DCM	Dichloromethane
PCET	Proton coupled electron transfer
NaOCl	Sodium hypochlorite
$t_{1/2}$	Half-life
OD	Optical density
TLC	Thin-layer chromatography
HCl	Hydrochloric acid
PB	Phosphate buffer
CytP450	Cytochrome P450
α-KG	α-ketogluterate dependent hydroxylase
MPPH	2-methyl-1-phenylpropan-2-yl hydroperoxide
2°	Secondary
3°	Tertiary
A/K	Alcohol ketone ratio

equiv	Equivalent
eq	Equation
AcOH	Acetic acid
H_2O_2	Hydrogen peroxide
AcOOH	Peracetic acid
O_3	Ozone
$KHSO_5$	Oxone
KIE	Kinetic isotope effect
min	Minute
sec	Second
Kcal	Kilocalorie
PhIO	Iodosyl benzene
TBHP	Tertiary butyl peroxide
[O]	Oxidant
Py	Pyridine
XAS	X-ray Absorption Spectroscopy
EXAFS	Extended X-Ray Absorption Fine Structure
EXANES	X-ray Absorption Near Edge Structure
rR	Resonance Raman
CV	Cyclic Voltametry
GC	Glassy Carbon
DFT	Density Functional Theory
HAT	Hydrogen Atom Transfer
OAT	Oxygen Atom Transfer
HOMO	Highest Occupied Molecular Orbital
LUMO	Lowest Unoccupied Molecular Orbital
MO	Molecular Orbital
WO	Water Oxidation
OEC	Oxygen Evolving Complex

Abstract of the Thesis

The selective functionalization of strong C−H bonds and the oxidation of water by cheap and nontoxic metals are some of the key targets of chemical research today. Natural metalloenzymes selectively functionalize strong C−H and O-H bonds *via* atom-economical transformations employing cheap and nontoxic metals under ambient pressure and temperature.[1] In photosystem II (PS II), a manganese oxo complex has been proposed to be an active intermediate for O-O bond formation step which is a crucial step during oxygen evolution. Similarly, iron-oxo species have been found to be key oxidising intermediates in the mechanism of C-H bond oxidation by mononuclear iron enzymes. Depending upon the oxidation state and valance electron arrangement, these oxo intermediates differ in their reactivity pattern. However, the difficulties in isolating short-lived biological intermediates to unravel their mode of action inspired synthetic chemist to design structural and functional mimic of these enzymes. The synthetic mimics mostly focused on cyclic heme analog (porphyrin, phthalocyanine, and corrolazine etc.) or non-heme analog having amine or imine based ligand system. Efforts have been made to synthesise the oxoiron(V) intermediate but the success has been limited. Iron(V)oxo complexes of biuret amide ligand based possess sufficient stability at room temperature to study their spectroscopic properties. These complexes can react with unactivated C-H bonds and olefins to afford oxidized products but their reactivity has not been correlated to their spectroscopic properties.

The proposed thesis is divided into five chapters. The first chapter represents a brief introduction into high-valent metal-oxo intermediates in nature and in synthetic models. The second chapter correlates spectroscopy and reactivity of a pair of bTAML complexes with Fe^VO and $Fe^{IV}O$ Units. The third chapter describes the mechanism of electrocatalytic water oxidation by $[Fe^{III}(bTAML)]^{2-}$ $[Co^{III}(bTAML)]^{1-}$ complex through a high-valent intermediate is presented. The fourth chapter explores the effect of changes in $[Fe^{III}(bTAML)]^{2-}$ electronics upon HAT and OAT rates. The focal theme of the fifth chapter is the synthesis of a new generation iron complex based on a tetra-uret framework. The details are presented below.

Chapter I include a comprehensive survey of literature showing the importance of oxidation in sustaining life where the natural enzymes play the crucial role of a myriad of

oxidation reactions by activating small molecules like O_2, H_2O_2 and H_2O. Sustained research over decades revealed that higher oxidized species of iron is the key intermediate for natural Fe-containing enzymes that catalyze selective oxidation reactions. This chapter also discusses the theoretical understanding of the reactivity of both $Fe^{IV}(O)$ and $Fe^{V}(O)$ toward hydrogen atom abstraction and olefin epoxidation. This chapter demonstrates the effect of axial and equatorial ligand electronic on the oxygenation reactivity of heme and nonheme model complexes.

Chapter II discusses Comparison of the geometric and electronic structures and reactivities of $[Fe^{V}(O)]^-$ and $[Fe^{IV}(O)]^{2-}$ species supported by the same ancillary nonheme biuret tetraamido macrocyclic ligand (bTAML) has been highlighted. Resonance Raman studies show that the Fe$=$O vibration of the $[Fe^{IV}(O)]^{2-}$ complex is at 798 cm^{-1}, compared to 862 cm^{-1} for the corresponding $[Fe^{V}(O)]-$ species, a 64 cm^{-1} frequency difference reasonably reproduced by density functional theory calculations. Extended X-ray absorption fine structure analysis of oxoiron(V) reveals an Fe$=$O bond length of 1.59 Å, which is 0.05 Å shorter than that found in oxoiron(IV). The redox potentials of oxoiron(IV) and oxoiron(V) are 0.44 V (measured at pH 12) and 1.19 V (measured at pH 7) versus normal hydrogen electrode, respectively, corresponding to the $[Fe^{IV}(O)]^{2-}$ /$[Fe^{III}(OH)]^{2-}$ and $[Fe^{V}(O)]^-$/$[Fe^{IV}(O)]^{2-}$ couples. Consistent with its higher potential (even after correcting for the pH difference), oxoiron(V) oxidizes benzyl alcohol at pH 7 with a second-order rate constant that is 2500-fold bigger than that for oxoiron(IV) at pH 12. Furthermore, oxoiron(IV) exhibits a classical kinteic isotope effect (KIE) of 3 in the oxidation of benzyl alcohol to benzaldehyde versus a nonclassical KIE of 12 for oxoiron(V), emphasizing the reactivity differences between oxoiron(V) and oxoiron(IV).

Chapter III discloses the mechanism of O-O bond formation by $Fe^{V}(O)$ and formal $Co^{V}(O)$ species during water oxidation. A detailed electrochemical investigation of a series of iron complexes Fe^{III}-bTAML which includes first electrochemical generation of $Fe^{V}(O)$ and demonstration of their efficacy as homogeneous catalysts for electrochemical water oxidation (WO) in aqueous medium. Spectroelectrochemical and mass spectral studies indicated $Fe^{V}(O)$ as the active oxidant, formed due to two redox transitions which have been assigned as $Fe^{IV}(O)/Fe^{III}(OH_2)$ and $Fe^{V}(O)/Fe^{IV}(O)$. The O$-$O bond formation step occurs due to nucleophilic attack of H_2O onto $Fe^{V}(O)$. Kinetic Isotope Effect (KIE) of 3.2 indicates an atom proton Transfer (APT) mechanism. The buffer base pK_a plays a

critical role in rate determining step by increasing several folds reaction rate. The electronic effect on redox potential WO rates and onset over potential was studied by employing a series of iron complexes. The catalytic activity was enhanced by the presence of electron-withdrawing groups on the bTAML framework- changing the substituents from –OMe to –NO$_2$ increase an 8-fold reaction rates, while over potential also increases by three-fold.

Biuret-modified tetraamidomacrocyclic cobalt complex [Co^{III}-bTAML]$^-$ is shown to catalyze electrochemical water oxidation at basic pH leading to the formation of O$_2$. Electrochemical and spectroscopic studies indicate a high valent cobalt oxo intermediate isoelectronic to Co^V(O) as the active oxidant. The kinetic isotope effect of 8.63 indicates an atom proton transfer mechanism.

Chapter IV explores the effect on ligand electronics on hydrogen atom transfer (HAT) and oxygen atom transfer (OAT). In this chapter, we have synthesized a wide variety of oxoiron(III)bTAML complexes having electron donating and electron withdrawing groups on the benzene ring of the head part of the complex. These complexes have been characterised by single crystal X-ray diffraction, HR-Ms, UV-Vis, electrochemistry and EPR spectroscopy. Then a series of oxoiron(V) complex was synthesized by using the equimolar amount of aqueous sodium hypochlorite solution in acetonitrile at room temperature. All the oxoiron(V) species have been characterised by HR-Ms, UV-Vis, electrochemistry and EPR spectroscopy. One electron reduced species (Fe^{IV}O) of all the substituted iron(V)oxo also have been synthesized at higher pH to calculate the pK_a values of Fe^{IV}(O-H) species. The observed enhanced HAT rate of toluene by electron rich methoxy substituted oxoiron(V) was explained on the basis of elevated pK_a (11.3) of one electron reduced Fe^{IV}(O-H) species similar to the natural heme enzyme. The OAT rate enhancement for electron deficient oxoiron(V) is solely responsible for the increase in redox potential of the electron deficient metal oxo species. However, the increase in OAT rate for electron rich oxoiron(V) species is a counterintuitive reactivity trend for an essentially electrophilic species.

Chapter V discusses the synthesis of new generation iron complex based on a tetrauret modified tetraamido macrocyclic ligand (PPh$_4$)[(tTAML)Fe^{III}(Cl)]. This [(tTAML)Fe^{III}Cl]$^{2-}$ complex was characterized by UV-Vis, HR-MS, EPR and single

crystal X-ray diffraction. The stability and reactivity of this complex will be conducted in a separate study.

Chapter VI presents an overall summary of the work and describes the major findings of the studies. Future directions based on the work reported in the thesis are also discussed.

Chapter I

Introduction and Literature Survey towards High-valent Metal Oxo Intermediate

1.1 Introduction

The selective oxidation of various substrates is an extremely vital process to maintain the sustenance of life processes. Oxidation also has an enormous industrial application, since the most important industrial processes for converting fossil fuel into value-added products is the oxidation of petroleum feedstocks. For bulk chemical synthesis, oxidation of natural hydrocarbons is the key step, but many challenges remain, such as the oxidation of methane to methanol on an industrial scale.[1] For decades, various research groups have been searching for efficient and cheap catalysts for selective oxidation reactions of hydrocarbons under ambient conditions, with the aim of finding alternative energy carriers to fossil-based oil for energy-conversion processes.[2] However, nature has evolved metalloenzymes by overcoming the kinetic barrier to activate molecular oxygen for selective and controlled oxidation of specific substrates.[3] These metalloenzymes are of great importance, because of the use of cheap and earth-abundant transition metals in their active sites, such as iron, copper, cobalt, and manganese.[4] These enzymes frequently exhibit substrate specificity as well as regioselectivity and stereo selectivity towards different substrate under mild conditions. The key metabolic functions mediated by metalloenzymes are desaturation of fatty acids in plants, DNA and RNA repairs, hydroxylation of methane in methanotrophs, biosynthesis of β-lactam antibiotics, and the sensing of hypoxia in mammalian cells to signal the formation of blood vessels.[5-8] The active sites in native metalloenzymes are deeply buried in protein scaffolds from potential deactivation routes, which helps them to adopt unique structures and exhibit unusual properties during metabolic functions. Inspired by nature, several transition metal complexes have been synthesized to activate the naturally abundant green oxidant molecular oxygen (O_2) and chemical oxidants (H_2O_2, NaOCl, *m*CPBA, etc.) efficiently to facilitate industrial oxidative transformations.[9,10] Hence, much effort has been devoted to understand the nature of active oxidant and their mechanisms in the way of C-H activation in a number of heme and non-heme monooxygenase enzymes.[5,11-21]

Oxidation is also fundamentally important process from the energy perspective. One reaction that discerns Earth from other planets is the photosynthesis process, in which plants convert solar energy into chemical energy. During photosynthesis sunlight-driven oxidation of water caused by the oxygen evolving complex (OEC, Figure 1.1), is composed of earth-abundant manganese and calcium metal oxide clusters. This process produces dioxygen, four protons, and four electrons, followed by a reduction of atmospheric CO_2, following a relay of reactions, to

synthesize carbohydrate as chemical energy reserver.[22,23] To date, the most likely mechanism of water oxidation catalyzed by natural OEC is not clear. To prepare functional synthetic mimics that can function as catalysts for efficient water oxidation (WO) that can be further be developed into a proton-reduction process to produce H_2, which is a cleaner energy source, great research effort is being persued worldwide.
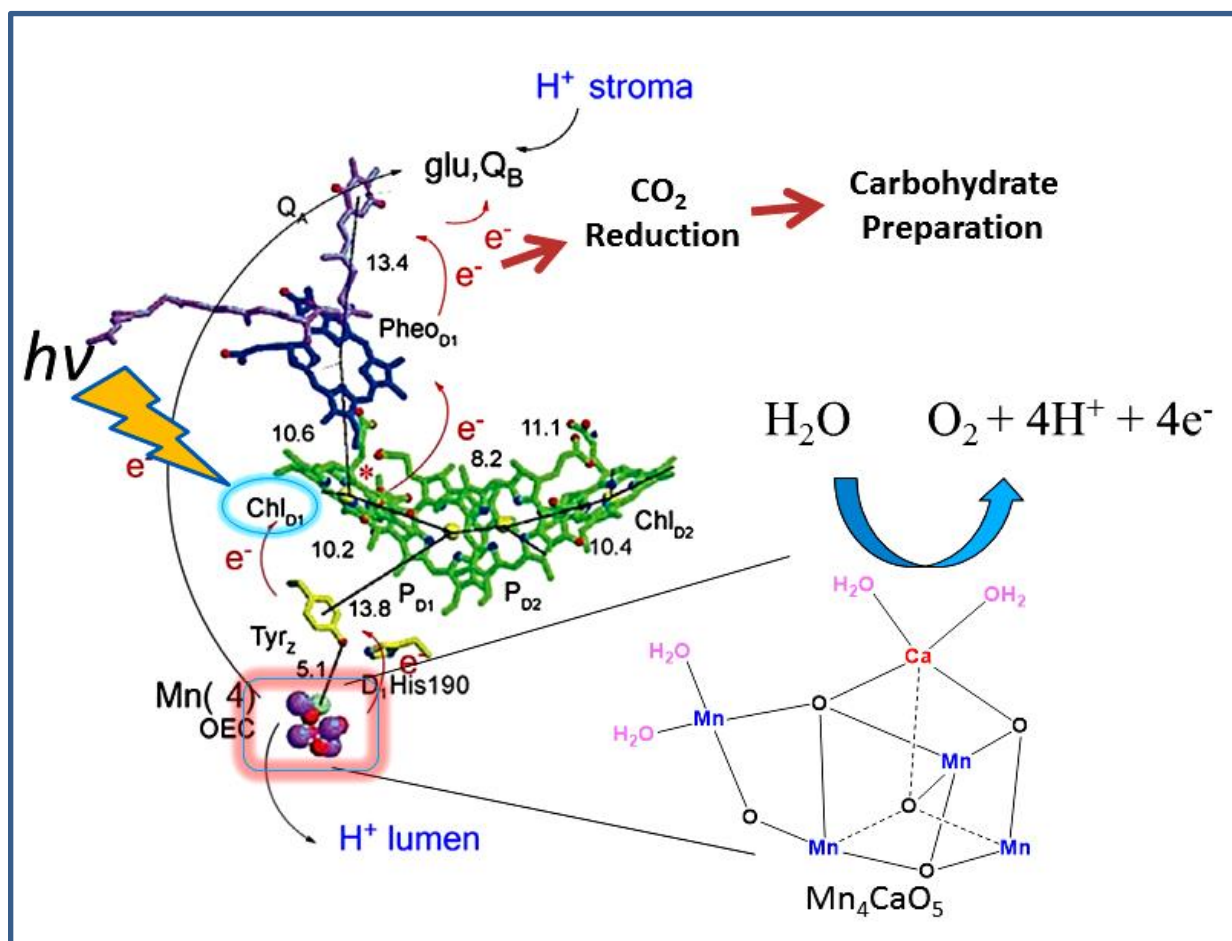
Figure 1.1: Natural O_2 evolution at Mn-OEC in photosystem II.[8]

1.2 Natural Metalloenzyme and Oxidation reactions

The majority of metalloenzymes are proteins that contain tightly bound metals (Table 1.1). It has been estimated that one-half of all known proteins contain metals and they are always isolated with the protein, while approximately one-third of the proteins are dependent on metals for their biological functions.[24]

Table 1.1 Lists of some metalloenzymes containing different metal in their active sites.

Metals	Examples of metalloenzymes
Iron	Catalase, Hydrogenase
Copper	Cytochrome c oxidase, Laccase
Zinc	Carboxypeptidase, Aminopeptidase
Nickel	Urease, Hydrogenase
Magnesium	Glucose 6-phosphatase, Hexokinase
Cobalt	Methionyl aminopeptidase, Nitrile hydratase
Manganese	Arginase
Molybdenum	Nitrate reductase, Sulfite oxidase
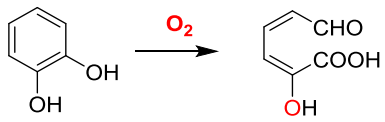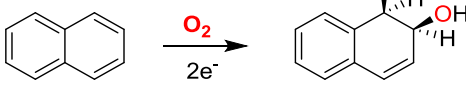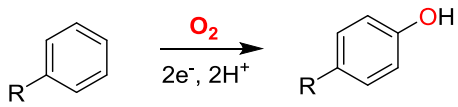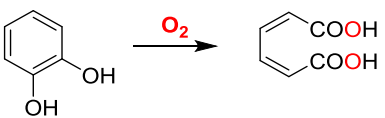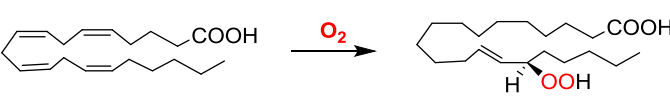
1.2.1 Iron based enzymes

Iron is the fourth most common element (up to 5% of the total elements present, after oxygen, silicon and aluminium) in the Earth's crust. Most metalloenzymes have evolved with an iron-containing active center because of their abundance, inherent electronic properties, and access to various redox states.[25] Based on the type of reaction they perform, these are classified as oxygenases, oxidases, reductases, hydrogenases, or dehydrogenases (Table 1.2). Biologically, iron plays vital roles in oxygen transport and storage as well as in electron transport.[25] There is a large number of metalloenzymes that contain iron in their active sites (Table 1.2). Myoglobin and hemoglobin were among the first proteins to be structurally characterized and both of them contain iron protoporphyrin IX (heme b) as an essential prosthetic center. Most importantly, these enzymes use molecular oxygen to perform various oxidation reactions relevant to biological processes, including the metabolism of drugs, DNA and RNA base repair, biosynthesis of hormones, and the biosynthesis of antibiotics.[5-8] Based on the nature of coordinating ligand, iron-containing enzymes that activate O_2 have been categorized into 'heme', with iron-porphyrin cofactors, and 'non-heme', with iron active centers bound to amino acid residues.[24-28]

1.2.1.1 Heme Enzymes

Heme enzymes have an active iron center coordinated to a porphyrin cofactor in a distorted square pyramidal fashion, with one axial cysteine/histidine ligand from the protein backbone, and the other axial position available for O_2/H_2O_2 binding and their subsequent activation. These enzymes are classified as oxidases or peroxidases depending on the activation of either O_2 or H_2O_2 (Scheme 1.1).

Table 1.2 Iron proteins implicated in oxidation reactions via dioxygen activation

Enzymes	Reactions
Heme Proteins	
CytP450	
Non-heme Proteins	
Extradiol-cleaving catechol dioxygenase	
Rieske dioxygenase	
α-ketogluterate dependent hydroxylase	
Pterin-dependent enzymes	
Other Fe(II) or Fe(III) dioxygenase	
Intradiol cleaving catechol dioxygenase (Fe^III^)	
Lipoxygenase (Fe^III^)	

Apocarotene dioxygenase (Fe^{III})	
Binuclear Center	
Methane Monooxygenase	
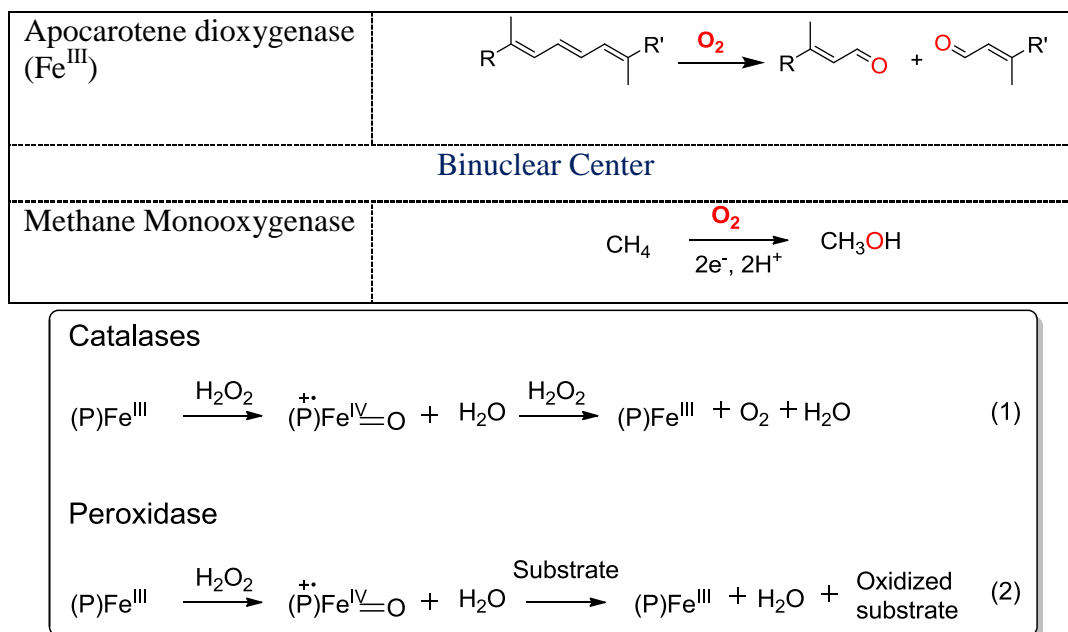
Scheme1.1: Peroxide activation mechanism by catalases and peroxidases.

Peroxidases are the class of heme enzymes where a histidine residue occupies one of the two axial coordination sites and the other axial site used for H_2O_2 activation. On the other hand, oxidases class of enzyme activate O_2 at one of the two axial sites while the axial cysteine ligand occupies trans position. Among monooxygenases, the most studied heme-containing enzyme is Cytochrome P450 (CytP450, Figure 1.2) which oxidizes the long aliphatic chain of cholesterol selectively during the biosynthesis of the female hormone progesterone. The active site has been explored through the X-ray crystal structure of CytP450-camphor.[29, 30] Accepted oxygen activation mechanism associated with cytochrome P450 is referred to as the heme paradigm (Scheme 1.2).[4]
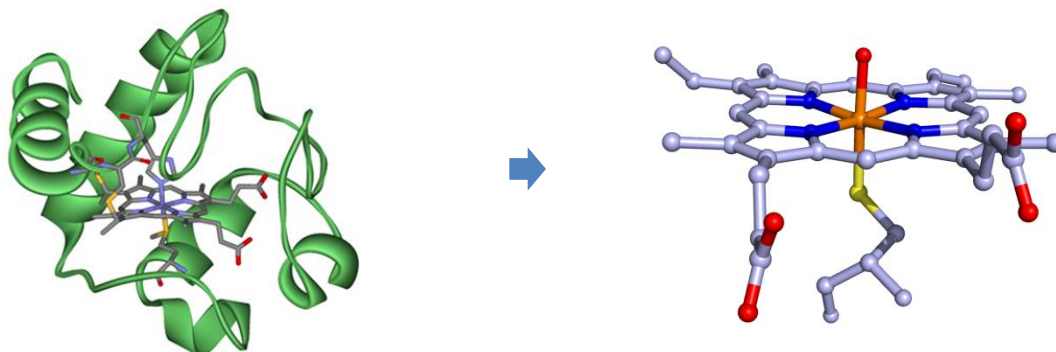
Figure 1.2 Molecular structures of catalytically active centers of cytochrome P450 in nature.

Activation of O_2 at iron center in CytP450 proceeds through iron superoxo and iron peroxo species formation, followed by O–O bond cleavage, to generate a formally oxoiron(V) or $Fe^V(O)$ oxidant that in turn, carries out the two-electron oxidation of the substrate.[29, 30] The proposed catalytic cycle for CytP450 has been shown in Scheme 1.2.
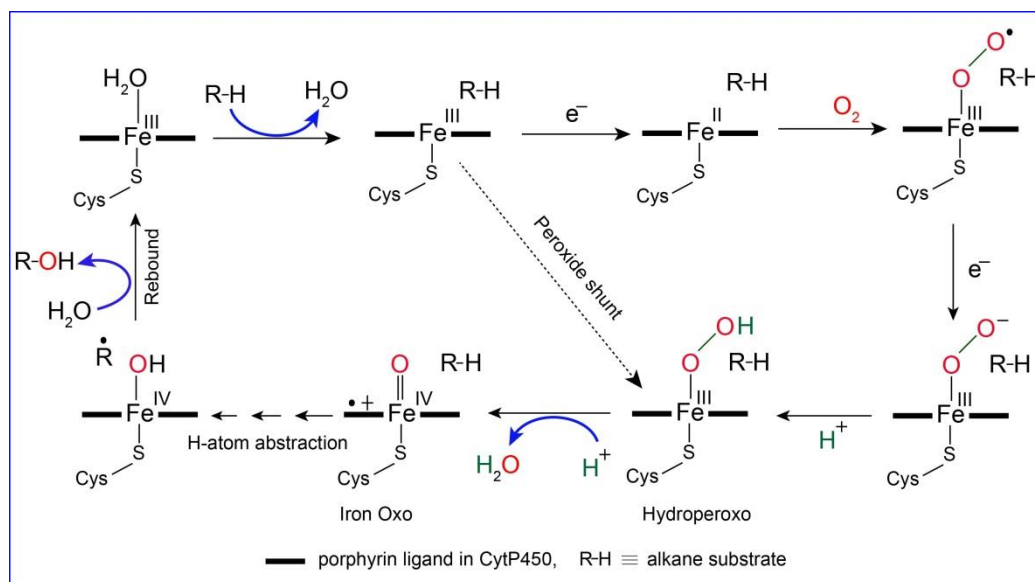
Scheme 1.2: Formation of high-valent iron-oxo and its reaction mechanism for alkane hydroxylation by CytP450.

Crucial steps for activation of C–H bonds by CytP450 include:[29]

i)   Substrate binding to active site induces a spin change of the iron center to achieve a favorable enzyme-substrate adduct

ii)   One electron reduction of iron(III) center by NADPH

iii)   Subsequent binding of O_2 to the reduced iron center results in Cyp450-superoxide complex

iv)   Addition of a second electron oxidises iron(III)superoxide to iron(III)peroxide intermediate which on subsequent protonation produce iron(III)hydroperoxy complex

v)   The formation of the high-valent oxoiron(IV) cation radical (compound I), isoelectronic to $Fe^V(O)$ species; a crucial step formed by protonation and heterolytic cleavage of the O-O bond followed by removal of one water molecule

vi)   H-atom abstraction and transfer of the O atom from the iron-oxo to the substrate to form a hydroxylated product through a two-step process known as 'oxygen rebound' mechanism

Direct formation of high valent oxo species from resting state of the catalyst can also be achieved synthetically by adding commercial oxidants like sodium hypochlorite (NaOCl), iodosyl benzene (PhIO), alkyl peroxides and peracids, *etc*. This pathway is considered as the 'peroxide shunt'(Scheme 1.2).[31-33]

1.2.1.2 Non-heme Enzymes

Non-heme iron containing enzymes do not contain Fe-porphyrin cofactor similar to heme iron enzymes. These non heme enzymes are broadly classified as mononuclear or dinuclear depending upon the number of metal in active site. Structure function relationship of these class of enzyme have been explored from the crystal structures of several mononuclear non-heme iron enzymes. Non-heme enzymes generally activate molecular oxygen to catalyse diverse oxidative transformations. According to available structural data of non-heme enzymes, a common structural motif consisting of a mononuclear iron(II) metal center ligated by two histidine residues and one carboxylate residue from protein back bone in a facial mode (Figure 1.3). The carboxylate ligand can either be a glutamate or aspartate residue. The structural motif has been termed as the '2-His-1-carboxylate facial triad'; nature's recurring motif like the heme cofactor and iron–sulfur clusters.[33, 34] The most versatile non-heme enzyme is Rieske dioxygenase, an analogue of CytP450 which catalyses the enantioselective cis-hydroxylation of arene, a transformation which is challenging in organic synthesis.[25, 35-37]
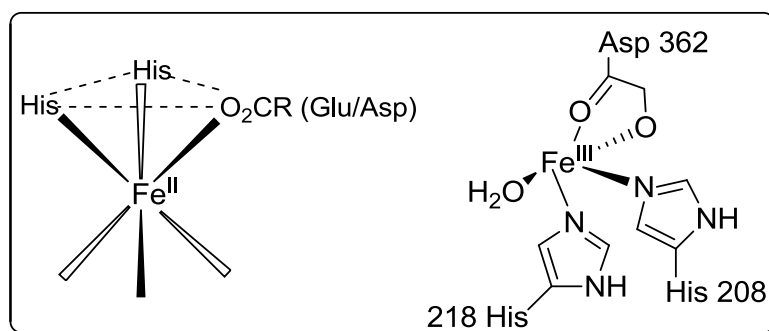
Figure 1.3: The common structural motif "2-His-1-carboxylate facial triad" for non-heme mononuclear iron enzymes (Left); Molecular structures of the active centres in Rieske dioxygenase (Right).

Redox innocence nature of coordinated nitrogen based ligand from amino acid residues unlike heme porphyrin (redox non-innocent), helps these enzymes to store two oxidizing equivalents in the metal center thereby facilitating formation of an $Fe^V(O)$ oxidant. To date, there is no direct spectroscopic evidence for a non-heme $Fe^V(O)$ species during the enzymatic cycle. However, the iron(III)–peroxo precursor on non-heme enzymes has been characterized by X-ray crystallography. It has been proposed that these enzymes form an high-valent iron oxo-hydroxo species [$Fe^V(O)(OH)$] as an active oxidising agent during monooxygenation, dioxygenation and desaturation via activation of dioxygen. One of the most studied example of this family is naphthalene 1,2-dioxygenase (NDO),[36, 38] which is a representative for other cis-dihydroxylating enzymes including benzoate 1,2-dioxygenase,[38] benzene dioxygenase [39] and phthalate dioxygenase.[40] Examples of a few dinuclear non-heme enzymes are methane monooxygenases, toluene monooxygenase and tyrosinases etc. For example, the di-iron enzyme methane monooxygenase (MMO, Figure 1.4)[28] activates O_2 to catalyse the conversion of methane to methanol via di-iron(III)–peroxo and diiron(IV) intermediates.
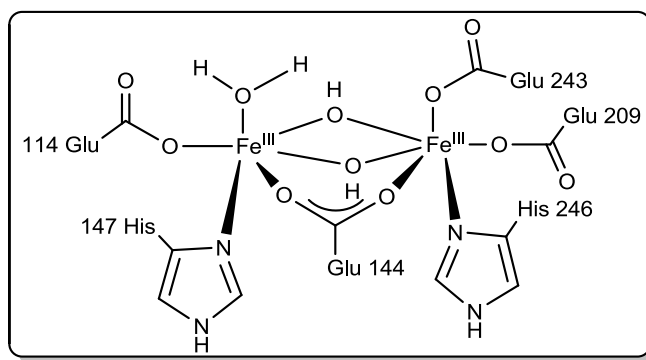
Figure 1.4: Molecular structure for the active site of the dinuclear non-heme iron enzyme methane mono oxygenase (MMO).

1.3   Understanding the Mechanism of Oxygen atom transfer to C–H and C=C bonds by Metal oxo intermediates

1.3.1 C-H bond oxygenation mechanism

Nature activates dioxygen and hydrogen peroxide to catalyze a variety of oxidation reactions such as O-atom transfer to C–H and C=C bonds. Monooxygenases enzyme utilize O_2 and 2e⁻ (provided by NADH or NADPH) to hydroxylate the C–H bond according to the following scheme: [23]

$$R\text{-}H + 2e^- + 2H^+ + O_2 \rightarrow R\text{-}OH + H_2O$$

During C-H abstraction by the high-valent iron-oxo species which contain multiple bonds: one σ bond and at least one π bond that comes from the donation of electrons on the oxygen atom into empty orbitals on the metal center. This donation causes the oxo ligand to be electrophilic. These electrophilic oxo-iron complexes react with alkanes to form an iron-bound hydroxo ligand and an alkyl radical, which then subsequently reacts rapidly with the resulting hydroxo ligand in a "rebound" step to form the alcohol product (Scheme 1.3). This mechanism is selective for the weakest C–H bond in the molecule, i.e., sp^3C–H $> sp^2$C–H and tertiary > secondary > primary. Such a mechanism is observed during biological oxidation of hydrocarbons with enzymes.
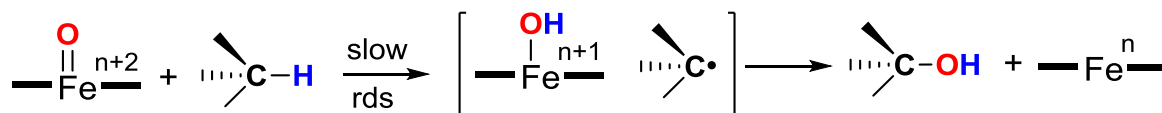
Scheme 1.3: General mechanism for hydroxylation: 'rebound mechanism.

H-atom transfer (HAT) typically involves the simultaneous transfer of an electron and a proton along a common path. During, C-H activation reactions mediated by metal–oxo intermediates, where the electrons and protons are transferred to different sites (proton to the oxo group and the electron to the metal ion through a concerted proton and electron transfer mechanism (CPET); emphasized the importance of the Bordwell/Polanyi[41] relationship in determining the thermodynamic affinity towards hydrogen atom abstraction. The thermochemical affinity (BDE). of $1H^+/1e^-$ (PCET) is equivalent to the affinity of the oxidized metal–oxo species for an electron (redox potential $E_{1/2}$ in V for the Fe^{n+2}(O)/Fe^{n+1}(O) couple and the affinity of the reduced metal–oxo species for a proton (acid dissociation constant K_a of the conjugate base Fe^{n+1}-OH), because a hydrogen atom is equivalent to $H^+ + e^-$ (see the thermodynamic cycle shown in Figure 1.5). Determination of BDE by this equation was first proposed by Bordwell and coworkers. [41] One of the examples for BDE calculation for CytP450 is discussed here (Figure 1.5).
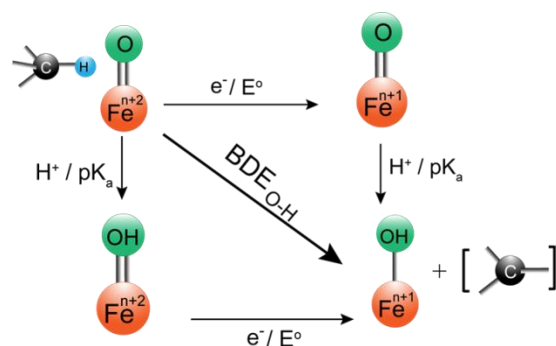
$$BDE(O\text{-}H) = 23.06 E°_{Fe^V(O)} + 1.37 pK_{aFe^{IV}\text{-}OH} + C$$

C is solvent constant.

Figure 1.5: Schematic presentation for calculation of BDE(O-H) of CytP450.

The calculated BDE(O-H) value of any metal oxo intermediate can explain the reactivity of C-H abstraction reaction. In case of CytP450, Michael T. Green *et al.* [42] determined that the rate constant for the cleavage of an unactivated C–H bonds by active oxidant Compound I was as high as 1.1×10^7 $M^{-1}s^{-1}$. This unusual high reactivity of the CytP450 in oxidizing strong C–H bonds is unexpected in comparison to Horseradish Peroxidase (HRP) although both of them are structurally similar, i.e., both contain Fe-heme except for the axial ligand bound to the Fe (thiolate for CytP450 and histidine for HRP).
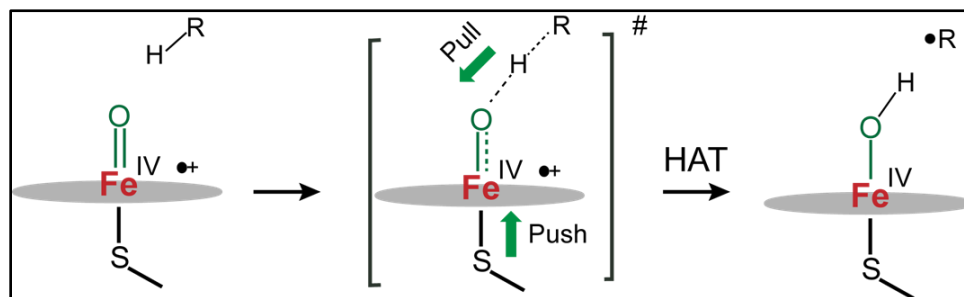
Figure 1.6: The oxygen rebound mechanism showing push-pull assistance of hydrogen atom transfer (HAT) mediated by the heme center of a P450 enzyme (bottom).

The ability of CytP450 to oxidize strong C–H bonds have been studied in great detail from past few years.[43] Experiments showed that the compound I of CytP450 abstracts H-atom from C–H bond of the substrate to yield an Fe^{IV}-OH species (protonated compound II) and a carbon radical without oxidising its own fragile protein network (tyrosine -OH group and other

functional groups in protein side chain). According to the Brodwell equation, the BDE(O-H) value can be controlled by two parameters, i.e., the pK_a and E^o value. The E^o value of the $Fe^{IV}(O)^{+\cdot}/Fe^{IV}(O)$ redox couple of CytP450 should be lower than 1 V to avoid the non-productive oxidation reactions. Both tyrosine and tryptophan have redox potential around 1 V or depending on their location in the protein moiety. CytP450 avoid this non-productive oxidation by increasing the pK_a of the $Fe^{IV}(O)$, due to axial thiol ligand that is bound to it *via* Cys. Thiolate is a strong electron donor and this electron 'push' from thiolate makes the $Fe^{IV}(O)$ oxygen very basic (Figure 1.6). Michael Green and coworkers were able to measure this pK_a to be around 12 for CYP 158-II and CYP 119-II (other class of thiolate-ligated CytP450). This higher pK_a of $Fe^{IV}=O$ (basic Fe=O) translates to high BDE(O-H) for the enzyme and is thus capable of cleaving strong C–H bonds of unactivated alkanes.

1.3.2 C=C bond oxidation mechanism

There are three main types of transition metal intermediates mediated an oxygen atom transfer to the alkenes: (i) oxo-metal complex (ii) metal-peroxo and (iii) metal mediated peroxo radical. The oxo-metal complexes from the middle of the transition metal series (e.g. Cr, Mn, Fe) are the main reactive intermediate towards the alkene epoxidation.[44, 45] These metal centers are consist of partly filled d-electrons which can be perturbed by structural and electronic changes through ligand modification. Furthermore, the metal-peroxo complexes are formed in the early transition metal series, where the transition metals are in highest oxidation state such as Ti^{IV}, V^V, Mo^{VI} and W^{VI}.[46] These metal-peroxo intermediates can catalyze epoxidation reaction with a variety of alkenes. For metal peroxo mediated epoxidation, formation of peroxometallacycle intermediate has been proposed due to attack of one of electrophilic peroxygen from metal peroxo species (Scheme 1.4(i)).[46] Similar to the metal peroxo, two type of intermediates have also been proposed for the transfer of oxygen atom from oxo-metal complex to an alkene: interaction of the oxygen atom of oxo-metal with C=C or interaction of the alkene with both oxygen atom and the metal center to form a metallacycle (Scheme 1.4(ii)).[47] The peroxo radicals are mainly operating where the systems can undergo electron-transfer process (Co, Ni) and the epoxidation takes place for alkenes in which abstraction of allylic hydrogen is disfavored compared to addition of C=C double bond.[48]

1.3.3 Theoretical insight of oxidation reactions by heme enzyme

        Insights into the oxidative reactivity of the M=O moiety in heme enzyme can also be obtained from DFT analysis. DFT analysis on heme-enzyme showed that the d^4 configuration $(d_{xy}^2 d_{yx}^1 d_{zx}^1)$ of the iron center can either antiferromagnetically or ferromagnetically couple to the unparied electron of porphyrin a_{2u}^1 (π- radical), leading to two different low-lying spin states: doublet ($S = 1/2$), and quartet ($S = 3/2$) (Figure 1.7). According to Figure 1.7 in course of H-atom abstraction, an β or α electron shifts from the $\sigma_{C\text{-}H}$ orbital of desired C-H bond to the singly occupied a_{2u} orbital in quartet and doublet states, respectively, leading to intermediate spin state of Fe^{IV} centers that are antiferromagnetically or ferromagnetically coupled to the substrate radical. In the rebound steps, the electron will shift from carbon center radical to the iron(IV) center to form the iron-hydroxo(Fe^{III}-OH) complex. In the case of doublet state, the rebound process involves from carbon centered radical to the low-lying d_{XZ}^1(FeO) orbital and thereby is nearly barrier-free. Whereas for the rebound step in quartet state the electron has to be shifted into the higher-lying empty d_Z^2 orbital thus leading to a significant rebound barrier.[49]
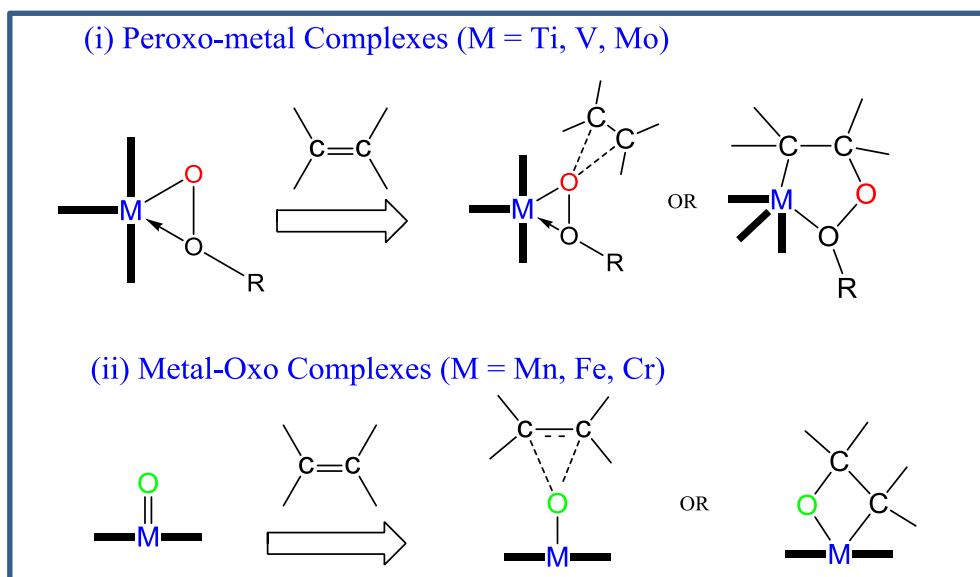
Scheme 1.4: Proposed intermediates for the reaction of alkenes with transition metal oxo and peroxo species.
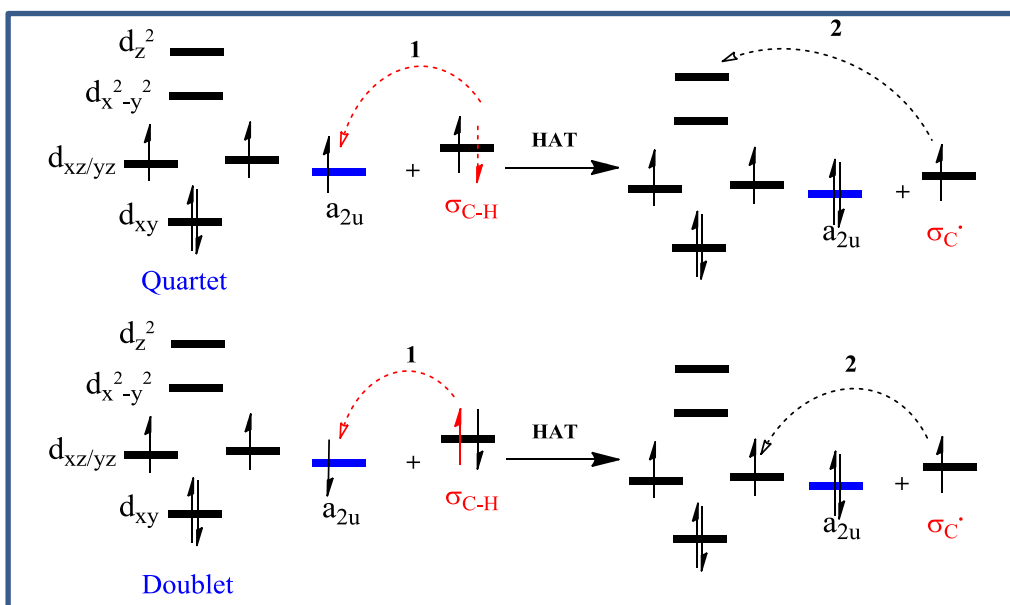
Figure 1.7: Schematic summary of the electronic changes along the C-H abstraction (1) and rebound (2) reaction pathway in the heme-base iron(IV)-oxo radication intermediate.

For the OAT process, on the other hand, two electrons need to be transferred simultaneously to the σ^* and π^* orbitals of the M=O core. The OAT and HAT reactivities of metal oxo cores can, therefore, be markedly affected by the properties of the supporting ligands such as electron density, and sterics, as well as the nature of the variable cis or trans ligands and also the spin states of the metal center. Whereas OAT reactions will be solely controlled by the $Fe^{IV+\cdot}(O)/Fe^{IV}(O)$ reduction potentials.[80]

1.4 Biomimetic Heme Ligands and Reactivity of their High-valent Oxo Species

Inspire by Nature, iron(III) porphyrin complexes have been synthesized and studied extensively as the biomimetic models for heme-containing enzymes. Systematic studies of stability and catalytic activity of heme high valent analogs lead to the successive generations of porphyrin ligands.[50] The first generation "flat metalloporphyrins" (with no substituents at the meso positions, Figure 1.8) were rapidly substituted by a series of porphyrin complexes having various substitution at meso position, due to very fast oxidation of the ligand framework.[51] The second generation is represented by substituents at the ortho, meta and para position of the phenyl ring by alkyl or halogen groups (Figure 1.8), e.g., *meso*-tetrakis(pentaflurophenyl) porphyrin TPFPP[52], *meso*-tetramesitylporphyrin (TMP)[53], *meso*-tetrakis(2,6-

difluorophenyl)porphyrin (TDFPP) and *meso*-tetrakis(2,6-dichlorophenyl)porphyrin (TDCPP).[54, 55] Similarly, the third generation catalysts were synthesised on the previous idea by introducing halogens at the β-position of pyrrols to make it more electron defficient. These include example of *meso*-tetrakis(2,6-diclorophenyl)-β-octabromoporphyrin, Br$_8$TDCPP,[56] *meso*-tetrakis(2,6-dichlorophenyl)-β-octachloroporphyrin, Cl$_8$TDCPP[57], *meso*-tetramesityl(2,6-dichlorophenyl)-β-octachloroporphyrin Br$_8$TMP[58] etc. Very recently, positively charged bulky substitution on porphyrin meso position showed dramatic enhancement of hydrogen atom transfer reactivity.

Biomimetic model Fe(III)-porphyrin heme complexes, first reported by Groves *et. al.* in 1979[59, 60] displayed selective oxidation of unactivated hydrocarbons like cyclohexane and adamantane to cyclohexanol(8%) and adamantanol (13%, 3°:2° selectivity of 48:1 for adamantane) in the presence of excess iodosyl benzene. These oxidants were shown to form the Fe(III)-OOR porphyrin species with various terminal oxidant, which subsequently underwent heterolytic cleavage of the O-O bond to form the active Fe^{IV}(O) radical cation (Mössbauer spectrum of the intermediate showed a quadrupole doublet centered at 0.05 mm/s with ΔEq = 1.49 mm/s which is similar to previously reported HRP δ = 0.08 mm/s and ΔQ = 1.25 mm/s).[60,61] The competition between homolytic *vs* heterolytic cleavage of O-O bond (Scheme 1.5) has been studied by Nam *et al.* and other in great details by using several mechanistic probes[62] (^{18}O$_2$, *cis*–DMCYH, MPPH, and *z*-stilbene).
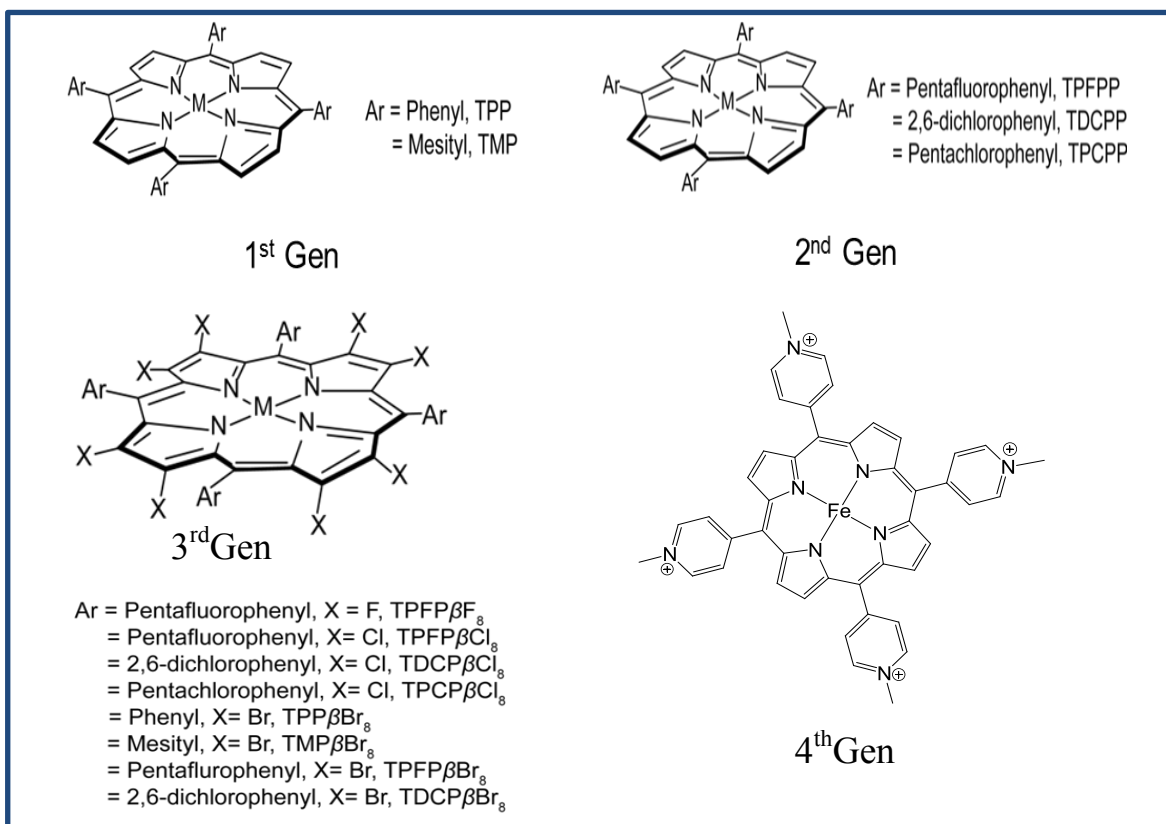
Figure 1.8: Different generation of porphyrin model catalyst
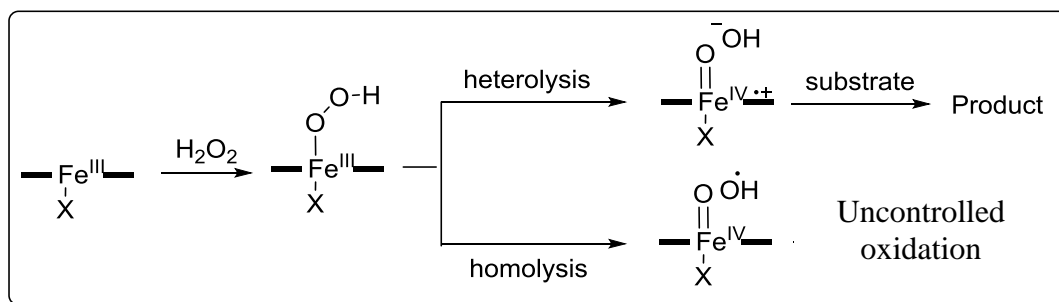
Scheme 1.5 Proposed mechanism for the formation of active oxidant from Fe^{III}-OOH for synthetic heme model complexes complexes.
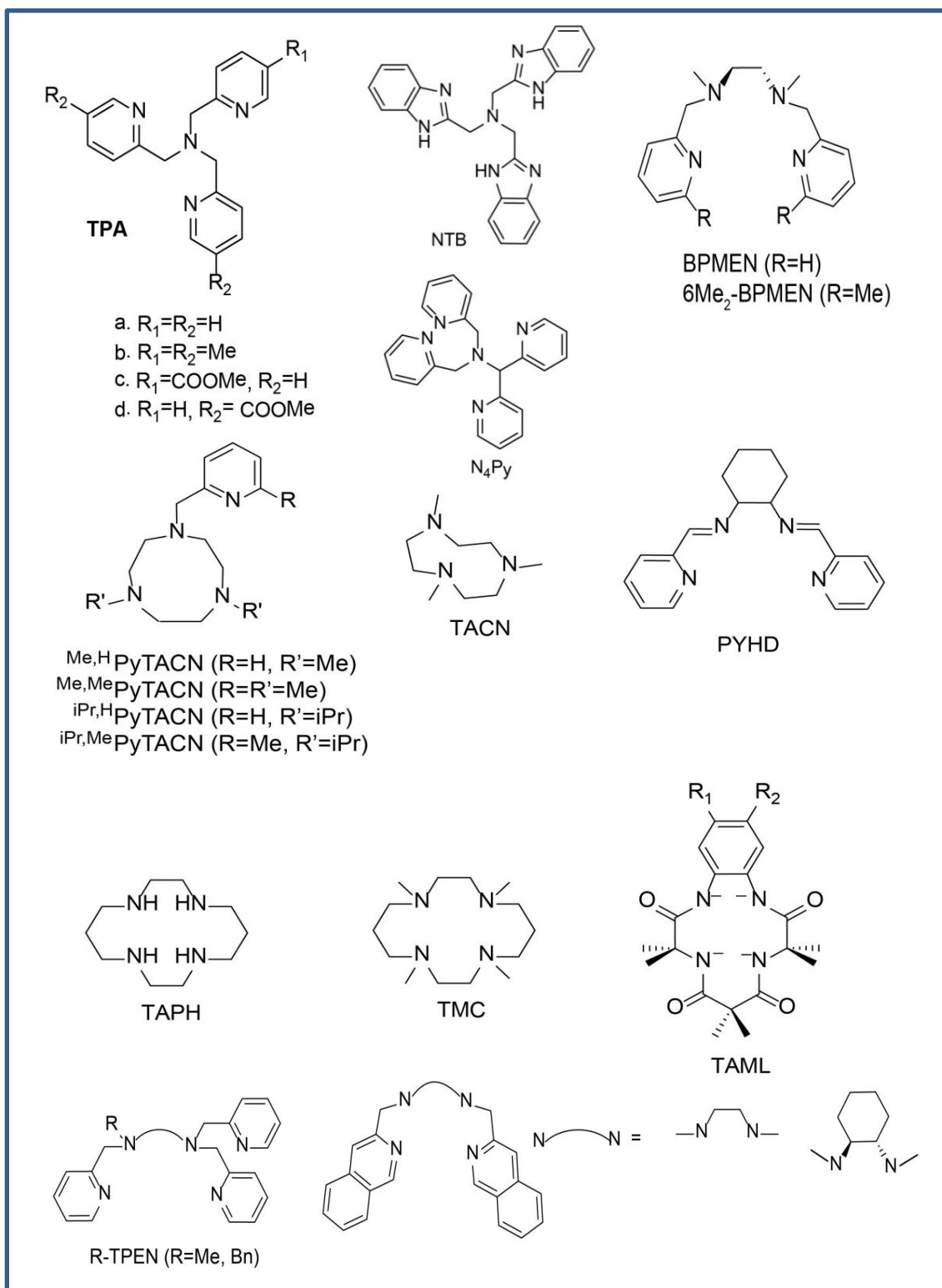
Figure 1.9: Some of the non-heme ligands used to generate high-valent iron(IV)-oxo complexes.
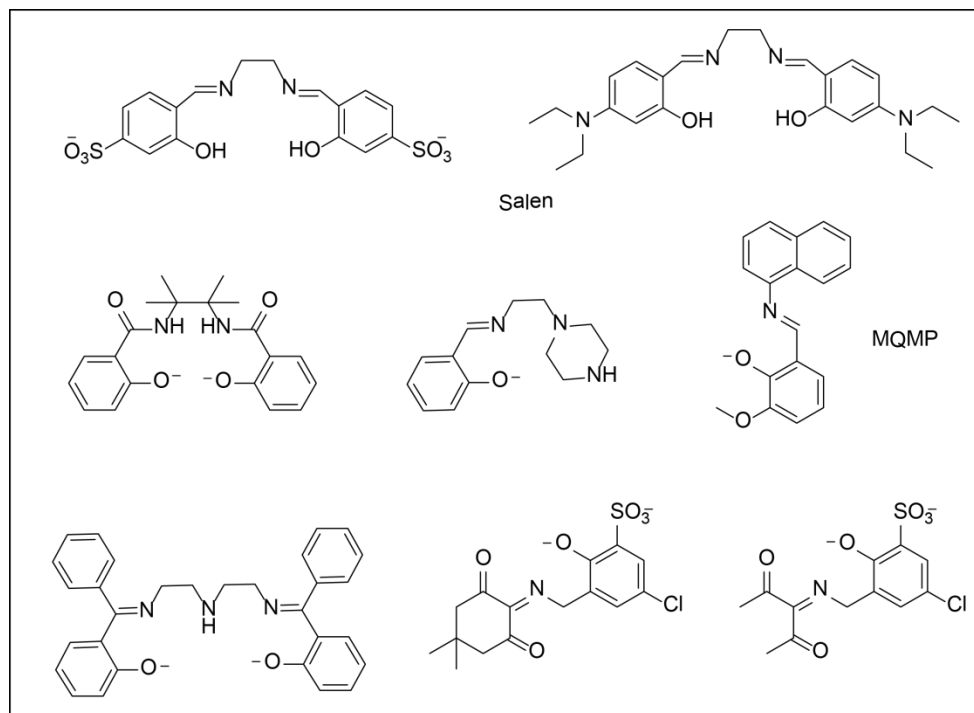
Figure 1.10 Salen and phenolate O-donor ligands used for C–H activation

1.5 Non-heme iron oxo analogues and theoretical understanding of their reactivity

1.5.1 Non-heme iron oxo analogues and their reactivity

To develop a functional mimic of non-heme enzymes, the bioinspired approach has been employed by designing organic ligands that would contain the amino acids that are bound to the Fe-center of the natural enzyme.[63a] Most of the nonheme iron complexes bearing multidentate imine N-donor ligands have been studied in detail for years.[63b] Synthesised iron complex using various N-donor ligand showed very high selectivity and reactivity towards oxidation of C–H and C=C bonds. This field is more appealing because of its relatively straightforward ligand modification compared to porphyrin ligands, which leads to numerous catalysts that are prepared and studied. Figure 1.9-1.10 depicts some of the non-heme ligands that have been studied to date.

The terminal oxidant oxidizes synthetic nonheme iron complexes to form high-valent iron-oxo which reacts with C-H selectively by ruling out the possibility of 'Fenton reaction (Scheme 1.6) ' which is related to non-selective reactions mediated by free oxygen atom centered radicals.[64-66]

$$\text{(i)} \quad Fe^{III} \ + \ ROOH \ \longrightarrow \ Fe^{II} \ + \ ROO^{\cdot} + \ H^{+}$$

$$\text{(ii)} \quad Fe^{II} \ + \ ROOH \ \longrightarrow \ Fe^{III} \ + \ RO^{\cdot} + \ \overline{O}H$$
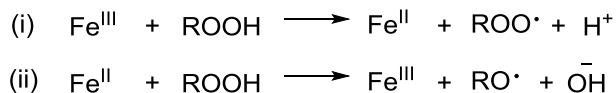
Scheme 1.6: Fenton-Haber-Weiss type reaction by iron(II) and iron(III) metal center.

1.5.2 Theoretical insight of C-H and C=C oxidation by non-heme model complex

Detail understanding of the oxidative reactivity by iron-oxo moiety can also be derived from considerations of simple ligand-field theory.[67] The reactivity of these iron-oxo complexes depend upon two factors firstly spin state of iron-oxo species and secondly the substrate approach toward Fe=O moiety. Due to the consequence of tetragonal compression associated with the strong Fe=O bond in C_{4v} symmetry, the d orbitals sequence according to energy will be $d_{xy} < d_{xz,yz} < d_{x^2-y^2} < d_{z^2}$ (see Figure 1.11). The energy order of $d_{x^2-y^2}$ and d_{z^2} orbital can be varied depending upon the nature of bonding in the equatorial plane, e.g., for weak equatorial donating ligand d_{z^2} will be highest in energy, but for strong equatorial bonding, $d_{x^2-y^2}$ will be highest in energy. The $d_{x^2-y^2}$ and d_{z^2} orbitals form strongly antibonding combinations with the σ orbitals of the ligands while the d_{xz} and d_{yz} orbitals lead to antibonding π^* orbitals by interacting with the p_x and p_y orbitals of the oxo group. The key frontier molecular orbitals (FMOs) involved in the HAT and OAT process are the π^* $d_{xz/yz}$ and the σ^* d_{z^2} orbitals. The hydrogen atom transfer from the σ(C-H) orbital to the $Fe^{IV}O$ species (solid arrows; Figure 1.11) will result in protonation of the oxo atom to from Fe-OH species and the injection of an electron into either a σ^* or a π^* orbital of iron-oxo will lead to a one-electron reduced iron-oxo species. The exact nature of the electron acceptor orbital will depend on the relative energies of the d_{z^2} and $d_{xz/yz}$ orbitals, which will be controlled by the electronics of the coordinated ligand and the covalency of the iron-oxo bond. As described earlier the orientation of substrate approach will also have crucial role in C-H activation. The cleaving C-H bond may attack the iron(IV)-oxo unit either from the top or an equatorial position (σ and π pathways respectively).[68] Both types of geometries in transition state lead to different reaction pathways. To maximize the overlap between the d_{z^2} and the σ_{C-H} orbitals in the σ pathway (Figure 1.11), the system directs a vertical approach of the target C-H bond towards the Fe=O core and the reaction will proceed through quintet spin state, thereby leading to a linear Fe-O-H arrangement. In contrast, the π channel involving $d_{xz,yz}$ based electron acceptor orbitals typically exhibits a bent Fe-O-H angle and the

reaction will go through triplet spin state. The steric interaction between the substrates and metal chelates as directed by the FMOs associated with the HAT step will, therefore, be of great importance in controlling the reactivity of metal–oxo cores toward C-H bonds. For oxo iron(V) species such pathways have not explored in great details probably due to unstability of oxoiron(V) species. Therefore, from all the theoretical studies it can be summarised that the quintet spins state oxo-iron species are aggressive oxidants than the corresponding triplet counterparts. Analysis of the changes in electronic structure along the reaction coordinate revealed that increased Pauli repulsion and attenuated orbital interaction increase the barriers for the triplet π-pathway.[49, 69 ,70]
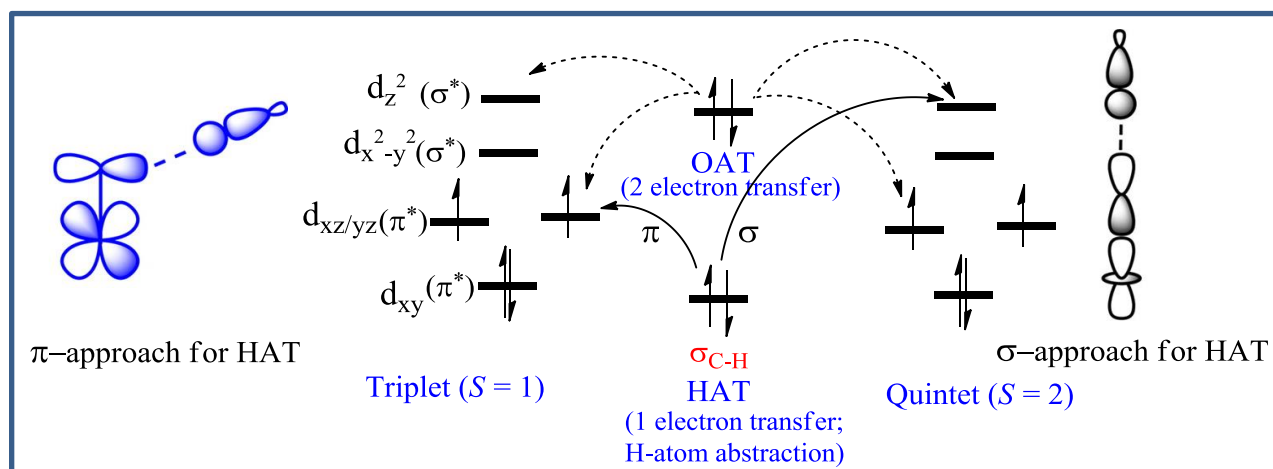
Figure 1.11: Schematic summary of the electronic structure changes along the H-atom abstraction (HAT) and O-atom transfer (OAT) reaction pathway in the triplet and quintet state of mononuclear non-heme iron(IV)-oxo complexes.

Direct experimental evidence for the higher reactivity of the quintet state ($S = 2$) is lacking in the literature because the majority of model complexes prefer the triplet ground states. A few recently reported iron(IV)oxo complexes having sterically bulky ligand framework in quintet spin ground state, showed reactivities toward C-H bond cleavage that are only comparable with their triplet spin state.[71] The OAT rate will solely depend upon the redox potential of iron-oxo species

1.6 Formation and characterisation of High-valent oxoiron species

The first fully characterized mononuclear nonheme oxoiron(IV) species was identified in 2000 by Weighardt and co-workers with $[Fe^{III}(cyclamacetato)(CF_3SO_3)]^+$ and ozone as an oxidant in acetone/ water mixture at –80°C.[72] The first X-ray crystal structure of an oxoiron(IV) ($S = 1$) was reported by Münck, Nam, Que, and their coworkers which was generated by oxidizing $Fe^{II}(TMC)(CF_3SO_3)_2$ with iodosyl benzene (PhIO) in CH_3CN at –40°C.[73] The pale green intermediate was characterized by UV–vis spectroscopy, ESI-MS, EPR, Mössbauer, Resonance Raman, magnetic circular dichroism and assigned as $[(TMC)Fe^{IV}=O]^{2+}$ (Figure 1.12). The EPR spectra for $Fe^{IV}(O)$, $S = 1$ shows no signal since the d^4 electronic configuration is EPR silent in the X-band. The assignment of oxidation state was predominantly done on the basis of Mössbauer, EXAFS, and EXANES spectroscopy. After the first discovery of mononuclear non-heme oxoiron(IV) intermediate, several oxoiron(IV) species with macrocyclic tetradentate N4, tripodal tetradentate N4, and pentadentate N5 and N4S ligands were reported using various oxygen atom donors such as PhIO, peracids (*m*CPBA and peracetic acid), $KHSO_5$, O_3, NaOX (X = Cl or Br), hydroperoxides (e.g., H_2O_2 and ^tBuOOH) and molecular oxygen (Figure 1.12).[62] Two-electron oxidation of Fe(II) to the Fe(IV) oxo species was proposed when single-oxygen atom donors oxidant (PhIO, NaOCl, etc.) have been used as a terminal oxidant (reaction a). While hydroperoxides used as a oxidant (reaction b) Fe(III)–OOR species was homolytically cleaved to form oxoiron(IV) species. For molecular O_2 activation (reaction c), mechanism of generation of $Fe^{IV}(O)$ species depends on electronics of iron(II) complexes and presence of pH atom donor in reaction mixture. In absence of a H-atom donor the ironsuperoxide species can take one electron from resting Fe(II) to from a peroxodimetallic system which will homolytically cleaved to two molecules of oxoiron(IV). In presence of H-atom donor the O_2 activation by iron complex can follow the reaction path b.

a) Single O-atom donors

$$[(L)Fe^{II}]^{n+} + X\text{-}O \longrightarrow [(L)Fe^{IV}=O]^{n+} + X$$

b) Hydroperoxides

$$[(L)Fe^{II}]^{n+} + ROOH \longrightarrow [(L)Fe^{III}\text{-}OOR]^{n+}$$

c) Molecular Oxygen
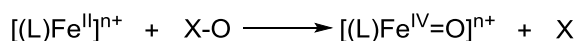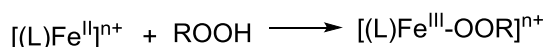
$$2[(L)Fe^{II}]^{n+} + O_2 \longrightarrow [(L)Fe^{III}\text{-}O\text{-}O\text{-}Fe^{III}(L)]^{2n+} \longrightarrow 2[(L)Fe^{IV}=O]^{n+}$$
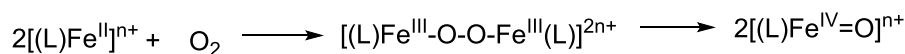
To date, a large number of non-heme Fe^{IV}-oxo species has been synthesised, characterised, and tested for C-H abstraction as well as epoxidation reaction but most of them demonstrate weak oxidative reactivity in comparison to its one-electron oxidized species (formally $Fe^{V}(O)$ oxidant) which is a key intermediate in the catalytic cycles of several iron enzymes that carry out difficult oxidations.[62] Rieske dioxygenases enzyme use O_2 to form oxoiron(V) which efficiently dihydroxylate C=C bonds in the biodegradation of aromatic complexes. However, there is a paucity of well characterized $Fe^{V}(O)$ species, some of which are listed below (Table 1.3, Figure 1.13). Most of the $Fe^{V}(O)$ species have been proposed based on only mass spectral and EPR evidences since their instability at room temperature and purity has eluded complete characterization by several spectroscopic technique (Table 1.3).
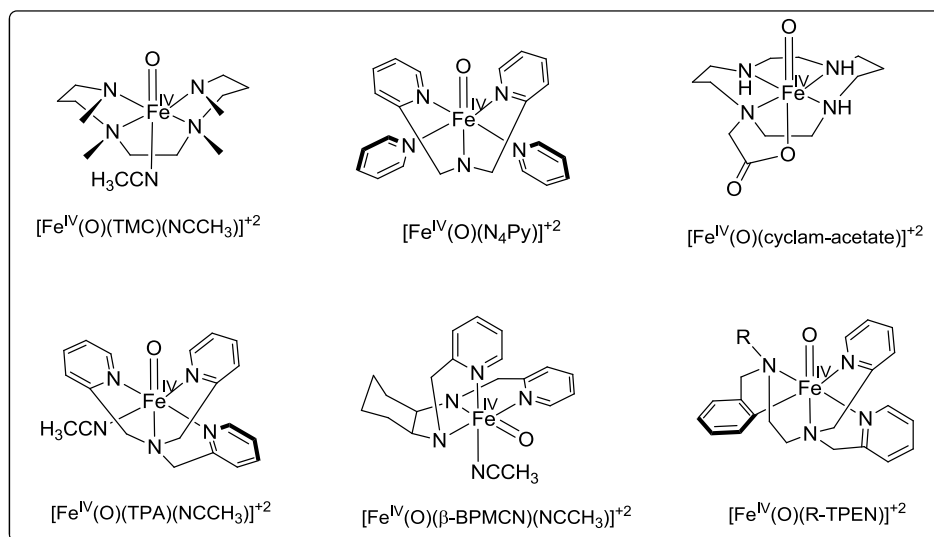
Figure 1.12 $Fe^{IV}(O)$ species reported for different non-heme ligands.
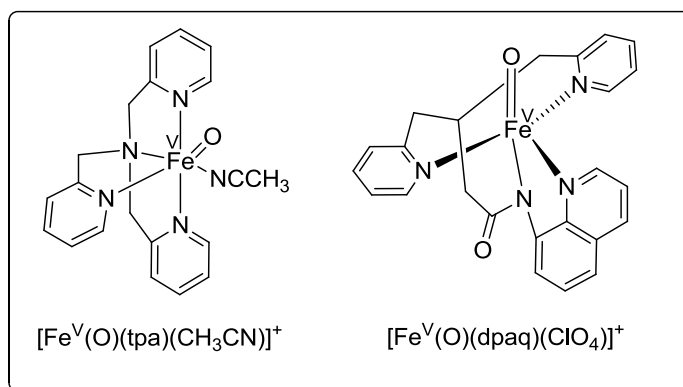
Figure 1.13 Proposed structures of $Fe^{V}(O)$ for non-heme ligands.

Table 1.3 Repoted partially charaterized $Fe^V(O)$ complexes and their formation conditions.

Complex	Reaction Condition	Spectroscopic Characterisation	Reaction
[74][Fe^V(O)(dpaq)](ClO$_4$)$^+$	H$_2$O$_2$ At -40 ^{o}C	Cold-spray Ionization mass spectrometry	Hydroxylation of cis-1,2-DMCH, Cyclohexane
[75][Fe^V(O)(tpa)(CH$_3$CN)]$^+$ [76][Fe^V(O)(bpmen)(CH$_3$CN)]$^+$	mCPBA, CH$_3$CO$_3$H, at -60 ^{o}C	EPR spectroscopy	Cyclohexene epoxidation
[77][Fe^V(O)(OH)(PyTACN)]$^+$	H$_2$O$_2$, H$_2$O at -40 ^{o}C	Cryospray Ionization mass spectrometry	Hydroxylation of cis-1,2-DMCH, epoxidation
[78][Fe^V(O)(TMC)(NC(O)CH$_3$]$^+$	^{t}BuOOH at −44°C	UV-vis, EPR spectra, Resonance Raman, Mössbaüer	

To date, only one spectroscopically well-characterized example of an Fe^V(O) based on the TAML[79] ligand framework (tetraamidomacrocylclic ligand, Scheme 1.7) and a modified TAML[80] (bTAML; biuret modified tetraamidomacrocylclic ligand, Scheme 1.8) is known in literature. The highly electron rich deprotonated amidate ligand coordinated iron complex form high-valent oxoiron(V) at -60°C in butyronitrile solvent when treated with 2.5 equivalent of mCPBA (Scheme 1.7). This green colored oxoiron(V) intermediate has been characterized by EPR (*S* = ½), ESI-MS, EXAFS (showing Fe-O bond length of 1.60 Å) and Mössbauer study (quadrupole splitting ΔE_Q = 4.25mm/s and isomer shift δ = −0.46(2) mm/s).[79] However, the unstability of this species at room temperature restricted its application in organic synthesis. The deactivation pathways of TAML complex was thought to be the intermolecular degradation of ligand moiety (C-H abstraction of dangling malonyl fragment, Figure 1.14). When this malonyl fragment was replaced by a planer biuret fragment which leads to bTAML complex, the reactivity and stability of its high-valent species changes drastically.[80] The bTAML iron complex stabilizes oxoiron(V) at room temperature with an half-life of four hours (Scheme 1.8).[80]
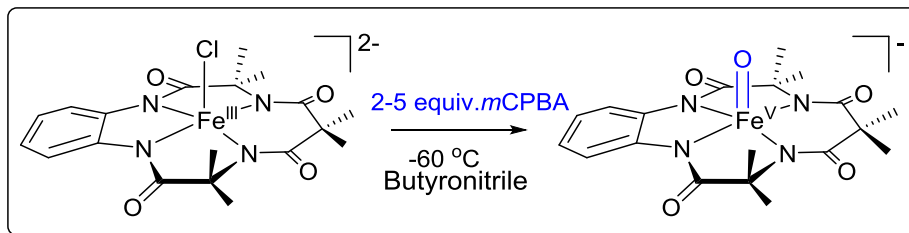
Scheme 1.7: Formation of Fe^V(O) from Fe-TAML system at -60 ^{o}C temperature.
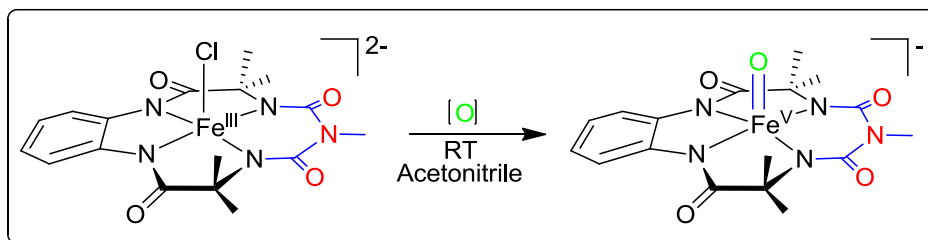
Scheme 1.8: Formation of Fe^V(O) from Fe-bTAML system at room temperature.
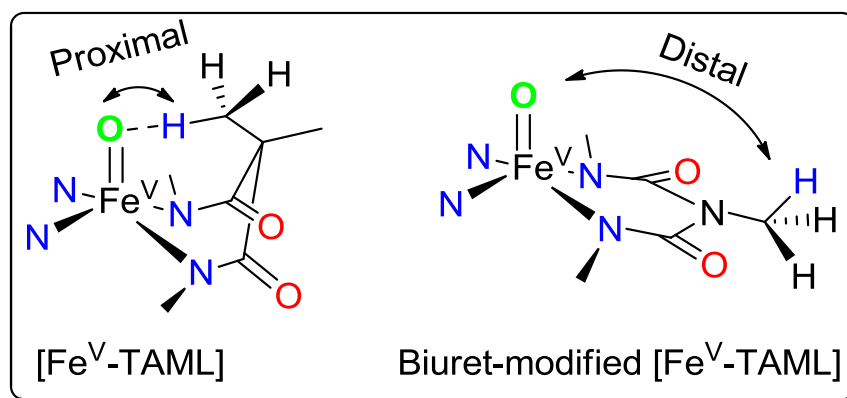
Figure 1.14: Presentation of potential intra-molecular hydrogen abstraction by the high-valent Fe^V(O) intermediate species leading to demetallation (oxidative decay) in case of Fe-TAMLs and biuret-modified Fe-TAML.

1.7 Effect of axial and equatorial ligand on the reactivity of iron-oxo complexes

High-valent ironoxo(IV) porphyrin species have been invoked as key intermediates in the catalytic cycles of heme iron enzymes, such as cytochromes P450, peroxidases, and catalases (Figure 1.15).[81] The proximal axial ligand in natural enzymes are thought to play an important role in tuning the reactivities of iron(IV)-oxo porphyrin p-cation radicals (compound I; Cpd I, Figure 1.15).[82]
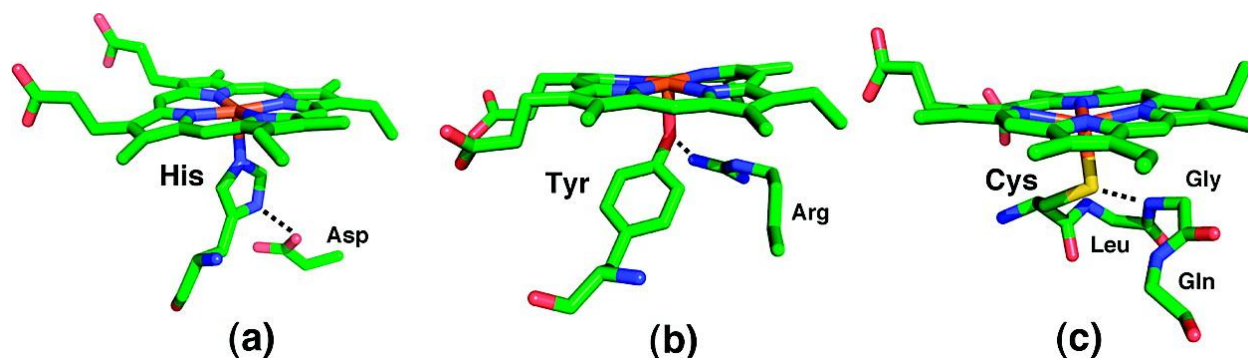
Figure 1.15: Active site structures of (a) peroxidase (HRP, PDB file 1DZ9), (b) catalase (*BL*-CAT, PDB file 2A9E), and (c) cytochrome P450 (Cytochrome P450cam, PDB file 1HCH).

Interestingly, in case of thiolate-ligated enzymes (CytP450) it has been observed that the electron donation from the axial ligand to the iron center increases the basicity of the iron-oxo group, thereby allowing a hydrogen atom to be abstracted from C-H bonds by Cpd I under mild conditions. In case of synthetic iron porphyrin complex the axial electron donating ligand increases the basicity of ferryl species thereby increase the hydrogen atom abstraction rate. For epoxidation reaction the higher rate has been explained on the basis of ease of oxo transfer from iron oxo species. The strong axial donation weakens the Fe-O bond which makes oxo transfer to olefin easier. Therefore it has been observed that for iron porphyrin HAT and OAT rates increases with increasing the axial donation strength (Figure 1.16, right).[83, 84]

For compound I (oxoiron(IV)porphyrin radical cation) complexes equatorial electron donating and electron withdrawing substitutions at meso position of porphyrin ligand can alter the reaction rate of higher oxidised heme complexes. Earlier studies on equatorial substitutions (fluoro benzene) at meso position of porphyrin ligand framework indicated that the σ-electron donation substituents increases the reactivity of cpd I (Figure 1.17). Recently, para- or meta trialkyl ammonium functional group substituted phenyl moiety at meso position of porphyrin ligand showed significant enhancement of HAT reaction rates by cpd I.[85]
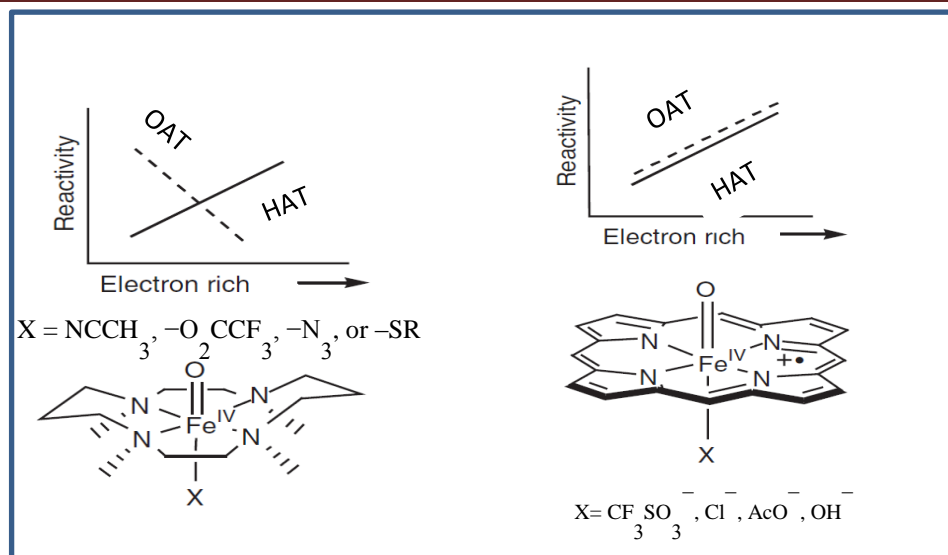
Figure 1.16: Axial ligand effects on the oxo-transfer (OAT) and hydrogen- atom abstraction (HAT) reactivities for a series of $[(TMC)FeIV(O)(X)]^{n+}$ (left) complexes and for a series of $[Fe^{IV}(O)$ porphyrin cation radical] species (right) with various axial donations.
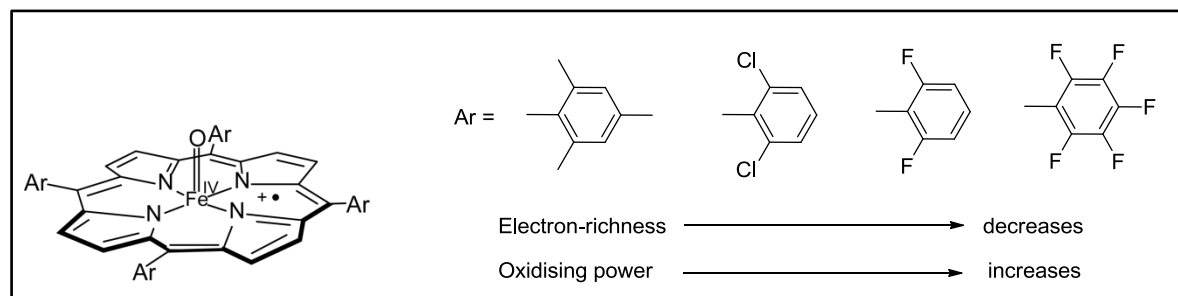
Figure 1.17: Schematic presentation of the relative reactivity by changing the substitution in the porphyrin ligand.

A contrasting HAT reactivity pattern was observed for $[(TMC)FeIV(O)(X)]^{2+}$ when the axially bound $NCCH_3$ ligand was substituted by anions ligands X = $NCCH_3$, CF_3COO^-, N_3^-, and RS^-; Figure 1.16, left).[86] While the reactivity rates of OAT to PPh_3 were found to decrease in the order $NCCH_3 > O_2CCF_3 > N_3 > SR$, consistent with the decreasing electrophilicity of the Fe=O unit. However, the HAT rate increased on the introduction of a more-electron-donating axial ligand. The reactivity of the $[(TMC)Fe^{IV}(O)(X)]^{n+}$ complexes bearing different axial ligands trans to oxo group can be explained on the basis of the change of the energies of the Fe=O σ^* and π^* antibonding molecular orbitals. DFT calculations[87] showed that the substitution of the CH_3CN

ligand by an anion leads in all cases to destabilization of the $d_z{}^2$ and $d_{xz,yz}$ orbitals (Figure 1.18), and stabilization of the $d_x{}^2{}_{-y}{}^2$ orbital. The modulation of Fe=O σ^* and π^* antibonding orbital decrease in the energy gap (ΔE_{TQ}) between the triplet ground state ($S = 1$) and the quintet excited state ($S = 2$), thereby making the more-reactive $S = 2$ state more accessible. Very recently Shaik and co-workers[87] have shown that the effect of a smaller ΔE_{TQ} value in the $[(TMC)Fe^{IV}(O)(X)]^{n+}$ ($X = NCCH_3$, CF_3COO^-, $N_3{}^-$, and RS^-) series plays the crucial role in controlling the reactivity. As the axial donation increases, the $S = 1$ Fe=O core tunnels more efficiently into the $S = 2$ transition state, thereby compensating for the increase in the classical activation barrier and revealing an antielectrophilic trend in the HAA reaction. The OAT reactions mediated by the iron-oxo complexes have been found to parallel the trends in the electrophilicity of the Fe=O core in all but one case.
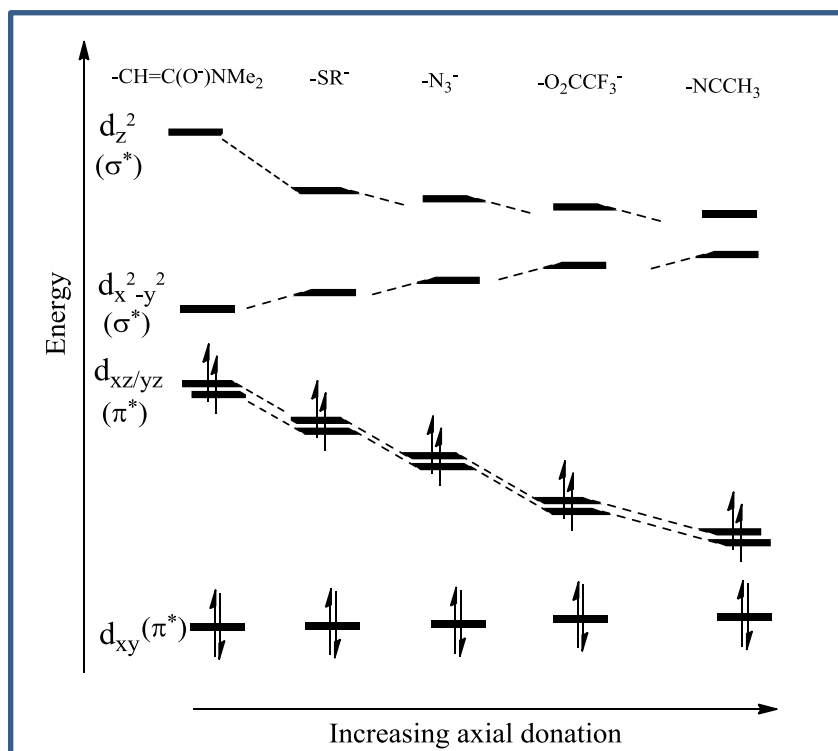
Figure 1.18: Axial ligand effects on the splitting of the 3d levels for a series of $[(TMC)Fe^{IV}(O)(X)]^{n+}$ complexes with various axial donations denoted as X.

1.8 Metal Oxo complex in O-O bond formation reactions

For the past couple of decades, in a quest to develop sustainable energy conversion processes, several scientists from worldwide have attempted water splitting using sunlight.[22, 88, 89]

Renewable energy production are of great interest to control the devastating impact on climate change by fossil's fuel consumption. Water splitting is an energetically uphill and a multi-proton coupled electron transfer (PCET) reaction consists of two processes: water oxidation (WO) leading to oxygen evolution (OE) and proton reduction.[89, 90] In comparison to proton reduction process, a multi-electron transfer WO reaction is much more challenging due to thermodynamic and kinetic limitations. WO is of interest also from a biological perspective, because it is one of the crucial steps that occur in the oxygen-evolving complex of photosystem II (OEC-PSII) in green plants and algae, which are responsible for photosynthesis. The oxygen-evolving complex is composed of metal-oxo clusters of earth-abundant elements manganese[88] and calcium (Figure 1.1) that use sequential cascade reactions to catalyze the four-electron oxidation of water to evolve oxygen (O_2).[91, 92]

The development of a catalyst for water oxidation to evolve oxygen is an important goal for a technology-based water splitting. Extensive efforts have been devoted in the field of WO catalysis especially with regard to the discovery of a large body of molecular transition-metal complexes and active metal oxide NPs with relatively large turnover numbers (TONs ~10000).[93] Most of them involve metal complexes of noble metals (Ru[93, 94-106], Ir[107-113]), polyoxometalates (POM)[95, 114] and metal oxide NPs.[115-119] The homogeneous catalysts have been tested for both chemical oxidation (with a sacrificial oxidant like Ce[IV]) as well as photochemical oxidation (in the presence of a photosensitizer and sacrificial oxidant like $Na_2S_2O_8$) to oxidize water. For ruthenium (Ru) catalyzed WO, high valent Ru[V](O) complexes have been identified as the reactive intermediate responsible for WO.[104, 120] However, the challenge lies in the development of the earth-abundant metal-based catalysts, such as iron complexes for WO, since they are expected to be environmentally benign and cheap.[88, 121, 122] Chemical WO using iron complexes were first reported by Collins, Bernhard, and co-workers employing a fluorine-substituted Fe-TAML as a catalyst and Ce[IV] as the oxidant.[123] Subsequently, Fillol and Costas et al. demonstrated very high TON of WO by using Fe complexes of tetradentate neutral.[124, 125] They demonstrated that a high valent iron oxo species was involved in the O-O bond formation step which is a rate determining step during oxygen evolution. Modulation in steric and electronic property of the liagnds was found to tune the reactivity of iron complexes.[117, 126, 127] Meyer and co-workers have proposed the existence of a Fe[V](O) species during electrochemical WO (without any spectroscopic characterizations) that run with lower catalytic efficiency (TONs of

29 over 15 hours).[128] In an another approach photo-electrochemical WO was achieved by anchoring molecular iron complexes to a solar responsive tungstate.[129] However, the ultimate goal is to develop first-row, transition metal-based systems that catalyze photochemical WO, as sunlight provides the largest renewable energy resource. For first-row transition metals, cobalt[130-132] and manganese[133-135] based molecular complexes, POMs and NPs have been shown to function as efficient catalysts for WO. Recently, Lau et al. have demonstrated that during light-driven WO catalyzed by a number of iron complexes and iron salts at pH 7-9 in borate buffer the active species responsible for WO was not a high valent iron oxo complex but Fe_2O_3 NPs that were formed upon decomposition of the iron complex. [115]
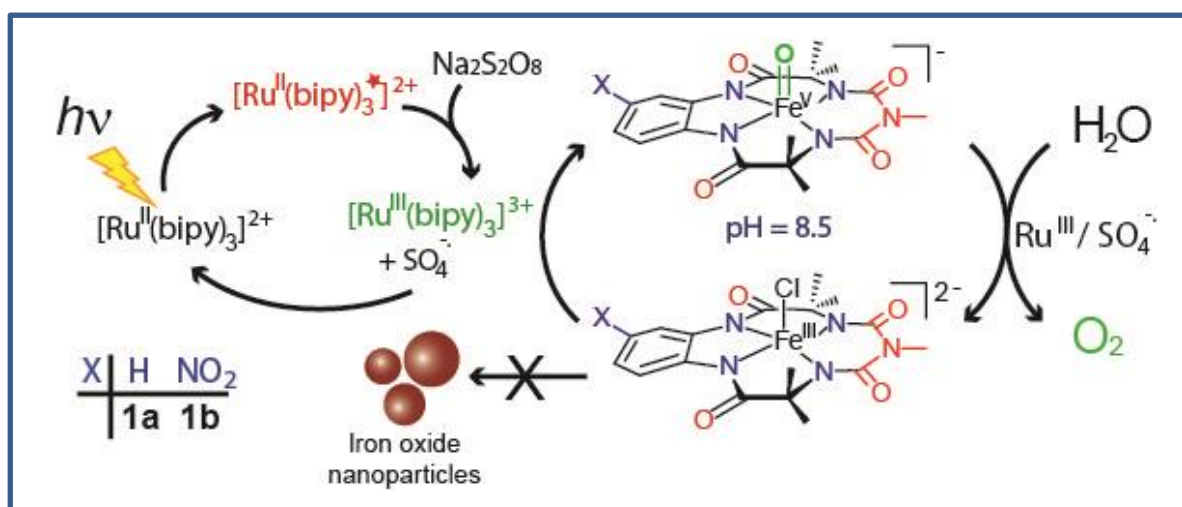
Figure 1.19: Homogeneous photochemical water oxidation using biuret-modified Fe-TAML.[136]

Very recently, during photochemical generation by Fe-bTAML catalyst, a well-defined high valent $Fe^V(O)$ was isolated as one of the key intermediates and elucidate its role in WO (Figure 1.19).[136] Although similar studies showing photochemical formation of a high valent $Fe^{IV}(O)$ have been conducted by Fukuzumi, Nam[137], Costas[138] and co-workers, photochemical WO has not been explored in any of them. Identification of such $Fe^V(O)$ reactive intermediate helps us elucidate the detail mechanism of WO as well as provide insight for designing newer generation WOC based on earth-abundant elements. Further, understanding the reactive intermediate involved in O-O bond formation is also crucial to develop more efficient WOC. This would

allow chemists to understand the electronic properties of the metal complex that can be used to design new WOC with improved activity.

1.9 Objectives and Motivation

High-valent metal–oxo cores have been proposed, and in a few cases isolated, as the common reactive intermediates in these biological reactions relevant to the formation of renewable energy. For selective C-H bond activation higher oxidized species of iron has been proposed for heme and non-heme enzyme. Heme and non-heme containing model complexes have been synthesized, where Fe^{IV}-O cation radical and Fe^{IV}-O are the intermediates. Reactivity and selectivity of an oxidant depends on BDE(Fe_{O-H}), which forms by dissociation of C-H bonds of substrates. For heme and nonheme iron complexes, the effect of axial and equatorial ligand on the reactivity of HAT and OAT have explained by considering a two state theory (TSR model) as proposed by Shaik et al.[87] The Fe^{V}-O intermediate has been proposed and C-H bond activation has been shown but no spectroscopic and theoretical study was performed to understand the reactivity. Further, the use of (bTAML)Fe^{V}(O) has been extended to catalytic reactions, where selective oxidation of tertiary C-H bonds over secondary C-H bonds were observed in a wide range of organic substrates.[139] The mechanism of C–H[80, 140], O–H,[141] and C=C bond oxidation,[142] as well as the role of Fe^{V}(O) in water oxidation, has also been explored using (bTAML)Fe complex.[136] Although, HAT abstraction, OAT and effect of water on HAT by Fe^{V}(O) was highlighted but no spectroscopic insight into HAT reactivity was explained. Fleeting nature of other synthetic iron(V) renders it difficult to obtain structural and mechanistic insights into their inherent reactivity differences with their one electron reduced analogue. In particular, a nitro substituted bTAML complex has been shown to have higher reactivity over the unsubstituted one but the careful understanding of equatorial ligand electronic on HAT and OAT was not reviewed to date. Recently, bTAML iron complex has been used in photochemical WO and Fe^{V}(O) was isolated as an active oxidant but the crucial O-O bond formation mechanism was not understood properly.

Therefore, the main objectives of this work are:

➢ To understand the structure–function relationship of the metalloenzymes

➢ To probe the spectroscopic correlation with C-H abstraction

➢ To understand the detailed mechanism of O-O bond formation

➢ To study the electronic effect on their reactivity towards C-H and C=C oxidation

➢ To develop new catalysts for oxidation reaction based on inexpensive and abundant materials

1.10 References

(1) a) Weissermel, K.; Arpe, H.-J. *Industrial Organic Chemistry*, 3rd ed.; Wiley-VCH: Weinheim, **1997**; b) Derouane, E. G.; Haber, J.; Lemon, F.; Ribeiro, F.; Guisnet, M. *Catalytic Activation and Functionalization of Light Alkanes – Advances and Challenges*; Kluwer Academic Publishers: **1998**; c) Olah, G. A.; Molnar, A. *Hydrocarbon Chemistry*, 2nd ed.; John Wiley and Sons Publishing: **2003**; d) Wittcoff, H. A.; Reuben, B. G.; Plotkin, J. S. *Industrial Organic Chemicals*, 2nd ed.; John Wiley and Sons Publishing: **2004**.; e) Arndtsen, B. A.; Bergman, R. G.; Mobley, T. A.; Peterson, T. H. *Accounts of Chemical Research* **1995**, *28*, 154.

(2) Hashiguchi, B. G.; Bischof, S. M.; Konnick, M. M.; Periana, R. A. *Accounts of Chemical Research* **2012**, *45*, 885.

(3) Labinger, J. A.; Bercaw, J. E. *Nature* **2002**, *417*, 507.

(4) Que, L.; Tolman, W. B. *Nature* **2008**, *455*, 333.

(5) Costas, M.; Mehn, M. P.; Jensen, M. P.; Que, L. *Chemical Reviews* **2004**, *104*, 939.

(6) Hausinger, R. P. *Critical Reviews in Biochemistry and Molecular Biology* **2004**, *39*, 21.

(7) Kovaleva, E. G.; Lipscomb, J. D. *Nat Chem Biol* **2008**, *4*, 186.

(8) Loenarz, C.; Schofield, C. J. *Nat Chem Biol* **2008**, *4*, 152.

(9) Arakawa, H.; Aresta, M.; Armor, J. N.; Barteau, M. A.; Beckman, E. J.; Bell, A. T.; Bercaw, J. E.; Creutz, C.; Dinjus, E.; Dixon, D. A.; Domen, K.; DuBois, D. L.; Eckert, J.; Fujita, E.; Gibson, D. H.; Goddard, W. A.; Goodman, D. W.; Keller, J.; Kubas, G. J.; Kung, H. H.; Lyons, J. E.; Manzer, L. E.; Marks, T. J.; Morokuma, K.; Nicholas, K. M.; Periana, R.; Que, L.; Rostrup-Nielson, J.; Sachtler, W. M. H.; Schmidt, L. D.; Sen, A.; Somorjai, G. A.; Stair, P. C.; Stults, B. R.; Tumas, W. *Chemical Reviews* **2001**, *101*, 953.

(10) Shilov, A. E.; Shul'pin, G. B. *Chemical Reviews* **1997**, *97*, 2879.

(11) Bollinger Jr, J. M.; Krebs, C. *Current Opinion in Chemical Biology* **2007**, *11*, 151.

(12) Bruijnincx, P. C. A.; van Koten, G.; Klein Gebbink, R. J. M. *Chemical Society Reviews* **2008**, *37*, 2716.

(13) Hohenberger, J.; Ray, K.; Meyer, K. *Nat Commun* **2012**, *3*, 720.

(14) Krebs, C.; Price, J. C.; Baldwin, J.; Saleh, L.; Green, M. T.; Bollinger, J. M. *Inorganic Chemistry* **2005**, *44*, 742.

(15) Nam, W. *Accounts of Chemical Research* **2007**, *40*, 465.

(16) Poulos, T. L. *Chemical Reviews* **2014**, *114*, 3919.

(17) Rolff, M.; Tuczek, F. *Angewandte Chemie International Edition* **2008**, *47*, 2344.

(18) Shaik, S.; Cohen, S.; Wang, Y.; Chen, H.; Kumar, D.; Thiel, W. *Chemical Reviews* **2009**, *110*, 949.

(19) Solomon, E. I.; Heppner, D. E.; Johnston, E. M.; Ginsbach, J. W.; Cirera, J.; Qayyum, M.; Kieber-Emmons, M. T.; Kjaergaard, C. H.; Hadt, R. G.; Tian, L. *Chemical Reviews* **2014**, *114*, 3659.

(20) Solomon, E. I.; Wong, S. D.; Liu, L. V.; Decker, A.; Chow, M. S. *Current Opinion in Chemical Biology* **2009**, *13*, 99.

(21) Tinberg, C. E.; Lippard, S. J. *Accounts of Chemical Research* **2011**, *44*, 280.

(22) McEvoy, J. P.; Brudvig, G. W. *Chemical Reviews* **2006**, *106*, 4455.

(23) Yano, J.; Kern, J.; Sauer, K.; Latimer, M. J.; Pushkar, Y.; Biesiadka, J.; Loll, B.; Saenger, W.; Messinger, J.; Zouni, A.; Yachandra, V. K. *Science* **2006**, *314*, 821.

(24) L. Que Jr., *Nat. Struct. Biol.* **2000**, *7*, 182-184.

(25) a) Collman, J. P.; Brauman, J. I.; Hampton, P. D.; Tanaka, H.; Bohle, D. S.; Hembre, R. T. *J. Am. Chem. Soc.* **1992**, *114*, 7980-7984; b) Naruta, Y.; Ishihara, N.; Tani, F.; Maruyama, K. *Bull. Chem. Soc. Jpn.* **1993**, *66*, 158 ; c) Sundermeyer, J. *Angew. Chem. Int. Ed.* **1993**, *32*, 1144-1146; d) J. P. Collman, V. J. Lee, X. Zhang, J. A. Ibers, J. I. Brauman, *J. Am. Chem. Soc.* **1993**, *115*, 3834-3835.

(26) Pirillo, S.; García Einschlag, F. S. n.; Rueda, E. H.; Ferreira, M. a. L. n. *Industrial & Engineering Chemistry Research* **2010**, *49*, 6745.

(27) Ulson de Souza, S. M. A. G.; Forgiarini, E.; Ulson de Souza, A. A. *Journal of Hazardous Materials* **2007**, *147*, 1073.

(28) McEvoy, J. P.; Brudvig, G. W. *Chemical Reviews* **2006**, *106*, 4455.

(29) Poulos, T. L.; Finzel, B.C.; Howard, A. J. *J. Mol. Biol.* **1987**, *195*, 687–700.

(30) Abu-Omar, M. M.; Loaiza, A.; Hontzeas, N. *Chem. Rev.* **2005**, *105*, 2227.

(31) Koehntop, K.; Emerson, J.; Que, L., Jr. *J. Biol. Inorg. Chem.* **2005**, *10*, 87.

(32) Hegg, E. L.; Jr, L. Q. *European Journal of Biochemistry* **1997**, *250*, 625.

(33) Parkin, G. *Chem. Rev.* **2004**, *104*, 699−768

(34) Karlsson, A.; Parales, J. V.; Parales, R. E.; Gibson, D. T.; Eklund, H.; Ramaswamy, S. *Science* **2003**, *299*, 1039.

(35) Krebs, C.; Galonić Fujimori, D.; Walsh, C. T.; Bollinger, J. M. *Accounts of Chemical Research* **2007**, *40*, 484.

(36) Merkx, M.; Kopp, D. A.; Sazinsky, M. H.; Blazyk, J. L.; Müller, J.; Lippard, S. J. *Angewandte Chemie International Edition* **2001**, *40*, 2782.

(37) Beauvais, L. G.; Lippard, S. J. *Journal of the American Chemical Society* **2005**, *127*, 7370.

(38) Wallar, B. J.; Lipscomb, J. D. *Chemical Reviews* **1996**, *96*, 2625.

(39) Shu, L.; Nesheim, J. C.; Kauffmann, K.; Münck, E.; Lipscomb, J. D.; Que, L. *Science* **1997**, *275*, 515.

(40) Dawson, J. *Science* **1988**, *240*, 433.

(41) a) Bordwell, F. G.; Cheng, J.-P.; Ji, G.-Z.; Satish, A. V.; Zhang, X. *J. Am. Chem. Soc.* **1991**, *113*, 9790–9795; b) Bordwell, F. G.; Bausch, M. J. *J. Am. Chem. Soc.* **1986**, *108*, 1979–1985.

(42) Green, M. T.; Dawson, J. H.; Gray, H. B., *Science* **2004**, 304, (5677), 1653-1656.

(43) Groves, J. T., *Nat. Chem.,* **2015***, 6, (2), 89-91.

(44) (a) Srinivasan, K.; Michaud, P.; Kochi, J. K. *J. Am. Chem. Soc.* **1986**, *108*, 2309.; (b) Samel, E. G.; Srinivasan, K.; Kochi, J. K. *J. Am. Chem. Soc.* **1985**, *107*, 7606.; (c) Yoon, H.; Borrows, C. J. *J. Am. Chem. Soc.* **1988**, *110*, 4087.

(45) a) Groves, J. T.; Kruper, W. J.; Haushalter, R. C. *J. Am. Chem. Soc.* **1980**, *102*, 6375.; b) Groves, J. T.; Nemo, T. E. *J. Am. Chem. Soc.* **1983**, *105*, 5786.
(46) a) Sheldon, R. A. In, *Aspects of Homogeneous Catalysis; Ugo, R., Ed.; D. Reidel: Dordrecht*, **1991**, *4*, 3.; b) White, P. J.; Kaus, M. J.; Edwards, J. O.; Rieger, P. H. *J. Chem. Soc., Chem. Commun.* **1976**, 419.; c) Bradley, D. C.; Mehrotra, R. C.; Gaur, D. P., In, *Metal Alkoxides*, Academic Press: New York, **1978**, Chapter 4.; d) Clark, R. J. H. *The Chemistry of Titenium and Vanadium*; Elsevier: Amasterdam, **1968**.

(47) a) Rappé, A. K.; Goddard, W. A. *J. Am. Chem. Soc.* **1982**, *104*, 3287.; b) Walba, D. M.; De Puy, C. H.; Grabowski, J. J.; Bierbaum, V. M. *Organometallics* **1984**, *3*, 498.; c) Kafafi, Z. H.; Hauge, R. H.; Billups, W. E.; Margrave, J. L. *J. Am. Chem. Soc.* **1987**, *109*, 4775.; d) Collman, J. P.; Brauman, J. I.; Meunier, B.; Hayashi, T.; Kodadek, T.; Raybuck, S. K. *J. Am. Chem. Soc.* **1985**, *107*, 2000.; e) Sevin, A.; Fontecave, M. *J. Am. Chem. Soc.* **1986**, *108*, 3266.

(48) a) Koola, J. D.; Kochi, J. K. *J. Org. Chem.* **1987**, *52*, 4545.; b) Nam, W.; Kim, H. J.; Kim, S. H.; Ho, R. Y. N.; Valentine, J. S. *Inorg. Chem.* **1996**, *35*, 1045.; c) Lim, S. Y.; Kang, M.; Kim, J.; Lee, I.-M. *Bull. Korean Chem. Soc.* **2005**, *26*, 887.

(49) S. Shaik, S. Cohen, S. P. de Visser, P. K. Sharma, D. Kumar, S. Kozuch, F. Ogliaro and D. Danovich, *Eur. J. Inorg. Chem.*, **2004**, 207-226.

(50) Meunier, B., *Chem Rev.,* **1992,** 92, (6), 1411-1456.

(51) Chang, C. K.; Kuo, M.-S., *J Am Chem Soc.,***1979,** 101, (12), 3413-3415.

(52) Chang, C. K.; Ebina, F., *J Chem Soc., Chem Comm.,* **1981**, (15), 778-779.

(53) Bortolini, O.; Meunier, B., *J Chem Soc., Chem Comm.* **1983**, (22), 1364-1366.

(54) Traylor, P. S.; Dolphin, D.; Traylor, T. G., *J Chem Soc., Chem Comm.* **1984**, (5), 279-280.

(55) de Poorter, B.; Meunier, B., *Tetrahedron Letters* **1984,** 25, (18), 1895-1896.

(56) Traylor, T. G.; Tsuchiya, S., *Inorg Chem.* **1987,** 26, (8), 1338-1339.

(57) Wijesekera, T.; Matsumoto, A.; Dolphin, D.; Lexa, D., *Angew Chem Int Ed.,* **1990,** 29, (9), 1028-1030.

(58) Hoffmann, P.; Labat, G.; Robert, A.; Meunier, B., *Tetrahedron Letters* **1990,** 31, (14), 1991-1994.

(59) Groves, J. T.; McClusky, G. A., *J Am Chem Soc.,* **1976,** 98, (3), 859-861.

(60) Groves, J. T.; Nemo, T. E.; Myers, R. S., *J Am Chem Soc.,* **1979,** 101, (4), 1032-1033.

(61) Groves, J. T.; Haushalter, R. C.; Nakamura, M.; Nemo, T. E.; Evans, B. J., *J Am Chem Soc.,* **1981,** 103, (10), 2884-2886.

(62) Nam, W., *Accounts of Chemical Research* **2007,** 40, (7), 522-531.

(63) a) Solomon, E. I.; Decker, A.; Lehnert, N. *Proc Nat Acad Sci.,* **2003,** 100, (7), 3589-3594.; b) Kim, J.; Harrison, R. G.; Kim, C.; Que, L. *J Am Chem Soc.,***1996,** 118, (18), 4373-4379.; c) Leising, R. A.; Norman, R. E.; Que, L. *Inorg Chem.,* **1990,** 29, (14), 2553-2555.; d) Walling, C., *Acc Chem Res.,* **1975,** 8, (4), 125-131.; e) Chen, K.; Costas, M.; Que, J. L. *J Chem Soc, Dalton Trans.,* **2002**, (5), 672-679.; f) Ho, R. Y. N.; Roelfes, G.; Feringa, B. L.; Que, L. *J Am Chem Soc.,* **1999,** 121, (1), 264-265.; g) Roelfes, G.; Vrajmasu, V.; Chen, K.; Ho, R. Y. N.; Rohde, J.-U.; Zondervan, C.; la Crois, R. M.; Schudde, E. P.; Lutz, M.; Spek, A. L.; Hage, R.; Feringa, B. L.; Münck, E.; Que, L. *Inorg Chem.,* **2003,** 42, (8), 2639-2653.; h) Mekmouche, Y.; Ménage, S.; Toia-Duboc, C.; Fontecave, M.; Galey, J.-B.; Lebrun, C.; Pécaut, J. *Angew Chem Int Ed.,* **2001,**

40, (5), 949-952.; i) Mekmouche, Y.; Ménage, S.; Pécaut, J.; Lebrun, C.; Reilly, L.; Schuenemann, V.; Trautwein, A.; Fontecave, M. *Eu J Inorg Chem.,* **2004,** 2004, (15), 3163-3171.; j) Britovsek, G. J. P.; England, J.; White, A. J. P. *Inorg Chem.,* **2005,** 44, (22), 8125-8134.; k) Hitomi, Y.; Arakawa, K.; Kodera, M. *Chem–Eu J.,* **2013**,19, (43), 14697-14701.; l) Company, A.; Gömez, L.; Güell, M.; Ribas, X.; Luis, J. M.; Que, L.; Costas, M. *J Am Chem Soc.,* **2007,** 129, (51), 15766-15767.; m) Salomo, G. C.; Olsen, M. H. N.; Drago, V.; Fernandes, C.; Cardozo Filho, L.; Antunes, O. A. C. *Catal Commun.,* **2007,** 8, (1), 69-72.; n) Foster, T. L.; Caradonna, J. P., *J Am Chem Soc.,* **2003,** 125, (13), 3678-3679.

(64) Walling, C. *Acc Chem Res.,* **1975,** 8, (4), 125-131.

(65) Sawyer, D. T.; Sobkowiak, A.; Matsushita, T., *Acc Chem Res.,* **1996,** 29, (9), 409-416.

(66) Goldstein, S.; Meyerstein, D. *Acc Chem Res.,* **1999,** 32, (7), 547-550.

(67) a) Ray, K.; Heims, F.; Pfaff, F. F. *Eur. J. Inorg. Chem.,* **2013**, 3784 –3807; b) J. Y. Lee, K. D. Karlin, *Curr. Opin. Chem. Biol.,* **2015**, *25*, 184–193.

(68) Bienemann, O.; Hoffmann, A.; Herres-Pawlis, S. *Inorg. Chem.*, **2011**, *31*, 83–108.

(69) Faponle, A. S.; Seebeck, F. P.; de Visser, S. P. *J. Am. Chem. Soc.*, **2017**, *139*, 9259-9270.

(70) a) Visser, S. P. *J. Am. Chem. Soc.*, **2006**, 128, 9813-9824.; b) Janardanan, D.; Wang, Y.; Schyman, P.; Que, Jr. L.; Shaik, S. *Angew. Chem. Int. Ed.*, **2010**, 49, 3342-3345.; c) Michel C.; Baerends, E. J. *Inorg. Chem.*, **2009**, 48, 3628-3638.; d) Shaik, S.; Chen, H.; Janardanan, D. *Nature Chem.*, **2011**, 3, 19-27.; e) Ye, S.; Neese, F. *Proc. Natl. Acad. Sci. USA.*, **2011**, 108, 1228-1233.

(71) a) Nam, W. *Acc. Chem. Res.*, **2007**, *40*, 522-531.; b) England, J.; Martinho, M.; Farquhar, E. R.; Frisch, J. R.; Bominaar, E. L.; Münck, E.; Que, Jr., L.*Angew. Chem. Int. Ed.*, **2009**, *48*, 3622-3626.; c) England, J.; Guo, Y. S.; Farquhar, E. R.; Young, V. G.; Münck, E.; Que, Jr., L.*J. Am. Chem. Soc.*, **2010**, *132*, 8635-8644.; d) Bigi, J. P.; Harman, W. H.; Lassalle-Kaiser, B.; Robles, D. M.; Stich, T. A.; Yano, J.; Britt, R. D.; Chang, C. J. *J. Am. Chem. Soc.*, **2012**, *134,* 1536-1542.

(72) Grapperhaus, C. A.; Mienert, B.; Bill, E.; Weyhermüller, T.; Wieghardt, K., *Inorg Chem.,* **2000,** 39, (23), 5306-5317.

(73) Rohde, J.-U.; In, J.-H.; Lim, M. H.; Brennessel, W. W.; Bukowski, M. R.; Stubna, A.; Münck, E.; Nam, W.; Que, L., *Science* **2003,** 299, (5609), 1037-1039.

(74) Y. Hitomi, K. Arakawa, T. Funabiki, M. Kodera, *Angew. Chem.*, **2012**, 124, 3504 – 3508

(75) Lyakin, O. Y.; Bryliakov, K. P.; Britovsek, G. J. P.; Talsi, E. P., *J Am Chem Soc.* **2009,** 131, (31), 10798-10799.

(76) Lyakin, O. Y.; Bryliakov, K. P.; Talsi, E. P., *Inorg Chem.,* **2011,** 50, (12), 5526-5538.

(77) McDonald, A. R.; Que, L., *Nat Chem* **2011** 3, (10), 761-762.

(78) Van Heuvelen, K. M.; Fiedler, A. T.; Shan, X.; De Hont, R. F.; Meier, K. K.; Bominaar, E. L.; Münck, E.; Que, L., *Proc. Natl. Acad. Sci.U. S. A.,* **2012**, 109, 11933– 11938

(79) de Oliveira, F. T.; Chanda, A.; Banerjee, D.; Shan, X.; Mondal, S.; Que, L.; Bominaar, E. L.; Münck, E.; Collins, T. J., *Science* **2007,** 315, (5813), 835-838.

(80) Ghosh, M.; Singh, K. K.; Panda, C.; Weitz, A.; Hendrich, M. P.; Collins, T. J.; Dhar, B. B.; Sen Gupta, S. *J. Am. Chem. Soc.* **2014**, *136*, 9524.

(81) a) P. R. Ortiz de Montellano, Cytochrome P450: Structure, Mechanism, and Biochemistry, 3rd ed., Kluwer Academic, New York, **2005**; b) I. G. Denisov, T. M. Makris, S. G. Sligar, I. Schlichting, *Chem. Rev.,* **2005**, *105*, 2253–2277; c) B. Meunier, S. P. de Visser, S. Shaik, Chem. Rev., **2004**, *104*, 3947–3980; d) S. Shaik, D. Kumar, S. P. de Visser, A. Altun, W. Thiel, *Chem. Rev*., **2005**, *105*, 2279 –2328.

(82) a) R. K. Behan, M. T. Green, *J. Inorg. Biochem*., **2006**, *100*, 448 –459; b) M. T. Green, J. H. Dawson, H. B. Gray, *Science*, **2004**, *304*, 1653–1656; c) J. H. Dawson, *Science*, **1988**, *240*, 433 – 439; d) F. Ogliaro, S. P. de Visser, S. Shaik, *J. Inorg. Biochem*., **2002**, *91*, 554 –567.

(83) Takahashi, A.; Kurahashi, T.; Fujii, H. *Inorg. Chem*., **2009**, *48*, 2614-2625.

(84) Kang, Y.; Chen, H.; Jeong, Y. J.; Lai, W.; Bae, E. H.; Shaik, S; Nam, W. *Chem. Eur. J*., **2009**, *15*, 10039 –10046

(85) a) Wijesekera, T.; Matsumoto, A.; Dolphin, D.; Lexa, D., *Angew Chem Int Ed.,* **1990,** 29, (9), 1028-1030.; b) Hoffmann, P.; Labat, G.; Robert, A.; Meunier, B., *Tetrahedron Letters* **1990,** 31, (14), 1991-1994.; c) Costas, M., *Coord Chem Rev.,* **2011**,255, 2912-2932.; d) Groves, J. T.; Nemo, T. E.; Myers, R. S., *J Am Chem Soc.,* **1979,** 101, (4), 1032-1033.

(86) Sastri, C. V.; Lee, J.; Oh, K.; Lee, Y. J.; Jackson, T. A.; Ray, K.; Hirao, H.; Shin, W.; Halfen, J. A.; Kim, J. *Proc. Natl. Acad. Sci. USA*, **2007**, *104*, 19181–19186.

(87) Jackson, T. A.; Rohde, J.; Seo, M. S.; Sastri, C. V.; Dehont, R.; Stubna, A.; Ohta, T.; Kitagawa, T.; Munck, E.; Nam, W. *J. Am. Chem. Soc*. **2008**, *130*, 12394–12407.

(88) Armstrong, F. A. *Philosophical Transactions of the Royal Society B: Biological Sciences* **2008**, *363*, 1263.

(89) Ciamician, G. *Science* **1912**, *36*, 385.

(90) Lewis, N. S.; Nocera, D. G. Proceedings of the National Academy of Sciences 2006, 103, 15729.

(91) Umena, Y.; Kawakami, K.; Shen, J.-R.; Kamiya, N. Nature 2011, 473, 55.

(92) Yano, J.; Kern, J.; Sauer, K.; Latimer, M. J.; Pushkar, Y.; Biesiadka, J.; Loll, B.; Saenger, W.; Messinger, J.; Zouni, A.; Yachandra, V. K. Science 2006, 314, 821.

(93) Duan, L.; Bozoglian, F.; Mandal, S.; Stewart, B.; Privalov, T.; Llobet, A.; Sun, L. Nat Chem **2012**, *4*, 418.

(94) Duan, L.; Araujo, C. M.; Ahlquist, M. S. G.; Sun, L. *Proceedings of the National Academy of Sciences* **2012**, *109*, 15584.

(95) Geletii, Y. V.; Huang, Z.; Hou, Y.; Musaev, D. G.; Lian, T.; Hill, C. L. *Journal of the American Chemical Society* **2009**, *131*, 7522.

(96) Jiang, Y.; Li, F.; Zhang, B.; Li, X.; Wang, X.; Huang, F.; Sun, L. *Angewandte Chemie International Edition* **2013**, *52*, 3398.

(97) Kärkäs, M. D.; Åkermark, T.; Chen, H.; Sun, J.; Åkermark, B. *Angewandte Chemie International Edition* **2013**, *52*, 4189.

(98) Kaveevivitchai, N.; Chitta, R.; Zong, R.; El Ojaimi, M.; Thummel, R. P. *Journal of the American Chemical Society* **2012**, *134*, 10721.

(99) Neudeck, S.; Maji, S.; López, I.; Meyer, S.; Meyer, F.; Llobet, A. *Journal of the American Chemical Society* **2013**, *136*, 24.

(100) Norris, M. R.; Concepcion, J. J.; Fang, Z.; Templeton, J. L.; Meyer, T. J. *Angewandte Chemie International Edition* **2013**, *52*, 13580.

(101) Romain, S.; Bozoglian, F.; Sala, X.; Llobet, A. *Journal of the American Chemical Society* **2009**, *131*, 2768.

(102) Sala, X.; Maji, S.; Bofill, R.; García-Antón, J.; Escriche, L.; Llobet, A. *Accounts of Chemical Research* **2013**, *47*, 504.

(103) Sala, X.; Romero, I.; Rodríguez, M.; Escriche, L.; Llobet, A. *Angewandte Chemie International Edition* **2009**, *48*, 2842.

(104) Tanaka, K.; Isobe, H.; Yamanaka, S.; Yamaguchi, K. *Proceedings of the National Academy of Sciences* **2012**, *109*, 15600.

(105) Tong, L.; Inge, A. K.; Duan, L.; Wang, L.; Zou, X.; Sun, L. *Inorganic Chemistry* **2013**, *52*, 2505.

(106) Wang, L.; Duan, L.; Stewart, B.; Pu, M.; Liu, J.; Privalov, T.; Sun, L. *Journal of the American Chemical Society* **2012**, *134*, 18868.

(107) Cline, E. D.; Adamson, S. E.; Bernhard, S. *Inorganic Chemistry* **2008**, *47*, 10378.

(108) Graeupner, J.; Hintermair, U.; Huang, D. L.; Thomsen, J. M.; Takase, M.; Campos, J.; Hashmi, S. M.; Elimelech, M.; Brudvig, G. W.; Crabtree, R. H. *Organometallics* **2013**, *32*, 5384.

(109) Grotjahn, D. B.; Brown, D. B.; Martin, J. K.; Marelius, D. C.; Abadjian, M.-C.; Tran, H. N.; Kalyuzhny, G.; Vecchio, K. S.; Specht, Z. G.; Cortes-Llamas, S. A.; Miranda-Soto, V.; van Niekerk, C.; Moore, C. E.; Rheingold, A. L. *Journal of the American Chemical Society* **2011**, *133*, 19024.

(110) Hull, J. F.; Balcells, D.; Blakemore, J. D.; Incarvito, C. D.; Eisenstein, O.; Brudvig, G. W.; Crabtree, R. H. *Journal of the American Chemical Society* **2009**, *131*, 8730.

(111) Lalrempuia, R.; McDaniel, N. D.; Müller-Bunz, H.; Bernhard, S.; Albrecht, M. *Angewandte Chemie International Edition* **2010**, *49*, 9765.

(112) McDaniel, N. D.; Coughlin, F. J.; Tinker, L. L.; Bernhard, S. *Journal of the American Chemical Society* **2007**, *130*, 210.

(113) Parent, A. R.; Brewster, T. P.; De Wolf, W.; Crabtree, R. H.; Brudvig, G. W. *Inorganic Chemistry* **2012**, *51*, 6147.

(114) Puntoriero, F.; La Ganga, G.; Sartorel, A.; Carraro, M.; Scorrano, G.; Bonchio, M.; Campagna, S. *Chemical Communications* **2010**, *46*, 4725.

(115) Chen, G.; Chen, L.; Ng, S.-M.; Man, W.-L.; Lau, T.-C. *Angewandte Chemie International Edition* **2013**, *52*, 1789.

(116) Gong, M.; Li, Y.; Wang, H.; Liang, Y.; Wu, J. Z.; Zhou, J.; Wang, J.; Regier, T.; Wei, F.; Dai, H. *Journal of the American Chemical Society* **2013**, *135*, 8452.

(117) Hong, D.; Mandal, S.; Yamada, Y.; Lee, Y.-M.; Nam, W.; Llobet, A.; Fukuzumi, S. *Inorganic Chemistry* **2013**, *52*, 9522.

(118) Hong, D.; Yamada, Y.; Nagatomi, T.; Takai, Y.; Fukuzumi, S. *Journal of the American Chemical Society* **2012**, *134*, 19572.

(119) Fu, S.; Liu, Y.; Ding, Y.; Du, X.; Song, F.; Xiang, R.; Ma, B. *Chemical Communications* **2014**, *50*, 2167.

(120) Moonshiram, D.; Alperovich, I.; Concepcion, J. J.; Meyer, T. J.; Pushkar, Y. Proceedings of the National Academy of Sciences 2013, 110, 3765.

(121) Kanan, M. W.; Nocera, D. G. *Science* **2008**, *321*, 1072.

(122) Singh, A.; Spiccia, L. *Coordination Chemistry Reviews* **2013**, *257*, 2607.

(123) Ellis, W. C.; McDaniel, N. D.; Bernhard, S.; Collins, T. J. *Journal of the American Chemical Society* **2010**, *132*, 10990.

(124) Codolà, Z.; Garcia-Bosch, I.; Acuña-Parés, F.; Prat, I.; Luis, J. M.; Costas, M.; Lloret-Fillol, J. *Chemistry – A European Journal* **2013**, *19*, 8042.

(125) Fillol, J. L.; Codolà, Z.; Garcia-Bosch, I.; Gómez, L.; Pla, J. J.; Costas, M. *Nat Chem* **2011**, *3*, 807.

(126) Zhang, B.; Li, F.; Yu, F.; Cui, H.; Zhou, X.; Li, H.; Wang, Y.; Sun, L. *Chemistry – An Asian Journal* **2014**, *9*, 1515.

(127) Hoffert, W. A.; Mock, M. T.; Appel, A. M.; Yang, J. Y. *European Journal of Inorganic Chemistry* **2013**, *2013*, 3846.

(128) Coggins, M. K.; Zhang, M.-T.; Vannucci, A. K.; Dares, C. J.; Meyer, T. J. Journal of the American Chemical Society 2014, 136, 5531.

(129) Chahbane, N.; Popescu, D.-L.; Mitchell, D. A.; Chanda, A.; Lenoir, D.; Ryabov, A. D.; Schramm, K.-W.; Collins, T. J. *Green Chemistry* **2007**, *9*, 49.

(130) Huang, Z.; Luo, Z.; Geletii, Y. V.; Vickers, J. W.; Yin, Q.; Wu, D.; Hou, Y.; Ding, Y.; Song, J.; Musaev, D. G.; Hill, C. L.; Lian, T. *Journal of the American Chemical Society* **2011**, *133*, 2068.

(131) Pizzolato, E.; Natali, M.; Posocco, B.; Montellano Lopez, A.; Bazzan, I.; Di Valentin, M.; Galloni, P.; Conte, V.; Bonchio, M.; Scandola, F.; Sartorel, A. *Chemical Communications* **2013**, *49*, 9941.

(132) McAlpin, J. G.; Surendranath, Y.; Dincă, M.; Stich, T. A.; Stoian, S. A.; Casey, W. H.; Nocera, D. G.; Britt, R. D. *Journal of the American Chemical Society* **2010**, *132*, 6882.

(133) Karlsson, E. A.; Lee, B.-L.; Åkermark, T.; Johnston, E. V.; Kärkäs, M. D.; Sun, J.; Hansson, Ö.; Bäckvall, J.-E.; Åkermark, B. *Angewandte Chemie International Edition* **2011**, *50*, 11715.

(134) Limburg, J.; Vrettos, J. S.; Liable-Sands, L. M.; Rheingold, A. L.; Crabtree, R. H.; Brudvig, G. W. *Science* **1999**, *283*, 1524.

(135) Robinson, D. M.; Go, Y. B.; Mui, M.; Gardner, G.; Zhang, Z.; Mastrogiovanni, D.; Garfunkel, E.; Li, J.; Greenblatt, M.; Dismukes, G. C. *Journal of the American Chemical Society* **2013**, *135*, 3494.

(136) Panda. C.; Debgupta. J.; Díaz. D. D.; Singh. K. K.; Gupta S. S. and Dhar. B. B.; *Journal of the American Chemical Society* **2014**, 136, 12273.

(137) Kotani, H.; Suenobu, T.; Lee, Y.-M.; Nam, W.; Fukuzumi, S. *Journal of the American Chemical Society* **2011**, *133*, 3249.

(138) Company, A.; Sabenya, G.; González-Béjar, M.; Gómez, L.; Clémancey, M.; Blondin, G.; Jasniewski, A. J.; Puri, M.; Browne, W. R.; Latour, J.-M.; Que, L.; Costas, M.; Pérez-Prieto, J.; Lloret-Fillol, J. *Journal of the American Chemical Society* **2014**, *136*, 4624.

(139) Jana, S.; Ghosh, M.; Ambule, M.; Sen Gupta, S. *Organic Letters,* **2017**, *19*, (4), 746-749.

(140) Ghosh, M.; Pattanayak, S.; Dhar, B. B.; Singh, K. K.; Panda, C.; Sen Gupta, S. *Inorganic Chemistry,* **2017**, *56*, (18), 10852-10860.

(141) Ghosh, M.; Nikhil, Y. L. K.; Dhar, B. B.; Sen Gupta, S. *Inorg. Chem.* **2015,** *54*, 11792.

(142) Singh, K. K.; Tiwari, M. k.; Dhar, B. B.; Vanka, K.; Sen Gupta, S. *Inorg. Chem.* **2015**, *54*, 6112.

Chapter II

Comparing Spectroscopy and Reactivity of a Pair of bTAML Complexes with Fe^VO and $Fe^{IV}O$ Units

2.1 Abstract

In this chapter we compare the geometric and electronic structures and reactivities of $[Fe^V(O)]^-$ and $[Fe^{IV}(O)]^{2-}$ species supported by the same ancillary non-heme biuret tetraamido macrocyclic ligand (bTAML). Resonance Raman studies show that the Fe=O vibration of the $[Fe^{IV}(O)]^{2-}$ complex **2** is at 798 cm^{-1}, compared to 862 cm^{-1} for the corresponding $[Fe^V(O)]^-$ species **3**, an 64-cm^{-1} frequency difference reasonably reproduced by DFT calculations. These values are respectively the lowest and the highest frequencies observed thus far for high-valent Fe=O complexes. EXAFS analysis of **3** reveals an Fe=O bond length of 1.59 Å, which is 0.05 Å shorter than that found in complex **2**. The redox potentials of **2** and **3** are 0.44 V (measured at pH 12) and 1.19 V (measured at pH 7) versus NHE, respectively, corresponding to the $[Fe^{IV}(O)]^{2-}/[Fe^{III}(OH)]^{2-}$ and $[Fe^V(O)]^-/[Fe^{IV}(O)]^{2-}$ couples. Consistent with its higher potential (even after correcting for the pH difference), **3** oxidizes benzyl alcohol at pH 7 with a second order rate constant that is 2500-fold bigger than that for **2** at pH 12. Furthermore, **2** exhibit a classical KIE of 3 in the oxidation of benzyl alcohol to benzaldehyde versus a nonclassical KIE of 12 for **3**, emphasizing the reactivity differences between **2** and **3**.
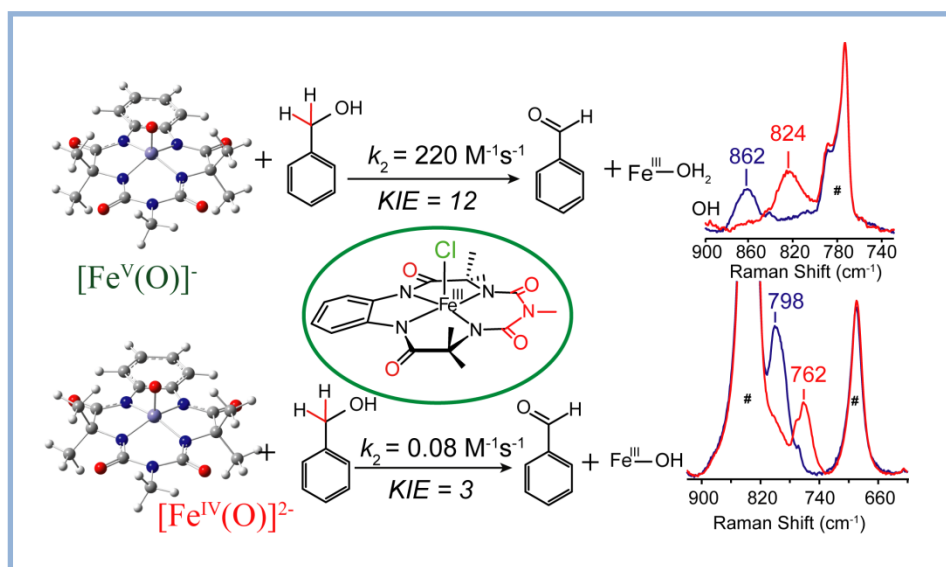
2.2 Introduction

Monomeric iron-oxo units have been proposed as intermediates involved in either C–H bond cleavage or O-atom transfer reactions for several oxidases and oxygenases.[1] For non-heme iron-containing enzymes, both iron(IV)- and iron(V)-oxo species have been proposed as active intermediates.[2] Understanding the role of the iron oxidation state in the thermodynamics and kinetics of C–H bond cleavage is important not only for understanding the underlying principles that guide these natural enzymes but also for designing synthetic catalysts that mimic the action of these enzymes. It has been shown that both the redox potential of the high valent species and the basicity of the terminal oxo unit contribute to the reactivity of C–H bond abstraction by metal oxo complexes.[3,4] In previous reports,[5] reactivity comparisons of model complexes of Cpd II (oxoiron(IV)) and Cpd I (isoelectronic to oxoiron(V)) have been reported, but no correlation of this intrinsic difference to their spectroscopic properties has been provided. Theoretical studies on the H-atom abstraction capabilities of Cpd I and Cpd II mimics have also demonstrated the sluggish oxidative properties for the latter, with H-atom abstraction barriers of 2–5 kcal/mol higher than those computed for the former.[6] For non-heme systems, the geometric and electronic structures as well as reactivities of oxoiron(IV) and oxoiron(V) species having the same ancillary non-heme ligand have, to date, not been experimentally compared, primarily due to the paucity of systems with reasonably stable oxoiron(V) species. However, it should be noted that computational investigations on hypothetical iron-oxo models have been performed by Neese et al. to correlate the electronic properties and reactivity of these high valent iron oxo complexes.[6d,e] In their study, the superior reactivity of the hypothetical $[Fe^V(O)(NH_3)_4(OH)_{axial}]^{2+}$ over its one-electron reduced species $[Fe^{IV}(O)(NH_3)_4(OH)_{axial}]^+$ in the oxidation of ethane was established based on the H-atom abstraction barrier, the radical character of the iron-oxo bond and the approach of C–H bond. Experimentally, the reactivities of two pairs of non-heme oxoiron(V) and oxoiron(IV) complexes have been compared in the literature, but no rate measurements have been reported.[6f,6g] However, the fleeting nature of these iron(V) species renders it difficult to obtain structural and mechanistic insights into their inherent differences.

On the other hand, oxoiron(V),[7a] oxoiron(IV),[7b,c] and (μ-oxo)diiron(IV)[7d] complexes of the tetraamido macrocyclic ligand (TAML) have been obtained in >95% yield and characterized.

Thus Fe-TAML represents an exciting system where the spectroscopic properties and reactivities of the high valent oxoiron species can be studied and correlated. To date however,
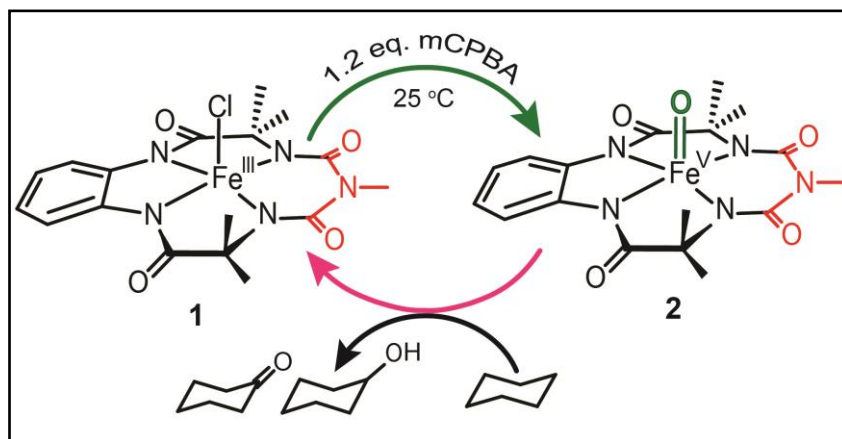
Scheme 2.1: Schematic presentation of $Fe^V(O)$ formation and reaction towards cyclohexane.

reactivity comparisons between the oxoiron(V) and oxoiron(IV) TAML complexes have not been reported.[7d,e] A likely reason is the instability of a completely characterized oxoiron(V) complex at temperatures above -40 °C, which precluded use of a common temperature and solvent system to study their reactivity towards substrates.

The synthesis of a room temperature stable oxoiron(V)-(bTAML) complex (bTAML depicted in Figure 2.1, Scheme 2.1) in >95% yield has been recently reported.[8a] This oxoiron(V) complex is also stable in solvent containing up to 70% water.[8b] Additionally, the oxoiron(IV) complex can be generated under the same conditions. Thus, we are able to prepare both the oxoiron(IV) and the oxoiron(V) complexes in very high purity at room temperature using the same solvent system, which facilitates reactivity comparisons using a common substrate. In this report, we compare resonance Raman, X-ray absorption and electrochemical data for the oxoiron(IV) and oxoiron(V) complexes of the bTAML ligand. Their room temperature reactivity difference in the oxidation of benzyl alcohol (BnOH) and its correlation with spectroscopic properties supported by density functional theory (DFT) calculations are also discussed in this chapter.
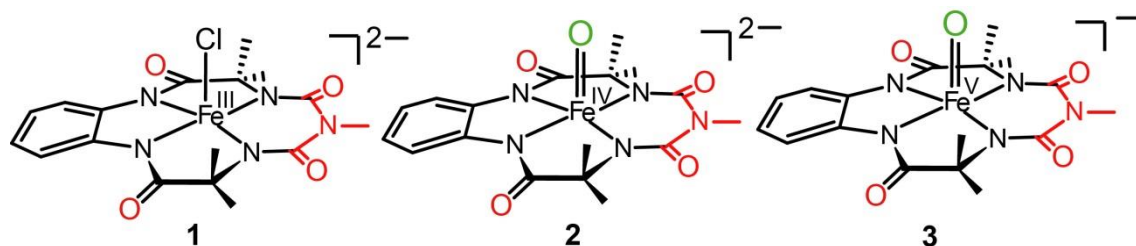
Figure 2.1: The bTAML complexes discussed in this chapter with tetraethylammonium cations as counterions for all complexes: **1** = chloroiron(III) complex; **2** = oxoiron(IV) complex, and **3** = oxoiron(V) complex.

2.3 Experimental Section

2.3.1 Materials

$(Et_4N)_2[Fe^{III}(Cl)(bTAML)]$ **1** was synthesized as described before.[8d] Aqueous sodium hypochlorite *(reagent grade, Aldrich, available chlorine 4.00–4.99%)* was used as received and quantified by iodometry. Acetonitrile (LCMS grade, Aldrich) was used by passing through an activated neutral alumina column and then dried as described elsewhere.[25] Benzyl alcohol (Aldrich, 99.8%) was passed through activated neutral alumina and distilled prior to use; its purity was checked by GC-MS. All reactions were carried out without any special precautions under atmospheric conditions unless otherwise specified. Deionized water was used to make all of the stock solutions for the reaction and kinetic runs. ^{18}O-enriched water (98%) was procured from the Shanghai Research Institute of Chemical Industry (China).

2.3.2 Instrumentation

UV-vis spectral studies were carried out using an Agilent diode array 8453 spectrophotometers attached with a Peltier temperature controller. Cyclic voltammetry experiments were carried out on a CHI-660 potentiostat. Solutions of **1** were placed in one compartment three-electrode cells. Glassy carbon (GC) (3 mm of diameter) was used as the working electrode, silver/silver chloride (3 M KCl) as reference electrode (unless explicitly mentioned), and Pt wire as counter electrode. Working electrode pre-treatment before each measurement consisted of polishing with 0.05 μm alumina paste, rinsing thereafter with water/acetone and finally blow-drying. All redox potentials in the present work are reported versus NHE by adding 0.21 V to the measured potential. Mössbauer spectra were recorded with two spectrometers using a Janis Research Super Varitemp dewar. The isomer shift was

reported relative to Fe metal. The Mössbauer spectrum of **2** was simulated with least-square fitting using the program *SpinCount* and the standard spin Hamiltonian.

Gas chromatography (GC) was performed on a PerkinElmer Arnel Clarus 500 instrument equipped with a hydrogen flame ionization detector and HP-5 (30 m × 0.32 mm × 0.25 μm) column. Helium was used as carrier gas at a flow rate of 30 mL min^{-1}. GC-MS analysis were performed on an Agilent 5977A mass-selective detector interfaced with an Agilent 7890B GC in similar conditions using a HP-5-Ms capillary column (30 m × 0.32 mm × 0.25 μm, J & W Scientific).

2.3.3 Generation of [Fe^{IV}(O)]$^{2-}$ (2) and [Fe^{V}(O)]$^{-}$ (3) samples

A 0.5 mM solution of [(bTAML)Fe^{III}Cl]$^{2-}$ (**1**) was converted to **3** by using 1.2 equivalents of sodium hypochlorite (NaOCl) in acetonitrile.[8b] On the other hand, the corresponding Fe^{IV}(O) complex **2** was obtained by two methods, either by treating the CH$_3$CN solution of **3** with 3 equivalents of tetrabutylammonium hydroxide or by addition of NaOCl to **1** in water (pH 12). In both cases, nearly quantitative conversion was confirmed by UV-Vis spectroscopy (Figure 2.2).
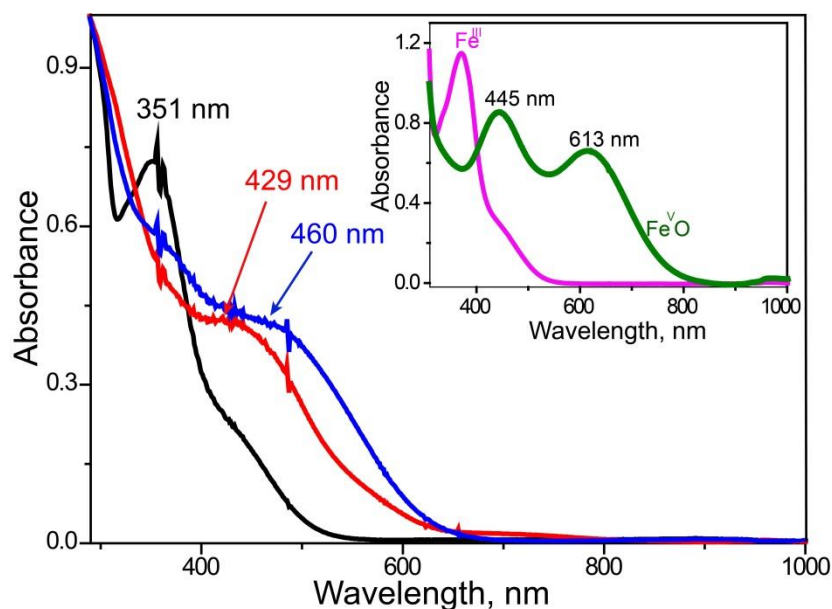
Figure 2.2: UV-vis absorption spectra of **2** (1.8 × 10^{-4} M) synthesized in acetonitrile (red) and UV-vis and in pH 12 water (blue). Both samples were prepared via oxidation of **1** (1.8 × 10^{-4} M; black). Inset: UV-vis absorption spectra of 2.8 × 10^{-4} M of **1** (pink) and **3** (green) in acetonitrile.

2.3.4 X-ray Absorption Spectroscopy

The XAS sample of **1** was prepared by dissolving isolated solid in CH_3CN to make a 5 mM solution at 20 °C, which was then transferred to an XAS cup and frozen in liquid nitrogen. The XAS sample of **3** was prepared by treating a 5 mM solution of **1** in anhydrous acetonitrile at 20 °C with 1.2 equivalents of NaOCl to generate **3** in near-quantitative yield. The green solution was transferred to an XAS cup, and the sample was frozen in liquid nitrogen. The sample of **2** was prepared by generating a 5-mM solution of **3** at 20 °C, then adding 3 equivalents of tetrabutylammonium hydroxide to form the $Fe^{IV}(O)$ complex. Iron K-edge X-ray absorption spectra for **1**, **2**, and **3** were collected on SSRL beam line 9-3 using a 100-element solid state Ge detector (Canberra) with a SPEAR storage ring current of ~500 mA at a power of 3.0 GeV. The incoming X-rays were unfocused using a Si(220) double crystal monochromator, which was detuned to 40% of the maximal flux to attenuate harmonic X-rays. Seven, nine and eight scans of the fluorescence excitation spectra for **1**, **3** and **2**, respectively, were collected from 6882 eV to 8000 eV at a temperature (10 K) that was controlled by an Oxford Instruments CF1208 continuous flow liquid helium cryostat. An iron foil was placed in the beam pathway prior to the ionization chamber I_0 and scanned concomitantly for an energy calibration, with the first inflection point of the edge assigned to 7112.0 eV. A 6-µm Mn filter and a Soller slit were used to increase the signal-to-noise ratio of the spectra. Photoreduction was monitored by scanning the same spot on the sample twice and comparing the first derivative peaks associated with the edge energy during collection, but none was observed in the present study.

The detector channels from the scans were examined, calibrated, averaged, and processed for EXAFS analysis using EXAFSPAK[26a] to extract χ(k). Theoretical phase and amplitude parameters for a given absorber-scatterer pair were calculated using FEFF 8.40[26b] and were utilized by the "opt" program of the EXAFSPAK package during curve fitting. Parameters for **1**, **2** and **3** were calculated using a model based on the available crystal structure of the **1** complex.[8b] In all analyses, the coordination number of a given shell was a fixed parameters and was varied iteratively in integer steps, while the bond lengths (R) and mean-square deviation (σ^2) were allowed to freely float. The amplitude reduction factor S_0 was fixed at 0.9, while the edge-shift parameter E_0 was allowed to float as a single value for all shells. Thus, in any given fit, the number of floating parameters was typically equal to (2 x num shells) + 1. The k range of the data is $2 - 15$ Å^{-1}.

Pre-edge analysis was performed on data normalized in the "process" program of the EXAFSPAK package, and pre-edge features were fit between 7108 eV to 7117 eV for **1** and 7108 eV to 7118 eV for **2** and **3** using the *Fityk*[26c] program with pseudo-Voigt functions composed of 50:50 Gaussian/Lorentzian functions.

2.3.5 Resonance Raman Spectroscopy

Resonance Raman spectra were obtained with excitation at 476.5 nm (40 mW at source, Ar^+ laser, Spectra-Physics). Data were obtained on samples at room temperature in flat-bottomed NMR tubes using a 90° backscattering arrangement (parallel to the slit direction) and at 77 K on frozen samples in NMR tubes using a 135º backscattering arrangement. The collimated Raman scattering was collected using two Plano convex lenses (f = 12 cm, placed at an appropriate distance) through an holographic super notch filter (Kaiser Optical Systems, INC) into an Acton AM-506M3 monochromator equipped with a Princeton Instruments ACTON PyLON LN/CCD-1340x400 detector. The detector was cooled to -120 ºC prior to the experiments. Spectral calibration was performed using the Raman spectrum of acetonitrile/toluene 50:50 (v:v).[27a] Each spectrum was accumulated, typically 60 times with 5 s acquisition time, resulting in a total acquisition time of 5 min per spectrum. The collected data was processed using Spekwin32,[27b] and a multipoint baseline correction was performed for all spectra (Figure 2.3 and Figure 2.4). Raman samples of **2** were prepared by treating a 0.5 mM solution of **3** generated using $Na^{16/18}OCl$ with 6 equivalents of tetrabutylammonium hydroxide at 20 °C. $Na^{18}OCl$ was prepared by dilution of 10% NaOCl in $H_2^{18}O$ in 1:9 ratio.[27c] Raman samples of **3** were generated by addition of 1.2 equivalents of $Na^{16/18}OCl$ to a 0.5 mM solution of **1** in CH_3CN at 20 °C with stirring.
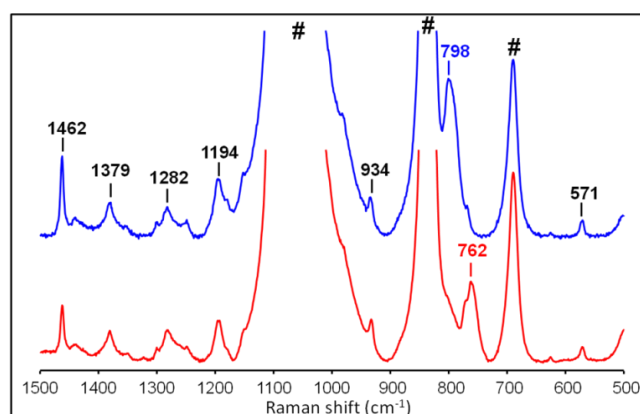
Figure 2.3: Resonance Raman spectra of **2** (top) at room temperature**.** Blue and red lines represent ^{16}O-and ^{18}O-labelled samples, respectively. Conditions: λ_{ex} = 476.5 nm, power ~40 mW in CH_3CN.
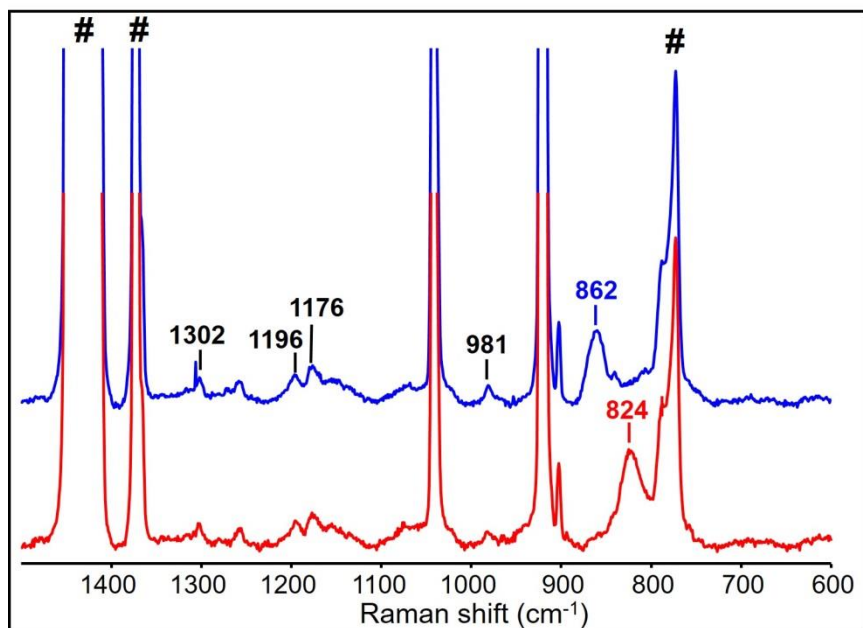
Figure 2.4: Resonance Raman spectra of **3** at 77 K. Blue and red lines represent ^{16}O-and ^{18}O-labelled samples, respectively. Conditions: λ_{ex} = 476.5 nm, power ~40 mW in CD$_3$CN.

2.3.6 Kinetic experiments

The kinetics for the oxidation of benzyl alcohol by **2** were monitored in the kinetic mode of the spectrophotometer using 1-cm quartz cell at 395 nm at the isosbestic points of Fe^{IV} species and Fe^{III} at 30.0 ± 0.5 °C as well as other temperatures. All the kinetic experiments were carried out in a premixed 80% CH$_3$CN/20% water solvent. For kinetic measurements, **3** was synthesized by using 1.2 equivalent of sodium hypochlorite as terminal oxidant. The concentration of **3** (5×10^{-5} M) was kept constant while substrate concentration was varied. The pseudo first-order rate constants k_{obs} (calculated by monitoring changes at 395 nm, Figure 2.5) were obtained from nonlinear curve fitting [(A$_t$ = A$_\alpha$ − (A$_\alpha$ − A$_o$)e$^{(-k_{obs}t)}$]. Resulting k_{obs} values correlated linearly with substrate concentration to afford the second order rate constant k_2.[28,29] For the kinetic studies of benzyl alcohol oxidation by **2**, the complex was generated in 80% CH$_3$CN/20% pH 12 water (adjusted by 5 mM NaOH) by using NaOCl (0.5 equivalent) at 30.0 ± 0.5 °C. The reaction kinetics was monitored at various temperatures by the decay in the characteristic absorbance of **2** at 460 nm to extract the pseudo first-order rate (Figure 2.6)
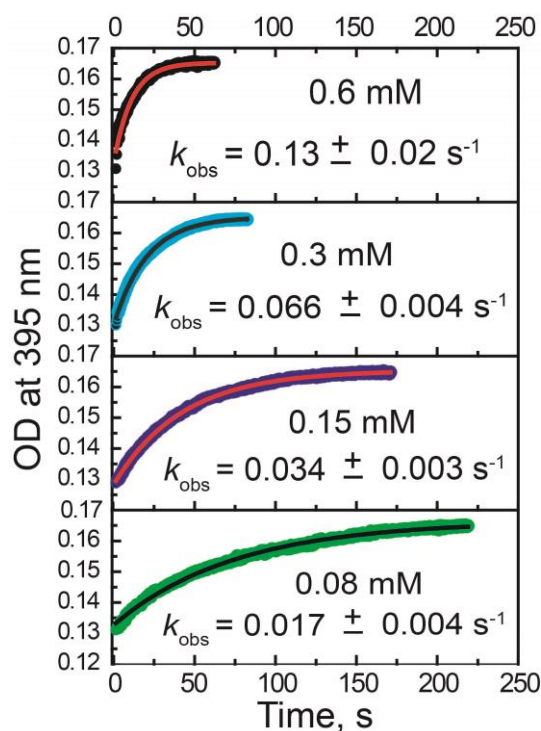
Figure 2.5: Kinetic traces for reaction of **3** (5×10^{-5} M) with benzyl alcohol at various concentrations of benzyl alcohol. The kinetic traces were fitted to the equation, [($A_t = A_\alpha - (A_\alpha - A_o)e^{(-k_{obs}t)}$] for obtaining k_{obs} values.
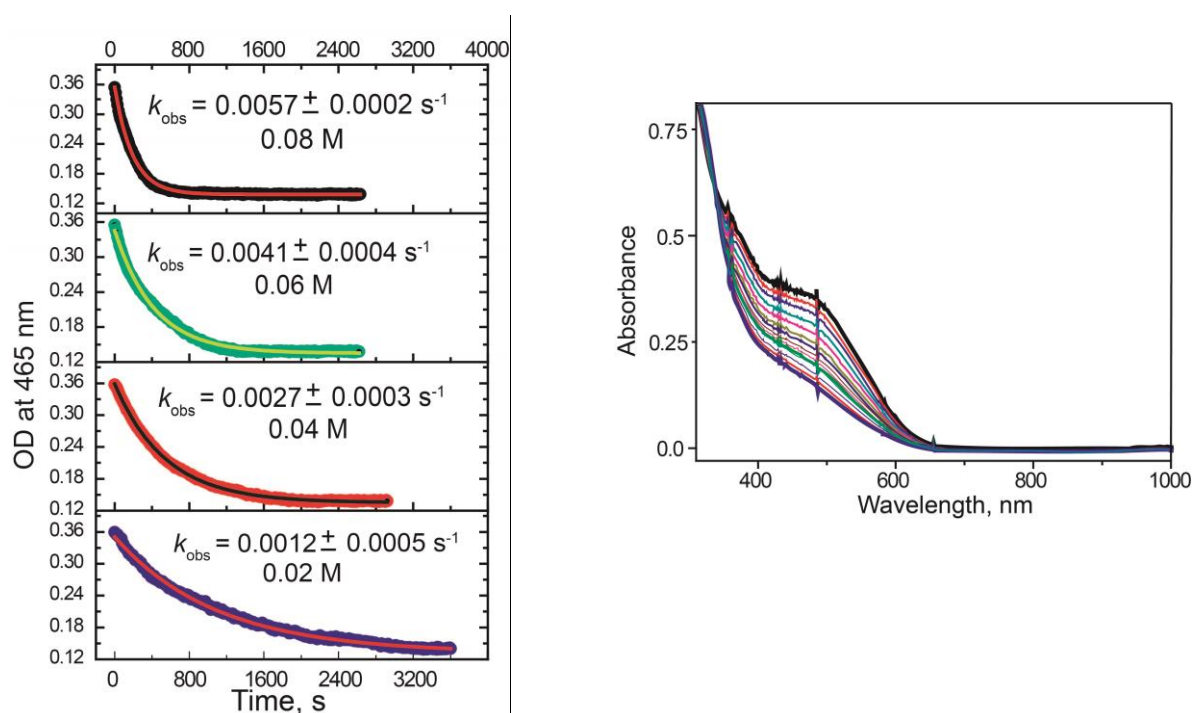
Figure 2.6: Spectral scanning (right), Kinetic traces (The kinetic traces were fitted to the equation, [($A_t = A_\alpha - (A_\alpha - A_o)e^{(-k_{obs}t)}$] for obtaining k_{obs} values, left) for reaction with 1.5×10^{-4} M of **2** and benzyl alcohol. Pseudo first order rate constant (k_{obs}) was obtained from

nonlinear curve fitting $[(A_t = A_\alpha - (A_\alpha - A_o)e^{(-k_{obs}t)}]$. Resulting k_{obs} values correlated linearly with substrate concentration to afford the second order rate constant k_2.[28,29]

2.3.7 Product Quantification

Products were first analyzed by gas chromatography-mass spectrommetry (GC-MS) methods. Gas chromatography (GC) was used for product quantification. To a solution of **3** or **2**[21] (10^{-4} M) in CH_3CN/water was added benzyl alcohol (1000 equiv, 10^{-1} M) at room temperature. After completion of reaction (determined by UV-vis absorption spectroscopy) the products were passed through a short alumina plug and immediately quantified by GC.

2.3.8 Mössbauer Spectroscopy

Mössbauer spectra were recorded with two spectrometers using a Janis Research Super-Vari-temp-dewar. The isomer shift was reported relative to Fe metal. The simulation of the Mössbauer spectra was calculated with least-square fitting using the program *SpinCount* and the standard spin Hamiltonian (2)

$$H = \beta_e \mathbf{B}.\mathbf{g}.\mathbf{S} + \mathbf{S}.\mathbf{D}.\mathbf{S} + \mathbf{S}.\mathbf{A}.\mathbf{I} - g_n b_n \mathbf{B}.\mathbf{I} + \frac{eQV_{zz}}{12}[3I_z^2 - I(I+1) + \eta(I_x^2 - I_y^2)] \quad (2)$$

$^{57}FeCl_3$ was purchased from Trace Sciences International Corporation (Canada).^{57}Fe-enriched **1** was prepared following the procedure used for synthesis of ^{56}Fe-bTAML; in this case $^{57}FeCl_3$ was used in place of $^{56}FeCl_2$ (yield 70 %). The corresponding ^{57}Fe-enriched **2** was prepared quantitatively by reacting **1** with 1.2 equivalent of *m*CPBA in ice bath.

2.3.9 Computational Details

Density Functional Theory (DFT) based methods have been employed to compare the electronic structures of **2** and **3**. All the minima, reported in this study were fully optimized at the UBP86/6-311+G* or UB3LYP/6-311+G* level of theory[30] using the Gaussian 09 suite of quantum-chemical programs.[31] The stationary points on the potential energy surface were characterized by evaluating the vibrational frequencies.

2.4 Results and Discussion

2.4.1 Synthesis

The complexes $[(bTAML)Fe^{IV}(O)]^{2-}$ (**2**) and $[(bTAML)Fe^{V}(O)]^{-}$ (**3**) were obtained from $[(bTAML)Fe^{III}(Cl)]^{2-}$ (**1**). Complex **3** was synthesized by addition of 1.2 equivalents of sodium hypochlorite (NaOCl) into a solution of **1** in acetonitrile (CH_3CN) as reported previously; it exhibits a visible spectrum with bands at 445 and 613 nm (Figure 2.2).[8a,b] On

the other hand, the corresponding $Fe^{IV}(O)$ complex **2** could be obtained by two methods, either by treating the CH_3CN solution of **3** with 3 equivalents of tetrabutylammonium hydroxide or by addition of NaOCl to **1** in water (pH 12). Complex **2** exhibits a visible spectrum with a λ_{max} of 429 nm in CH_3CN and 460 nm in water pH 12 (Figure 2.2). Its Mössbauer spectrum shows a doublet with an isomer shift (δ) of -0.21 mm/s and a quadrupole splitting (ΔE_Q) of 3.89 mm/s (Figure 2.8), similar to those found for the corresponding $Fe^{IV}(O)^{2-}$ species supported by the related TAML ligand.[7b,c] Based on their Mössbauer spectra, the purities of both **2** and **3**[8a,b] complexes were determined to be > 95%.

Fe(IV)O

δ -0.214
ΔEq 3.885
Γ 0.316
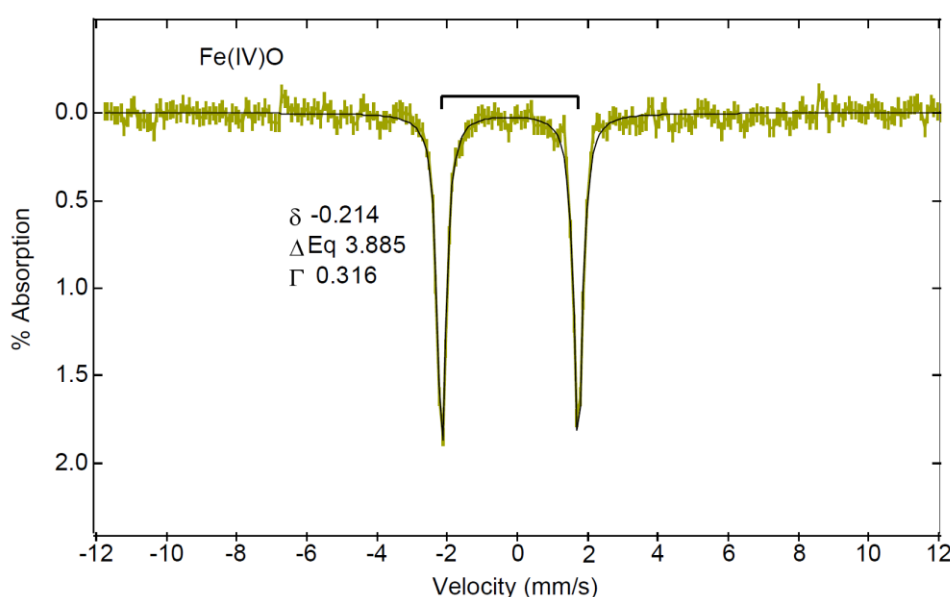
Figure 2.8: Mossbauer spectra of $[Fe^{IV}(O)]^{2-}$ (**2**) synthesized in water (pH 12).

2.4.2 Resonance Raman Spectroscopy for Characterizations of Iron oxo intermediates

Resonance Raman data for **2** and **3** were obtained in acetonitrile solvent using 476.5-nm excitation. The Fe=O vibration of **2** is observed at 798 cm^{-1} (Figure 2.9, blue), which shifts to 762 cm^{-1} (Figure 2.9, red) upon ^{18}O substitution ($\Delta^{18}O/^{16}O$ = 36 cm^{-1}). The Fe=O vibration of **2** is the lowest value reported for a non-heme Fe^{IV}=O species[9a,9b] and reflects the highly basic nature of the bTAML ligand. On the other hand, the corresponding Fe=O vibration for **3** is observed at 862 cm^{-1} (Figure 2.9, blue) and downshifts to 824 cm^{-1} (Figure 2.9, red) upon ^{18}O substitution (see Figure 2.3, 2.4 for full spectra), the observed $\Delta^{18}O/^{16}O$ of 38 cm^{-1} being in excellent agreement with that calculated by Hooke's Law for an Fe=O unit. The ν(Fe=O) of **3** is higher than any other Fe=O vibration measured to date,[9a,9b] presumably

because of the Fe^{V} oxidation state. The next highest $\nu_{(Fe=O)}$ was observed by IR spectroscopy at 856 cm^{-1} for the recently reported $[Fe^{IV}(O_{syn})(TMC)(OTf)]^{+}$ complex.[9c] The 64-cm^{-1} difference observed between **3** and **2** represents the first time the vibrations of Fe^{V}=O and Fe^{IV}=O units supported by a common ligand can be compared. Clearly, the oxidation of the Fe(IV) center to Fe(V) results in significant strengthening of the Fe=O bonds. For comparison, the $\nu(Fe=O)$'s of Fe^{IV}=O and Fe^{III}–O units supported by trianionic urea-based tripodal ligand ($[H_3buea]^{3-}$) reported by Borovik exhibit a frequency difference of 128 cm^{-1} and an Fe–O bond length difference of 0.15 Å.[10]
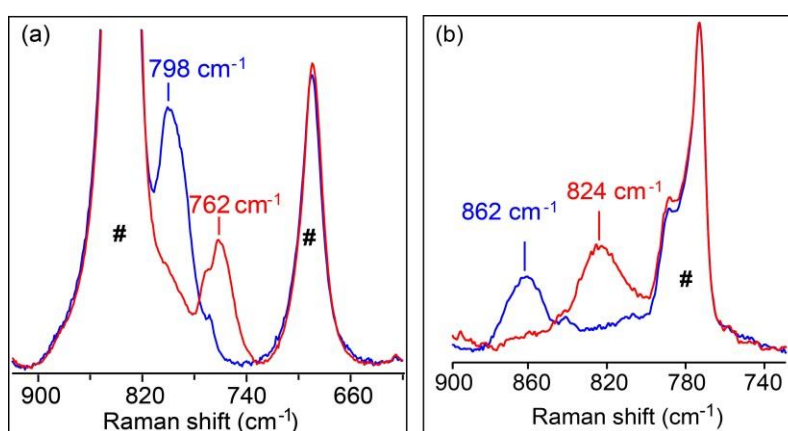
Figure 2.9: Resonance Raman spectra of **2** in CH$_3$CN at room temperature (left) and **3** in CD$_3$CN at 77 K (right)**.** Blue and red lines represent ^{16}O-and ^{18}O-labelled samples, respectively. λ_{ex} = 476.5 nm; power ~40 mW. # indicates solvent-derived features.

2.4.3 X-ray Absorption Spectroscopy for Characterizations of Iron oxo intermediates

X-ray absorption spectroscopic data were collected at the Fe K-edge for **1**, **2** and **3** in CH$_3$CN to gain insight into their iron coordination environments. The X-ray absorption near edge structure (XANES) region provides information on the oxidation state and symmetry of an iron center. The Fe K-edge of **1** (Figure 2.10) was observed at 7122.1 eV, with a pre-edge peak area of 14.1 units (Table 2.1), consistent with a five-coordinate ferric center (Figure 2.11, left panel).[11] Analysis of the extended X-ray absorption fine structure (EXAFS) region of **1** gives iron-scatterer distances that correspond to 4 N/O atoms at 1.87 Å, 1 Cl atom at 2.37 Å, 6 C atoms at 2.83 Å and multiple scattering pathways involving the carbonyl groups of the ligand at 3.99 Å (Figure 2.12, top row; Appendix A5), distances congruent with those from the crystal structure of **1**.[8c]
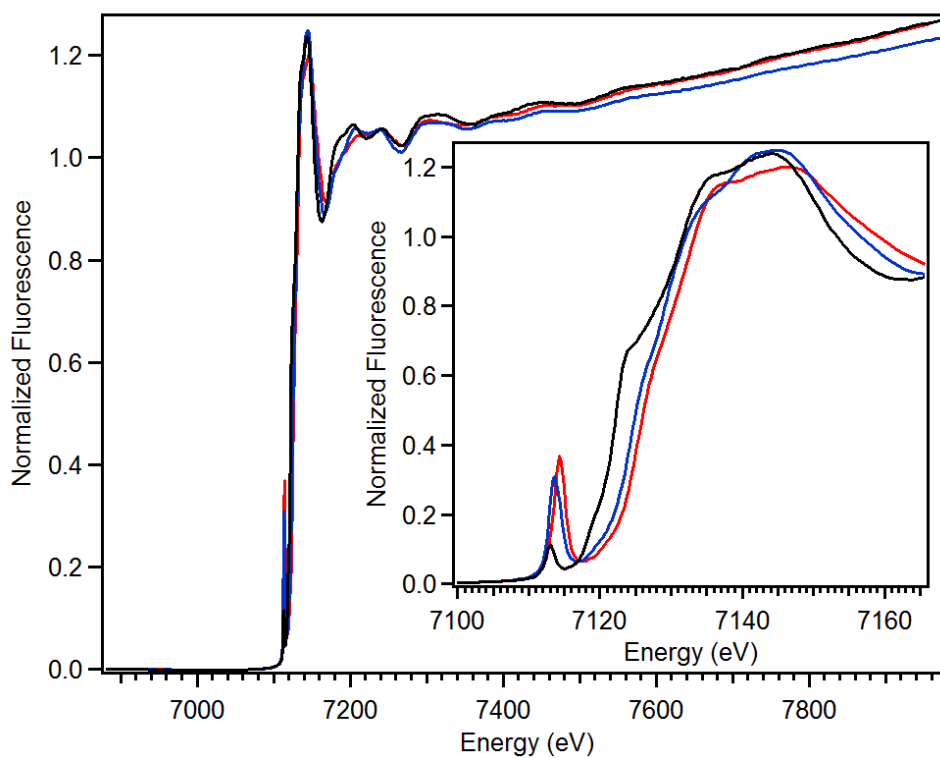
Figure 2.10: Normalized Fe K-edge fluorescence spectra of **1** (black), **2** (blue) and **3** (red); inset – zoom in on the XANES region.

Table 2.1: XAS Pre-edge Peak Analysis of 1, 2 and 3

Species	Peak Position (eV)	Area (units)	Relative Area
1	7113.0	14.1	1.0
2	7113.5	36.7	2.4
	7114.4	15.1	1.0
	Total	51.8	
3	7114.3	65.3	4.4
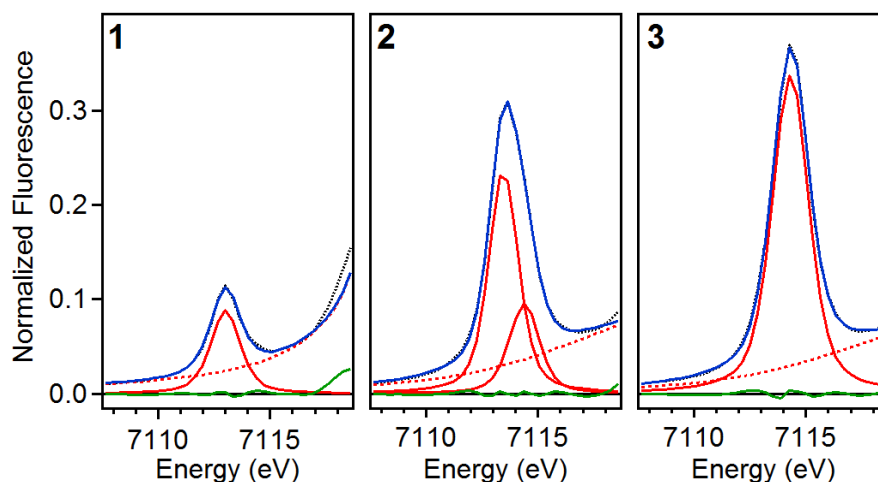
Figure 2.11: Observed X-ray absorption pre-edge regions of **1** (left), **2** (middle), and **3** (right). Experimental data are represented by black dotted lines, with the best fits as blue solid lines, the modeled baselines as red dashed lines, the fitted component peaks as red solid lines, and the residuals as green solid lines.
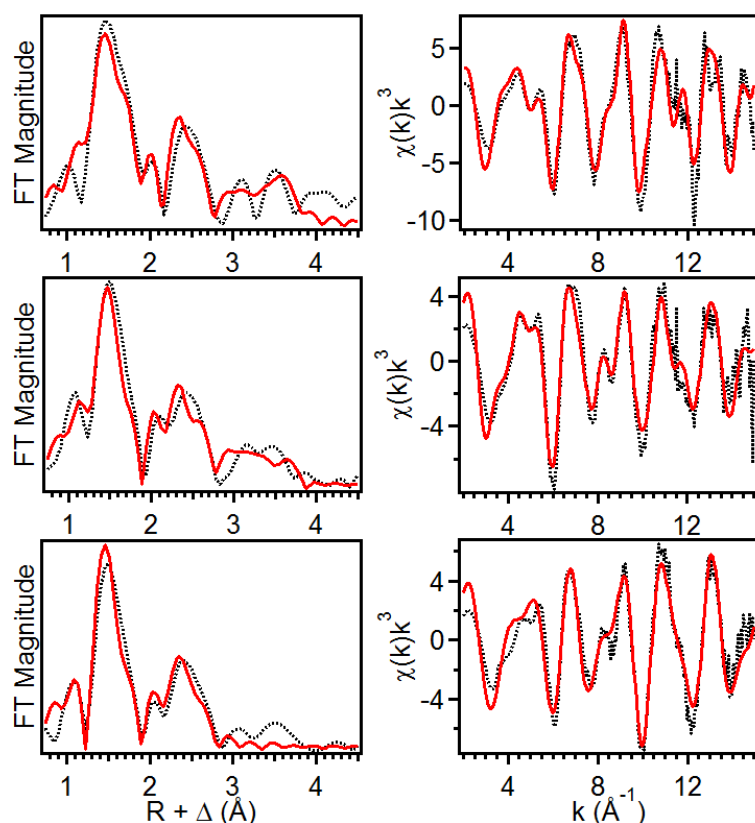
Figure 2.12: Left column: Fourier transforms of the EXAFS data (black dotted) with best fit (solid red) for **1** (top), **2** (middle), **3** (bottom), k range = $2 - 15$ Å^{-1}. Right column: unfiltered EXAFS data (black dotted) with best fit (red solid) for **1** (top), **2** (middle), and **3** (bottom).

Oxidation of **1** to **2** results in an upshift of the K-edge energy to 7124.2 eV (Figure 2.10), which is comparable to that reported for $[Fe^{IV}(O)(TAML)]^{2-}$ (7124.5 eV)[7c] and consistent with its assignment as an Fe^{IV} center. However, the K-edge energy of **2** is 2.1 eV higher than for that for **1**. This larger difference in K-edges is likely due to the bound Cl in **1**, as chloride ligands are known to decrease the K-edge energies of the metal centers to which they are bound.[7f] Complex **2** exhibits a pre-edge area of 52 units (Figure 2.11, middle panel; Table 2.1), which is larger than that found for $[Fe^{IV}(O)(TAML)]^{2-}$ (41 units).[7c] EXAFS analysis of **2** shows 1 O/N atom at 1.64 Å, 4 N/O at 1.86 Å, 6 C at 2.82 Å, and scatterers at 4.01 Å involving ligand carbonyl groups (Figure 2.12, middle row; Appendix A6). The 0.05-Å shorter Fe=O bond distance found for **2** compared to that of $[(TAML)Fe^{IV}(O)]^{2-}$ (1.69 Å)[7c] may rationalize the larger pre-edge area observed for **2**.

Complex **3** exhibits a K-edge at 7125.4 eV (Figure 2.10), which is very close to that of the related $[(TAML)Fe^{V}(O)]^{-}$ complex reported by Collins (K-edge = 7125.3 eV).[7a] Complex **3** also gives rise to a pre-edge feature at 7114.3 eV with a very large peak area of 65 units (Figure 2.11, right panel; Table 2.1), which is comparable in size to that of $[(TAML)Fe^{V}(O)]^{-}$ (~70 units).[7a] These quite large values reflect a high degree of distortion from centrosymmetry that is matched only by that estimated for the aqueous oxoiron(IV) complex described by Pestovsky *et al.*[12] Analysis of the EXAFS region of **3** gives iron-scatterer distances that correspond to 1 O/N atom at 1.59 Å, 4 N/O atoms at 1.86 Å, and 6 C atoms at 2.82 Å (Figure 2.12, bottom row; Appendix A7), which agree with the results for $[Fe^{V}(O)(TAML)]^{-}$ (0.7 O/N at 1.58 Å, 4 N/O at 1.87 Å, and 5 C at 2.82 Å).[7a] Within error, the structures of the two complexes are identical. The significant shortening of the axial Fe=O bond in what is postulated to be a square pyramidal complex is very likely the factor that gives rise to the much larger pre-edge area observed for **3**,[11] as well as the 64-cm^{-1} higher Fe=O stretching frequency of **3** over **2**.

2.4.4 Density Functional Theory

DFT calculations are used to obtain hypothetical three-dimensional models for species **2** and **3**. The optimized geometries for **2** and **3** show Fe–O bond lengths of 1.64 Å and 1.59 Å, respectively, consistent with results from the EXAFS analysis. The predicted 0.05 Å shortening of the Fe–O bond in **3** relative to the $[Fe^{IV}(O)]^{2-}$ state is complemented by an increase in the computed ν_{Fe-O} from 895 cm^{-1} to 964 cm^{-1}, the calculated difference of 69 cm^{-1}

approaching the experimentally observed difference of 64 cm^{-1}. The MO diagram (Figure 2.13) of **2** indicates the presence of a strong σ interaction with the Fe $3d_{z^2}$ and the O $2p_z$ orbital (Figure 2.13, left, contour 2nd from top). For a $S = 1$ ground state, this d_z^2 orbital is unoccupied. Additional strong π interactions between the singly occupied Fe $3d_{xz/yz}$, and O $2p_{x/y}$ orbitals (Figure 2.13, left, contour at the bottom) result in an Fe–O formal bond order of 2 (1 σ + 2 half π). Note that the strong equatorial ligand field of bTAML raises the energy of the $d_{x^2-y^2}$ above that of the d_{z^2} orbital, which is σ antibonding with respect to the strong axial oxo ligand. This is in contrast to most known non-heme Fe systems where the strong σ interaction of the oxo ligand places d_{z^2} orbitals higher in energy than the $d_{x^2-y^2}$.[7b,c,g,h,j] Rather the higher $d_{x^2-y^2}$ orbital energy, as observed here, is a common feature of heme systems where the porphyrin ligand provides a strong equatorial ligand field.[6a,7i] The same situation has been encountered recently in a Fe(IV)=O species having a tetracarbene macrocycle in the equatorial plane.[7g]

The calculations show that there is strong charge transfer from the tetraanionic equatorial ligand in **2**, which appears to result in a decrease in the oxo ligand character of the Fe=O bond. Thus the O_{2p} coefficients in the Fe–O σ (10% $O_{2p(z)}$ in d_z^2) and π (17.36% $_{2p(x)}$, 54.99% d_{xz}) (Figure 2.13 left) in **2** are much smaller than those encountered for other non-heme Fe(IV)=O complexes with weaker equatorial ligands, e.g. 32% $O_{2p(z)}$ in d_{z^2} and 36% $O_{2p(x)}$ 54% $d_{xz(Fe)}$.[7h-7j] These differences may be interpreted as a decrease in the bond covalency of the Fe=O unit in **2** relative to these other complexes, as reflected by the lower Fe=O frequency it exhibits.

The [Fe^V(O)]$^-$ species is one-electron oxidized, which results in depopulation of one of the two singly occupied $d_{xz/yz}$ orbitals (~55% metal 3d contribution, Figure 5 right), indicating that the oxidation is metal-based and not ligand-based as is the case for high-valent heme systems (e. g., Compound I[6a,7i]). Thus the oxidation leads to depopulation of a Fe-O π^* orbital and results in an increase in the Fe–O bond order to 2.5 (1 σ + 1.5 π) in **3**. The increase in the Fe–O bond order upon oxidation is reflected in the shorter Fe–O bond observed in EXAFS and the higher ν_{Fe-O} value in **3** relative to **2** observed in Raman data.
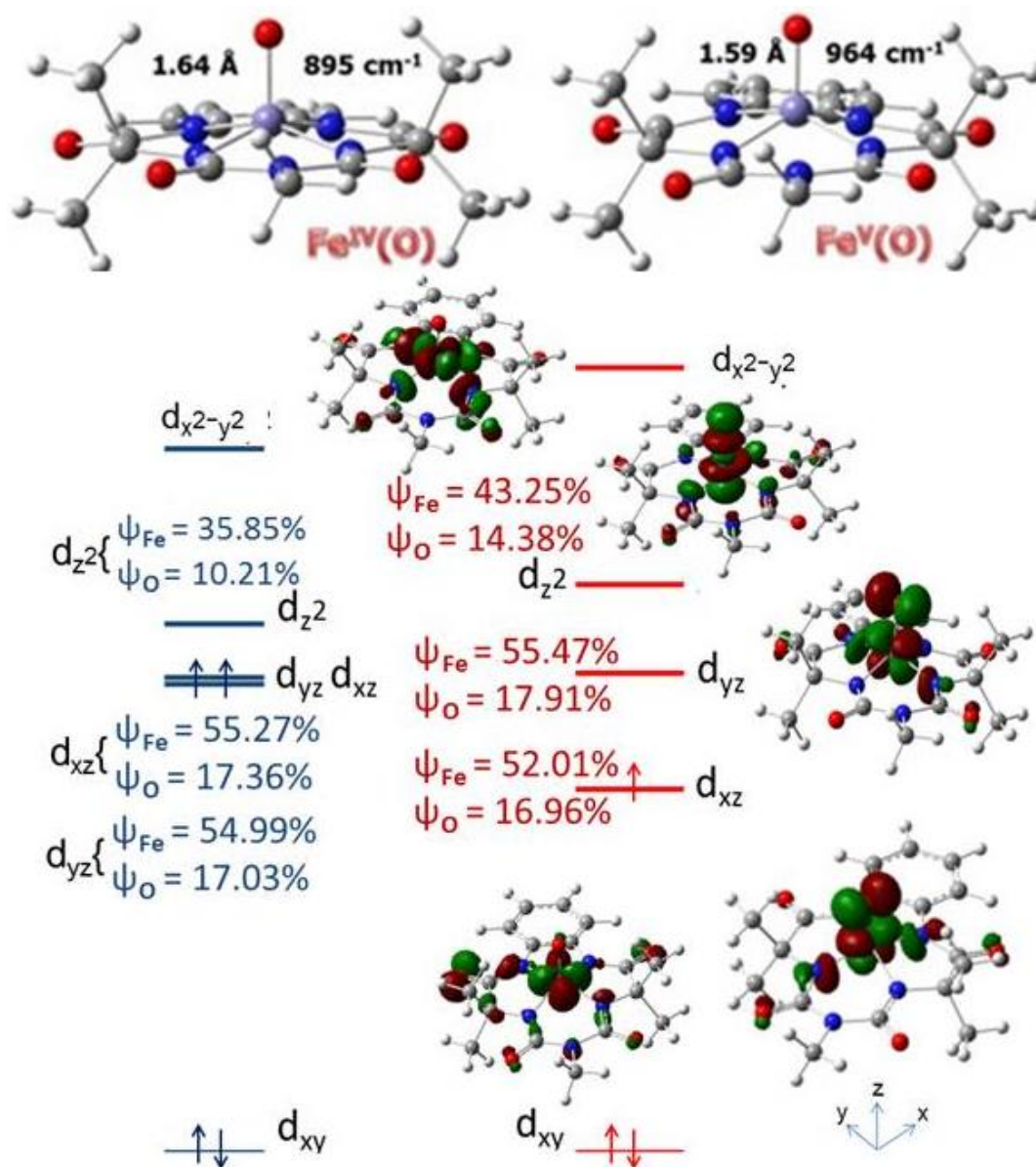
Figure 2.13: Optimized geometries (top) and molecular orbital (MO) diagrams (bottom) for $[(bTAML)Fe^{IV}(O)]^{2-}$ (**2**), left and $[(bTAML)Fe^{V}(O)]^{-}$ (**3**), right. ψ_{Fe} and ψ_{o} indicate contributions of Fe and oxo centers in the individual orbitals. Note that only d orbitals of **3** are shown for clarity and the energy of the non-bonding d_{xy} orbital is set to zero for **2** and **3**.

2.4.5 Electrochemistry

The electrochemical properties of the bTAML complexes **1** – **3** were investigated in water. Cyclic voltammetry (CV) of **1** was performed between pH 11 and 12.5 using a scan window of 0.2 to 0.9 V *vs* NHE (Appendix A2). It should be noted that $[(bTAML)Fe^{III}Cl]^{2-}$ in water converts to the di-aqua complex $[(bTAML)Fe^{III}(H_2O)_2]^{-}$.[13,14] The first p$K_a$ of the coordinated water has been determined to be ~10.3, leading to the formation of $[(bTAML)Fe^{III}(OH)(OH_2)]^{2-}$.[14] A quasi-reversible one-electron wave at $E_{1/2} = 0.44$ V *vs* NHE

(with a peak-to-peak separation of ΔE_p = 66 mV and $i_{p,a}$ / $i_{p,c}$ ~ 0.8) was observed by cyclic voltammetry of chemically synthesized **2** at pH 12 (Figure 2.14A). This feature corresponds to the $Fe^{IV}(O)/Fe^{III}(OH)(OH_2)$ couple. Furthermore, controlled potential electrolysis of a pH 12 solution of **1** at 0.55 V *vs* NHE afforded the well characterized deep red $[(bTAML)Fe^{IV}(O)]^{2-}$ complex described before in this work. The $Fe^{IV/III}$ electrochemical wave is pH dependent between 10.5 and 12.2 with the $E_{1/2}$ *vs* pH decreasing by 58 mV per pH unit (Figure 2.14B), indicating a proton-coupled electron transfer (PCET).[15] Based on all these observations, we propose that the $Fe^{IV/III}$ couple is consistent with the following electrochemical process between pH 10.5 to pH 12.2:

$$[(bTAML)Fe^{IV}O]^{2-} + H_2O \xrightarrow{H^+, e^-} [(bTAML)Fe^{III}(OH)(H_2O)]^{2-}$$
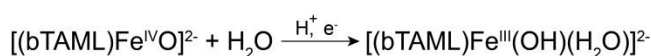
Below pH 10, a $[Fe^{IV}(O)]^{2-}/[Fe^{III}(OH_2)_2]^-$ couple corresponding to a two-proton/one-electron transfer process was observed, as recently reported.[16a] The redox potential for the $[Fe^V(O)]^-$/$[Fe^{IV}(O)]^{2-}$ couple in H_2O has been determined by square wave voltammetry experiments at pH 7 to be $E^{0'}$ = 1.19 V *vs* NHE.[16a] There is an apparent difference in potential of 750 mV between the redox couples $[Fe^V(O)^-/Fe^{IV}(O)^{2-}]$ at pH 7 and $[Fe^{IV}(O)^{2-}/Fe^{III}(OH)^{2-}]$ at pH 12.
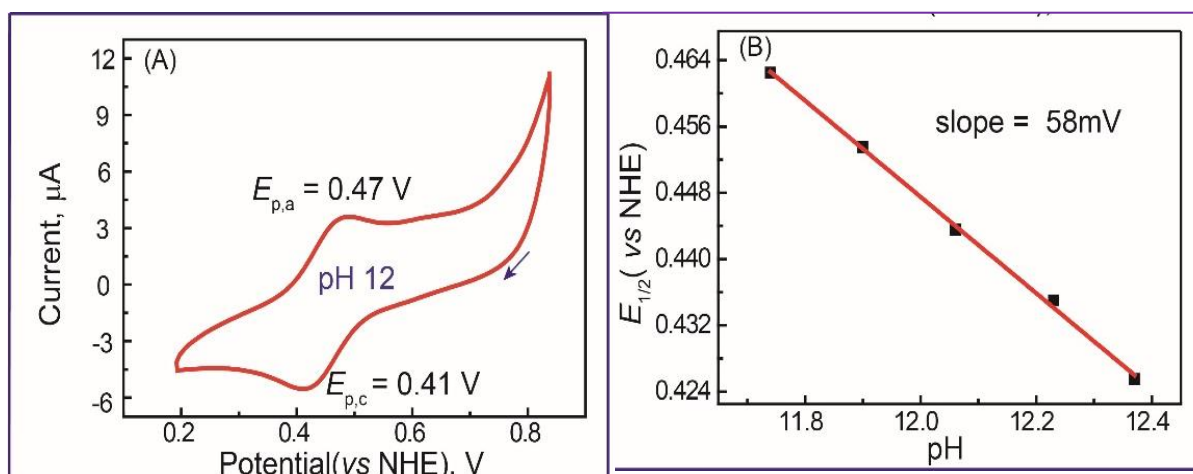
Figure 2.14: (A) CV of **2** synthesized from **1** and NaOCl in a pH 12 aqueous solution (conditions: GC working electrode, Pt counter electrode, 0.2 M KNO_3 as supporting electrolyte, scan rate 50 mV s^{-1}; arrow indicates the direction of potential scanning) (B) Plot of $E_{1/2}$ *vs* pH for **1** in water.

After correcting for the pH difference based on the observation of a $[Fe^{IV}(O)]^{2-}/[Fe^{III}(OH_2)_2]^-$ couple between pH 7 and 10, we estimate a redox potential of 0.9 V *vs* NHE at pH 7, decreasing the redox potential gap to about 300 mV. For comparison, the corresponding heme analogs that serve as models of Cpd I and Cpd II exhibit a difference of about 250 mV.[16b]

Table 2.2: Comparison of Properties of **2** and **3**

Properties	2	3
ν(Fe=O) (cm^{-1})	798	862
r(Fe=O) (Å)	1.64	1.59
XAS pre-edge area	52	65
E^0 (V vs NHE)	0.44 (pH 12)	1.19 (pH 7)
k_2 (BnOH) @ RT	0.08(1) M^{-1}s^{-1}	220(20) M^{-1}s^{-1}
KIE (BnOH oxd'n)	~3	~12
$\Delta H^{\ddagger}$ (kcal/mol)	10.7±0.7	7.9±0.5
$\Delta S^{\ddagger}$ (cal/mol/K)	-27±2	-23±2
T$\Delta S^{\ddagger}$ (kcal/mol)	-8.1±0.6	-6.9±0.6
$\Delta G^{\ddagger}$ (kcal/mol)	19±1.2	15±1

2.4.6 Reactivity towards C-H bond

In order to compare the reactivity of these related iron-oxo species towards C–H bonds, the choice of substrate was important. The calculated BDE (Bond Dissociation Energy) of Fe^{III}(O–H) that corresponds to one-electron reduced [(bTAML)Fe^{IV}(O)]$^{2-}$ has a value of only 83 ± 2 kcal/mol,[17] obtained using the modified Bordwell equation.[18] The expected inability of the oxoiron(IV) complex **2** to oxidize strong C–H bonds is confirmed by its unchanged UV-vis spectrum upon addition of cyclohexane, toluene and cumene. This moderate BDE of [Fe^{III}(bTAML)O−H]$^{2-}$ (~83 kcal/mol) is similar to that of non-heme iron complexes such as [Fe^{III}(N4Py)O−H]$^{2+}$ (~78 kcal/mol)[18] but lower than their heme analogs ([Fe^{III}(TMP)O−H] (~88 kcal/mol),[5i] and [Fe^{III}(TMPS)O−H] (~90 kcal/mol)).[16b,19a] On the other hand, the oxoiron(V) complex **3** is known to react with strong C–H bonds like cyclohexane.[8a] The Fe^{IV}O–H BDE of [(bTAML)Fe^{IV}OH]$^{-}$ is estimated to be about 99 kcal/mol,[20] which is roughly the same as that for the Compound I mimic [(4-TMPyP$^{+.}$)Fe^{IV}(O)] with an Fe^{IV}O–H BDE of 100 kcal/mol. We therefore chose benzyl alcohol (BnOH) as the substrate as it has a C–H bond with a BDE of <80 kcal/mol.[19b]

The reaction of **3** with benzyl alcohol in CH$_3$CN has recently shown to be a 2-electron process involving abstraction of a C–H bond in the rate determining step.[21a] The ET/PT (Electron transfer/ Proton Transfer) mechanism after H–atom abstraction from the benzylic position over rebound of hydroxyl radical was proved by using cyclobutanol as a radical clock probe.[21a] In order to compare the reactivity of both oxoiron (bTAML) complexes under the same conditions, their reactions with benzyl alcohol were carried out under pseudo first

order conditions in 80% CH_3CN:20% H_2O as the solvent, which is compatible with both oxoiron(V) and oxoiron(IV) complexes (Scheme 2.2).
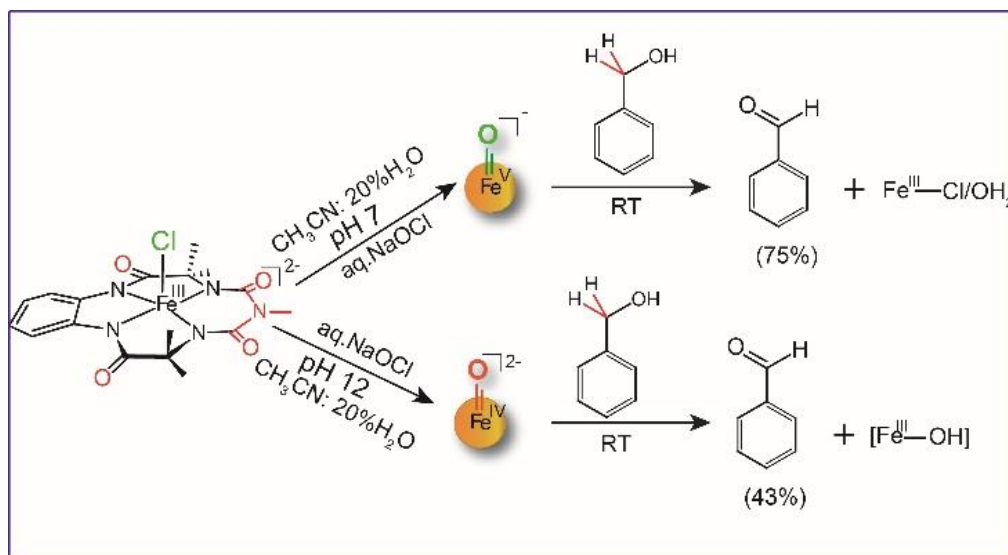
Scheme 2.2: Reactivity of **2** and **3** with BnOH

The kinetics of BnOH oxidation to benzaldehyde by **2** in an 80:20 acetonitrile-water solvent mixture pH 12 at RT was studied under pseudo first order conditions. A decrease in the characteristic $[Fe^{IV}(O)]^{2-}$ absorption band at 460 nm was observed (Figure 2.6 right) due to oxidation of BnOH to benzaldehyde (yield ~ 43%) (Appendix A3 and A4). The less than 50% yield and generation of $[Fe^{III}–OH]^{2-}$ at the end of the reaction indicate a non-rebound mechanism similar to that reported for other nonheme oxoiron(IV) complexes.[21c] Analysis of the pseudo-first order reactions as a function of substrate concentration gave a second order rate constant k_2 of 0.08(0.01) $M^{-1}s^{-1}$ (Figure 2.15A, 2.6 left) and a classical k_H/k_D KIE of ~3 (Table 2.2). For comparison, the reaction of **3** with BnOH in an 80:20 acetonitrile-water (pH 7) solvent mixture was monitored by UV-Vis absorption spectroscopy as a function of BnOH concentration as recently reported by us (yield of benzaldehyde ~75% yield).[21a] Resulting k_{obs} (Figure 2.5) values from pseudo first-order fits correlated linearly with substrate concentration to give a second order rate constant k_2 (220 ± 20 $M^{-1}s^{-1}$) (Figure 2.15B). A nonclassical kinetic isotope effect k_H/k_D ~12 was determined (Table 2.2). Thus **2** has a BnOH oxidation rate that is significantly lower (~2500-fold) than that of **3**. It should be noted that oxidation of benzyl alcohol was carried out by **2** and **3** at pH 12 and 7 respectively. The pH of

the medium can have a crucial role in hydrogen atom abstraction, as has been observed for $[Fe^{IV}(O)N4Py]^{2+}$.[21b]
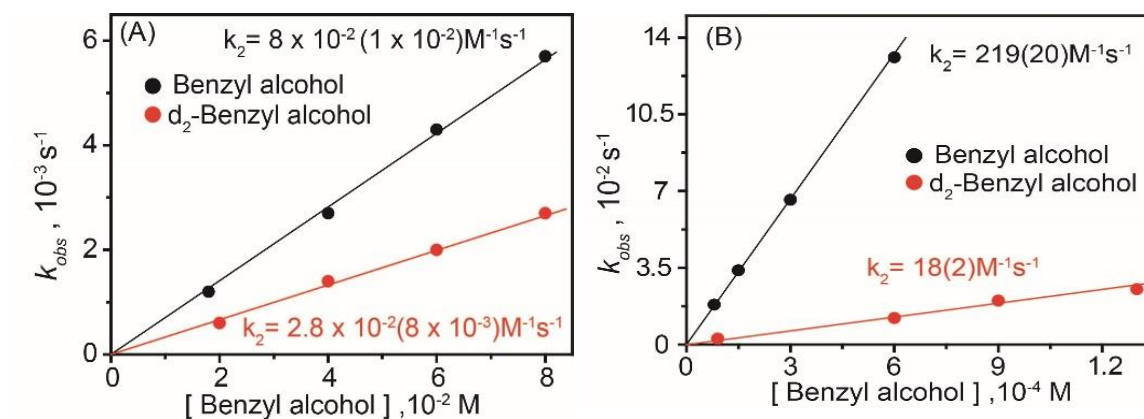
Figure 2.15: Plots of k_{obs} *vs* benzyl alcohol concentration for reactions with (A) **2** (1.5×10^{-4} M) and (B) **3** (5×10^{-5} M) performed in a 80:20 acetonitrile-water solvent mixtures at room temperature.
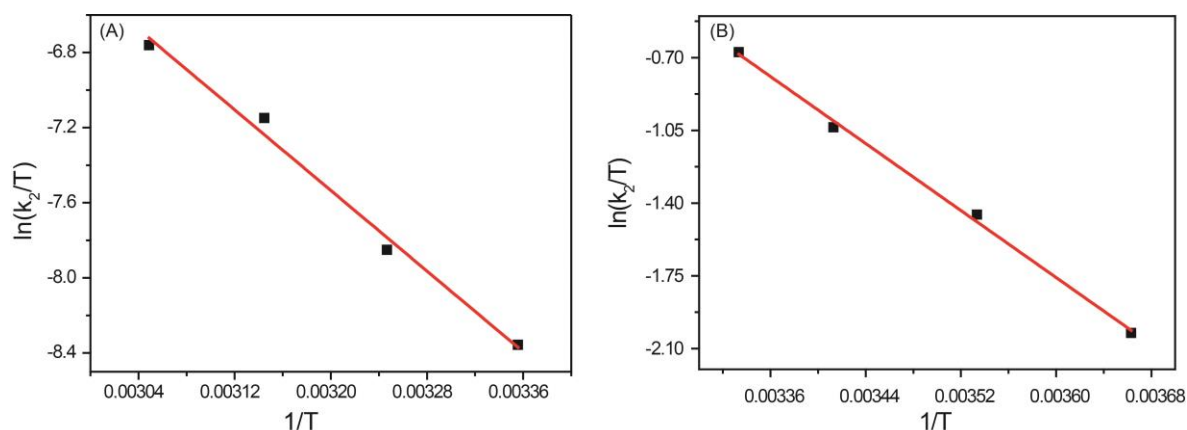
Figure 2.16: (A) Eyring plots for reaction of **2** with benzyl alcohol from 298 K to 328 K (B) Eyring plots for reaction of **3** with benzyl alcohol from 273 K to 300 K.

To gain better insight into the differential reactivity of **2** and **3** towards BnOH, an Eyring analysis was carried out to obtain their activation enthalpies ($\Delta H^{\neq}$) and entropies ($\Delta S^{\neq}$) (Table 2.2 and Figure 2.16). For both of the oxidants, the negative entropy of activation observed is indicative of a tightly bound transition state involving both the iron oxo and the substrate. The contribution of $\Delta H^{\neq}$ to the free energy of activation is greater than that of the $T\Delta S^{\#}$ term for both **2** and **3**, indicating that the process is enthalpically driven. However, for **3**, the difference between $\Delta H^{\neq}$ and $T\Delta S^{\neq}$ term is much smaller (~ 1 kcal/mol). These results are in

contrast to alcohol oxidation by Cpd I and II mimics reported by van Eldik where the process is entropically controlled for the Cpd I mimic but enthalpically controlled for the Cpd II mimic.[22] The difference in reactivity of benzyl alcohol oxidation to benzaldehyde between both the Cpd I and II mimics reported by van Eldik is only ~100-fold.[22] Groves et al.[5j] have also reported a highly reactive Cpd I analog $[(4\text{-TMPyP}^{+\cdot})Fe^{IV}=O]^+$ in comparison to its one-electron reduced Cpd II analog $[(4\text{-TMPyP})Fe^{IV}=O]$ towards xanthene oxidation albeit with a low KIE (2.1). This large reactivity difference of the highly cationic compound I analog was rationalized by considering a low-lying a_{2u} porphyrin HOMO that facilitated spin-state crossing in the course of the reaction. In contrast, studies on the $[Mn(H_3buea)]$ complexes reported by Borovik showed a higher reactivity towards dihydroanthracene (DHA) for the monomeric $[Mn^{III}(O)]^{2-}$ complex relative to the $[Mn^{IV}(O)]^-$ complex, which was attributed to the much enhanced basicity of the $[Mn^{III}(O)]^{2-}$ complex.[23a]

Before concluding, two important points would be worth noting, First, for C–H bond abstraction of benzyl alcohol by **2** and **3**, the events accompanying formation of the transition state are not only determined by the electron affinity of the oxidant (which is manifested in the huge difference in their redox potential reported earlier) but also by the proton affinity of the one-electron reduced species formed after electron transfer. The pK_a of the one-electron reduced species generated from **2** (i.e. $[Fe^{III}(O)]^{3-}$) should be significantly higher than for the one-electron reduced species of **3** (i.e. $[Fe^{IV}(O)]^{2-}$; pK_a ~10) but could not be determined experimentally (Supporting Information Figure S3). The pKa of a related $[Fe^{III}(O)(H_3buea)]^{2-}$ species has been determined by Borovik to be >20.[10] This high pK_a of the putative $Fe^{III}(O)$ would offset the reactivity of **3** in comparison to **2** that would be expected only due to the 300 mV redox potential difference.

The second relates to the respective KIEs of 3 and 12 observed for the reactions of **2** and **3** with BnOH. These values indicate that H-atom abstraction is likely an important contributor to the RDS for both these complexes.[24] Interestingly, the pattern of KIE values observed for **2** and **3** is the reverse of what is observed for nonheme oxoiron(IV) complexes supported by neutral N4 or N5 ligands. For the latter, non-classical KIE values are observed for $S = 1$ $Fe^{IV}(O)$ complexes,[3,24c] but classical KIE values are found for catalytic alkane hydroxylation by related nonheme iron complexes for which a powerful $Fe^V(O)(OH)$ oxidant has been implicated.[24f,g,h] The KIE differences could arise from differences in electronic structure between **2** and other $S = 1$ nonheme $Fe^{IV}(O)$ complexes. As shown for **2** in Figure 5, the d_{x^2}

$_{y2}$ orbital lies well above the d$_z$2 orbital due to the strong equatorial field of the bTAML ligand, resulting in a d$_{xy}^1$d$_{xz}^1$d$_{yz}^1$d$_{z2}^1$ configuration for the excited quintet (S = 2) state instead of the more typical d$_{xy}^1$d$_{xz}^1$d$_{yz}^1$d$_{x2-y2}^1$ configuration associated with the other nonheme Fe^{IV}=O complexes supported by neutral polydentate ligands. A consequence for **2** is that its S = 2 excited state is calculated to be 20-26 kcal mol^{-1} higher in energy than its ground triplet state (S = 1), depending on which functional (UBP86 or UB3LYP) is used (Table 2.3 and 2.4), A similarly large energy gap is calculated for the Fe^{IV}=O(tetracarbene) complex reported by Neese and Meyer,[7g] but the triplet-quintet energy gap calculated for the prototypical [Fe^{IV}(O)(TMC)(NCCH$_3$)]$^{2+}$ complex is much smaller at 3-5 kcal mol^{-1}.[24e,i] For **2** and the tetracarbene complex, the presence of an unpaired electron in the d$_z$2 orbital of the excited S = 2 state significantly weakens the Fe=O bond, thereby destabilizing this spin state. On the other hand, our calculations on **3** show that its doublet (S = ½) spin state is more stable than the quartet (S = 3/2) by 10-14 kcal mol^{-1} (Table 2.3). Future work will focus on gaining further insight into the consequences of these differences in electronic structure on the reactivity of the high-valent oxoiron complexes supported by tetraanionic TAML ligands versus its neutral counterparts.

Table 2.3: The relative energies of [Fe^V(O)(bTAML)]$^-$ (**3**) in doublet and quartet electronic states in kcal/mol using UBP86 or UB3LYP functionals and the 6-311+G* basis set in acetonitrile solvent.

	ΔE(kCal) UBP86(UB3LYP)	Δ(E+ZPE)(kCal) UBP86(UB3LYP)	ΔG(kCal) UBP86(UB3LYP)
S=1/2	0.0(0.0)	0.0(0.0)	0.0(0.0)
S=3/2	14.1(10.4)	13.1(9.3)	11.7(7.3)

Table 2.4: The relative energies of [Fe^{IV}(O)(bTAML)]$^{2-}$ (**2**) in triplet and quintet electronic states in kcal/mol using UBP86 or UB3LYP functionals and the 6-311+G* basis set in acetonitrile solvent.

	ΔE(kCal) UBP86(UB3LYP)	Δ(E+ZPE)(kCal) UBP86(UB3LYP)	ΔG(kCal) UBP86(UB3LYP)
S=1	0.0(0.0)	0.0(0.0)	0.0(0.0)
S=2	26.0(19.5)	24.8(18.2)	23.0(16.5)

2.5 Conclusions

In summary, the resonance Raman and XAS properties of $[Fe^{IV}(O)]^{2-}$ (**2**) and $[Fe^{V}(O)]^{-}$ (**3**) species have been characterized, allowing the first detailed comparison of complexes with oxoiron(IV) and oxoiron(V) units supported by the same ancillary bTAML ligand under the same conditions. These results show significant strengthening and shortening of the Fe=O bond upon oxidation from Fe^{IV} to Fe^{V} due to an increase in π bond order. This structural change translates into a significant difference in redox potential between **2** and **3** and a 2500-fold greater reactivity of **3** over its one-electron analogue **2** in oxidizing benzyl alcohol. DFT calculations provide a computational basis for rationalizing the observed differences in properties.

2.6 References

1.   (a) Denisov, I. G.; Makris, T. M.; Sligar, S. G.; Schlichting, I. *Chem. Rev.* **2005**, *105*, 2253-2278. (b) Ortiz de Montellano, P. R. *Chem. Rev*. **2010**, *110*, 932−948. (c) Groves, J. T. Models and Mechanisms of Cytochrome P450 Action. *In Cytochrome P450: Structure, Mechanism and Biochemistry*, 3rd ed.; Ortiz de Montellano, P. R., Ed.; Kluwer Academic/Plenum Publishers: New York, **2005**.

2.   (a) Sono, M.; Roach, M. P.; Coulter, E. D.; Dawson, J. H. *Chem. Rev*. **1996**, *96*, 2841−2888. (b) Nam, W. *Acc. Chem. Res.* **2007**, 40, 522−531. (c) Rittle, J.; Green, M. T. *Science,* **2010**, *330*, 933−937. (d) Meunier, B.; de Visser, S. l. P.; Shaik, S. *Chem. Rev.* **2004**, *104*, 3947-3980. (e) Costas, M.; Mehn, M. P.; Jensen, M. P.; Que, L., Jr. *Chem. Rev.* **2004**, *104*, 939-986. (f) Abu-Omar, M. M.; Loaiza, A.; Hontzeas, N. *Chem. Rev.* **2005,** *105*, 2227-2252.

3.   Sastri, C. V.; Lee, J.; Oh, K.; Lee, Y. J.; Lee, J.; Jackson, T. A.; Ray, K.; Hirao, H.; Shin, W.; Halfen, J. A.; Kim, J.; Que, L., Jr.; Shaik, S.; Nam, W. *Proc. Natl. Acad. Sci. U.S.A.* **2007**, *104*, 19181−19186.

4.   Borovik, A. S. *Chem. Soc. Rev*. **2011,** *40*, 1870-1874.

5.   (a) Groves, J. T.; Gross, Z.; Stern, M. K. *Inorg. Chem*. **1994**, *33*, 5065−5072. (b) Nam, W.; Lee, H. J.; Oh, S.-Y.; Kim, C.; Jang, H. G. *J. Inorg. Biochem.* **2000**, *80*, 219−225. (c) Nam, W.; Park, S.-E.; Lim, I.K.; Lim, M. H.; Hong, J.; Kim, J. *J. Am. Chem. Soc*. **2003**, *125*, 14674−14675. (d) Nehru, K.; Seo, M. S.; Kim, J.; Nam, W. *Inorg. Chem.* **2007**, *46*, 293−298. (e) Park, M. J.; Lee, J.; Suh, Y.; Kim, J.; Nam, W. *J. Am. Chem. Soc*. **2006**, *128*, 2630−2634. (f) Jeong, Y. J.; Kang, Y.; Han, A.-R.; Lee,Y.-M.; Kotani, H.; Fukuzumi, S.; Nam, W. *Angew. Chem. Int. Ed*. **2008**, *47*, 7321−7324. (g)

Fukuzumi, S.; Kotani, H.; Lee, Y. -M.; Nam, W. *J. Am. Chem. Soc*. **2008**, *130*, 15134−15142. (h) Ji, L.; Franke, A.; Brindell, M.; Oszajca, M.; Zahl, A.; van Eldik, R. *Chem. - Eur. J.* **2014**, *20*, 14437−14450. (i) Fertinger, C.; Hessenauer-Ilicheva, N.; Franke, A.; van Eldik, R. *Chem. -Eur. J.* **2009**, *15*, 13435–13440. (j) Bell, S. R.; Groves, J. T. *J. Am. Chem. Soc.* **2009**, *131*, 9640–9641.

6. (a) Altun, A.; Shaik, S.; Thiel, W. *J. Am. Chem. Soc*. **2007**, *129*, 8978–8987. (b) Tahsini, L.; Bagherzadeh, M.; Nam, W.; de Visser, S. P. *Inorg. Chem*. **2009**, *48*, 6661–6669. (c) Ricciardi, G.; Baerends, E. J.; Rosa, A. *ACS Catal.*, **2016**, *6*, 568–579. (d) Berry, J. F.; DeBeer George, S.; Neese, F. *Phys. Chem. Chem. Phys.* **2008,** *10*, 4361–4374. (e) Geng, C.; Ye, S.; Neese, F. *Dalton Trans.* **2014**, *43*, 6079–6086 (f) Lyakin, O. Y.; Bryliakov K. P.; Evgenii. T. P. *Inorg. Chem.* **2011**, *50*, 5526. (g) Oloo, W. N.; Feng, Y.; Iyer, S.; Parmelee, S.; Xue, G.; Que, L., Jr. *New. J. Chem.* **2013**, *37*, 3411-3415.

7. (a) de Oliveira, F. T.; Chanda, A.; Banerjee, D.; Shan, X.; Mondal, S.; Que, L.; Bominaar, E. L.; Münck, E.; Collins, T. J. *Science* **2007**, *315*, 835–838. (b) Popescu, D.-L.; Vrabel, M.; Brausam, A.; Madsen, P.; Lente, G.; Fabian, I.; Ryabov, A. D.; van Eldik, R.; Collins, T. J. *Inorg. Chem.* **2010**, *49*, 11439-11448. (c) Chanda, A.; Shan, X.; Chakrabarti, M.; Ellis, W. C.; Popescu, D. L.; Tiago de Oliveira, F.; Wang, D.; Que, L.; Collins, T. J.; Münck, E.; Bominaar, E. L. A *Inorg. Chem.* **2008**, *47*, 3669-3678. (d) Ghosh, A.; Tiago de Oliveira, F.; Yano, T.; Nishioka, T.; Beach, E. S.; Kinoshita, I.; Münck, E.; Ryabov, A. D.; Horwitz, C. P.; Collins, T. J. *J. Am. Chem. Soc*. **2005**, *127*, 2505– 2513. (e) Kundu, S.; Thompson, J. V.; Ryabov, A. D.; Collins, T. J. *J. Am. Chem. Soc*. **2011**, *133*, 18546. (f) Sarangi, R. *Coord. Chem. Rev.,* **2013**, 257, 459-472. (g) Ye, S.; Kupper, C.; Meyer, S.; Andris, E.; Navratil, R.; Krahe, O.; Mondal, B.; Atanasov, M.; Bill, E.; Roithova, J.; Meyer, F.; Neese, F. *J. Am. Chem. Soc*. **2016**, *138*, 14312-14325. (h) Decker, A.; Rohde, J.-U.; Que, L.; Solomon, E. I. *J. Am. Chem. Soc*. **2004**, *126*, 5378-5379. (i) Decker, A.; Solomon, E. I. *Angew. Chem. Int. Ed.* **2005**, *44*, 2252-2255. (j) Solomon, E. I.; Light, M. K.; Liu, V. L.; Srnec, M.; Wong, D. S. *Acc. Chem. Res*. **2013**, *46*, 2725-2739.

8. (a) Ghosh, M.; Singh, K. K.; Panda, C.; Weitz, A.; Hendrich, M. P.; Collins, T. J.; Dhar, B. B.; Gupta, S. S., *J. Am. Chem. Soc*. **2014**, *136*, 9524–9527. (b) Singh, K. K.; Tiwari, M. k.; Ghosh, M.; Panda, C.; Weitz, A.; Hendrich, M. P.; Dhar, B. B.; Vanka,

K.; Gupta, S. S. *Inorg. Chem.* **2015**, *54*, 1535-1542. (c) Panda, C.; Ghosh, M.; Panda, T.; Banerjee, R.; Gupta, S. S. *Chem. Commun.,* **2011**, *47*, 8016-8018.

9. (a) McDonald, A. R.; Que, L., Jr., *Coord. Chem. Rev*. **2013**, *257*, 414-428. (b) Klein, J. E. M. N.; Que, L. Biomimetic High-Valent Mononuclear Nonheme Iron-Oxo Chemistry in *Encyclopedia of Inorganic and Bioinorganic Chemistry (EIBC)*; John Wiley & Sons, Ltd, **2016**, DOI: 10.1002/9781119951438.eibc2344. (c) Prakash, J.; Rohde, G. T.; Meier, K. K.; Münck, E.; Que, L., Jr., *Inorg. Chem.* **2015**, *54*, 11055-11057.

10. (a) Lacy, D. C.; Gupta, R.; Stone, K. L.; Greaves, J.; Ziller, J. W.; Hendrich, M. P.; Borovik, A. S. *J. Am. Chem. Soc.* **2010**, *132*, 12188-12190. (b) MacBeth, C. E.; Golombek, A. P.; Young, V. G., Jr.; Yang, C.; Kuczera, K.; Hendrich, M. P.; Borovik, A. S., *Science* **2000**, *289*, 938-941.

11. (a) Roe, A. L.; Schneider, D. J.; Mayer, R. J.; Pyrz, J. W.; Widom, J.; Que, L., Jr., *J. Am. Chem. Soc.* **1984**, *106*, 1676–1681. (b) Westre, T. E.; Kennepohl, P.; DeWitt, J. G.; Hedman, B.; Hodgson, K. O.; Solomon, E. I. *J. Am. Chem. Soc.* **1997**, *119*, 6297–6314. (c) Chandrasekaran, P.; Stieber, S. C. E.; Collins, T. J.; Que, L., Jr.; Neese, F.; DeBeer, S., *Dalton Trans*., **2011**, *40*, 11070-11079.

12. Pestovsky, O.; Stoian, S.; Bominaar, E. L.; Shan, X.; Münck, E.; Que, L., Jr.; Bakac, A. *Angew. Chem. Int. Ed.* **2005**, *44*, 6871-6874.

13. Ghosh, A.; Ryabov, A. D.; Mayer, S. M.; Horner, D. C.; Prasuhn, D. E.; Sen Gupta, S.; Vuocolo, L.; Culver, C.; Hendrich, M. P.; Rickard, C. E. F.; Norman, R. E.; Horwitz, C. P.; Collins, T. J., *J. Am. Chem. Soc.* **2003**, *125*, 12378-12379

14. Warner, G. R.; Mills, M. R.; Enslin, C.; Pattanayak, S.; Panda, C.; Panda, T. K.; Gupta, S. S.; Ryabov, A. D.; Collins, T. J. *Chem. -Eur. J.* **2015**, *21*, 6226-6233.

15. (a) Huynh, M. H. V.; Meyer, T. J. *Chem. Rev*. **2007**, *107*, 5004. (b) Weinberg, D. R.; Gagliardi, C. J.; Hull, J. F.; Murphy, C. F.; Kent, C. A.; Westlake, B. C.; Paul, A.; Ess, D. H.; McCafferty, D. G.; Meyer, T. J. *Chem. Rev*. **2012**, *112*, 4016−4093.

16. (a) Pattanayak, S.; Chowdhury, R. D.; Garai, B.; Sing, K. K.; Paul, A.; Dhar, B. B.; Gupta, S. S. *Chem.-Eur. J.* DOI: 10.1002/chem.201605061 (b) Liu, M.-h.; Su, Y. O. *J. Electroanal. Chem.* **1998**, *452*, 113– 125.

17. BDE (Fe^{III}−OH) = 23.06 × $E^{0'}$(Fe$^{IV/III}$) + 1.37pH + 57
   = 23.06 × 0.44 V + 1.37 × 12 + 57 = 83 ± 2 kcal/mol.

18. Wang, D.; Zhang, M.; Bühlmann, P.; Que, L., Jr. *J. Am. Chem. Soc.* **2010**, *132*, 7638-7644.

19. (a) Wolak, M.; van Eldik, R. *Chem.—Eur. J.* **2007**, *13*, 4873- 4883. (b) Brandi, P.; Gali, P, *J. Org. Chem.* **2005**, *70*, 9521-9528.

20. $BDE(Fe^{IV}-OH) = 23.06 \times E^{0'}(Fe^{V/IV}) + 1.37 pK_a + 57$
   $= 23.06 \times 1.19\ V + 1.37 \times 10.05 + 57 = 99 \pm 2\ kcal/mol$.

21. (a) Ghosh, M.; Nikhil, Y. L. K.; Dhar, B. B.; Gupta, S. S. *Inorg. Chem.* **2015**, *54*, 11792-11798. (b) Park, J.; Lee, Y.-M.; Nam, W.; Fukuzumi, S. *J. Am. Chem. Soc.* **2013**, *135*, 5052-5061. (c) Cho, K.-B.; Hirao, H.; Shaik, S.; Nam, W. *Chem. Soc. Rev.* **2016,** *45*, 1197-1210.

22. Oszajca, M.; Franke, A.; Drzewiecka-Matuszek, A.; Brindell, M. G.; Stochel, G. Y.; van Eldik, R. *Inorg. Chem.* **2014**, *53*, 2848-2857.

23. (a) Parsell, T. H.; Yang, M.-Y.; Borovik, A. S. *J. Am. Chem. Soc.* **2009**, *131*, 2762-2763. (b) Singh, K. K.; Tiwari, M. K.; Dhar, B. B.; Vanka, K.; Gupta, S. S. *Inorg. Chem.* **2015**, *54*, 6112-6121. (c) Schröder, D.; Shaik, S.; Schwarz, H. *Acc. Chem. Res.* **2000,** *33*, 139-145. (d) Shaik, S.; Danovich, D.; Fiedler, A.; Schröder, D.; Schwarz, H. *Helv. Chim. Acta* **1995**, *78*, 1393–1407. (e) Shaik, S.; Filatov, M.; Schröder, D.; Schwarz, H. *Chem. - Eur. J.* **1998**, *4*, 193–199. (f) Shaik, S.; Hirao, H.; Kumar, D. *Acc. Chem. Res.* **2007**, *40*, 532-542.

24. (a) Mayer, J. M. *Acc. Chem. Res*. **1998**, *31*, 441– 450. (b) Shaik, S., Kumar, D., de Visser, S. P. A *J. Am. Chem. Soc*. **2008**, *130*, 10128– 10140. (c) Kaizer, J.; Klinker, E. J.; Oh, N. Y.; Rohde, J.-U.; Song, W. J.; Stubna, A.; Kim, J.; Münck, E.; Nam, W.; Que, L., Jr. *J. Am. Chem. Soc*. **2004**, *126*, 472-473. (d) Hirao, H.; Kumar, D.; Que, L., Jr.; Shaik, S. *J. Am. Chem. Soc*. **2006**, *128*, 8590-8606. (e) Mandal, D.; Ramanan, R.; Usharani, D.; Janardanan, D.; Wang, B.; Shaik, S. *J. Am. Chem. Soc*. **2015**, *137*, 722-733. (f) Chen, K.; Que, L., Jr. *J. Am. Chem. Soc*. **2001**, *123*, 6327-6337. (g) Chen, K.; Costas, M.; Kim, J.; Tipton, A. K.; Que, L., Jr. *J. Am. Chem. Soc*. **2002**, *124*, 3026-3035. (h) Oloo, W. N.; Que, L., Jr. *Acc. Chem. Res.* **2015***, 48*, 2612-2621. (i) Swart, M. *Chem. Commun.* **2013***, 49,* 6650-6652.

25. Armarego, W. L. F.; Perrin, D. D., Purification of Laboratory Chemicals; 4th ed.; Elsevier Science, USA, 1997.

26. (a) George, G. N., EXAFSPAK: A Suite of Computer Programs for Analysis of X-ray Absorption Spectra (1990) [http://www-ssrl.slac.stanford.edu/exafspak.html]. (b)

Ankudinov, A. L.; Ravel, B.; Rehr J. J.; Conradson, S. D. *Phys. Rev. B* **1998**, *58*, 7565–7576. (c) Wojdyr, M., *Fityk*: a general-purpose peak fitting program, *J. Appl. Cryst.*, **2010**, *43*, 1126-1128,

27. (a) ASTM E1840-96 (2007) Standard Guide for Raman Shift Standards for Spectrometer Calibration, ASTM International, DOI: 10.1520/E1840-96R07. (b) Menges, F., "Spekwin32 - optical spectroscopy software", Version 1.72.0, **2015**, http://www.effemm2.de/spekwin/ (c) Draksharapu, A.; Codolà, Z.; Gómez, L.; Lloret-Fillol, J.; Browne, W. R.; Costas, M. *Inorg. Chem.* **2015**, *54*, 10656-10666.

28. Cho, K.; Leeladee, P.; McGown, A. J.; DeBeer, S.; Goldberg, D. P. *J. Am. Chem. Soc.* **2012**, *134*, 7392- 7399.

29. Espenson, J. H., Chemical Kinetics and Reaction Mechanisms; 2nd ed.; McGraw-Hill, Inc.: New York, **1995**.

30. (a) Perdew, J. P.; Chevary, S. H.; Vosko, K. A.; Jackson, K. A.; Pederson, M. R.; Singh, D. J.; Fiolhais, C., *Phys. Rev. B* **1992**, *46*, 6671. (b) Perdew, J. P.; Chevary, S. H.; Vosko, K. A.; Jackson, K. A.; Pederson, M. R.; Singh, D. J.; Fiolhais, C. *Phys. Rev. B* **1993**, *48*, 4978. (c) Perdew, J. P.; Burke, K.; Wang, Y., *Phys. Rev. B* **1996**, *54*, 16533. (d) Adamo, C.; Barone, V. *J. Chem. Phys.* **1998**, *108*, 664. (e) Becke, A. D., Density-functional thermochemistry. III. The role of exact exchange. *J. Chem. Phys.* **1993**, *98*, 5648. (f) Lee, C.; Yang, W.; Parr, R. G. *Phys. Rev. B* **1988**, *37*, 785. (g) Roothan, C. C. *J. Rev. Mod. Phys.* **1960**, *36*, 179. (h) McWeeny, R.; Dierksen, G. *J. Chem. Phys.* **1968**, *49*, 4852. (i) Pople, J. A.; Nesbet, R. K. *J. Chem. Phys.* **1954**, *22*, 571.

31. Frisch, M. J.; Trucks, G. W.; Schlegel, H. B.; Scuseria, G. E.; Robb, M. A.; Cheeseman, J. R.; Scalmani, G.; Barone, V.; Mennucci, B.; Petersson, G. A.; Nakatsuji, H.; Caricato, M.; Li, X.; Hratchian, H. P.; Izmaylov, A. F.; Bloino, J.; Zheng, G.; Sonnenberg, J. L.; Hada, M.; Ehara, M.; Toyota, K.; Fukuda, R.; Hasegawa, J.; Ishida, M.; Nakajima, T.; Honda, Y.; Kitao, O.; Nakai, H.; Vreven, T.; Montgomery, J. A., Jr.; Peralta, J. E.; Ogliaro, F.; Bearpark, M.; Heyd, J. J.; Brothers, E.; Kudin, K. N.; Staroverov, V. N.; Kobayashi, R.; Normand, J.; Raghavachari, K.; Rendell, A.; Burant, J. C.; Iyengar, S. S.; Tomasi, J.; Cossi, M.; Rega, N.; Millam, J. M.; Klene, M.; Knox, J. E.; Cross, J. B.; Bakken, V.; Adamo, C.; Jaramillo, J.; Gomperts, R.; Stratmann, R. E.; Yazyev, O.; Austin, A. J.; Cammi, R.; Pomelli, C.; Ochterski, J. W.; Martin, R. L.; Morokuma, K.; Zakrzewski, V. G.; Voth, G. A.; Salvador, P.; Dannenberg, J. J.; Dapprich, S.; Daniels, A. D.; Farkas, Ö.; Foresman, J. B.; Ortiz, J. V.; Cioslowski, J.; Fox, D. J. Gaussian 09, revision B.01; Gaussian, Inc.: Wallingford, CT, **2009**.

Chapter III

Electrochemical Water Oxidation by High-valent Iron (Chapter IIIA) and Cobalt (Chapter IIIB) Oxo Intermediate

3A.1 Abstract

We report a detailed electrochemical investigation of a series of iron complexes (biuret modified tetraamido iron mcrocycle; Fe^{III}-bTAML; **1a**) which includes first electrochemical generation of Fe^V(O) and demonstration of their efficacy as homogeneous catalysts for electrochemical water oxidation (WO) in aqueous medium. Spectroelectrochemical and mass spectral studies indicated Fe^V(O) as the active oxidant, formed due to two redox transitions which have been assigned as Fe^{IV}(O)/Fe^{III}(OH$_2$) and Fe^V(O)/Fe^{IV}(O). The spectral properties of both these high valent iron oxo species perfectly match their chemically synthesized versions which are thoroughly characterized by several spectroscopic techniques. The O−O bond formation step occurs due to nucleophilic attack of H$_2$O onto Fe^V(O). Kinetic Isotope Effect (KIE) of 3.2 indicates an atom proton Transfer (APT) mechanism. The reaction of chemically synthesized Fe^V(O) in CH$_3$CN and water was directly probed by electrochemistry and was found to be first-order in water. The buffer base pK_a plays a critical role in rate determining step by increasing several folds reaction rate. The electronic effect on redox potential WO rates and onset over potential was studied by employing a series of iron complexes. The catalytic activity was enhanced by the presence of electron-withdrawing groups on the bTAML framework- changing the substituents from −OMe to −NO$_2$ increase an 8-fold reaction rates, while over potential also increases by three-fold.
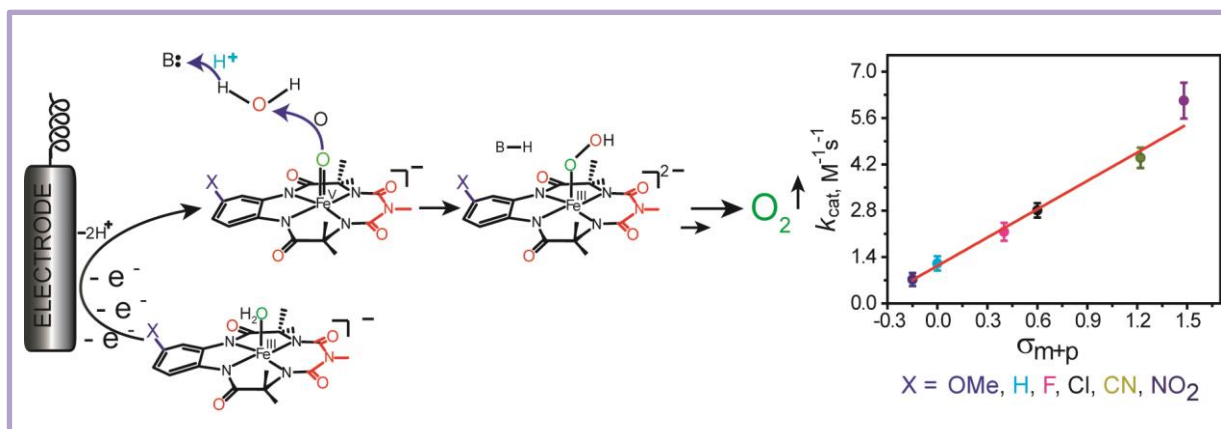
3A.2 Introduction

Water oxidation (WO; $2H_2O \rightarrow O_2 + 4H^+ + 4e^-$, $E^o = 1.23$ V *vs* NHE at pH 0) is a key half reaction in natural photosynthesis by oxygen evolving complex of photosystem II (OEC PSII).[1] The key reaction in this process is the loss of $4e^-/4H^+$ leading to the O−O bond formation. The defining property of oxygen evolving complex (OEC) in the oxygen evolution reaction (OER) is the formation of the O−O bond having turn-over frequency (TOF) of 100-400 s^{-1} without generation of long-lived intermediates such as H_2O_2.[2,3] Rapid development of both homogeneous[4] and heterogeneous[5] OER catalysts propel the necessity to synthesize suitable WO catalyst. Homogeneous WO catalysts have advantage over heterogeneous WO catalysts because the former can be used for comprehensive mechanistic studies.[4] Use of homogeneous WO catalysts including transition metals such as Ru,[6] Co,[7] Mn,[8] Ni,[9] Ir,[10] and Cu[11] have been attempted by several researchers with varied success. Among these catalysts, molecular complexes based on earth abundant metals are very attractive due to several advantages including low cost, environmental compatibility and controllable redox features.[4] Of particular interest are complexes synthesized from the cheap and biocompatible iron, since its group 16 analogue Ru has one of the best developed WO chemistry.[6] The challenge with Fe-based catalysts is the relatively slow TOF (< 1 s^{-1})[12a] which is thousand fold slower than what would be required to match a practical solar energy conversion scheme (although, very recent reports on WO by a pentanuclear iron complex display very high rate (1900 s^{-1}) of O-O bond foration[12c]). The slow TOF in case of mononuclear iron complexes, is due to the sluggish O−O bond formation which is the rate determining step of the reaction. Achieving high reaction rates for the O− O formation, a critical goal for these complexes to have commercial applications, would first require understanding of the O− O bond formation during OER. Hence, mechanistic insights for the formation of O−O bond catalyzed by Fe-complexes are very important. Furthermore, useful strategies would be required to understand how systematic synthetic modifications in the ligand can potentially modify the redox potentials of the iron complexes thus altering the rates of O−O bond formation.[4] Mechanistic insight into WO by mononuclear iron complexes have revolved around identification of the high-valent iron-oxo species formed and its reaction with H_2O in the rate-determining O−O bond formation step. For iron complexes bearing neutral chelating ligand such as mcp,[12b] Pytacn,[13] tpa,[14] and bquen[15] the involvement of $Fe^{IV}(O)$ intermediate has been proposed based on ESI-MS (Electrospray Ionisation-Mass Spectrometry) studies. In contrast, theoretical calculations on water oxidation by Fe-complexes have proposed the $Fe^V(O)$ as the

key intermediate involved in the O−O bond formation reaction.[16] Recently, the involvement of $Fe^{IV}(O)$ and/or $Fe^{V}(O)$ has been proposed for neutral macrocyclic N_4 ligand in chemical WO based on high-resolution ESI-MS, ^{18}O-labelling experiments, cyclic voltammetry, and DFT (Density Functional Theory) calculations.[17] Thummel has recently proposed $Fe^{V}(O)$ intermediate during chemical WO for a Fe-complex with a N_4 quaterpyridine backbone based on cyclic voltammetry and UV-Vis studies.[18] The Meyer group was the first to propose the involvement of the $Fe^{V}(O)$ intermediate for a monoanionic pentadentate N_5 ligand during electrocatalytic WO.[19] They used a monomeric amidate-ligated Fe^{III}-aqua complex as a catalyst in nonaqueous propylene carbonate solvent, however the complex did not catalyze WO in aqueous medium. Upon analysis of the electrochemical kinetics, it was proposed that WO occurs first by oxidation of Fe^{III} to the $Fe^{V}(O)$ followed by its reaction with water. In all these reports, although experimental results points out to the involvement of the $Fe^{V}(O)$, no spectroscopic evidence of the electrochemical generation of $Fe^{V}(O)$ as the active intermediate for WO was provided.[19]
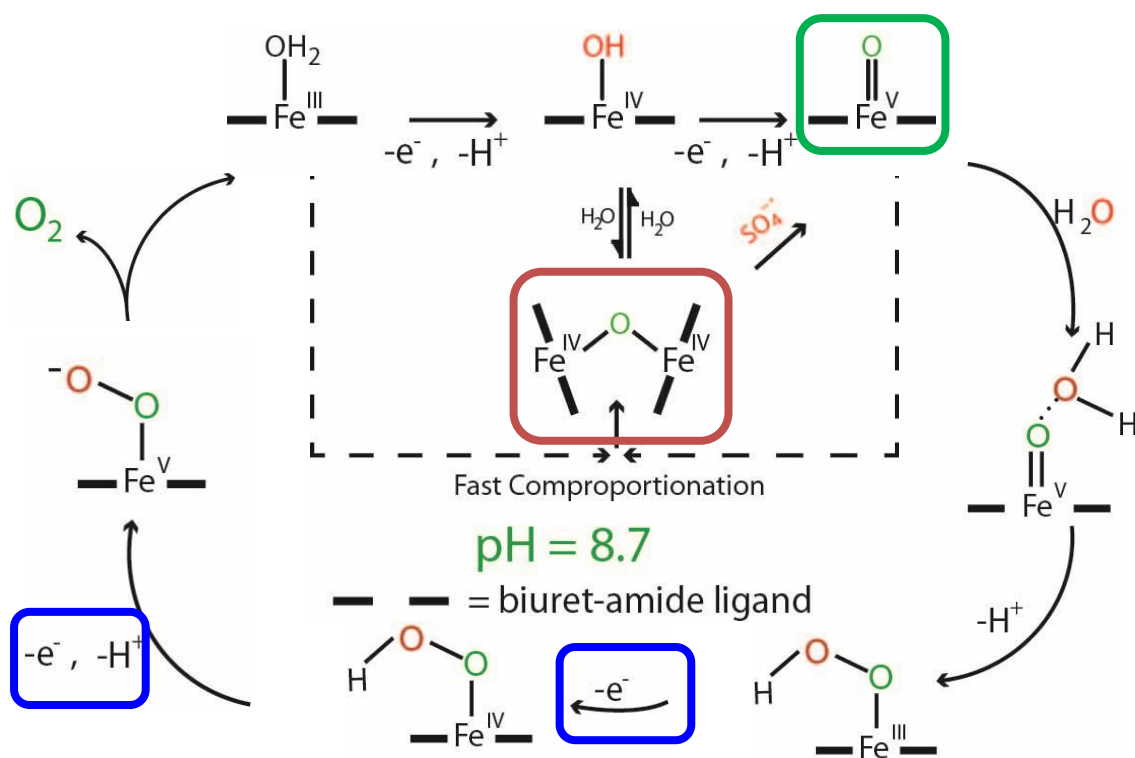
Figure 3A.1: Mechanism of Photochemical water oxidation by oxoiron(V)bTAML compplex.

Recently, we have experimentally demonstrated for the first time the presence of $Fe^{V}(O)$ as the active intermediate for the photochemical oxidation of water to O_2 using a biuret modified Fe-TAML (Fe-bTAML) complex (Figure 3A.1).[20] The $Fe^{V}(O)$ generated during WO matched

perfectly with the chemically generated $Fe^V(O)$ which was characterized using several advanced techniques such as EXAFS (Extended X-ray Absorbtion Fine Structure), Mössbauer, EPR (Electron Paramagnetic Resonance), HR-MS (High Resolution-Mass Spectrometry), Resonance Raman, and UV-Vis.[21] This $Fe^V(O)$bTAML is unique since it is the only room temperature stable $Fe^V(O)$ species which is fully characterized. We have also experimentally verified a single site mechanism and proposed that the crucial step for O−O bond formation involved the nucleophilic attack of water molecule onto the $Fe^V(O)$ followed by deprotonation and back electron transfer to form the monomeric Fe^{III}-hydroperoxo species.[20] However, we were unable to experimentally determine the kinetic parameters of the O−O bond formation step during the OER. Such kinetics parameters for O−O bond formation and the role of ligand electronics can be easily estimated by electrochemical strategies; especially through "non-destructive techniques"[16f, g] such as cyclic voltammetry.[22] During electrochemical WO using monomeric amidate-ligated Fe^{III}-aqua complex as a catalyst in non-aqueous propylene carbonate solvent, Meyer and coworkers had determined that O−O bond formation step to be first-order with respect to both the catalyst and water.[19] The kinetics pointed to a single site mechanism similar to Ru complexes albeit with much slower rates ($k_0 = 0.035$ M^{-1}s^{-1}). Further, absence of kinetic isotope effect of monomeric amidate-ligated Fe^{III}-aqua complex[19] in water indicated the absence of atom proton transfer (APT) during O−O bond formation, contrary to what is observed with Ru complexes.[6u-w]

Earlier attempts to use the 1st generation Fe-TAML (synthesized by Collins and co-workers) as homogeneous electrocatalysts for OER resulted in no O_2 evolution.[23] However, heterogenizing 1st generation Fe-TAML on electrode showed electrocatalytic activity with limited selectivity towards O_2 formation and very high CO_2 formation was observed.[23] Further, the absence of clear mechanistic studies regarding the formation of active species in the cyclic voltammetry (CV), preclude insights into the mechanism of OER including determination of kinetic parameters for the O−O bond formation. The absence of electrocatalytic activity for homogeneous 1st generation Fe-TAML in earlier studies was likely due to the lack of both hydrolytic and oxidative robustness of these complexes towards the high thermodynamic potential required during WO. We hypothesized that high stability of the biuret modified Fe-TAML (Fe^{III}-bTAML) in comparison to the 1st generation Fe-TAML would be well suited for electrocatalytic water oxidation.[24,25a] In addition, the remarkably high stability of the active $Fe^V(O)$ intermediate for bTAML ligand system[26] at

room temperature (RT) would allow us to use cyclic voltammetry as a tool to understand the kinetics and mechanism of O−O bond formation.

Herein, we showed a detailed electrochemical investigation of a series of substituted Fe^{III}-bTAML complexes and demonstrate their efficacy as catalysts for electrochemical WO. The $Fe^{V}(O)$ was generated electrochemically for the first time and was subsequently characterized using spectroelectrochemistry and mass spectrometry. Further, from cyclic voltammetry experiments, we were able to study the reaction between $Fe^{V}(O)$ and water leading to O−O bond formation via atom-proton transfer (APT). In another experiment, addition of increasing amount of water onto a chemically synthesized room temperature stable $Fe^{V}(O)$ increased the catalytic current indicating a bimolecular reaction with water. Subsequently, we were able to extract both the order and kinetic rate constant (k_{cat}) for reaction between $Fe^{V}(O)$ and water. Furthermore, we demonstrate the interplay between ligand's electronic effect on redox potential, the reaction rates (k_{cat}), and overpotential during the OER which would act as a guiding principle towards designing more efficient catalysts for WO.
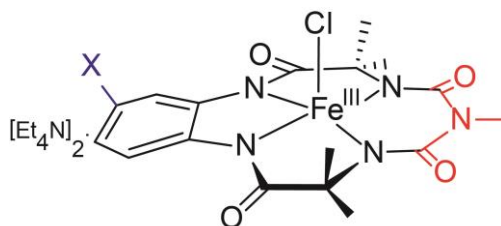
Figure 3A.2: Pictorial representation of [Fe^{III}-(X-bTAML)]; X = H (**1a**)[25a]; OMe (**1b**); F (**1c**); Cl (**1d**); CN (**1e**) and NO$_2$ (**1f**).[20a]

3A.3 Experimental Section

3A.3.1 Reagents

All reagents and solvents were purchased from commercial sources and were used as received, unless noted otherwise. All the Fe^{III}-bTAML (Figure 3A.2), complexes were synthesized as their tetraethyl ammonium salt [(Et_4N)$_2$[Fe(Cl)X-bTAML](**1a-f**)] using published procedures.[25a] These complexes were characterized by several techniques including UV-Vis, single crystal X-ray diffraction technique, and high resolution mass spectrometry (HR-MS).[20] The axial chloro complex **1a** was then converted to its corresponding axial aquo complex **1a**-H_2O (PPh$_4$ salt) by methods published before for similar complexes.[24] Complex **1a**-H_2O was crystallized from water and characterized using single crystal X-ray and HR-MS (see Appendix B; B1-B5). All the materials used in this study were purchased from various

commercial sources (Sigma Aldrich, Fisher Scientific etc.). N, N dichloroformylmethylamine was obtained from ChemCollect, Gmbh. LCMS grade acetonitrile from Fisher was used in CPE (controlled potential experiment). High purity mili-Q water was used in all electrochemical study. All solvent for synthesis was dried and purified as described elsewhere.

3A.3.2 Electrochemical Studies

Electrochemical experiments were carried out using potentiostats of CH Instruments, Austin, TX (Model CHI 760D and CHI 620E). Experiments were performed by using three electrodes configuration in which glassy carbon (GC) electrode and platinum wire were used as a working and counter electrode respectively.[25b] The reference electrode (saturated calomel electrode (SCE) or Ag/AgCl (3 M KCl) or Ag/Ag$^+$ nonaqueous acetonitrile) was chosen depending upon the solvent used. All the experiments were performed under ambient conditions at $25 \pm 2°C$. Irrespective of the reference electrodes used in particular experiment; all the potentials in this manuscript have been reported against normal hydrogen electrode (NHE). Cyclic voltammetry and differential pulse voltammetry experiment were carried out on a CHI-660 potentiostat. Solutions of [Fe^{III}-bTAML]1- were placed in one compartment three-electrode cells. Glassy Carbon (GC) (3 mm of diameter) was used as working electrodes, Silver/Silver chloride (3M KCl salt) as reference electrode (unless explicitly mentioned) and Pt wire as counter electrode. Working electrode pre-treatment before each measurement consisted of polishing with 0.05μm alumina paste, rinsing thereafter with water/acetone and finally blow-drying. All redox potentials in the present work are reported versus NHE by adding 0.21 V to the measured potential. CVs were collected at 100 mVs-1 scan rates except when specified otherwise. Square Wave Voltammetry (SQWV) was performed using following parameters in CH instruments: Increment potential (ΔE) = 4mV, amplitude = 25mV, Frequency = 5Hz. DPVs were obtained with the following parameters: amplitude = 50 mV, step height = 4 mV, pulse width = 0.06 s, pulse period = 0.5 s and sampling width = 0.02 s. Formal potentials ($E0'$) values for the redox processes studied in this work are estimated according to the potential at the Imax in DPV and SQWV measurements. Both kinds of measurements were done without IR compensation. When acetonitrile was used as organic solvent, tetrabutylammonium hexafluorophosphate ([NBu$_4$]PF$_6$) was added in a concentration of 0.1M to act as supporting electrolyte.

3A.3.3 Spectroelectrochemical Studies

The electrochemical event during electrolysis was followed by a UV-Vis spectrophotometer at room temperature using three electrodes system (Pt mesh working, non-aqueous Ag/Ag$^+$ as reference, and Pt wire as counter electrode) in a quartz crystal cell in 90% acetonitrile - 10% water solvent having 0.1 M potassium hexafluorophosphate (KPF$_6$). Conversion of **1a** to its higher oxidation state congeners by constant potential electrolysis (CPE) was confirmed by UV-Vis spectroscopy and HR-MS.

3A.3.4 Electrochemical Kinetic studies

CVs were used for the determination of kinetic rate constants for WO. For multistep homogeneous catalytic reaction such as WO the overall rate constant (composite rate constant of elementary steps, k_{obs}) was calculated by FOWA (Foot-of-the-wave analysis) method [25c-f, 11e] (equation I) as has been described by Savéant, Costentin, and others.

$$\frac{i_{cat}}{i_p^0} = \frac{8.96\sqrt{\frac{RT}{Fv} C_A^0 \, k_{cat}}}{1 + \exp\left[\frac{F}{RT}(E^{0'} - E)\right]} \qquad \text{(I)}$$

For a second-order reaction with rate constant, k_{cat}, the catalytic current (i_{cat}) is given by equation (I), where, R, T, F, C_A^0, v, E, i_p^0 and $E^{0'}$ are the universal gas constant (8.314 Jmol^{-1}K^{-1}), absolute temperature, Faraday constant, concentration of substrate (55.56 M for water), scan rate, applied potential, baseline corrected current in absence of substrate (here we consider this current to the current associated with the Fe$^{IV/III}$ couple) and the formal redox potential for the catalysis initiating redox couple respectively. Under pseudo first-order conditions (when substrate concentration is much higher compared to the catalyst), k_{cat} is related to the first order catalytic rate constant, k_{obs}, by the equation (II).

$$k_{obs} = k_{cat}[H_2O] \qquad \text{(II)}$$

Substituting equation (II) to equation (I), equation (III) is obtained:

$$\frac{i_{cat}}{i_p^0} = \frac{8.96\sqrt{\frac{RT}{Fv} \, k_{obs}}}{1 + \exp\left[\frac{F}{RT}(E^{0'} - E)\right]} \qquad \text{(III)}$$

Catalytic WO rate constants (k_{obs}) were obtained using equation (III), in which the current at peak potential for the Fe$^{IV/III}$ wave and Fe$^{V/IV}$ wave were used to measure i_p^0 and i_{cat}

respectively. Plots of background corrected i_{cat}/i^0_p *vs* $1/[1+\exp\{F/RT(E^{0'}-E)\}]$ were used to obtain the first-order rate constants (k_{obs}) (Equation III).[25c-f,11e]

3A.3.5 Electrolysis

Controlled potential electrolysis (CPE) was performed in a four-neck electrochemical cell using three electrodes (the volume for each cell is 18 mL). A platinum wire counter electrode, platinum foil as working electrode and an Ag/AgCl reference electrode (saturated KCl) was placed in the electrochemical cell. The oxygen sensor was calibrated before each experiment following a two point calibration of 0% (zero solution) and 100% (air). The membrane in the electrode which selectively allows O_2 to pass through was replaced for each new measurement in order to avoid any error associated with its functioning under reaction conditions. The O_2 product analysis was determined using a calibrated Clark type electrode probe. The electrolyte was degassed by bubbling with high purity of argon for 2 hrs. After recording the partial pressure of O_2 for 2 h in the absence of any applied potential, electrolysis was initiated at 1.26 V *vs* NHE utilizing amperometry (*i-t*) experiment. Amperometric *i-t* traces were recorded without *iR* compensation. Electrolysis with O_2 sensing was continued for 2 hrs. At the end of the experiment, total charge passed during electrochemical experiment was calculated after subtracting the background charge. Background charge was determined by performing the same set of experiments but without the addition of Fe^{III}-bTAML. Thereafter, expected number of moles of O_2 evolved (m_{EC}) according to electrochemical experiment was estimated dividing Q_T (total charge) by $4F$, since number of electron transfer during water oxidation is four. Moles of O_2 evolved measured by the O_2 sensor has been assigned as m_E. Finally, Faradic efficiency (FE) was calculated utilizing equation IV.

$$FE = \frac{m_E * 100}{m_{EC}} \qquad (IV)$$

3A.3.6 Physical Measurements

Various organic compounds synthesized were characterized using ^1H and ^{13}C NMR spectroscopy on a Bruker (200 or 500 MHz) or JEOL (400MHz) at room temperature. All chemical shift (δ) and coupling constant (J) are expressed in ppm and Hz respectively. All NMR measurements were done in DMSO-d6 using residual protons as internal references. UV-vis spectra were monitored using an Agilent 8453 diode array and a PerkinElmer-λ35

spectrophotometer using 1.00 cm quartz cell at a constant temperature of 25 ± 5 °C. High resolution mass spectrometry (HRMS) was done in the negative ion mode of a Thermo Scientific Q-Exactive, using electron spray ionization source, Orbitrap as analyzer and connected with a C18 column (150 mm $\times$ 4.6 mm $\times$ 8 μm). Dissolved O2 measurements in controlled potential electrolysis (CPE) reaction were performed using a Clark type electrode (dissolved oxygen meter) from MicroSet (MS 0257), India, working in the range of 0 to 45 ppm with resolution of 0.01 ppm. SEM (Scanning Electron Microscope) imaging and EDX was recorded in a FEI Tecnai TF-20 instrument. For each set, solution pH was measured with a pH meter (LABINDIA, PICO+) with calibrated electrode with accuracy of ± 0.2 pH.

3A.3.7 *Details of Dissolved Oxygen measurement during CPE by using a Clark type electrode*

In order to measure the Oxygen during CPE a Clark type electrode was used which was previously calibrated before each experiment following a two point calibration- 0% (zero solution) and 100% (air). CPE was performed in a four neck electrochemical cell. The electrochemical cell was filled with 15 mM pH 7.4 buffer and 1mM [Fe^{III}-bTAML] $^{2-}$. A platinum foil (1 cm2) along with Ag/AgCl (std) as reference and platinum wire as counter electrode was used for electrolysis. A Clark electrode was also fitted in the cell for dissolved oxygen measurement. 0.1M sodium nitrate was used as supporting electrolyte. Before applying potential, the dissolved O$_2$ was completely removed from water in the electrochemical cell by purging with high purity argon gas under slow stirring. Before applying potential the oxygen sensor displayed 0 ppm oxygen level. As soon as 1.4V *vs* NHE potential was applied, oxygen evolution was observed by increase in ppm level detection of oxygen in Clark electrode sensor. CPE was carried out for 2 hrs and oxygen evolution was monitored by Clark electrode. The results of the water oxidation catalysis by [Fe^{III}-bTAML] $^{2-}$ were compared with control experiment under the same conditions but in the absence of [Fe^{III}-bTAML] $^{2-}$. The Faraday efficiency was calculated according to the total charge passed (charge passed for control experiment was subtracted) during the CPE and the total amount of generated oxygen (considering WO as a 4 electron process).

3A.3.8 *Sample preparation for SEM and EDX experiment*

A clean platinum foil (five times cleaned with water after sonication) surface was imaged for EDX analysis. The same platinum electrode was used in CPE for 2 hrs and then the foil was rinsed carefully by mili-pore water and then dried in high vacuum for 10-hrs. The

dry platinum foil surface was visualized under microscopy and the SEM image with its EDX report was compared with the results of clean platinum foil surface before CPE.

3A.3.9 Spectroelectrochemical study and HRMS

For spectroelectrochemical studies, a three electrodes electrochemical cell was used consisting of a high surface area Pt mesh electrode as the working electrode, a Pt wire as a counter electrode, and an $Ag/AgNO_3$ (10 mM $AgNO_3$) non-aqueous electrode as a reference electrode. The dimension of the working electrode was 6.5 mm x 10 mm x 0.55 mm (Length x Width x Thickness). Spectroelectrochemical cell has two regions. The lower and upper parts of cell have path lengths of 0.1 and 1 cm. The high surface area Pt mesh working electrode was kept close to the Pt counter electrode in the narrow path length of 0.1 cm. The reference electrode was placed just above the working and counter electrodes in the 1 cm path length region. A small volume of electrolyte solution (300μL) was used. For these studies, along with the electrochemical experiments, simultaneous UV-vis spectroscopy experiments were also performed using a Shimadzu UV 1800 spectrophotometer or Ocean Optics HR 4000 spectrophotometer. $[Fe^{III}\text{-}bTAML]^{2-}$ were dissolved in CH_3CN (90%): H_2O (10%) solvent mixture having 0.1 M Bu_4NPF_6 electrolyte. The cell was placed in the spectrophotometer chamber in manner so that light passed through the cell of 0.1 cm path length. Spectroelectrochemistry experiments were performed in 90:10 CH_3CN-water solvent mixtures by CPE at 1.25V *vs* NHE. The oxidised species was immediately frozen in a -40 °C bath and directly injected in HRMS.

3A.3.10 Crystallographic Details

For the single Crystal X-ray diffraction experiment, as synthesized crystals of the respective materials were taken out of the solution and coated with Paratone-N oil. It was then placed in a nylon cryoloop (Hampton research) and then mounted in the diffractometer. The data collection was done at 298 K. The crystals were mounted on a Super Nova Dual source X-ray Diffractometer system (Agilent Technologies) equipped with a CCD area detector and operated at 250 W power (50 kV, 0.8 mA) to generate Mo Kα radiation (λ = 0.71073 Å) and Cu Kα radiation (λ = 1.54178 Å) at 298(2) K. Initial scans of each specimen were performed to obtain preliminary unit cell parameters and to assess the mosaicity (breadth of spots between frames) of the crystal to select the required frame width for data collection. CrysAlisPro program software was used suite to carry out overlapping φ and ω scans at detector (2θ) settings (2θ = 28). Following data collection, reflections were sampled from all regions of the Ewald sphere to redetermine unit cell parameters for data integration. Following exhaustive review of collected frames, the resolution of the data set was judged.

Data were integrated using CrysAlisPro software with a narrow frame algorithm. Data were subsequently corrected for absorption by the program SCALE3 ABSPACK1 scaling algorithm. These structures were solved by direct method and refined using the SHELXTL 972 software suite. Atoms were located from iterative examination of difference F-maps following least squares refinements of the earlier models. Final model was refined anisotropically (if the number of data permitted) until full convergence was achieved. Hydrogen atoms were placed in calculated positions (C-H = 0.93 Å) and included as riding atoms with isotropic displacement parameters 1.2-1.5 times U_{eq} of the attached C atoms. In some cases modeling of electron density within the voids of the frameworks did not lead to identification of recognizable solvent molecules in these structures, probably due to the highly disordered contents of the large pores in the frameworks. Highly porous crystals that contain solvent-filled pores often yield raw data where observed strong (high intensity) scattering becomes limited to ~1.0 Å at best, with higher resolution data present at low intensity. Additionally, diffused scattering from the highly disordered solvent within the void spaces of the framework and from the capillary to mount the crystal contributes to the background and the 'washing out' of the weaker data. Electron density within void spaces has not been assigned to any guest entity but has been modeled as isolated oxygen and/or carbon atoms. The foremost errors in all the models are thought to lie in the assignment of guest electron density. The structure was examined using the *ADSYM* subroutine of PLATON[3] to assure that no additional symmetry could be applied to the models. The ellipsoids in ORTEP diagrams are displayed at the 50% probability level unless noted otherwise.

$[Fe^{III}$-(F-bTAML)$]^{2-}$ (**1c**), $[Fe^{III}$-(Cl-bTAML)$]^{2-}$ (**1d**), $[Fe^{III}$-(CN-bTAML)$]^{2-}$ (**1e**) and $[Fe^{III}$-(NO2-bTAML)$]^{2-}$ (**1f**) were found to crystallize in *P*42/mbc space group of tetragonal crystal system while $[Fe^{III}$-(OMe-bTAML)$]^{2-}$ (**1b**) was crystallized in *P*21/c space group of monoclinic crystal system. For the first set of crystal structures, the corresponding substituent (-F, -Cl, -CN and $-NO_2$) were located on two positions of the base phenyl ring because of the symmetry operation for determination of assymetric unit. The chemical occupancy of the substituent in each of the positions was 50%, indicating the equal probability of finding the substituent on both the positions. The overall chemical composition is one per macrocycle. However, for the case of $[Fe^{III}$-(OMe-bTAML)$]^{2-}$ (**1b**), the assymetric unit already consists of the whole macrocyle and the singly substituted macrocyle is clearly visible (Appendix B6-B11).

3A.3.11 Kinetic Isotope Effect Analysis

The KIE was studied in 0.1M deuterated buffer (pD = 7.2) and protonated buffer (pH = 7.2). The pH of the deuterated buffer was measured by pH meter to be 6.8. To obtain the exact pD value, 0.4 was added to the pH meter reading. The shift in the pK_a of the protonable groups is about the same value, since the protonation level of these groups is almost the same as in H_2O and D_2O, respectively, at the same pH meter reading.

3A.4 Results and Discussion

3A.4.1 Characterization

Complexes **1b-f** (bTAML with various substituents in the aromatic ring, Figure 3A.2) were synthesized (see Appendix B12 for details of synthesis and Characterisation) and characterized by single crystal XRD (Appendix B1-B5, bottom and Appendix B6-B12),[25a] HR-MS (Appendix B1-B5a, top)[25a,20a] and UV-Vis (Appendix B13)[20a] Single crystals were obtained by slow vapor diffusion of diethyl ether over catalyst solution of **1b-f** in acetonitrile. The distorted square pyramidal geometry of the complexes **1b-f** with an axial chloride ligand resembles **1a** which has been previously reported.[25a] The crystal structure of **1b (**OMe-bTAML**), 1c** (F-bTAML), **1d** (Cl-bTAML), and **1e** (CN-bTAML) contains water molecules close to methoxide, fluoride, chloride and cyanide substituent respectively. The axial chloro complex **1a** was then converted to its corresponding axial aquo complex **1a**-H_2O (PPh$_4$ salt) by methods published before for similar complexes.[24] Complex **1a**-H_2O was characterized by single crystal XRD (Appendix B5b). The mass-to-charge ratio (*m/z*) and isotope distribution patterns of **1a-f** in HR-MS (observed without the axial labile chloride ligand in negative ion mode) matched perfectly with simulated patterns (Appendix B1-B5a). The UV-Vis spectra of **1b-d** are similar to that of **1a** (S = 3/2 Fe^{III} complex) (Appendix B13a, B14).[25a] In water, both **1a** and **1a**-H_2O showed identical UV-Vis spectra (Appendix B14, λ_{max} = 356 nm).
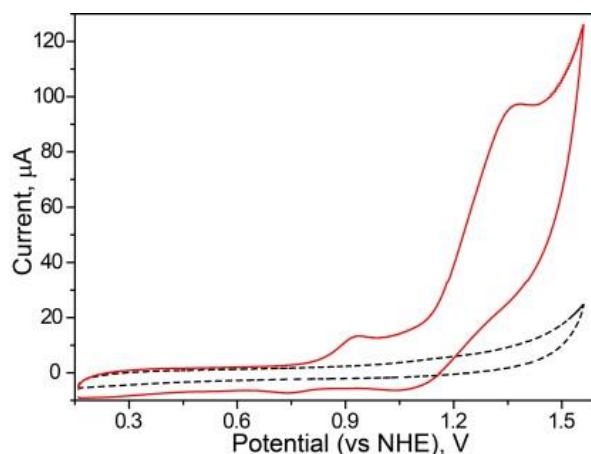
Figure 3A.3: CVs of (red- 0.5 mM **1a**) and blank (black dotted) in 0.1 M NaNO$_3$ water (scan rate 300 mV/s, GC working, platinum counter electrode).

3A.4.2 Electrochemical Properties of the Complexes in Water

The CVs of **1a** and **1a**-H$_2$O were collected in water (I = 0.1 M, NaNO$_3$) using a GC electrode and potentials were measured versus a standard calomel electrode. The CV of **1a** and **1a**-H$_2$O were found to be identical (Appendix B13b inset). In water, **1a** and **1a**-H$_2$O exists as a six co-ordinate [(bTAML)Fe^{III}(H$_2$O)$_2$]$^-$ complex with both the water molecules located at the axial position of Fe^{III}.[27, 28] pK_a of the axial H$_2$O molecules in an aqueous solution of **1a** has been determined to be 10.3 by UV-Vis titration experiments.[28] The CV of this complex in water (pH 7.2) shows a first oxidation wave at $E_{p,a}$ = 0.9 V *vs* NHE and a second oxidation wave having drastically enhanced current above the background at $E_{p,a}$ of 1.25 V *vs* NHE (Figure 3A.3). The corresponding reduction waves are barely discernible in the CV. The formal potentials ($E^{0\prime}$) for Fe$^{V/IV}$ and Fe$^{IV/III}$ redox couples for all the catalysts **1a**-**f** were determined by cyclic voltammetry (CV) and square wave voltammetry (SQWV). The $E^{0\prime}$ for the Fe$^{IV/III}$ couple in water (corresponding to the redox process Fe^{IV}(O)/Fe^{III}(OH$_2$)) was determined from CV experiments by calculating the average of the anodic and cathodic peak potentials (Figure 3A.3, Appendix B15). We were unable to determine the $E^{0\prime}$ for Fe$^{V/IV}$ couple in water by CV (corresponding to the redox process Fe^{V}(O)/Fe^{IV}(O)) since no cathodic peak was observed (Figure 3A.3). Chemically synthesized [Fe^{V}(O)bTAML]$^-$ (>95% pure) in CH$_3$CN display a quasireversible peak corresponding to the Fe^{V}(O)/Fe^{IV}(O) with $E_{1/2}$ at 1.25 V *vs* NHE.[20b] The CV of the corresponding Fe^{III} complex (**1a**-H$_2$O) in acetonitrile solvent indicates the presence of two reversible redox processes at 0.88 and 1.21 V for Fe$^{IV/III}$ and Fe$^{V/IV}$ respectively (Figure 3A.4).
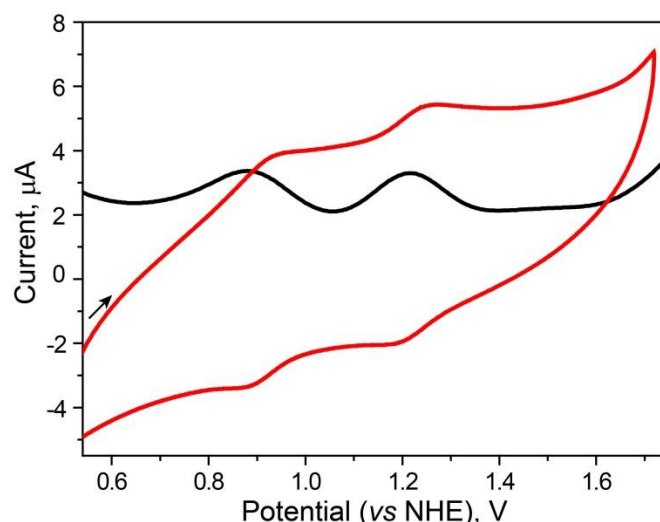
Figure 3A.4: CV (red) and DPV (black) of **1a**-H_2O (0.3 mM) in acetonitrile (glassy carbon as working and platinum wire used as counter electrode, scan rate 100 mVs^{-1}, 0.1 M KPF$_6$ as electrolyte).

The $E_{1/2}$ of the Fe$^{V/IV}$ couple for **1a**-H_2O matched very closely to the Fe^V(O)/Fe^{IV}(O) of the chemically synthesized Fe^V(O)bTAML. The SQWV experiments of **1a** in water were performed to estimate the Fe^V(O)/Fe^{IV}(O) couple in water. SQWV display a first set of redox waves for both forward and reverse scan at 0.88 V and 1.22 V and then a second set at 1.16 V and 0.84 V respectively (Appendix B15 inset). Difference spectra of forward and reverse scan for the first set of redox wave at 0.85 V matches quite well with the $E^{0'}$ for the Fe$^{IV/III}$ couple in water (corresponding to the redox process Fe^{IV}(O)/Fe^{III}(OH$_2$)) (Appendix B15 inset). For the second set of redox waves, the difference SQWV shows a peak at 1.2 V which also matches with the formal potential for Fe^V(O)/Fe^{IV}(O) redox couple in CH$_3$CN. Hence for complex **1a**-**f**, the difference spectra of forward and reverse scan for the second redox wave was used as the $E^{0'}$ for the Fe^V(O)/Fe^{IV}(O) couple (Appendix B16) as has been used for Ru based WO catalyst.[25f] The electrochemical wave at 0.85 V was pH dependent and the $E^{o'}$ *vs* pH decreased by 117 mV/pH (between pH 7 to 10) (Figure 3A.5). This indicates a proton-coupled electron transfer process (EPT/PET or CPET)[29a,b,c] associated with the transfer of two H$^+$ and one e$^-$ (Figure 3A.5) as has been recently shown for related Osmium complex.[29d] To gain better insight of the electron and proton transfer process, CVs of **1a** in D$_2$O under identical condition was performed. The CVs in D$_2$O show a positive shift (80 mV) in the peak potential for Fe$^{IV/III}$ couple while the peak potential for Fe$^{V/IV}$ couple remain unchanged. This shift in peak potential when D$_2$O was used as solvent instead of H$_2$O points to a coupled proton and electron transfer (CPET) process, although detailed electrochemical studies need

to be carried out to establish this mechanism as has been shown recently for Osmium complexes.[29d]
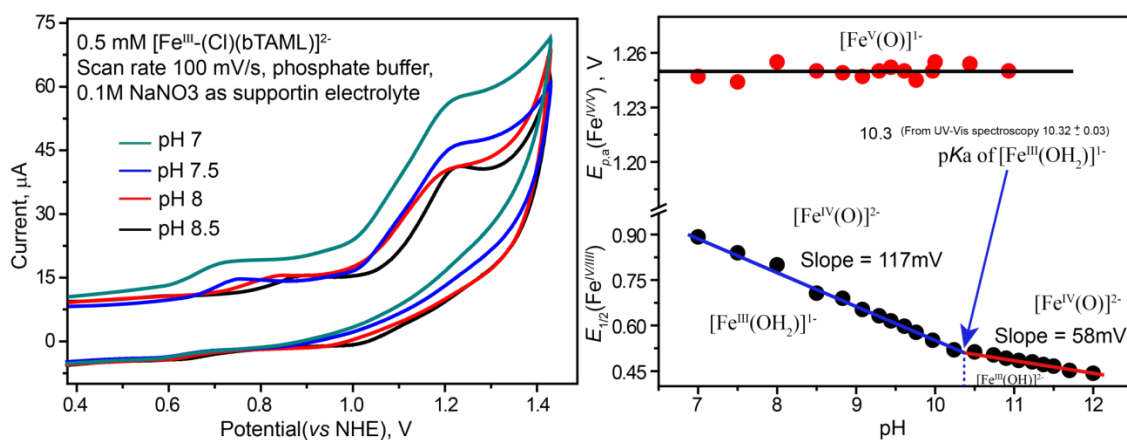
Figure 3A.5: (A) CVs (black-pH 7, red-pH 7.5, blue-pH 8, and green-pH 8.5) of 0.5 mM **1a** in water (0.1 M $NaNO_3$ supporting electrolyte). (B) Pourbaix diagram of $Fe^{IV/III}$ and $Fe^{V/IV}$.

We assign this process to the following reduction couple:

$$[(bTAML)Fe^{IV}(O)(H_2O)]^{2-} \xrightarrow{+2H^+, +e^-} [(bTAML)Fe^{III}(H_2O)_2]^- \quad (V)$$

Or,
$$[(bTAML)Fe^{IV}(O)]^{2-} + H_2O \xrightarrow{+2H^+, +e^-} [(bTAML)Fe^{III}(H_2O)_2]^- \quad (VI)$$
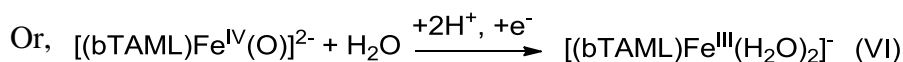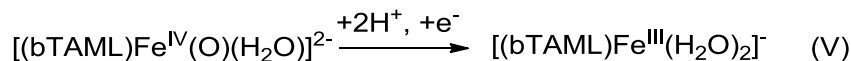
CPE (Controlled potential electrolysis) of an aqueous solution of **1a** (pH 12) led to the formation of a dark red colored solution of $Fe^{IV}O$ (Appendix B17).[21] The UV-Vis spectrum of this dark red colored solution formed after CPE completely matched with the chemically synthesized $Fe^{IV}(O)$ that has been fully characterized by Mössbauer, Resonance Raman and EXAFS previously.[21] At pH 7, CPE at 0.9 V *vs* NHE led to the formation of the related $Fe^{IV}{}_2O$ which can be obtained upon protonation of $Fe^{IV}O$ (pK_a of $Fe^{IV}O$ is 10.05).[21]

At a higher anodic potential, an additional irreversible oxidation wave having a peak ($E_{p,a}$) at 1.25 V *vs* NHE appeared with a drastically enhanced current above the background, consistent with a catalytic reaction (Figure 3A.3). This oxidation wave was pH independent between pH 7 and 10 (Figure 3A.4). We assign the second irreversible oxidation wave at 1.25

V *vs* NHE to the oxidation of $[(bTAML)Fe^{IV}(O)(H_2O)]^{2-}$ to the corresponding $Fe^V(O)$ species, $[(bTAML)Fe^V(H_2O)(O)]^-$.

$$[(bTAML)Fe^V(O)]^- + H_2O \xrightarrow{+e^-} [(bTAML)Fe^{IV}(O)(H_2O)]^{2-} \quad (VII)$$
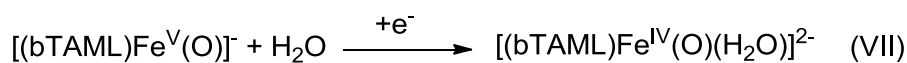
Attempts to isolate the $Fe^V(O)$ formed during CPE failed since the reaction of $Fe^V(O)$ with water was instantaneous under CPE condition. This observation was expected since we have earlier reported that upon increasing the H_2O concentration above 50%, the stability $Fe^V(O)$ rapidly decreases with no $Fe^V(O)$ formation observed at 100% H_2O. However, in CH_3CN-H_2O solvent mixtures containing up to 30% H_2O, the half-life of $Fe^V(O)$ reduces only by 10%.[30] We therefore attempted CPE of **1a** in 90% CH_3CN:H_2O; a solvent system known to be compatible with the stability of $Fe^V(O)$ (see Appendix B18 for CV of **1a** in 90% CH_3CN:H_2O). Although the nature of the exact species (such as axial ligands etc.) might vary in both the solvents, identification of the nature of the high-valent iron oxo complex in 90% CH_3CN:H_2O can be used to improve our understanding about the key features of the catalytic cycle in water. A dilute solution of 5 μM **1a** and a very short reaction window of < 60 s was employed to accumulate enough $Fe^V(O)$ for detection using UV-Vis. Electrolysis at 1.25 V *vs* NHE for 60 sec led to the immediate formation of the light green $Fe^V(O)$ species displaying the characteristic UV-Vis peaks at 445 nm and 613 nm. The sample was then immediately freeze-quenched in liquid nitrogen and subsequently characterized by HR-MS. (Figure 3A.6).[20,26,30] This represents the first experimental evidence for the electrochemical generation of $Fe^V(O)$.

3A.4.3 Controlled Potential Electrolysis

To ascertain if the irreversible oxidation wave at 1.25 V *vs* NHE resulted in electrochemical WO, control potential electrolysis experiment of **1a** was carried out in neutral pH at 1.26 V (*vs* NHE) for 2 h by using a 1cm^2 Pt electrode as a working electrode and the amount of oxygen evolved was quantified. During 2 h CPE, total 0.8 C charges was passed through the solution to yield 186 μM of dissolved oxygen corresponding to 89.9% Faradaic efficiency (Figure 3A.7). This sustained electrocatalytic oxygen evolution displayed about 50% change in current (~0.0002A) during the 2 h period. This decay in current density during WO is inconsistent with UV-Vis spectra obtained for **1a** after WO which was identical to the starting **1a**. In order to understand this inconsistency, the pH of solution was measured

at every 300 s interval during WO since this process is expected to decrease the pH upon release of H^+ along with the production of O_2. In fact, a decrease in pH was observed over the whole WO period which resulted in the decay of current density. When the same experiment was carried out by maintaining the pH at 7.2 during the WO, the current density remained constant over the whole period (Appendix B19b). Control experiments without catalyst show production of 28.96 μM oxygen due to 0.11C charges (Figure 3A.7, B). Identical UV-Vis spectra of catalyst was obtained before and after the CPE experiment, indicates that catalyst **1a** was robust and did not degrade during WO (Appendix B19a). We performed a number of control experiments to assess the possible formation of heterogeneous metal oxide films. First, no change in the characteristic visible spectrum of Fe^{III}-(bTAML) at 356 nm was observed after 2 h under active water oxidation catalysis (WOC) (Appendix B19a). This indicates that the Fe^{III}-(bTAML) was stable during WO- an observation which was also found
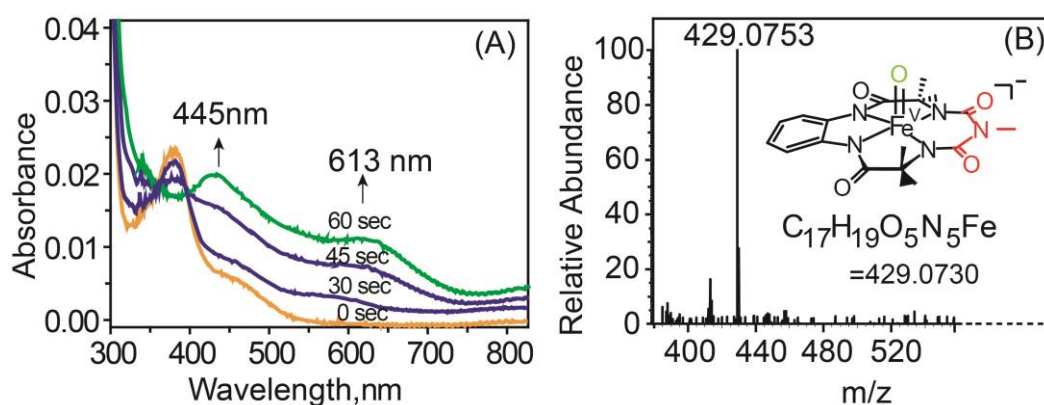
Figure 3A.6: (A) Electrochemically synthesized $Fe^V(O)$ in 90% acetonitrile-water mixture by CPE at 1.25 V *vs* NHE in presence of 0.1 M KPF_6 as supporting electrolyte. (B) HR-MS of electrochemically synthesized $Fe^V(O)$.

during homogeneous photochemical WO by Fe^{III}-(bTAML).[20a] Moreover, the presence of Chelex 100 sodium form beads or EDTA disodium salt had no effect on the observed WO current with Fe^{III}-(bTAML) (Appendix B20, B21). Analysis of the surface morphology and composition of the platinum foil electrodes by scanning electron microscope (SEM) and energy dispersive X-ray spectroscopy (EDX) analysis after and before CPE showed no sign of any heterogeneous iron phase (Appendix B22). This precludes formation of iron oxide nanoparticle at electrode surface to catalyze WO.
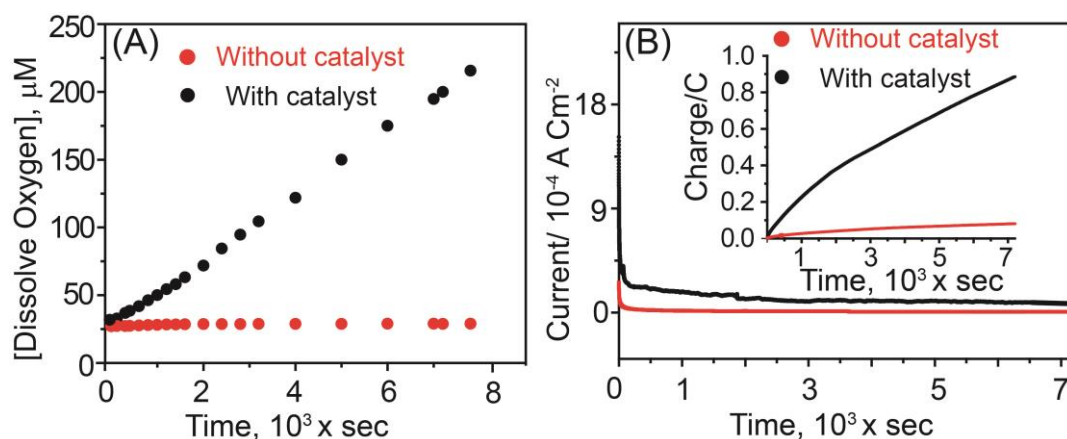
Figure 3A.7: (A) Amount of dissolved oxygen evolution measured by Clark electrode. (B) Current obtained (inset charge passed in 2h) during CPE at 1.26 V (*vs* NHE) of 1 mM **1a** in pH 7.2 phosphate buffer (15 mM) for 2 h on 1 cm^2 platinum foil (0.1 M NaNO$_3$ was used as supporting electrolyte).

3A.4.4 Rate constant of O-O bond formation determination in water

CV responses were analyzed at different scan rates (v) to understand the rate law and subsequently the kinetic rate constants for WO by Fe^V(O) were determined. The CV responses of **1a** in 15 mM phosphate buffer (pH 7.2, *I* = 0.1 M) shows that the current associated with Fe$^{V/IV}$ redox process increases with increasing scan rate (Figure 3A.8 A). However, the CV responses did not elicit an ideal S shaped catalytic curve and the catalytic current decreased after reaching the maxima at 1.25 V thus resulting into a peak shaped catalytic wave (Appendix B23). Recently, Savéant and Costentin have developed a new foot-of-the-wave analysis (FOWA).[25c,d,e] for homogeneous catalytic waves that deviate from the ideal S shaped catalytic wave (caused by various side phenomena such as substrate depletion, catalyst degradation and other competitive side reaction). CVs of **1a** were analyzed by FOWA method to determine the rate constant of water oxidation (Figure 3A.8 A, see experimental section for details about FOWA equation). FOWA analysis (Figure 3A.8 B) shows a linear relationship of i_{cat}/i^0_p *vs* $1/[1+\{\exp(F/RT(E^{0'}-E))\}]$ at the initial portion of the catalytic wave where almost no side phenomena is expected. Formal redox potential for Fe$^{V/IV}$ required for the FOWA analysis was obtained from SQWV voltammetry (see experimental section for details). From the slope of the linear portion of curve obtained at different scan rates (100 mV/s to 400 mV/s) where (i_{cat}/i^0_p >1),[25c] the second order rate for WO was determined. The observed rate constant for water oxidation were found to be independent of the scan rate (Appendix B24). The increase of i_{cat} at 1250 mV with increasing

concentrations (Appendix B25) of **1a** shows a linear fit (Figure 3A.8 C) indicating first-order dependence of water oxidation rate on catalyst concentration.[29e] At higher catalyst concentration (beyond 0.25 mM of **1a**), deviation of i_{cat} from linearity was observed indicating presence of side phenomena such as substrate or catalyst depletion (Figure 3A.8 C, Appendix B25). The possibility of substrate depletion in reaction diffusion layer is highly unlikely since the concentration of bulk water is 55.56 M. Catalyst depletion due to catalyst decomposition is also unlikely since after 2 h of CPE no change in the UV-Vis spectra of 1a was observed as reported earlier. However for a multistep reaction like water oxidation, depletion of any active intermediate (such as $Fe^V O$, Fe^{III}-OOH and its higher oxidation analogs) responsible for water oxidation during the catalytic process can result in deviation from ideal plateau shaped CVs. Out of the several pathways that can lead to depletion of 1a, one possibility might be the previously well-studied fast comproportion reaction ($k_2 = 105$ M^{-1}s^{-1})[26] between Fe^V(O) and **1a** to form a μ-O-Fe(IV) dimer (Appendix B23). The second order kinetic rate constant for WO by **1a** was found to be 1.2 ± 0.2 M^{-1}s^{-1} in 15 mM phosphate buffer (pH 7.2, $I = 0.1$ M, NaNO$_3$) (Figure 3A.8 B and Appendix B24).
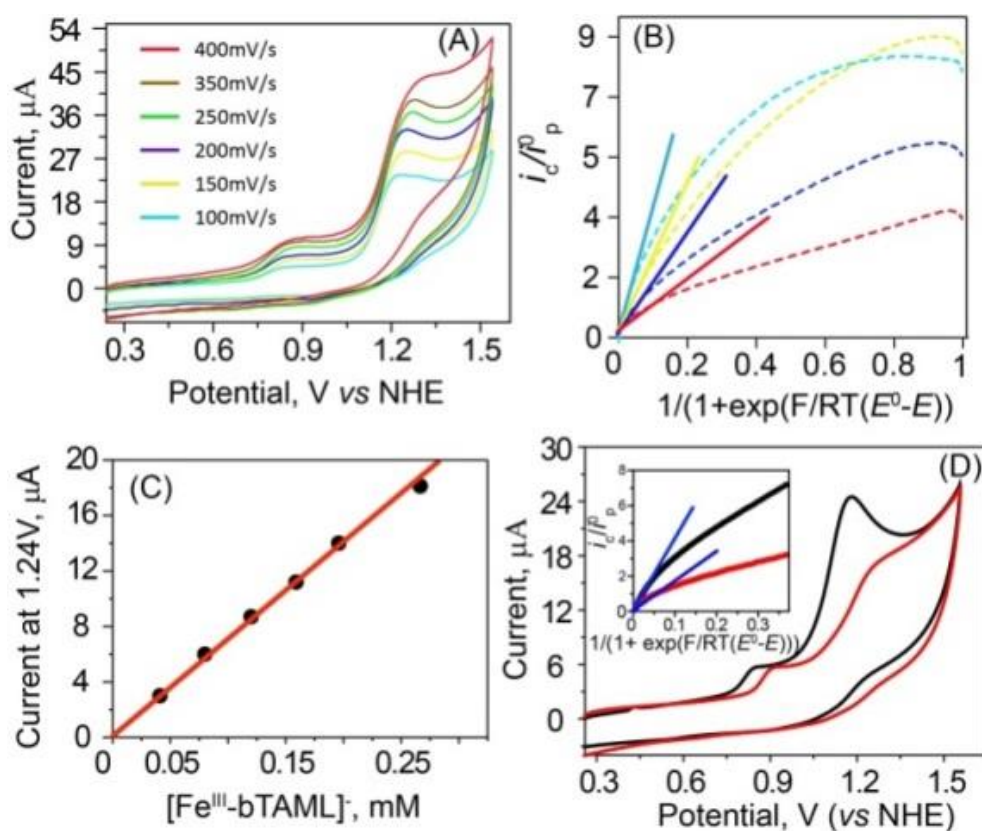
Figure 3A.8: (A) CVs of 0.3 mM **1a** in 15 mM phosphate buffer of pH 7.2, $I = 0.1$ M; NaNO$_3$ at different scan rates on a glassy carbon working electrode. Currents were

normalized by baseline corrected i^0_p. (B) The plot of i_{cat}/i^0_p *vs* $1/[1+\exp\{F/RT(E^{0'}-E)\}]$ has been shown for electrocatalytic WO by **1a** which was used for the measurement of kinetic rate constant. The dotted line represent experimentally determined values and the solid line represents the best linear fit (in all the studies, intercept was close to zero in accordance to equation VIII) line that was used for kinetic rate constant determination. (C) The plot of i_{cat} *vs* concentrations of **1a** has been shown. (D) The plot of CVs has been shown for electrocatalytic D_2O and H_2O oxidation by **1a** in D_2O (red) and H_2O (black) solvent respectively (pD 7.2 for D_2O and pH 7.2 for H_2O; 15 mM phosphate buffer $I = 0.1$ M); inset shows plot of i_{cat}/i^0_p *vs* $1/[1+\exp\{F/RT(E^{0'}-E)\}]$ for D_2O (red) and H_2O (black).

The CV of **1a** in D_2O instead of H_2O was also conducted. The CV displayed a shift of peak potential (80 mV) (Figure 3A.8 D) of $Fe^{IV/III}$ indicating a CPET process and a significantly lower catalytic current than that obtained for H_2O (Figure 3A.8 D). The second order kinetics for WO by 1a in D_2O was found to be 0.36 ± 0.02 $M^{-1}s^{-1}$ (Figure 3A.8 D, inset). The kinetic isotope effect (KIE) of 3.2 was obtained according to the equation: KIE = $k_{cat},H_2O/k_{cat},D_2O$ (Figure 3A.8 D, inset). This is in contrast to the KIE reported for Meyer et al. for a related iron-amidate complex in non-aqueous solvent (KIE = 1.08), which indicates absence of APT in the rate determining O−O formation step.[19]

In order to experimentally verify the bimolecular rate law for the reaction between $Fe^V(O)$ and H_2O, the reaction between chemically synthesized $Fe^V(O)$ and H_2O was monitored electrochemically. Low concentration of $Fe^V(O)$ (5×10^{-5} M) was synthesized in acetonitrile at room temperature and electrocatalysis was studied by increasing amounts of water (from 1 to 2.87 M) (Figure 3A.9) . The cyclic voltammograms were analyzed at a constant ionic strength of 0.3 M using ($[(nBu)_4N]PF_6$). Under these conditions, no decay of the $Fe^V(O)$ was observed in the absence of added H_2O using UV-Vis spectroscopy. Increase in the catalytic current was observed with increasing amounts of H_2O. The plot of i_{cat}/i_p *vs* $[H_2O]^{1/2}$ was found to be linear which indicates a bimolecular reaction having first order dependence on both **1a** (in water, Figure 3A.8 C) and H_2O (in acetonitrile, Figure 3A.9 B). Determination of the second order rate constant for the reaction by using FOWA method will be incorrect as the foot of the wave is contaminated by other redox process (Figure 3A.9 A).
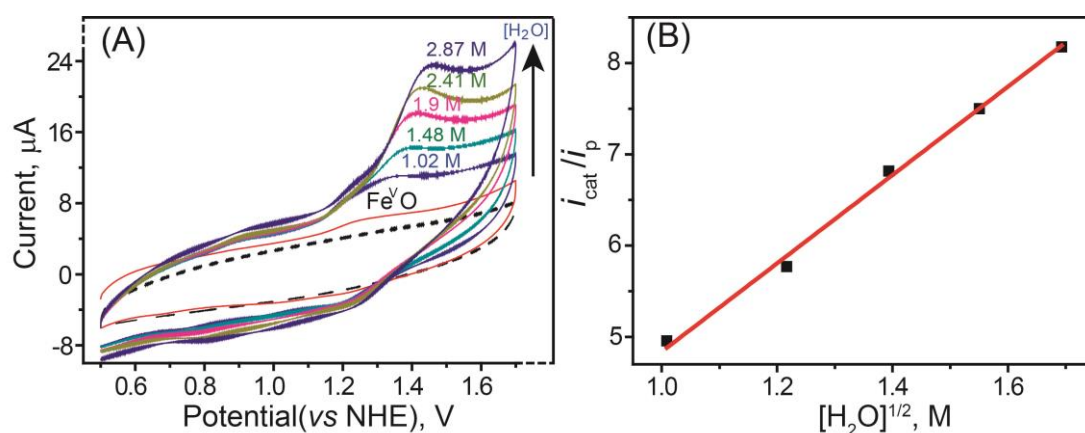
Figure 3A.9: (A) Increasing amount water onto synthetically made Fe^{V}O from **1a** blank (black dotted), red (5 x 10^{-5} M Fe^V(O). (B) The plot of i_{cat}/i_p *vs* [H$_2$O]$^{1/2}$ according to eq. I, red line is the linear fit (Y = 4.8X, R^2 = 0.99).

3A.4.5 Effect of different buffer on the WO

Several experiments were performed to examine the role of the buffer on the catalytic water oxidation activity. A significant enhancement of the fixed-potential catalytic current, i_{cat}, was observed with increasing concentrations of HPO$_4^{2-}$ buffer (the total concentration of the buffer anion kept constant and its degree of protonation varied) up to 40 mM (Figure 3A.10 A and Appendix B26).[6v,7c,9a,9d] Care was taken during these measurements to maintain the ionic strength of the solution at 0.5 M with addition of NaNO$_3$. Moreover, a decrease of the catalytic current was observed when the concentration of the buffer base was increased beyond 40 mM due to possible buffer assisted catalyst decomposition reported for TAML complex at high buffer concentrations.[25,32]
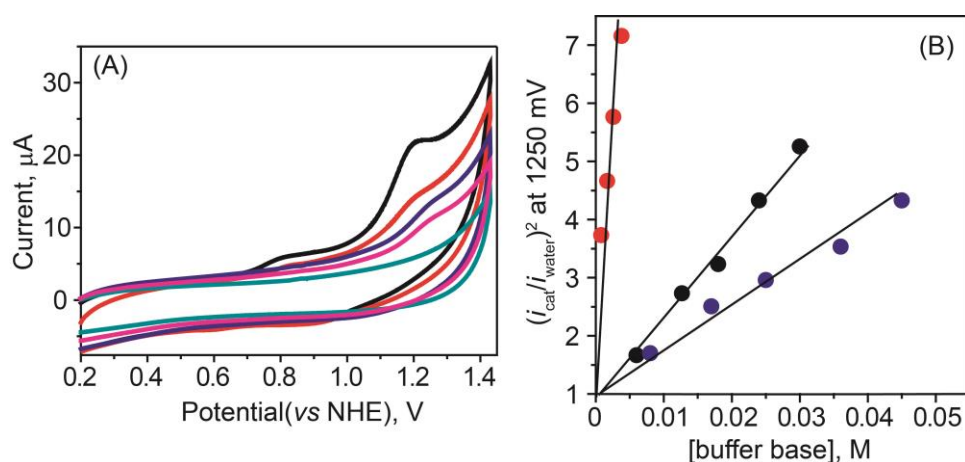
Figure 3A.10: (A) CVs of 0.2 mM of **1a** at different phosphate buffer base concentration in water at pH 7.2 (scan rate 100 mVs^{-1}, I = 0.5 M NaNO$_3$ in water); blank (green), water

(magenta), 0.006 M (blue), 0.013 M (red) and 0.024 M (black) [HPO_4^{2-}]. (B) Plot of $(i_{cat}/i_{water})^2$ at 1250 mV against different buffer dianion concentration of phenyl phosphate (red), phosphate (black), bicarbonate (blue) at pH 7.2

Besides phosphate (pK_a = 7.21), [Fe^{III}-(bTAML)] also catalyzed water oxidation at pH 7.2 with buffers having varying pK_a values including bicarbonate (pK_a = 6.37),[33a] and phenyl phosphate (pK_a = 9.9)[33b] (Appendix B26-B28). For such a base-assisted process in water, the overall O–O bond formation rate (k_{cat}) can be expressed by the sum of the rate in unbuffered solution (k_{water}) and the rate contributed by the addition of buffer base (k_b[B]), as shown in equation VIII (k_b and [B] represent the buffer assisted WO rate constant and buffer anion concentration respectively). According to equation IX, a plot of $(i_{cat}/i_{water})^2$ as a function of the buffer base concentration [B] should give a linear correlation with a slope equal to k_b/k_{water} (equation. IX).[6u,7c,9a,9d] In fact, this prediction was observed experimentally for all the three buffers used (Figure 3A.10 B), indicating that one equivalent of buffer base was involved in the rate-limiting O–O bond formation step.

$$k_{cat} = k_{water} + k_b[B] \qquad\qquad \text{(VIII)}$$

$$(i_{cat}/i_{water})^2 = k_{cat}/k_{water} = 1 + k_b[B]/k_{water} \qquad \text{(IX)}$$

As shown in Figure 3A.10, the $(i_{cat}/i_{water})^2$ value showed a linear dependence on the concentration of each buffer base. The k_b value for all the three buffers were determined from the slope of the plot of $(i_{cat}/i_{water})^2$ as a function of buffer concentration (Figure 3A.10). The k_{water} value was determined from an independent kinetic study in water at pH 7 using $NaNO_3$ as the electrolyte (Appendix 29). The k_b values for phenylphosphate, phosphate and bicarbonate were determined to be 2.1 × 10^4, 2.8 × 10^3 and 11.4 × 10^2 M^{-1}s^{-1}respectively (Figure 3A.10 B). Notably, a Brønsted relationship for acid or base catalyzed reaction could be observed from the plot of log (k_b/k_{water}) as a function of the pK_a of the buffer used (Figure 3A.11). The plot was found to be linear with a slope of 0.34. This observation further suggests that there is a significant component of proton transfer from the catalyst to the buffer anion in the transition state for the rate-limiting O–O bond formation step.
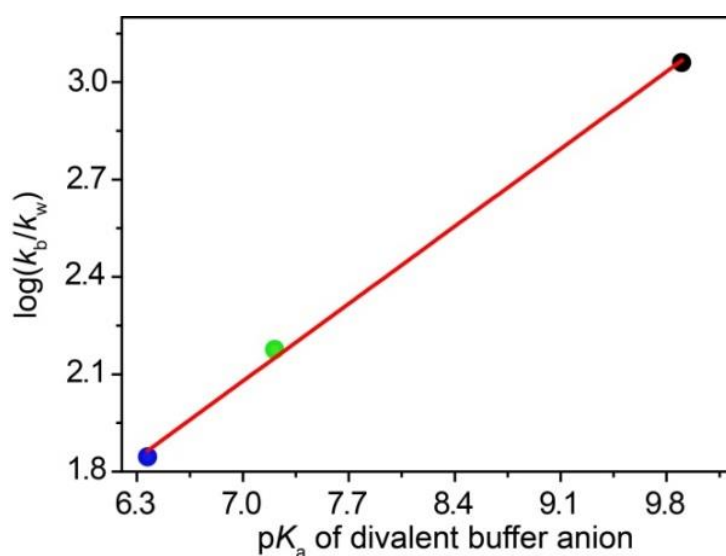
Figure 3A.11: Bronsted relationship between $\log(k_b/k_{water})$ *vs* pK_a of different divalent buffer base anion used at pH 7.2

3A.4.6 Effect of Ligand Electronics on WO Rates

        In order to understand the effect of ligand electronics on WO kinetics, Fe^{III}-(bTAML) molecules having different substituent groups on the benzene ring (**1b**-**f**) were synthesized. Similar to **1a**, CVs of **1b**-**f** in water (pH 7.2, 15 mM phosphate buffer) solvent using 0.1 M NaNO$_3$ as electrolyte) also depict two successive one-electron transfer processes with altered redox potentials (Appendix B16). The change in the redox potential follows a trend which could be explained by the electronic nature of the substituent group X (OMe, F, Cl, CN and NO$_2$) in the phenyl ring of Fe^{III}-bTAML (Appendix B14, B30). The electron donating group –OMe in **1b** increases the electron density on the metal center thereby reducing the electron acceptance tendency of central metal Fe^{III}, which consequently lowers its formal potential (Table 3A.1). Similarly, electron withdrawing groups in **1c**-**1f** increases its ease towards electron acceptance and thereby increases the redox potential of catalyst. Kinetics of WO by **1a**-**f** was studied by cyclic voltammetry (Appendix B31) and the results are summarized in Table 3A.1.

Table 3A.1 Kinetic rate constants for WO by different catalyst in 15 mM phosphate buffer (pH ~7.2, $I = 0.1$ M, $NaNO_3$).

Catalyst	Substituent	σ_{m+p}	$E^{o\prime}{}_{Fe}{}^{IV/III}$ vs NHE[b]	$E^{0\prime}{}_{Fe}{}^{V/IV}$ vs NHE[b]	$\Delta E^{0\prime}$ ($Fe^{V/IV}$ − $Fe^{IV/III}$)	Rate Constant ($M^{-1}s^{-1}$)	Onset Over Potential[c] (mV)
1a	-H	0.00	0.85	1.20	0.35	1.2 ± 0.21	~ 250
1b	-OMe	-0.15	0.73	1.12	0.37	0.72± 0.15	~ 170
1c	-F	0.40	0.89	1.25	0.36	2.16± 0.27	~ 290
1d	-Cl	0.60	0.93	1.31	0.38	2.81 ± 0.21	~ 330
1e	-CN	1.22	0.99	1.39	0.40	4.39 ± 0.30	~ 370
1f	-NO₂	1.48	1.11	1.43	0.31	6.12 ± 0.5	~ 540

[b]Potentials are calculated from SQWV (Appendix B16) at pH 7.2 in water, and

[c]Onset over potential was calculated at pH 7.2 (Appendix B16).
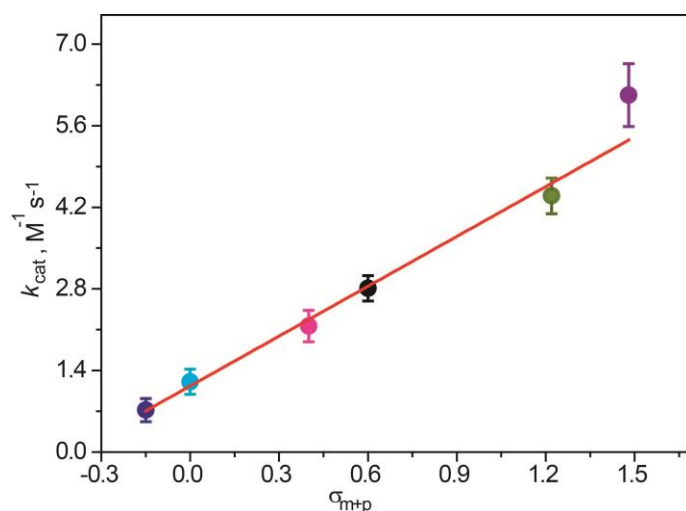
Figure 3A.12: k_{cat} for WO of 1a-f is correlated linearly with Hammett parameter (σ) of electronic substitution on catalyst **1b** (blue), **1a** (yellow-green), **1c** (magenta), **1d** (black), **1e** (green), **1f** (violet).

The results demonstrate that when the bTAML ligand had electron withdrawing groups, the WO kinetics became faster whereas electron donating group made the WO kinetics slower. Catalytic rate constant for WO are correlated linearly with the Hammett parameter (σ_{m+p}, m-meta and p-para position in benzene ring) (Figure 3A.12).

3A.5 Summary and Conclusions

The results show that the Fe^{III}-bTAML is an efficient catalyst for the electrochemical oxidation of water to oxygen with an onset over potential of ~250 mV at neutral pH (Figure 3A.3). The 90% faradaic yield for oxygen production indicates nearly exclusive 4e− oxidation of H_2O. It has been recently demonstrated that at neutral to basic pH, iron complexes serve only as pre-catalysts for WO. The real catalysts are iron oxide-hydroxide nanoparticles which are formed upon decomposition of the ligand under the oxidative conditions.[15,34,35] Although, the TAML framework is known to be very robust under oxidative conditions, several experiments were carried out which conclusively show that this is a homogeneous system. The stability of the resting Fe^{III} complex over 2 h of measurement and the lack of any effects on catalytic efficiency by metal ion sequestration (EDTA or with Chelex resin) show that free iron ions are not contributing to the observed WO activity. These observations further conclude the efficiency of Fe^{III}-bTAML to act as a homogeneous electrocatalytic WO catalyst. Moreover, scan-rate dependence of the rate limiting O–O bond formation step and linear dependence of catalytic current on catalyst concentration argue that Fe-bTAML is a single-site molecular catalyst similar to iron amidate complex in nonaqueous medium.[19]

The titration of the acidic proton in $Fe^{III}(OH_2)_2$−bTAML (pK_a= 10.3) indicate that the resting state of the Fe-TAML catalyst at pH 7 is H_2O–Fe^{III}–OH_2.[27,28] The cyclic voltammetry study of starting $Fe^{III}(H_2O)_2$-bTAML as a function of pH indicate that the first oxidation wave at 0.9 V *vs* NHE represents oxidation of the $Fe^{III}(OH_2)_2$-bTAML to the corresponding $Fe^{IV}(O)$-bTAML. The second anodic oxidation at 1.25 V *vs* NHE represents a 1e- oxidation resulting in $Fe^{V}(O)$-bTAML and this coincides with water oxidation. The formation of the both $Fe^{IV}(O)$ and $Fe^{V}(O)$ at 0.82 and 1.2 V were confirmed by CPE experiments. For Ru polypyridine complexes, Meyer[6u-w] and Berlinguette[6s] has shown that the reaction pathway mediated by $[Ru−OH_2]^{2+}$ begins with two consecutive PCET steps to form $[Ru^{IV}=O]^{2+}$. The first two redox signals appear at close proximity and appears as a single broad $[Ru^{IV}=O]^{2+}$/$[Ru-OH_2]^{2+}$ couple in several complexes. A subsequent oxidation process

generates the highly electrophilic $[Ru^V=O]^{3+}$ fragment that reacts with water to form the requisite O-O bond.[6] It is interesting to note that from $Fe^{III}(OH_2)_2$-bTAML, the generation of $Fe^V(O)$ does not occur through two consecutive CPET processes. This is likely due to the instability of $Fe^{IV}-OH$ which is the product expected to be formed from Fe^{III}-OH_2 after one CPET step.
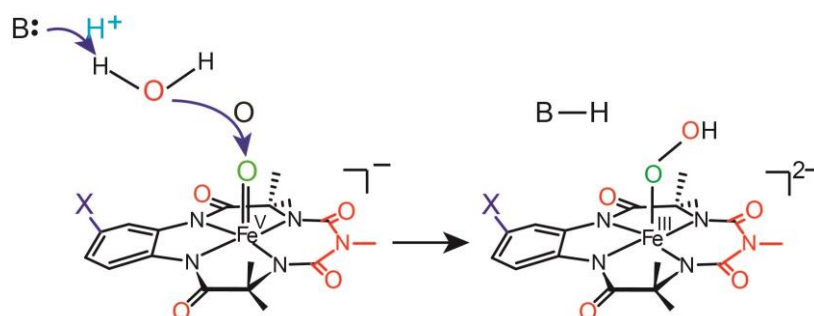
Scheme 3A.1 Proposed buffer assisted O-O bond formation catalysed by high valent $Fe^V O$ in water (B = buffer anion in water).

The more thermodynamically favoured Fe^{IV} species i.e. $Fe^{IV}(O)$ or the related $(Fe^{IV})_2O$ is formed. Subsequently, $Fe^V(O)$ is electrochemically formed via 1 electron oxidation of $Fe^{IV}(O)$. We have earlier demonstrated that the addition of water to chemically synthesised $Fe^V(O)$ did not result into O_2 evolution.[20a] In fact, upon addition of water to chemically synthesized $Fe^V(O)$ in CH_3CN (such that the water concentration is > 90%), instantaneous reaction is observed leading to the formation of the μ-O-Fe^{IV} dimer. Further, at water concentrations of 95% and above, no formation of $Fe^V(O)$ can be achieved upon addition of NaOCl to Fe^{III}-bTAML. We believe that at water concentrations of 90% and higher, $Fe^V(O)$ instantaneously reacts with water to form the Fe^{III}-OOH which immediately decays to form the μ-O-Fe^{IV} dimer. For photochemical water oxidation catalysed by Fe-bTAML, we have demonstrated that the presence of $Fe^V(O)$, water and additional equivalents of 1e$^-$ oxidant (like Ru^{3+}, whose redox potential is very close to $Fe^V(O)/Fe^{IV}(O)$ potential) is required for O_2 evolution from water.[20a] All these experimental observations lead us to propose following two models for O_2 evolution:

(i) First $Fe^V(O)$ is formed which instantaneously reacts with water to form the Fe^{III}-OOH. This peroxo gets further oxidized due to the applied electrode potential to form Fe^V-(O_2^{2-}), finally leading to O_2 evolution.

(ii) Water oxidation occurs when $Fe^V(O)$ and water are further oxidized under electrochemical conditions, at a red-ox potential corresponding to Fe(VI)/Fe(V) couple which can be close to the Fe(V)/Fe(IV) couple. This would then indicate the involvement of $Fe^V(O)L^{\cdot+}$ or $Fe^{VI}(O)$ as the active species (as supported by DFT studies[16c]).

Although both these scenarios are possible, we believe the first model to be more likely. In 100% water, the reaction of $Fe^V(O)$ with water leading to formation of Fe^{III}-OOH is very fast. Hence further oxidation of Fe^{III}-OOH leading to O_2 evolution seems to be more reasonable.

KIE of 3.2 in water indicate that proton abstraction is concomitant with water attack in the rate determining step. This KIE has been attributed to atom proton transfer (APT) in which the O-O bond formation occurs with simultaneous proton transfer to another H_2O or hydroxide or to a base anion (depending upon the pH and buffer used) to form a low energy hydroperoxidic intermediate (scheme 3A.1)[6v,7c,9a,9d] The hydroperoxidic species formed undergo sequential oxidation to release O_2 which results in an increase in catalytic current in CV. First order dependency of catalytic current to catalyst concentration indicates the association of a monomeric $Fe^V(O)$ involved in water oxidation. Variation of buffer indicates a first order dependency with respect to buffer base anion on WO rates. In order to determine the order with respect to H_2O, the reaction of $Fe^V(O)$ with H_2O was probed electrochemically. Since we are able to generate stable $Fe^V(O)$ quantitatively at room temperature in CH_3CN, CV of this species with increasing amounts of water showed a first order dependency in water during the O−O bond formation step. Hence the O−O bond formation is an overall second order reaction between $Fe^V(O)$ and H_2O. This represents a rare example in which reaction order has been directly determined from reactive intermediates that are fully characterized in solution.

Presence of base anion has been found to assist the rate determining proton abstraction in the O−O bond forming step during WO process[6u-w,7c,9a,9d] Groves, Meyer and very recently Cao and Sun showed that effect of buffer anion can enhances the O−O bond formation rate significantly for Co porphyrin,[7c] Cu-polypeptide,[11b] Ru-polypyridyl,[6v] Ni-porphyrin,[9a] and Ni-pyridine[9d] based metal complex. Electrocatalysis of **1a** performed at either pH 10 or in the presence of different concentrations of buffer anion display saturation behaviour catalytic current with enhanced WO rate constants compared to pH 7.2. This clearly elucidates the role of base anion in proton abstraction during the nucleophilic attack of H_2O onto iron-oxo leading to the O−O bond formation. For these base assisted processes, the plot of $(i_{cat}/i_{water})^2$ as a function of buffer base concentration [B] was found to be linear and the rate contributed

from the buffer base ($k_b[B]$) was determined from the slope. Using three different buffer base anions, a Brønsted relationship for base catalyzed WO having a slope of 0.34 (Figure 3A.11) was determined which indicates that the proton is "in flight" in the transition state. This value is very similar to that determined by Groves (0.38) for WO with Co-porphyrin complexes.[7c] Such an O-atom transfer coupled with a proton transfer to added acceptor base during WO for Fe-complexes in water is rare for electrocatalytic homogeneous WO by Fe-complexes.

Finally, Fe-bTAML with varying electronic substitution showed different WO rates and onset overpotential. Fe-bTAML with varying electronic substitution showed different WO rates and onset overpotential. The most efficient catalyst should strike a balance between easily accessing the higher redox levels of the metal ion (electron-donating substituents) and the reactivity of the M(O) (electron withdrawing substituents). For chemical WO by Ru complexes, electron donating substituents on the ligand have been shown by Berlinguette to enhance the catalytic rates.[6s] In these complexes, the rate determining step was proposed to be the O_2 evolution from the $[Ru^{IV}-OO]^{2+}$[6s] In contrast, for chemical WO by Fe-complexes the rates of WO enhanced with installation of electron withdrawing groups.[12a] In this case, the rate determining step was proposed to be the O−O bond formation. Hence understanding the effects of both electron withdrawing/donating groups on the catalyst for the O−O bond formation step is very important. Such study of electronic effect on O−O bond formation rate and overpotential by CV for Fe-based homogeneous electrocatalyst is rare. In this work, we demonstrate that both the WO rates and onset overpotential increased with the introduction of electron withdrawing substituents. This is reasonable since the electron withdrawing substituent on aromatic ring decreases the electron density on iron centre thereby increasing the electrophilicity of the O-atom in the $Fe^V(O)$. This would translate into faster reaction rate between the $Fe^V(O)$ and H_2O in the rate determining O−O bond formation step. On the other hand, increasing electron withdrawing groups would increase the $E^{0'}$ of the $Fe^V(O)/Fe^{IV}(O)$ couple which would in turn increase the onset potential for WO. For a series of substituted Fe-bTAML, three folds higher O−O bond forming rate for **1f** compared to **1b** was observed in expanse of three-fold increase in onset overpotential. However, when the overpotential contribution to the rate constant was substracted by applying TOF-η equations (see Appendix B32 for details about equations and calculations of TOF^0 at zero overpotential) as suggested recently by Saveant[25d] and Llobet,[25g] the catalyst having lower overpotential showed higher reactivity (Appendix B32). The onset potential of 170 mV for the most electron rich Fe-

bTAML **1b** in this work is similar to electron rich Cu-tertdentate amidate[11g] ligand which is among the lowest for first row transition metal based electrocatalysts.

3A.6 References

(1)   Hammarström, L.; Hammes-Schiffer, S. *Acc. Chem. Res.* **2009**, *42*, 1859-   1860.

(2)   Umena, Y.; Kawakami, K.; Shen, J.-R.; Kamiya, N. *Nature* **2011**, *473*, 55-60.

(3)   Dismukes, G. C.; Brimblecombe, R.; Felton, G. A. N.; Pryadun, R. S.; Sheats, J. E.; Spiccia, L.; Swiegers, G. F. *Acc. Chem. Res.* **2009**, *42*, 1935-1943.

(4)   a) Blakemore, J. D.; Crabtree, R. H.; Brudvig, G. W. *Chem. Rev.* **2015**, *115*, 12974-13005; b) Kärkäs, M. D.; Verho, O.; Johnston, E. V.; Åkermark, B. *Chem. Rev.* **2014**, *114*, 11863; c) McEvoy, J. P.; Brudvig, G. W. *Chem. Rev.* **2006**, *106*, 4455-4483; d) Dau, H.; Limberg, C.; Reier, T.; Risch, M.; Roggan, S.; Strasse, P. *Chem. Cat. Chem.* **2010**, *2*, 724–761.

(5)   Kanan, M. W.; Nocera, D. G. *Science* **2008**, *321*, 1072-1075.

(6) a) Meyer, T. J. *Acc. Chem. Res*. **1989**, *22*, 163–170; b) Kaveevivitchai, N.; Chitta, R. R.; Zong, M.; Ojaimi, El.; Thummel, R. P. *J. Am. Chem. Soc*. **2012**, *134*, 10721; c) Neudeck, S.; Maji, S.; López, I.; Meyer, S.; Meyer, F.; Llobet, A. *J. Am. Chem. Soc*. **2013**, *136*, 24-27; d) Concepcion, J. J.; Jurss, J. W. J.; Templeton, L.; Meyer, T. J. *J. Am. Chem. Soc.* **2008**, *130*, 16462; e) Chen, Z.; Concepcion, J. J.; Jurss, J. W.;. Meyer, T. J *J. Am. Chem. Soc.* **2009**, *131*, 15580-15581; f) Concepcion, J. J.; Jurss, J. W.; Brennaman, M. K.; Hoertz, P. G.; Patrocinio, A. O. V. T.; Murakami Iha, N. Y.; Templeton, J. L.; Meyer, T. J. *Acc. Chem. Res.* **2009**, *42*, 1954-1965; g) Duan, L.; Araujo, C. M.; Ahlquist, M. r. S. G.; Sun, L. *Proc. Natl. Acad. Sci. U. S. A*. **2012**, *109*, 15584-15588; h) Duan, L.; Bozoglian, F.; Mandal, S.; Stewart, B.; Privalov, T.; Llobet, A.; Sun, L. *Nat. Chem.* **2012**, *4*, 418-423; i) Badiei, Y. M.; Polyansky, D. E.; Muckerman, J. T.; Szalda, D. J.; Haberdar, R.; Zong, R.; Thummel, R. P.; Fujita, E. *Inorg. Chem.* **2013**, *52*, 8845-8850; j) Geletii, Y. V.; Huang, Z.; Hou, Y.; Musaev, D. G.; Lian, T.; Hill, C. L. *J. Am. Chem. Soc.* **2009**, *131*, 7522-7523; k) Kärkäs, M. D.; Åkermark, T.; Chen, H.; Sun, J.; Åkermark, B. *Angew. Chem., Int. Ed.* **2013**, *52*, 4189-4193; l) Muckerman, J. T.; Kowalczyk, M.; Badiei, Y. M.; Polyansky, D. E.; Concepcion, J. J.; Zong, R.; Thummel, R. P.; Fujita, E. *Inorg. Chem.* **2014**, *53*, 6904-6913; m) Polyansky, D. E.; Muckerman, J. T.; Rochford, J.; Zong, R.; Thummel, R. P.; Fujita, E. *J. Am. Chem. Soc.* **2011**, *133*, 14649-14665; n) Murakami, M.; Hong, D.; Suenobu, T.; Yamaguchi, S.; Ogura, T.;

Fukuzumi, S. *J. Am. Chem. Soc.* **2011**, *133*, 11605-11613; o) Radaram, B.; Ivie, W. M.; Singh, R. M.; Grudzien, J. H.; Reibenspies, C. E.; Webster, Zhao, X. *Inorg. Chem.* **2011**, *50*, 10564-10571; p) Romain, S.; Bozoglian, F.; Sala, X.; Llobet, A. *J. Am. Chem. Soc.* **2009**, *131*, 2768-2769; q) Tseng, H.-W.; Zong, R.; Muckerman, J. T.; Thummel, R. *Inorg. Chem.* **2008**, *47*, 11763-11773; r) Wang, L.; Duan, L.; Stewart, B.; Pu, M.; Liu, J.; Privalov, T.; Sun, L. *J. Am. Chem. Soc.* **2012**, *134*, 18868-18880; s) Wasylenko, D. J.; Ganesamoorthy, C.; Henderson, M. A.; Koivisto, B. D.; Osthoff, H. D.; Berlinguette, C. P. *J. Am. Chem. Soc.* **2010**, *132*, 16094-16106; t) Yagi, M.; Tajima, S.; Komi, M.; Yamazaki, H. *Dalton Trans.* **2011**, *40*, 3802-3804; u) Chen, Z.; Concepcion, J. J.; Luo, H.; Hull, J. F.; Paul, A.; Meyer, T. J. *J. Am. Chem. Soc.* **2010**, *132*, 17670– 17673; v) Chen, Z.; Concepcion, J. J.; Hu, X.; Yang, W.; Hoertz, P. G.; Meyer, T. J. *Proc. Natl. Acad. Sci. U. S. A.* **2010**, *107*, 7225– 7229; w) Song, N.; Concepcion, J. J.; Binstead, R. A.; Rudd, J. A.; Vannucci, A. K.; Dares, C. J.; Coggins, M. K.; Meyer, T. J. *Proc. Natl. Acad. Sci. U. S. A.* **2015**, *112*, 4935-4940.

(7)   a) Dogutan, D. K.; McGuire, R.; Nocera, D. G. *J. Am. Chem. Soc.* **2011**, *133*, 9178– 9180; b) Kanan, M. W.; Nocera, D. G. *Science* **2008**, *321*, 1072– 1075; c) Wang, D.; Groves, J. T. *Proc. Natl. Acad. Sci. U.S.A.* **2013**, *110*, 15579– 15584; d) Gerken, J. B.; McAlpin, J. G.; Chen, J. Y. C.; Rigsby, M. L.; Casey, W. H.; Britt, R. D.; Stahl, S. S. *J. Am. Chem. Soc.* **2011**, *133*, 14431– 14442; e) Leung, C.-F.; Ng, S. -M.; Ko, C. -C.; Man, W.-L.; Wu, J.; Chen, L.; Lau, T.-C. *Energy Environ. Sci.* **2012**, *5*, 7903-7907; f) McCool, N. S.; Robinson, D. M.; Sheats, J. E.; Dismukes, G. C. *J. Am. Chem. Soc.* **2011**, *133*, 11446-11449; g) Wasylenko, D. J.; Ganesamoorthy, C.; Borau-Garcia, J.; Berlinguette, C. P. *Chem. Comm.* **2011**, *47*, 4249-4251; h) Yin, Q.; Tan, J. M.; Besson, C.; Geletii, Y. V.; Musaev, D. G.; Kuznetsov, A. E.; Luo, Z.; Hardcastle, K. I.; Hill, C. L. *Science* **2010**, *328*, 342-345; i) Zhou, T.; Wang, D.; Chun-Kiat, G. S.; Hong, J.; Han, J.; Mao, J.; Xu, R. *Energy Environ. Sci.* **2015**, *8*, 526-534; j) Huang, Z.; Luo, Z.; Geletii, Y. V.; Vickers, J. W.; Yin, Q.; Wu, D.; Hou, Y.; Ding, Y.; Song, J.; Musaev, D. G.; Hill, C. L.; Lian, T. *J. Am. Chem. Soc.* **2011**, *133*, 2068-2071; k) Costentin, C.; Porter, T. R.; Savéant, J.-M. *J. Am. Chem. Soc.* **2016**, *138*, 5615−5622; l) Das, D.; Pattanayak, S.; Singh, K. K.; Garai, B.; Sen Gupta, S. *Chemical Communications* **2016**, *52*, 11787-11790

(8)   a) Brimblecombe, R.; Koo, A.; Dismukes, G. C.; Swiegers, G. F.; Spiccia, L. *J. Am. Chem. Soc.* **2010**, *132*, 2892-2894; b) Mullins, C. S.; Pecoraro, V. L. *Coord. Chem. Rev.* **2008**, *252*, 416–443; c) Najafpour, M. M. *Chem. Comm.* **2011**, *47*, 11724-11726; d) Limburg, J.; Vrettos, J. S.; Liable-Sands, L. M.; Rheingold, A. L.; Crabtree, R. H.;

Brudvig, G. W. *Science* **1999**, *283*, 1524-1527; e) Gao, Y.; Ãkermark, T. r.; Liu, J.; Sun, L.; Ãkermark, B. r. *J. Am. Chem. Soc.* **2009**, *131*, 8726-8727; f) Young, K. J.; Takase, G. W. Brudvig, *Inorg. Chem.* **2013**, *52*, 7615-7622; g) F. M. Ashmawy, C. A. McAuliffe, M. K.; Parish, R. V.; Tames, J. *J. Chem. Soc., Dalton Trans.* **1985**, *7*, 1391-1397; h) W. Sameera, M. C.; McKenzie, C. J.; McGrady, J. E. *Dalton Trans.* **2011**, *40*, 3859-3870.

(9) a) Han, Y;. Wu, Y.; Lai, W.; Cao, R. *Inorg. Chem.* **2015**, *54*, 5604-5613; b) Zhang, M.; Zhang, M. -T.; Hou, C.; Ke, Z. F.; Lu, T. B. *Angew. Chem., Int. Ed.* **2014**, *53*, 13042–13048; c) Luo, G. -Y.; Huang, H. -H.; Wang, J.-W.; Lu, T. -B. *Chem. Sus. Chem.* **2016**, doi: 10.1002/cssc.201501474; d) Wang, L.; Duan, L.; Ambre, R. B.; Daniel, Q.; Chen, H.; Sun, J.; Das, B.; Thapper, A.; Uhlig, J.; Dinér, P.; Sun, L. *J. Catal.* **2016**, *335*, 72-78; e) Dincă, M.; Surendranath, Y.; Nocera, D. G. *Proc. Natl. Acad. Sci., U.S.A*. **2010**, *107*, 10337-10341.

(10) a) McDaniel, N. D.; Coughlin, F. J.; Tinker, L. L.; Bernhard, S. *J. Am. Chem. Soc*. **2008**, *130*, 210–217; b) Hull, J. F.; Balcells, D.; Blakemore, J. D.; Incarvito, C. D.; Eisenstein, O.; Brudvig, G. W.; Crabtree, R. H. *J. Am. Chem. Soc.* **2009**, *131*, 8730; c) Lalrempuia, R.; McDaniel, N. D.; Müller-Bunz, H.; Bernhard, S.; Albrecht, M. *Angew. Chem., Int. Ed*. **2010**, *49, 9765–9768.

(11) a). Barnett, M.; Goldberg K. I.; Mayer, J. M. *Nat Chem.* **2012**, *4*, 498-502; b) Chen, Z. F.; Meyer, T. J. *Angew. Chem., Int. Ed*. **2013**, *52*, 700–703; c) Coggins, M. K.; Zhang, M. -T.; Chen, Z.; Song, N.; Meyer, T. J. *Angew. Chem., Int. Ed*. **2014**, *53*, 12226-12230; d) Zhang, T.; Wang, C.; Liu, S.; Wang, J .-L.; Lin, W. *J. Am. Chem. Soc.* **2014**, *136*, 273-281; e) Garrido-Barros, P.; Funes-Ardoiz, I.; Drouet, S.; Benet-Buchholz, J.; Maseras, F.; Llobet, A. *J. Am. Chem. Soc*. **2015**, *137*, 6758– 6761; f) Xiang, R.-J.; Wang, H. -Y.; Xin, Z.-J.; Li, C. -B.; Lu, Y.-X.; Gao, X. -W.; Sun, H.-M.; Cao, R. *Chem. –Eur. J.* **2016**, *22*, 1602-1607.

(12) a) Ellis, W. C.; McDaniel, M. D.; Bernhard, S.; Collins, T. J. *J. Am. Chem. Soc*. **2010**, *132*, 10990-10991; b) Codolà, Z.; Gómez, L.; Kleespies, S. T.; Que, L. Jr.; Costas, M.; Lloret-Fillol, J. *Nat. Commun.* **2015**, *6*, 5865; c) Okamura, M.; Kondo, M.; Kuga, R.; Kurashige, Y.; Yanai, T.; Hayami, S.; Praneeth, V. K. K.; Yoshida, M.; Yoneda, K.; Kawata, S.; Masaoka, S. *Nature* **2016**, *530*, 465-468.

(13) Fillol, J. L.; Codolà, Z.; Garcia-Bosch, I.; Gómez, L.; Pla, J. J.; Costas, M. *Nat. Chem.* **2011**, *3*, 807-813.

(14) Hoffert, W. A.; Mock, M. T.; Appel, A. M.; Yang, J. Y. *Eur. J. Inorg. Chem.* **2013**, *2013*, 3846-3857.

(15)   Hong, D.; Mandal, S.; Yamada, Y.; Lee, Y.-M.; Nam, W.; Llobet, A.; Fukuzumi, S. *Inorg. Chem.* **2013**, *52*, 9522-9531.

(16)   a) Acuña-Parés, F.; Costas, M.; Luis, J. M.; Lloret-Fillol, J. *Inorg. Chem.* **2014**, *53*, 5474-5485; b) Acuña-Parés, F.; Codolà, Z.; Costas, M.; Luis, J. M.; Lloret-Fillol, J. *Chem. – Eur. J.* **2014**, *20*, 5696; c) Ertem, M. Z.; Gagliardi, L.; Cramer, C. J. *Chem. Sci.* **2012**, *3*, 1293; d) Kasapbasi, E. E.; Whangbo, M. -H. *Inorg. Chem.* **2012**, *51*, 10850; e) Poater, A. *Catal. Comm.* **2014**, *44*, 2; f) Savéant, J. -M. *Elements of Molecular and Biomolecular Electrochemistry*, Wiley-Interscience, New York, **2006**; g) Savéant, J. -M. *Energy Environ. Sci.* **2012**, *5*, 7718-7731.

(17)   To, W.-P.; Wai-Shan Chow, T.; Tse, C. -W.; Guan, X.; Huang, J. -S.; Che, C. -M. *Chem. Sci.* **2015**, *6*, 5891-5903.

(18)   Wickramasinghe, L. D.; Zhou, R.; Zong, R.; Vo, P.; Gagnon, K. J.; Thummel, R. P. *J. Am. Chem. Soc.* **2015**, *137*, 13260-13263.

(19)   Coggins, M. K.; Zhang, M. -T.; Vannucci, A. K.; Dares, C. J.; Meyer, T. J. *J. Am. Chem. Soc.* **2014**, *136*, 5531-5534.

(20)   a) Panda, C.; Debgupta, J.; Diaz Diaz, D.; Singh, K. K.; Sen Gupta, S.; Dhar, B. B. *J. Am. Chem. Soc.* **2014**, *136*, 12273– 12282; b) Singh, K. K.; Tiwari, M. K.; Dhar, B. B.; Vanka, K.; Sen Gupta, S. *Inorg. Chem.* **2015**, *54*, 6112-6121.

(21)   Pattanayak, S.; Jasniewski, A. J.; Rana, A.; Draksharapu, A.; Singh, K. K.; Weitz, A.; Hendrich, M.; Que, L., Jr.; Dey, A.; Sen Gupta, S. *Inorg. Chem.* **2017**, *56*, 6352.

(22)   Galus, Z. Fundamentals of Electrochemical Analysis; Ellis Horwood Ltd.: Chichester, U.K., **1976.**

(23)   Demeter, E. L.; Hilburg, S. L.; Washburn, N. R.; Collins, T. J.; Kitchin, J. R. *J. Am. Chem. Soc.* **2014**, *136*, 5603– 5606.

(24)   Collins, T. J.; Gordon-Wylie, S. W. Long-Lived Homogeneous Oxidation Catalysts, U.S. Patent **5,847,120,** December 8, **1998**.

(25)   a) Panda, C.; Ghosh, M.; Panda, T.; Banerjee, R.; Sen Gupta, S. *Chem. Commun.* **2011**, *47*, 8016; b) Bard, A. J.; Faulkner, L. R Electrochemical Methods: Fundamentals and Applications; Wiley: New York, **1980**; c) C. Costentin, G. Passard, J.-M. Savéant, *J. Am. Chem. Soc.* **2015**, *137*, 5461-5467; d) Costentin, C.; Drouet, S.; Robert, M.; Savéant, J-M. *J. Am. Chem. Soc.* **2012**, *134*, 11235- 11242; e) Costentin, C.; Savéant, J.-M. *Chem. Electro. Chem.* **2014**, *1*, 1226-1236; f) Sander, A. C.; Maji, S.; Franc, L.; Bçhnisch, T.; Dechert, S.; Llobet, A.; Meyer, F. *Chem. Sus. Chem.* **2015**, *8*, 1697 – 1702; g) Matheu, R.; Neudeck, S.; Meyer, F.; Sala, X.; Llobet, A. *ChemSusChem*, **2016**, *9*, 3361 –3369.

(26)   Ghosh, M.; Singh, K. K.; Panda, C.; Weitz, A.; Hendrich, M. P.; Collins, T. J.; Dhar, B. B.; Sen Gupta, S. *J. Am. Chem. Soc*. **2014**, *136*, 9524-9527.

(27)   Ghosh, A.; Ryabov, A. D.; Mayer, S. M.; Horner, D. C.; Prasuhn, D. E.; Sen Gupta, S.; Vuocolo, L.; Culver, C.; Hendrich, M. P.; Rickard, C. E. F.; Norman, R. E.; Horwitz, C. P.; Collins, T. J. *J. Am. Chem. Soc*. **2003**, *125,* 12378.

(28)   Warner, G.; Mills, M.; Enslin, C.; Pattanayak, S.; Panda, C.; Panda, T.; Sen Gupta, S.; Ryabov, A.D.; Collins, T. J. *Chem. Eur. J.* **2015**, *21*, 6226.

(29)   a) Huynh, M. H. V.; Meyer, T. J. *Chem. Rev*. **2007**, *107*, 5004; b) Weinberg, D. R.; J. Gagliardi, J. F. Hull, C. F. Murphy, C.   A. Kent, B. C. Westlake, A. Paul, D. H. Ess, C.; McCafferty, D. G.; Meyer, T. J. *Chem. Rev*. **2012**, *112*, 4016−4093; c) Costentin, C.; Robert, M.; Savéant, J. -M. *Chem. Rev*. **2010**, *110*, 1-40; d) Costentin,   C.; Robert, M.; Savéant, J. -M.; Teillout, A. -L. *Proc. Natl. Acad. Sci. U. S. A*. **2009**, *106*, 11829-11836; e) Rountree, E. S.; McCarthy, B. D.; Eisenhart, T. T.; Dempsey, J. L. *Inorg. Chem*. **2014**, *53*, 9983–10002.

(30)   Singh, K. K.; Tiwari, M. K.; Ghosh, M.; Panda, C.; Weitz, A.; Hendrich, M. P.; Dhar, B. B.; Vanka, K.; Sen Gupta, S. *Inorg. Chem*. **2015**, *54*, 1535−1542.

(31)   Bard, A. J.; Faulkner, L. R. Electrochemical Methods: Fundamentals and Applications; Wiley: New York, **1980.**

(32)   Ellis, W. C.; Tran, C. T.; Roy, R.; Rusten, M.; Fischer, A.; Ryabov, A. D.; Blumberg, B.; Collins, T. J. *J. Am. Chem. Soc*. **2010**, *132*, 9774.

(33)   a) The pK_a for bicarbonate buffering is only accurate at low bicarbonate concentrations due to coupled equilibria for the decomposition of carbonic acid to dissolved CO_2. b) Denu, J. M.; Lohse, D. L.; Vijayalakshmi, J.; Saper, M. A.; Dixon, J. E. *Proc. Natl. Acad. Sc. U. S. A.* **1996**, *93*, 2493-2498.

(34)   Chen, G.; Chen, L.; Ng, S. -M.; Man, W. -L.; Lau, T.-C. *Angew. Chem., Int. Ed*. **2013**, *52*, 1789.

(35)   Najafpour, M. M.; Safdari, R.; Ebrahimi, F.; Rafighi, P.; Bagheri, R. *Dalton Trans*. **2016**, **DOI:** 10.1039/C5DT04467G,

(36)   Codolà, Z.; Garcia-Bosch, I.; Acuña-Parés, F.; Prat, I.; Luis, J. M.; Costas, M.; Lloret-Fillol, J. *Chem. –Eur. J.* **2013**, *19*, 8042-8047.

3B.1 Abstract

Biuret-modified tetraamidomacrocyclic cobalt complex [Co^{III}-bTAML]$^-$ is shown to catalyze electrochemical water oxidation at basic pH leading to formation of O$_2$. Electrochemical and spectroscopic studies indicate a high valent cobalt oxo intermediate isoelectronic to Co^V(O) as the active oxidant. Kinetic isotope effect of 8.63 indicates an atom proton transfer mechanism.

Water Oxidation by a Molecular Cobalt Complex
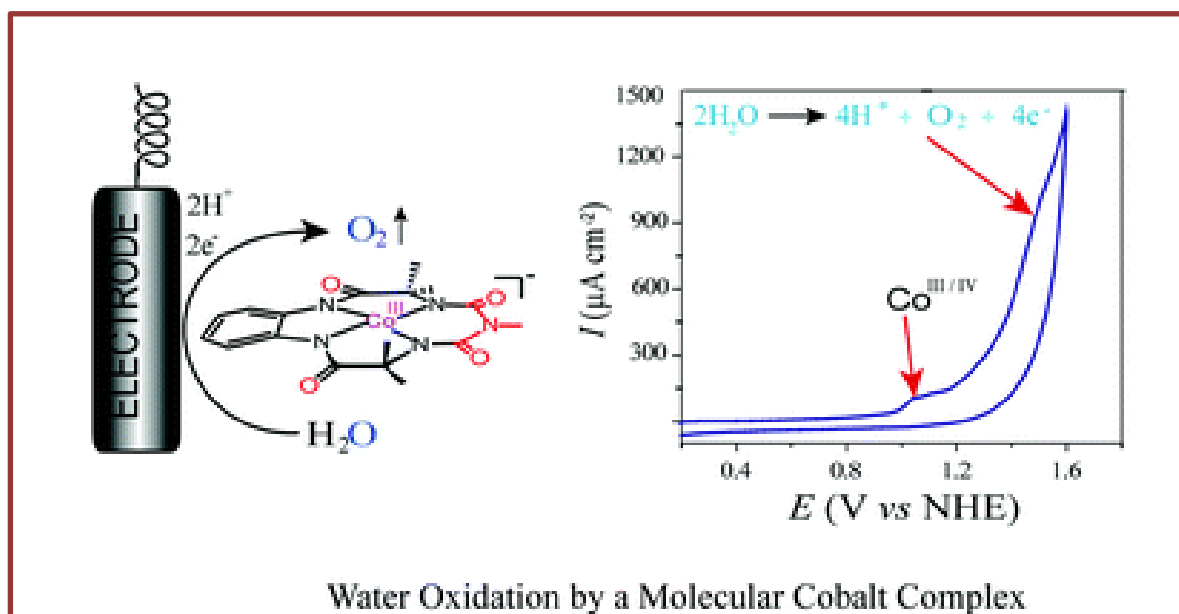
3B.2 Introduction

Practical large scale production of chemical fuels (O$_2$ and H$_2$) by water splitting necessitates the use of homogeneous or heterogeneous catalysts based on earth abundant transition metals.[1–3] Among all first row transition metals, cobalt based systems,[4–6] such as the widely studied heterogeneous cobalt phosphate based catalysts,[7] have shown efficiencies that approach those of Mn based PSII enzymes. However, further design of more efficient cobalt-based water oxidation (WO) catalysts requires a mechanistic understanding of their role in the catalytic cycle, which is very challenging for heterogeneous systems.[8–10] For homogeneous systems, it has been well established that WO is mediated through high-valent metal oxo intermediates in most of the cases[11] and the O–O bond formation step includes the nucleophilic attack of water on the [M=O]$^{n+}$ metal oxo site.[3] Radical coupling of M–O species leading to O–O bond formation[12] has been reported for some Ru based catalysts. A complete understanding of the key O–O bond formation step still remains elusive, especially for complexes of Co, Ni and Cu metals which fall on the right hand side of the ''oxowall''.[13]

The main challenge lies in the spectroscopic identification of the high valent metal–oxo species of these elements, which are ill-defined mostly due to the non-innocent nature of the
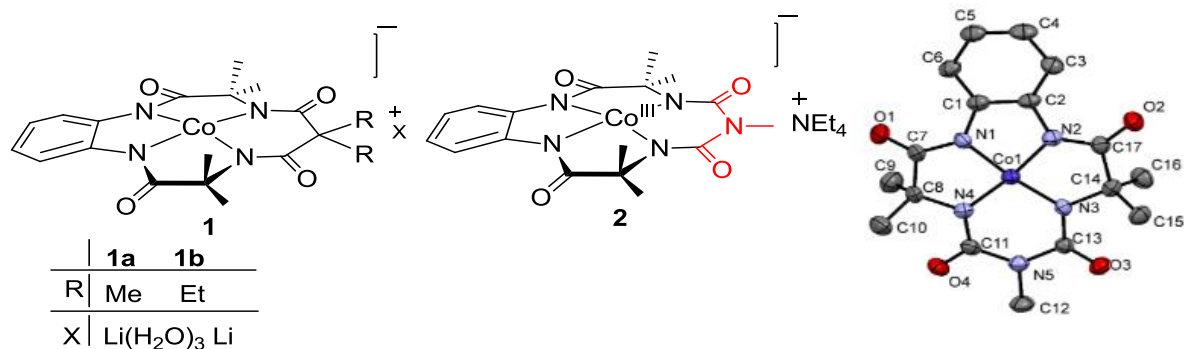
Figure 3B.1 (Left) Pictorial representation of [Co^{III}-TAML]$^-$ (**1**) and (Middle) [Co^{III}-bTAML]$^-$ (**2**) complexes. (Right) Molecular structure of anionic part of complex **2** with thermal ellipsoids at 50% probability level. Hydrogen atom and NEt$_4$ cation are ommited for clarity.

intermediate that can be described as an intermediate between [M$^{(n+1)+}$–O$^·$] and [M$^{(n+2)+}$=O].[14] For cobalt complexes, Berlinguette *et al.* have indicated the involvement of a [Co^{IV}]O]$^{2+}$ species as the key intermediate for the O–O bond formation during electrochemical WO using a mononuclear cobalt(II) pentapyridine complex under slightly basic conditions.[4,15] For single site cobalt(III)hangman corrole an oxo cobalt(IV)corrole radical cation (H$^{+·}$ ^{ßF}CX-CO$_2$HCo^{IV}O)[8] has been identified as the active intermediate by Cramer[16] and Chen[17] based on theoretical calculations. We focussed our attention on the cobalt(III) complex of bTAML (bTAML = biuret-modified tetraamidomacrocyclic) ligands, the first member of the fifth generation of TAML ligands[18] containing a biuret moiety in the ligand framework.[19] The highly electron donating N-donors are known to stabilize high valent metal oxidation states such as the elusive Fe^V=O.[20] We therefore explored if (i) the [Co^{III}-bTAML]$^-$ complex is competent to catalyse WO and (ii) spectroscopic evidence of high-valent oxocobalt species could be determined. A high valent square planar neutral [Co-TAML] complex (formally Co^{IV}) was first reported by Collins and co-workers from **1b** via both electrochemical and chemical oxidation routes (Fig. 1).[21] Recently, high-valent Co^{IV}(O) species has been reported by Ray and Nam.[14,22] In this communication, we report the use of [Co^{III}-bTAML]$^-$ as a catalyst for the base assisted electrochemical WO. We show by using electrochemical and spectroscopic techniques that the key intermediate responsible for O–O bond formation is a high valent cobalt oxo complex which is isoelectronic to Co^V(O).

3B.3 Physical measurements

^{1}H NMR was performed in Bruker 400 and was reported in δ(ppm) *vs* (CH$_3$)$_4$Si with the deuterated solvent (CD$_3$CN) proton residuals as internal standard standards. The number of scans was kept 2000. HRMS (High Resolution Mass Spectroscopy) was done in Thermo Scientific Q-Exactive, using electron spray ionization source, Orbitrap as analyzer, connected with a C18 column (150 mm × 4.6 mm × 8 μm) and Maxis Impact (BRUKER) Sr no.282001.0008 respectively. Dissolved oxygen measurements during water oxidation (WO) were performed using a Clark type electrode (dissolved oxygen meter) from MicroSet (MS 0257), India, working in the range of 0 to 45 ppm with resolution of 0.01 ppm. Dynamic Light Scattering (DLS) analyses were run in Zetasizer Nano series Nano ZS90. For each set, solution pH was measured with a pH meter (LABINDIA, PICO+) with calibrated electrode with accuracy of ±0.2 pH. SEM (Scanning Electron Microscopy) imaging and EDX (Energy Dispersive X-ray spectroscopy) was recorded in a FEI Tecnai TF-20 instrument.

3B.3.1 Details of Dissolved Oxygen measurement during CPE by using a Clark type electrode

In order to measure the evolved oxygen during CPE (controlled potential electrolysis) a Clark type electrode was used. The Clark electrode was previously calibrated before each experiment following a two point calibration 0% (zero solution) and 100% (air). CPE was performed in a four necked electrochemical cell. The electrochemical cell contained 1mM [Co^{III}-bTAML]$^-$ dissolved in 0.1 M pH = 9.2 phosphate buffer. An ITO electrode (1 cm^2) along with Ag/AgCl (satd) as reference and platinum wire as counter electrode was used for electrolysis. The Clark electrode was also fitted in the cell for measuring the dissolved oxygen. A solution of 0.1M pH = 9.2 phosphate buffer was used as supporting electrolyte. Before applying potential, the dissolved O$_2$ was completely removed from the buffer in the electrochemical cell by purging with high purity argon gas under slow stirring. Before applying potential the oxygen sensor displayed 0 ppm oxygen level. With the application of electrolysis potential (1.5V *vs* NHE), oxygen evolution was noted in the Clark electrode due to increase in ppm level of oxygen in the electrochemical cell. CPE was carried out for 3 hours and oxygen evolution was monitored by Clark electrode. The results of the WO catalyzed by [Co^{III}-bTAML]$^-$ were compared with control experiment performed under the same conditions but in the absence of [Co^{III}-bTAML]$^-$. The Faradic efficiency was calculated according to the total charge passed (charge passed for control experiment was subtracted) during CPE and the total amount of evolved oxygen (considering WO as a 4 electron process).

3B.3.2 Sample preparation for SEM and EDX experiment

The surface of a clean ITO slide (five times cleaned with water after sonication) was imaged for SEM and EDX analysis. The same ITO electrode was used during CPE for 3 hrs and then the ITO was rinsed carefully by Milli-pore water and then dried in high vacuum for 10-hrs. The dry surface was visualized under microscopy and the SEM image with its EDX report was compared with the results of clean ITO surface before CPE.

3B.3.3 Details of Electrochemistry

Cyclic voltammetry experiments were carried out on a CHI-660 potentiostat. Glassy Carbon (GC) (3 mm of diameter), Silver/Silver chloride (saturated KCl salt), and Pt wire was used as working electrode, as reference electrode (unless explicitly mentioned) and counter electrode respectively. Before each measurement pre-treatment of the working electrode was done by polishing with 0.05 μm alumina paste, rinsing thereafter with water/acetone and finally blow-drying. Pre-treatment of the ITO electrodes were done by sonication in acetone, ethanol and Milli-Q ultrapure water sequentially for 10 min. All redox potentials in the present work are reported versus NHE by adding 0.19 V to the measured potential. $E_{1/2}$ values for the redox processes studied in this work are estimated from half of the sum of potential at the I_{max} of cathodic and anodic in CV measurements. IR compensation was done for the experiment where the buffer concentration was slowly increased in acetonitrile containing **2**. All other kinds of measurements were done without IR compensation. When acetonitrile was used as organic solvent, 0.1M potassium hexafluorophosphate (KPF6) was added as a supporting electrolyte and Ag/AgNO$_3$ (0.01M) was used as a non-aqueous reference electrode. All redox potentials (*vs* Ag/Ag+) were reported to the values versus NHE by adding 0.5 (unless explicitly mentioned).

3B.3.4 Crystallographic Details

For the single Crystal X-ray diffraction experiment, as synthesized crystals of the respective materials were taken out of the solution and coated with Paratone-N oil. It was then placed in a nylon cryoloop (Hampton research) and then mounted in the diffractometer. The data collection was done at 298 K. The crystals were mounted on a Super Nova Dual source X-ray Diffractometer system (Agilent Technologies) equipped with a CCD area detector and operated at 250 W power (50 kV, 0.8 mA) to generate Mo K$_\alpha$ radiation (λ = 0.71073 Å) and Cu K$_\alpha$ radiation (λ = 1.54178 Å) at 298(2) K. Initial scans of each specimen were performed to obtain preliminary unit cell parameters and to assess the mosaicity (breadth of spots between frames) of the crystal to select the required frame width for data

collection. CrysAlisPro program software was used suite to carry out overlapping φ and ω scans at detector (2θ) settings (2θ = 28). Following data collection, reflections were sampled from all regions of the Ewald sphere to redetermine unit cell parameters for data integration. Following exhaustive review of collected frames, the resolution of the data set was judged. Data were integrated using CrysAlisPro software with a narrow frame algorithm. Data were subsequently corrected for absorption by the program SCALE3 ABSPACK scaling algorithm.

These structures were solved by direct method and refined using the SHELXTL 972 software suite. Atoms were located from iterative examination of difference F-maps following least squares refinements of the earlier models. Final model was refined anisotropically (if the number of data permitted) until full convergence was achieved. Hydrogen atoms were placed in calculated positions (C-H = 0.93 Å) and included as riding atoms with isotropic displacement parameters 1.2-1.5 times Ueq of the attached C atoms. In some cases modeling of electron density within the voids of the frameworks did not lead to identification of recognizable solvent molecules in these structures, probably due to the highly disordered contents of the large pores in the frameworks. Highly porous crystals that contain solvent-filled pores often yield raw data where observed strong (high intensity) scattering becomes limited to ~1.0 Å at best, with higher resolution data present at low intensity. Additionally, diffused scattering from the highly disordered solvent within the void spaces of the framework and from the capillary to mount the crystal contributes to the background and the 'washing out' of the weaker data. Electron density within void spaces has not been assigned to any guest entity but has been modeled as isolated oxygen and/or carbon atoms. The foremost errors in all the models are thought to lie in the assignment of guest electron density. The structure was examined using the *ADSYM* subroutine of PLATON3 to assure that no additional symmetry could be applied to the models. The ellipsoids in ORTEP diagrams are displayed at the 50% probability level unless noted otherwise.

3B.3.5 Materials

All the materials used in this study were purchased from various commercial sources (Sigma Aldrich, Fisher Scientific etc). N, N dichloroformylmethylamine was obtained from ChemCollect, Gmbh. LCMS grade acetonitrile from Fisher was used. High purity Milli-Q water was used in all electrochemical study. All the solvents for synthesis were dried and purified as described elsewhere.4 Indium tin oxide (ITO) electrode (8-10 ohm/sq) was obtained from global nanotech, India.

3B.3.6 Synthesis of (Et₄N)[Co^{III}-bTAML]

Synthesis of the ligand (**L1**) was carried out by following the previously reported methodology for related teraammido macrocyclic ligand.[57] A solution containing compound **L2** (X = H; 50 mg, 0.138 mmol) in 10 ml of dry terahydrofuran was deoxygenated. Then to this solution n-BuLi (0.4 ml of 1.4 M solution in hexane, 0.567 mmol, 4.1 equivalents) was added at 0°C under Argon atmosphere followed by addition of 1.2 equivalents solid anhydrous cobalt(II)chloride under positive argon flow. The reaction was allowed to proceed under Argon at room temperature for overnight after which it was opened to air and stirred for one more hour to yield a dark purple brown precipitate. The precipitate was filtered through a frit funnel and was dissolved in methanol to afford a purple brown solution. The solution (5 ml) containing the complex was then loaded onto a cationic ion-exchange resin (Amberlite-120; strong acid) column that had been pre-saturated with tetraethyl ammonium ion so as to exchange the lithium counter cation. The purple band was eluted with methanol and the solvent was removed under reduced pressure to yield a purple solid**.** Further purification was achieved by column chromatography using basic alumina with dichloromethane: methanol = 99:1 as the eluent. X-ray diffracting quality crystals were obtained by slow vapor diffusion of diethyl ether into the solution of the complex in acetonitrile.
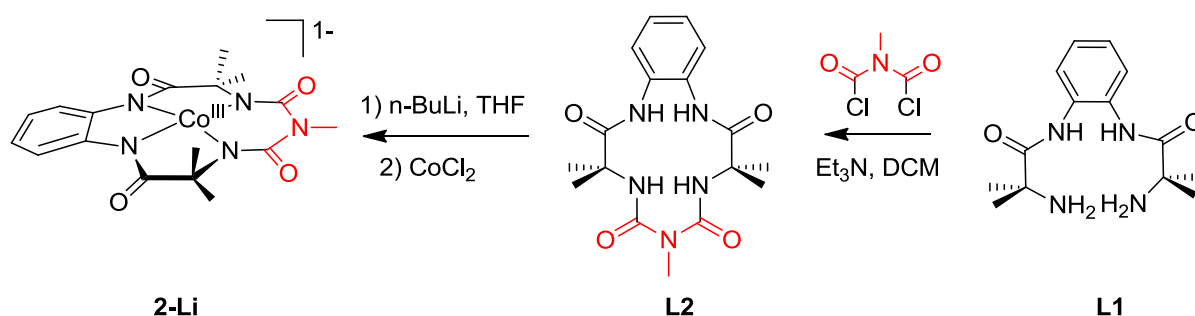
Scheme 3B.1: Synthesis scheme of complex **2-Li.** Complex **2** was obtained as lithium counter cation.

3B.3.7 Synthesis of [oxocobalt(IV)(bTAML)]²⁻

3B.3.7.1 By controlled potential electrolysis in acetonitrile

Complex **2** was dissolved in acetonitrile (0.1M KPF6 used as supporting electrolyte) and bulk electrolysis was performed at -15°C using 9 cm2 ITO electrode as the working electrode, platinum foil as counter electrode and Ag/AgNO3 as reference electrode. Low temperature UV-Vis spectra were recorded to detect the high valent cobalt oxo intermediates.

3B.3.7.2By using chemical oxidant (ceric ammonium nitrate) in acetonitrile and dichloromethane

Complex **2**(0.5mM) was dissolved in acetonitrile and dichloromethane. To it was added 100 µM (4 equivalents) of ceric ammonium nitrate (precooled at -40°C) and the UV-Vis and HRMS was recorded immediately.

3B.3.8 Kinetic Isotope Effect Analysis

The KIE was studied in 0.1M deuterated buffer (pD = 9.2) and protonated buffer (pH = 9.2). The pH of the deuterated buffer was measured by pH meter to be 8.8. To obtain the exact pD value, 0.4 was added to the pH meter reading.6 The shift in the p*K*a of the protonable groups is about the same value, since the protonation level of these groups is almost the same as in H_2O and D_2O respectively, at the same pH meter reading.

3B.3.9 Details of electrochemical Kinetics analysis

Kinetic rate constants for diffusion limited WO were determined from the CV experiments. The catalytic current (i_{cat}) for a second-order reaction is given by eq. 1, where ncat, F, A, [Co], D, kcat are the number of electron transported during catalytic reaction (n = 4 for water oxidation), the Faraday constant, electrode area, catalyst concentration, the diffusion coefficient, second-order rate constant respectively.

$i_{cat} = n_{cat} FA[Co]D^{1/2}k_{cat}^{1/2}[H_2O]^{1/2} = n_{cat} FA[Co]D^{1/2}k_{obs}^{1/2}$ …………………(1)

The second order rate constant k_{cat} is correlated with the first order catalytic rate constant, k_{obs}, by eq. 2 under pseudo first-order conditions.

$k_{obs} = k_{cat}[H_2O]$ ……………… (2)

The current at the anodic peak potential ($E_{p,a}$) is calculated from the Randles-Sevcik equation (eq. 3),where n_{cat}, n, ν, R, T are the number of electron transferred during WO, scan rate of voltammetry, universal gas constant, and temperature respectively. Here n = 1, no of electron transfer per catalyst in redox wave (where catalysis is not involved) and n_{cat} = 4, no of electron required to evolve one molecule of oxygen during WO.

$$i_P = 0.446nFA[Co]\sqrt{\frac{nF\nu D}{RT}} \qquad (3)$$

Dividing eq. 3 by eq. 1 provides eq. 4.

$$\frac{i_{cat}}{i_p} = \frac{n_{cat}\sqrt{RT}k_{obs}^{1/2}}{n^{3/2}0.446\sqrt{F}\nu^{1/2}} = \frac{n_{cat}\sqrt{RT}k_{cat}^{1/2}[H_2O]^{1/2}}{n^{3/2}0.446\sqrt{F}\nu^{1/2}} \qquad ………..(4)$$

Background corrected ratio of i_{cat} and i_p was plotted as a function of the inverse of the square root of scan rate. A linear fit (y = 3.41x) with zero intercept between $i_{cat/}$ i_p and square root of scan rate results a slope (m = 3.41). From this slope rate constants for WO were obtained.

3B. 4 Results and Discussion

The complex $(Et_4N)[(Co^{III}\text{-}bTAML)]$ **2** was synthesized by the addition of anhydrous cobalt(II)chloride onto deprotonated biuret-tetraamidomacrocyclic (bTAML) ligand **L1** (Scheme 3B.1). The molecular structure of **2** was determined by X-ray crystallography (Figure 3B.1) which displayed a square planar geometry. The ^{1}H-NMR spectrum of the complex **2** showed paramagnetically shifted signals of ligand indicating the paramagnetic nature of this complex (Appendix C1). The UV-Vis spectra of complex **2** display two bands at 485 and 618 nm which can be assigned to ligand to metal charge transfer transitions. The CV responses of **2** (0.5 mM) at room temperature in acetonitrile containing 0.1 M potassium hexafluoro phosphate (KPF_6) as supporting electrolyte exhibit two redox waves (Figure 3B.2).
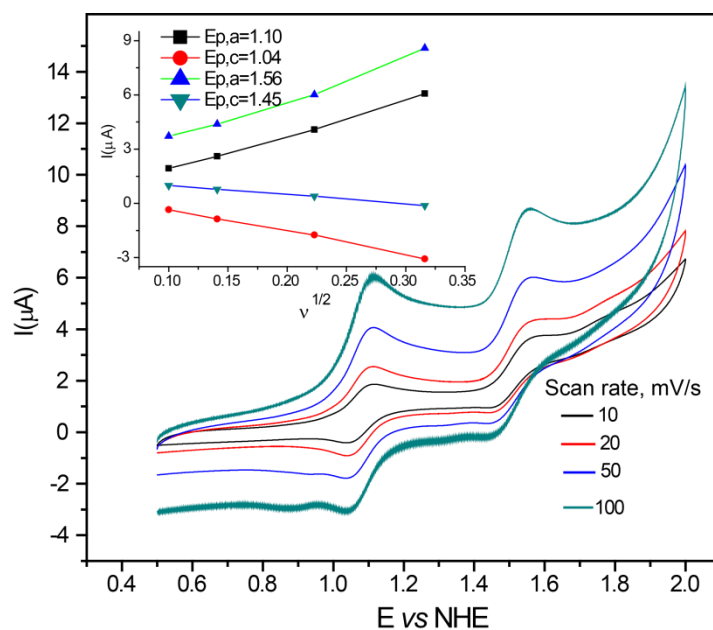
Figure 3B.2: CVs of 0.5 mM **2** in acetonitrile (0.1 M potassium hexafluoro phosphate as the supporting electrolyte) at room temperature with varying scan rates. Inset shows $I_{p,a}$ and $I_{p,c}$ for two redox couple at different scan rates *vs* the square root of scan rate.
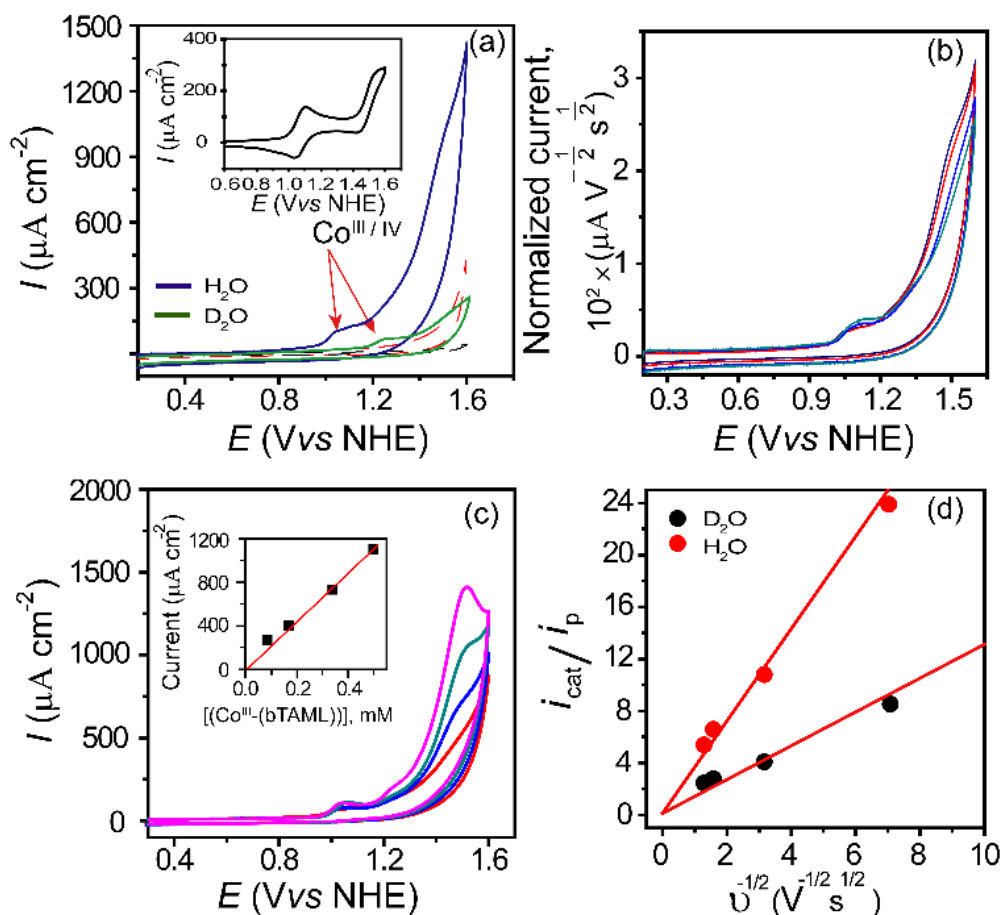
Figure 3B.3 (a) CVs of 0.25mM **2** in 0.1M phosphate buffer at pH = 9.2 (blue) and in pD = 9.2 0.1M duetarated phoshate buffer (green) (scan rate 100 mV s^{-1}). The red and black dotted line represents the CV in 0.1M phosphate buffer and 0.1M duetarated phoshate buffer respectively in absence of the catalyst. (b) Normalized CVs of 0.25 mM complex in 0.1 M phosphate buffer (pH = 9.2) at scan rates 600 mV/s (green), 400 mV/s (blue), 100 mV/s (red) and 80 mV/s (black) (c) CVs of different catalyst concentrations (0.084mM (red), 0.168 mM (blue), 0.34 mM (green), 0.5 mM (pink)) of **2** in 0.1M phosphate buffer at pH = 9.2. Inset shows variation of catalytic current with catalyst concentration. Black circles represent catalytic current and the red line represents the best fit line (y = 221x, R^2 = 0.99) (d) A background corrected plot of i_{cat}/i_p *vs* v$^{-1/2}$ has been represented for electrocatalytic WO by 2 in 0.1M phosphate buffer at pH = 9.2 (red circle) and 0.1M duetarated phoshate buffer at pD = 9.2 (black circle). The red line represent the linear fit (y = 3.41x R^2 = 0.99 for water and y = 1.16x R^2 = 0.98 for D$_2$O) that was used for kinetic rate constant determination.

The first reversible (Figure 3B.2) and 1e$^-$ oxidation (ΔE_p = 67 mV) wave at $E_{1/2}$ = 1.09 V *vs* NHE is attributed to the oxidation of Co^{3+} to Co^{4+}. A similar reversible 1e$^-$ oxidation wave for complex **1a** (Figure 3B.1) has been previously reported.[14] On further scanning towards

more positive potential, a second reversible couple (Figure 3B.3 a inset & Figure 3B.2) with $1e^-$ transfer wave at $E_{1/2} = 1.5$ V *vs* NHE was observed.
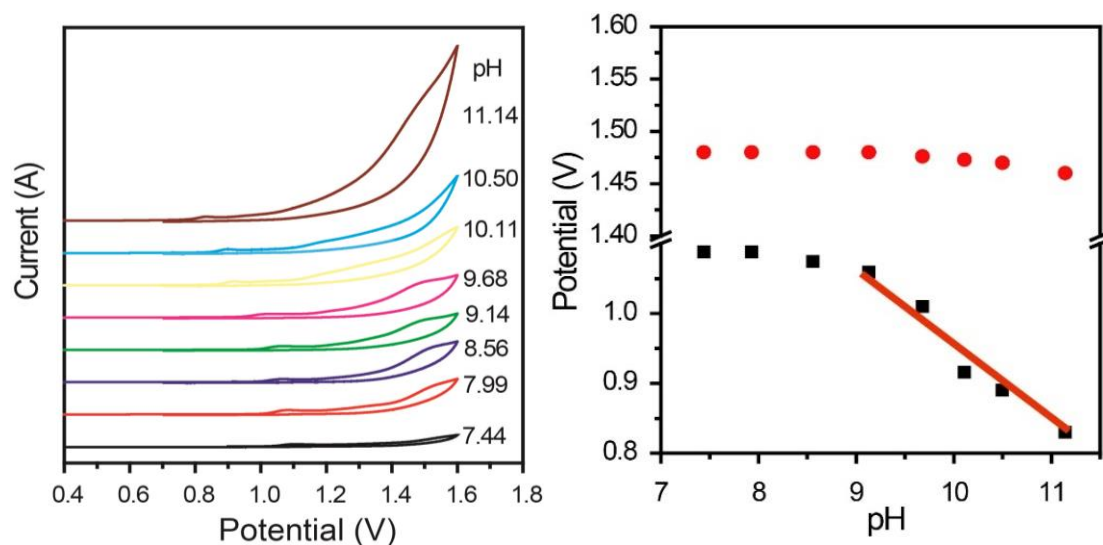
Figure 3B.4: CVs of 0.5 mM $(EtN_4)[Co^{III}(b\text{-}TAML)]$ (**2**) at 100mV/s scan rate in 0.1M phosphate buffer at different pH (left). Plots of first (black circles) and second (red circles) anodic peak potential *vs* different pH. The red line indicates linear fit from pH 9 to pH 11with a slope of 118mV (right).

The CV of **2** in aqueous solution (pH 7.4, 0.1 M phosphate buffer) displayed features which were different from the one observed in acetonitrile (Figure 3B.4). A first irreversible wave was observed at $E_{p,a} = 1.1$ V *vs* NHE and a second one at 1.5 V *vs* NHE which had an enhanced current above background indicating a catalytic process (Figure 3B.3 a, Figure 3B.4). In order to assign the redox couple associated with both the waves, pH dependence of peak potential was examined in aqueous solution. On varying the pH from 7 to 11, $E_{p,a}$ *vs* pH plot for the first electrochemical wave at $E_{p,a} = 1.1$ V showed an intial linear region from pH 7 to 9 followed by a decrease having a slope of 118 mV per pH unit (Figure 3B.4). A decrease of 118 mV peak potential per pH change between pH 9 and 11 reflect either a step wise or concerted two proton and one elctron transfer process associated with the $Co^{IV}(O)/Co^{III}$ redox couple as has been shown in equation (III).

In contrast, the irreversible peak at 1.5 V (Figure 3B.3 a) related to the catalytic process was found to be nearly pH independent over the complete pH range. This redox event can be assigned to the $[Co^{IV}(O)(bTAML)]^{2-}/[Co(O)(bTAML)]^{1-}$ couple indicating formation of a high valent cobalt oxo species isoelectronic to $Co^V(O)$ (Equation (IV)). To have a better understanding of the redox processes, the CV of **2**

was measured in 0.1 M phosphate buffer in both H_2O and D_2O (pH and pD of 9.2). In pH = 9.2 phosphate buffer CV responses of **2** (0.25 mM) displayed two irreversible oxidation waves first at $E_{p,a}$ = 1.1 V and second at $E_{p,a}$ = 1.5 V with an enhanced current above background indicating a catalytic process (Figure 3B.3 a, Figure 3B.4). At 0.1 M duetarated phosphate buffer of pD = 9.2, the first irreversible wave was shifted by 0.2V while the second wave remained constant. This indicates that the first irreversible wave is associated with a concerted proton-electron transfer (CPET)[23] process ($Co^{IV}(O)/Co^{III}$ redox couple) while the second wave is likely an pH independent electron transfer process.

$$[(bTAML)Co^{III}]^- + H_2O \xrightarrow{-2H^+, -e^-} [(bTAML)Co^{IV}(O)]^{2-} \qquad (III)$$

$$[(bTAML)Co^{IV}(O)]^{2-} \xrightarrow{-e^-} [(bTAML)Co^V(O)]^- \text{ or } [(bTAML^{\bullet+})Co^{IV}(O)]^- \qquad (IV)$$
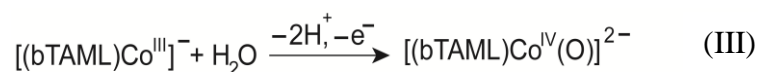
To find out if the irreversible oxidation wave at 1.5 V *vs* NHE is responsible for electrochemical WO, controlled potential electrolysis (CPE) experiment was carried out. CPE was carried out with 1 mM of **2** in 0.1 M phosphate buffer (pH = 9.2) at 1.5 V *vs* NHE for three hours using 1cm^2 Indium Tin Oxide (ITO) electrode as the working electrode to generate O_2 which was subsequently detected and quantified using a Clark type oxygen sensor electrode. As a control, the same CPE experiment was carried out with 0.1 M phosphate buffer (pH = 9.2) in the absence of **2**. During three hours of CPE, total 0.6 C charges was passed through the solution to yield 1.55 μmol of dissolved oxygen (Appendix C2). Control experiments in absence of catalyst show production of 0.5 μmol oxygen due to 0.2 C charges. Based on the 4e$^-$ process, the Faradaic efficiency was thus calculated to be 62%. We performed a number of controls to negate the possible formation of heterogeneous metal oxide films during CPE. The robustness of the molecular catalyst was strongly supported by the identical UV-Vis spectra (characteristic absorbance at 485nm and 618nm) before and after CPE (Appendix C3).

To verify the homogeneous nature of the catalyst consecutive scan cycles were carried out with the glassy carbon (GC) electrode when the current was found to decrease steadily and stabilize after twenty consecutive scan cycles (Figure 3B.5). This is in contrast to heterogeneous systems[24] where the catalytic current increases constantly on repeated scanning. Moreover, the GC electrode was taken out from the solution and washed carefully with only deionized water. On using washed GC
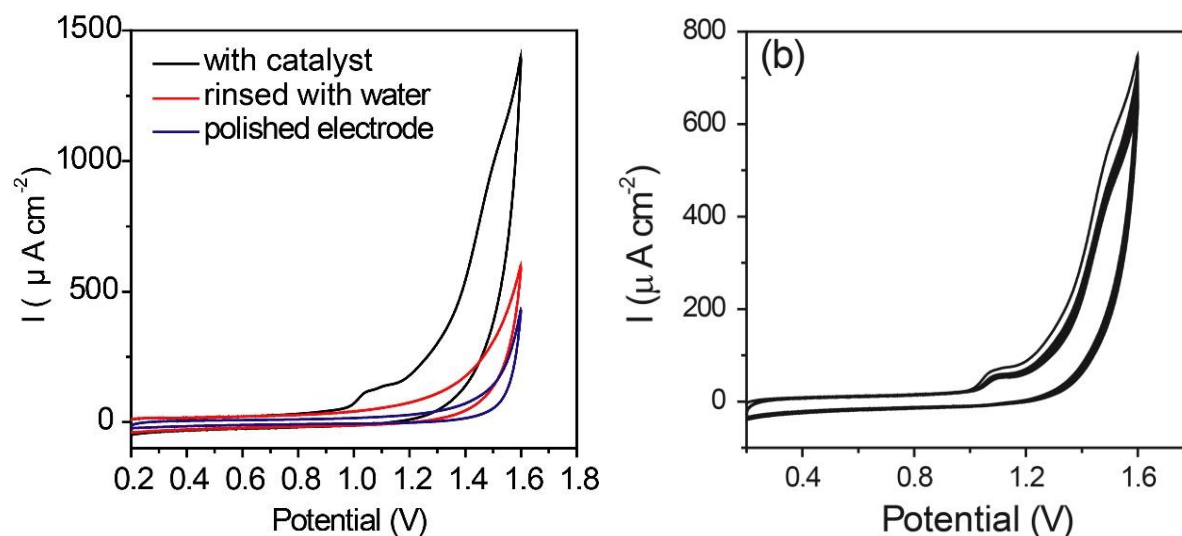
Figure 3B.5: CVs (left, scan rate 100mV/s) were compared with the one recorded in the 0.1M phosphate buffer (pH 9.2) without catalyst containing electrolyte with a polished glassy carbon electrode. The glassy carbon electrode was cycled forty times in 0.25 mM complex **2** at pH 9.2. It was gently rinsed off with deionised water, but was not polished, and then cycled in 0.1M phosphate buffer (pH = 9.2) without catalyst. Twenty continuous cycles in 0.1M phosphate buffer (pH = 9.2) at 100mV/s scan rate (right).

electrode (unpolished) in 0.1 M phosphate buffer no catalytic current was obtained which indicates the molecular nature of **2** during WO (Figure 3B.5).[25,26] Thus, these experiments support that the homogeneous nature of **2** is retained in course of WO. Scanning electron microscopy (SEM) and Energy dispersive X-ray spectroscopy (EDX) of the working electrode before and after three hours of CPE were examined (Appendix C4 and C5). The inspection revealed identical surface morphology and composition of the ITO electrode ruling out the possibility of any heterogeneous cobalt oxide nanoparticles on the working electrode. In addition, examination of the aqueous solution after CPE by dynamic light scattering negate the formation of any cobalt oxide (CoO_x) based nanoparticles. (Appendix C6)

CV responses of **2** was analyzed at different scan rates (v) to understand the reactions involved in the catalytic process and determine the rate constants involved during O—O bond formation. The plot of normalized current [$I/(v)^{1/2}$] at 1.5 V *vs* potential display decrease in current with increasing scan rate indicated WO and the likelihood of O-O bond formation[9] (Figure 3B.3 b). The catalytic current was found to be linearly dependent on the concentration of the catalyst (Figure 3B.3 c) indicating **2**

to be a molecular catalyst with single site nature.[9] The rate constant k_{obs} (k_{obs} = $k_{cat}[H_2O]$) for O_2 formation was determined using the equation i_{cat}/i_p = $2.24n(RTk_{obs}/Fv)^{1/2}$ where i_{cat} was determined from the current peak corresponding to $[Co(O)bTAML]^-/[Co(O)bTAML]^{2-}$ couple at 1.5 V, i_p was estimated from the current at peak potential (E_p) for the $[Co^{IV}(O)bTAML]^{2-}/[(Co^{III}\text{-}bTAML)]^-$ wave, n = 4 (n is number of electrons for WO) and v represents scan rate (see experimental section). The first-order rate constant (k_{obs} = 5.68 s^{-1}) was determined from the slope of the linear fit of i_{cat}/i_p vs $v^{-1/2}$. To validate the involvement of atom proton transfer (APT)[27] mechanism during WO, CV of **2** was performed in deuterated (D$_2$O) phosphate buffer (pD = 9.2). A decrease in catalytic current in deuterated (D$_2$O) phosphate buffer (pD = 9.2) compared to phosphate buffer (pH = 9.2) indicates the role of proton transfer in the mechanism of WO by **2** (Figure 3B.3 a). H/D kinetic isotope effect (KIE) of 8.63 determined from $k_{obs\text{-}H2O}/k_{obs\text{-}D2O}$ indicates operation of the APT mechanism during WO (Figure 3B.3 d). Attempts were then made to obtain further insights into the intermediates involved in the catalytic cycle of WO. We first directed our efforts towards the spectroscopic characterization of the species generated during CV experiments after 1e$^-$ and 2e$^-$ oxidation of the parent [Co^{III}-bTAML]. All our attempts to identify the nature of 1e$^-$ oxidized species in phosphate buffer (pH = 9.2, 0.1 M) by controlled potential electrolysis (CPE) of complex **2** at 1.2 V was unsuccessful probably due to instability of this cobalt(IV) complex in aqueous medium. We therefore decided to change the solvent to acetonitrile, a solvent known to be compatible with cobalt(IV) complexes reported earlier.[14] Although the nature of the exact species (such as axial ligands etc.) might vary in both the solvents, identification of the nature of the high-valent cobalt-complex in acetonitrile can be used to improve our understanding about the key features of the catalytic cycle in water. In fact, the different CV responses in aqueous and non-aqueous solution can be correlated by recording CV reponses of **2** in acetonitrile with gradual addition of increasing amounts of phosphate buffer (10 μl; 0.1M pH = 9.2)**.** It was observed that with increasing amounts of phosphate buffer the peak at 0.59 V *vs* Ag/AgNO$_3$ for Co^{3+}/Co^{4+} shifted towards more positive potential and at a 1.75% buffer concentration the peak approached 1 V *vs* NHE which was the $E_{1/2}$ observed for **2** in pure pH = 9.2 phosphate buffer (Appendix C7). The second redox couple at 1.5V *vs* NHE in acetonitrile remained unchanged upon addition of pH = 9.2 phosphate buffer

(Appendix C7, left). CPE of **2** at 1.2 V *vs* NHE in acetonitrile at -15^{0}C displayed a change in color of the solution from purple to blue close to the surface of working electrode (ITO).
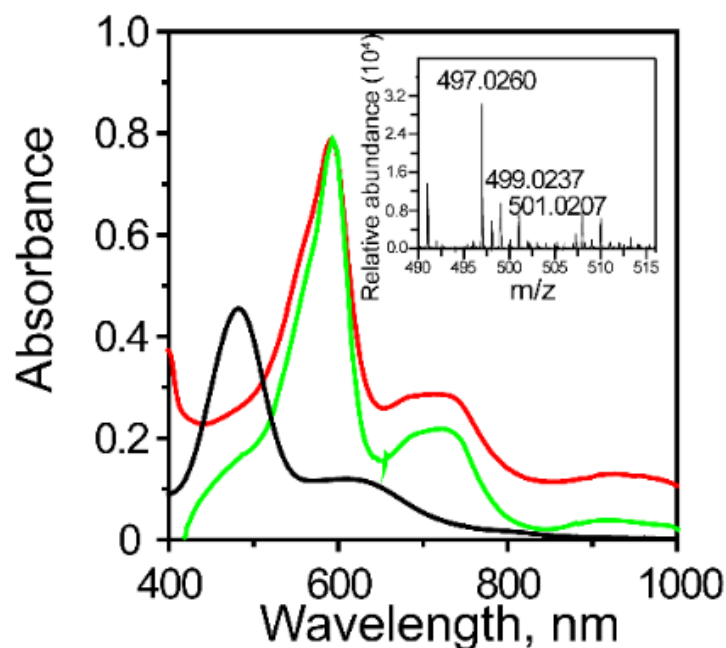
Figure 3B.6: Absorption spectra of: (i) 0.1 mM complex **2** (black), (ii) [Co(O)bTAML]2- synthesized chemically by addition of ceric ammonium nitrate to **2** (green) and (iii) , [Co(O)bTAML]$^{2-}$ synthesized electrochemically by CPE at 1.2 V *vs* NHE (red). Inset shows HRMS of [(Zn)Co(O)bTAML]-[H]$^+$

UV-Vis spectral scan during CPE exhibited appearance of two new peaks at 600 and 740 nm (shoulder peak) along with the parent cobalt(III) peak at 485 nm through a isosbestic point at 510 nm (Appendix C8). When this spectrum was deconvoluted the bands at 600 nm and 740 nm was clearly observed (Appendix C9). The deconvulated spectrum of this new species was very similar to the high-valent Co^{IV}(O) species that was reported by Roy and Nam.[14] Also, conversion of **2** to one electron oxidized species through isosbestic point indicates the associated equilibrium with this process (Figure 3B.6). When the oxidized blue species was taken out from the electrochemical cell, it immediately converted back to its more stable form **2** in absence of oxidation potential. It has been previously demonstrated that the binding of Lewis acid metal ions (M^{n+} = Sc^{3+}, Y^{3+} Ce^{3+}, Zn^{2+}) to the cobalt oxo core shifted the redox tautomerisation equilibrium towards more stable [Co^{IV}(O)(M^{n+})(TAML)] from

$[Co^{III}(O^{\bullet})(TAML)]^{2-}$. To maximize the stability of more stable redox tautomer, CPE of **2** in acetonitrile was performed in presence of Lewis acid. In presence of zinc chloride ($ZnCl_2$) at -15^0C, **2** (0.1mM) converted completely to the blue color species with peaks at 600 nm and 740 nm (Figure 3B.6). Although the UV-Vis spectrum of this high-valent cobalt-oxo was identical in presence and absence of Lewis acid, its stability in presence of Lewis acid was significantly enhanced. An attempt to perform High Resolution Mass Spectrometry (HRMS) of this electrochemically generated species was unsuccessful probably due to interfering electrolytes. Interestingly, the same blue colored species having peaks at 600 nm and 740 nm in the UV-Vis could be generated by addition of the one electron oxidizing agent (ceric ammonium nitrate) to **2** at -40^oC in both dichloromethane and acetonitrile in presence of Lewis acid $ZnCl_2$ ((Appendix C10). This chemically synthesized blue species in dichloromethane in presence of Lewis acid $ZnCl_2$ revealed one high resolution ion peak at mass to charge (*m/z*) ratio of 497.026 in HRMS whose mass and isotope distribution patterns correspond to $[Co^{IV}(O)(Zn)(bTAML)(H^+)]$ (Figure 3B.6 inset, Appendix C11). Thus this blue colored complex formed after $1e^-$ oxidation in acetonitrile can be assigned as $[Co^{IV}(O)(Zn)bTAML]$ and the first redox process at 1.09 V *vs* NHE can be assigned to $[Co^{IV}(O)(bTAML)]^{2-}/[Co^{III}(bTAML)]^{1-}$ couple. Interestingly, this $Co^{IV}(O)/Co^{III}$ couple found in acetonitrile is also observed in aqueous phosphate buffer from pH dependent CV experiments. Although, we were unable to trap the $2e^-$ oxidized species, CV experiments in water indicate formation of a species which is isoelectronic to $Co^V(O)$.

We propose that during electrochemical WO at pH = 9.2, an $1e^-$ oxidation of the $[Co^{III}\text{-bTAML}]^-$ with the loss of two protons affords $[Co^{IV}(O)bTAML]^{2-}$. Further oxidation generates $[Co(O)bTAML]^-$, which is isoelectronic to $Co^V(O)$ and stores two oxidation equivalents above cobalt(III). Due to the non-innocent nature of the bTAML ligand, we are unable to comment on the exact oxidation state of cobalt. We believe that it can be either $Co^V(O)$ or a $Co^{IV}(O)bTAML$ radical cation, similar to what has been proposed for porphyrins or corroles.

Scheme 3B.2: Atom proton transfer (APT) mechanism during O-O bond formation. B represents the base anion.

This 2e⁻ oxidized species is likely the key intermediate responsible for O—O formation in the catalytic cycle during WO and is responsible for WO. Positive KIE values points out to a APT mechanism (Scheme 3B.2) involving base assisted nucleophilic addition of H_2O to $[Co(O)bTAML]^-$ to form the O–O bond. The formation of a highly unstable cobalt-hydroperoxo or peroxo species upon the attack of H_2O to oxocobalt is subsequently oxidized to produce O_2 resulting in a catalytic current. A large number of theoretical studies have also invoked a similar mechanism of O-O bond formation.[17]

3B.5 Summary and Conclusions

In summary, we report the synthesis of **2** which is capable of catalyzing electrochemical WO at pH = 9.2. The O—O bond formation step occurs due to the attack of H_2O to a high valent intermediate (probably a $[Co(O)bTAML]^-$. The O—O bond formation step is assisted by the presence of a base. We believe our study provides mechanistic insights which would help develop more active cobalt-based molecular electrocatalysts for WO.

3B.6 References

(1) Kärkäs, M. D.; Johnston, E. V.; Verho O.; Åkermark, B. *Acc.Chem. Res.* **2014**, *47*, 100–111.

(2) Kärkäs M. D.; Åkermark, B. *Dalton Trans.* **2016**, DOI: 10.1039/c6dt00809g

(3) Blakemore, J. D.; Crabtree, R. H.; Brudvig, G. W. *Chem. Rev.* **2015**, *115*, 12974−13005.

(4) Wasylenko, D. J.; Ganesamoorthy, C.; Borau-Garcia, J.; Berlinguette, C. P. *Chem. Commun.* **2011**, *47*, 4249–4251.

(5) Wasylenko, D. J.; Palmer, R. D.; Schott, E.; Berlinguette, C. P. *Chem. Commun.* **2012**, *48*, 2107–2109.

(6) a) Chen, B. -T.; Morlanés, N.; Adogla, E.; Takanabe, K.; Rodionov, V. O. *ACS Catal.* **2016**, *6*, 4647–4652; b) Lei, H.; Han, A.; Li, F.; Zhang, M.; Han, Y.; Du, P.; Lai, W.; Cao, R. *Phys. Chem. Chem. Phys.* **2014**, *16*, 1883—1893.

(7) a) Surendranath, Y.; Kanan, M. W.; Nocera, D. G. *J. Am. Chem. Soc.* **2010**, *132*, 16501–16509; b) Costentin, C.; Porter, T. R.; Savéant, J. -M. *J. Am. Chem. Soc.* **2016**, *138*, 5615–5622.

(8) Dogutan, D. K.; McGuire, R.; Nocera, D. G. *J. Am. Chem. Soc.* **2011**, *133*, 9178–9180.

(9) Wang, D.; Groves, J. T. *Proc. Natl. Acad. Sci. USA* **2013**, *110,* 15581–15584.

(10) Nguyen, A. I.; Ziegler, M. S.; Oña-Burgos, P.; Sturzbecher-Hohne, M.; Kim, W.; Bellone, D. E.; Tilley, T. D. *J. Am. Chem. Soc.* **2015**, *137,* 12865−12872.

(11) McEvoy, J. P.; Brudvig, G. W. *Chem. Rev.* **2006**, *106*, 4455–4483.

(12) Duan, L.; Bozoglian, F.; Mandal, S.; Stewart, B.; Privalov, T.; Llobet, A.; Sun, L. *Nat. Chem.* **2012**, *4*, 418–423.

(13) Winkler, J. R.; Gray, H. B. *Molecular Electronic Structures of Transition Metal Complexes I*, D. M. P Mingos,. P. Day, J. P. Dahl, Springer: New York, **2012**.

(14) Hong, S.; Pfaff, F. F.; Kwon, E.; Wang, Y.; Seo, M. –S.; Bill, E.; Ray, K.; Nam, W. *Angew. Chem. Int. Ed.* **2014**, *53*, 10403–10407.

(15) Crandell, D. W.; Ghosh, S.; P.Berlinguette, C.; Baik, M. -H. *Chem Sus Chem.* **2015**, *8*, 844–852.

(16) Ertem, M. Z.; Cramer, C. J. *Dalton Trans*. **2012**, *41*, 12213–12219.

(17) Lai, W.; Cao, R.; Dong, G.; Shaik, S.; Yao, J.; Chen, H. *J. Phys. Chem. Lett.* **2012**, *3*, 2315−2319.

(18) Collins, T. J. *Acc. Chem. Res.* **1994**, *27*, 279−285.

(19) Panda, C.; Ghosh, M.; Panda, T.; Banerjee. R.; Sen Gupta, S. *Chem. Commun*. **2011**, *47*, 8016–8018.

(20) Panda, C.; Debgupta, J.; DíazDíaz, D.; Singh, K. K.; Sen Gupta, S.; Dhar, B. B. *J. Am. Chem. Soc.* **2014**, *136*, 12273–12282.

(21) Collins, T. J.; Powell, R. D.; Slebodnick, C.; Uffelman, E. S. *J. Am. Chem. Soc*. **1991***, 113,* 8419-8425.

(22) Pfaff, F. F.; Kundu, S.; Risch, M.; Pandian, S.; Heims, F.; Pryjomska-Ray, I.; Haack, P.; Metzinger, R.; Bill, E.; Dau, H.; Comba, P.; Ray, K. *Angew. Chem. Int. Ed.* **2014**, *50*, 1711–1715.

(23) a) Costentin, C.; Robert, M.; Savéant, J. -M. *Phys. Chem. Chem. Phys.* **2010**, *12*, 11179–11190; b) Wasylenko, D. J.; Tatlock, H. M.; Bhandari, L. S.; Gardinier, J. R.; Berlinguette, C. P. *Chem. Sci.* **2013**, *4*, 734–738.

(24) a) Singh, A.; Chang, S. L. Y.; Hocking, R. K.; Bach, U.; Spiccia, L. *Catal. Sci. Technol.* **2013**, *3*, 1725–1732; b) Singh, A.; Chang, S. L. Y.; Hocking, R. K.; Bach, U.; Spiccia, L. *Energy Environ. Sci.* **2013**, *6*, 579–586; c) Dincǎ, M.; Surendranath, Y;. Nocera, D. G. *Proc. Natl. Acad. Sci. USA* **2010**, *107*, 10337–10341.

(25) Zhang, M.; Zhang, M. -T.; Hou, C.; Ke, Z. -F.; Lu, T. -B. *Angew. Chem. Int. Ed.* **2014**, *53*, 13042–13048.

(26) Barnett, S. M.; Goldberg, K. I., Mayer, J. M. *Nat. Chem.* **2012**, *4*,498–502.

(27) Chen , Z.; Concepcion, J. J.; Hu , X.; Yang, W.; Hoertz, P. G.; Meyer, T. J. *Proc. Natl. Acad. Sci. USA* **2010**, *107*, 7225–7229.

Chapter IV

Intriguing reactivity of Oxoiron(V) Complexes: Electronic Effects on the Oxygenation Reactions

4.1 Abstract

High-valent iron(IV)-oxo porphyrin species have been implicated as key intermediates in the catalytic cycles of heme iron enzymes, such as cytochromes P450, peroxidases, and catalases. In these enzymes, proximal axial ligands are thought to play an important role in tuning the reactivities of iron(IV)-oxo porphyrin p-cation radicals, referred to as compound I (Cpd I). To understand the effect of axial ligand on several model complexes have been synthesized and changes in their reactivity were explored using experimental and theoretical analysis. However consequences of equatorial electronics on the oxygenation reaction by heme and non-heme high valent oxoiron complexes have not been reviewed in details probably due to the importance of a trans ligand on an Fe=O center in tuning the oxidative reactivity of various heme enzymes. Till date, there is no report reflecting the electronic effect on the HAT (Hydrogen atom transfer) and OAT (oxygen atom transfer) reaction by oxoiron(V) complex. In this chapter, we have synthesized a wide variety of oxoiron(III)bTAML complexes (**1b**-**1f**) having varying electron donating and withdrawing groups on the benzene ring of the head part of the complex. These complexes have been characterised by single crystal X-ray diffraction, HR-Ms, UV-Vis, electrochemistry and EPR spectroscopy. Then a series of oxoiron(V) complex (**2b**-**2f**) were synthesized by using the equimolar amount of aqueous sodium hypochlorite solution in acetonitrile at room temperature. All the oxoiron(V) species have been characterised by HR-Ms, UV-Vis, electrochemistry and EPR spectroscopy. The corresponding one electron reduced species ($Fe^{IV}O$) of **2a**-**2f** also have been synthesized at higher pH to calculate the pK_a values of $Fe^{IV}(O\text{-}H)$ species. The iron(V)oxo complexes, containing an equatorial electron donating and withdrawing group have been used to understand the electronic effect on HAT and OAT reactions. The HAT rate for toluene increases linearly with increasing the redox potential of iron(V) oxo species. On the other hand, the elevated pK_a of one electron reduced $Fe^{IV}(O\text{-}H)$ species is found to be responsible for the enhancement of HAT rate by electron rich oxoiron(V) species in line with the natural heme enzyme. The OAT rate enhancement for electron deficient oxoiron(V) is solely responsible for the increase in redox potential of the electron deficient metal oxo species. However, the increase in OAT rate for the electron rich oxoiron(V) species is a counterintuitive reactivity trend for an species which is considered to be essentially electrophilic.

4.2 Introduction

The selective transformation of the inert C−H bond to functional groups has far-reaching practical implications and it has been studied for over several years.[1-7] High-valent oxoiron(IV) and oxo iron(V) species have been implicated as the key intermediates in the catalytic cycles of heme and nonheme oxygen activating iron enzymes that selectively functionalize aliphatic C−H bonds.[8-9] Significant progress in the understanding of the electronic and spectroscopic properties of these compounds, and how they react with C−H bonds in these enzymatic reactions has been done via both experimental and theoretical investigations.[10-12] Several synthetic heme and nonheme high valent oxoiron(IV) intermediates has been synthesized to understand the intricate structural and spectroscopic properties of numerous iron-containing enzymes.[13] For both heme and nonheme oxoiron(IV) complexes effect of spin state, electronics, and sterics on the reactivity has been investigated in detail by analysing both the spectroscopic and theoretical results.[10-12] The dramatic enhancement in hydrogen atom transfer (HAT) rate by electron donating axially ligated oxoiron(IV) complexes has been explained on the basis of two-state-reactivity (TSR).[14] According to TSR, the axial ligand helps to reduce the energy gap between the less reactive $S = 1$ and more reactive $S = 2$ spin states which is reflected in higher HAT reactivity. However consequences of equatorial electronics on the oxygenation reaction by heme and nonheme high valent oxoiron complexes have not been reviewed in detail probably due to the importance of a trans ligand on an Fe=O center in tuning the oxidative reactivity of various heme enzymes. For non heme oxoiron(IV) complex contrasting effect of equatorial vs axial ligand in HAT reaction revealed that the equatorial ligand has minor effect on the reactivity. Further, the effects of equatorial electronics on the oxoiron(IV) complexes generated from hypothetical model complexes (e.g $[Fe^{IV}(O)(CN)_5]^{3-}$, $[Fe^{IV}(O)(NC)_5]^{3-}$, and $[Fe^{IV}(O)(F)_5]^{3-}$) for HAT reaction were explained by a new hybrid pathway (the Fe−O−H arrangement in this hybrid pathway is bent in sharp contrast to the collinear character as observed for the classical quintet σ-pathways before) that mixes features of the classical σ- and π-pathways in quintet surfaces.[15] For compound I (oxoiron(IV)porphyrin radical cation) complexes equatorial electron donating and electron withdrawing substitutions at meso position of porphyrin ligand can alter the reaction rate of higher oxidised heme complexes. Earlier studies on equatorial substitutions (fluoro benzene) at meso position of porphyrin ligand framework indicated that the σ-electron donation substituents increases the reactivity of cpd

I.[16a] Recently, para- or meta trialkyl ammonium functional group substituted phenyl moiety at the meso position of porphyrin ligand significantly enhances the HAT reaction rates by cpd I.[16b] However there is no report till date reflecting the electronic effect on the HAT and OAT (oxygen atom transfer) reaction by oxoiron(V) complex. Recently, a fully characterised nonheme [(bTAML)Fe^V-O]$^-$ (bTAML reperesent biuret modified tetraamido macrocyclic ligand) complex that is moderately stable at room temperature was shown to have great promise for the selective activation of strong C-H bond during organic transformation.[17] Previous DFT calculations suggests that the electronics of Fe=O bond can be manipulated by either an axial or equatorial substituent which will affect the energy of LUMO molecular orbital.[18] Therefore, we assumed that the electron donating and withdrawing substituent on TAML ligand frame work will affect the redox potential of metal centre and pK_a of the Fe=O moiety by altering the electronic structure of oxoiron complexes which will also reflect in their subsequent reactivity towards HAT and OAT. An highly electron rich oxoiron(V) complex increases the pK_a of its one electron reduced species (oxoiron(IV)) to >12 which is very close to that of CytP450 enzyme. Therefore, an electron rich high valent oxoiron(V) will have a lower reduction potential and higher pK_a of one electron reduced species which will help discriminate between a productive C-H oxidation over non-productive proton coupled electron transfer process, although the latter is more energetically favoured than the former process. Interestingly for an electron deficient oxoiron(V), the expected non-productive oxidation over productive oxidation due to its high reduction potential has not been observed in recent report. Therefore, it will be highly important to understand how electron donating and withdrawing substituent can alter the reactivity by manipulating the electronic structure which will help us to design complexes for complex organic transformations.

In this chapter we showed the effect of electron donating as well as electron withdrawing substituent on the HAT and OAT reaction by oxoiron(IV) complexes. Effect of electronic substitution on the electronic structure and the reactivity pattern towards HAT and OAT reaction has been investigated in details.

4.3 Experimental Section

4.3.1 Materials

(Et$_4$N)$_2$[Fe^{III}(Cl)(X-bTAML)] **1** was synthesized as described before.[19] Aqueous sodium hypochlorite *(reagent grade, Aldrich, available chlorine 4.00–4.99%)* was used as

received and quantified by iodometry. Acetonitrile (LCMS grade, Aldrich) was used by passing through an activated neutral alumina column and then dried as described elsewhere.[20] All the substrate were purchased from sigma-aldrich as 99.8% pure and were passed through activated neutral alumina and distilled prior to use; its purity was checked by GC-MS. All reactions were carried out in argon environment, unless otherwise specified. Deionized water was used to make the sodium hypochlorite stock solutions for the reaction and kinetic runs.

4.3.2 Instrumentation

UV-vis spectral studies were carried out using an Agilent diode array 8453 spectrophotometers attached to a Peltier temperature controller. The X-band electron paramagnetic resonance (EPR) spectrum was recorded in a Bruker EMX X-band spectrometer operating at a field modulation of 100 kHz, modulation amplitude of 7 G and microwave radiation power of 10 mW at 90 K, unless otherwise specified.

Gas chromatography (GC) was performed on a PerkinElmer Arnel Clarus 500 instrument equipped with a hydrogen flame ionization detector and HP-5 (30 m × 0.32 mm × 0.25 μm) column. Helium was used as carrier gas at a flow rate of 30 mL min^{-1}. GC-MS analysis were performed on an Agilent 5977A mass-selective detector interfaced with an Agilent 7890B GC in similar conditions using a HP-5-Ms capillary column (30 m × 0.32 mm × 0.25 μm, J & W Scientific).

4.3.3 Generation of $[Fe^{V}(O)]^{-}$ samples and kinetic study with various substarte

A 0.45 mM solution of $[X\text{-}(bTAML)Fe^{III}Cl]^{2-}$ (**1**) was converted to **3** by using 1.2 equivalents of sodium hypochlorite (NaOCl) in acetonitrile.[19, 17] In all cases, nearly quantitative conversion was confirmed by UV-Vis spectroscopy (Figure 2.2). After the formation of oxoiron(V) substrate was added by gas tight micro syringe under an argon atmosphere and the reaction was monitored by UV-kinetics. The kinetics for the oxidation of toluene and cyclooctene by oxoiron(V) were monitored in the kinetic mode of the spectrophotometer using 1-cm quartz cell at 395 nm at the isosbestic points of Fe^{IV} species and Fe^{III} at 30.0 ± 0.5 °C as well as other temperatures. All the kinetic experiments were carried out in a degassed acetonitrile solvent. The pseudo first-order rate constants k_{obs} (calculated by monitoring changes at around 395 nm) were obtained from nonlinear curve fitting $[(A_t = A_\alpha - (A_\alpha - A_o)e^{(-k_{obs}t)}]$. Resulting k_{obs} values correlated linearly with substrate concentration to afford the second order rate constant k_2.[21,22]

4.4 Results and Discussion

4.4.1 Synthesis and Characterisations

A series of electron withdrawing and donating group substituted biuret modified tetraamido iron(III) chloro complex ([(X-bTAML)Fe^{III}-Cl]$^{2-}$; X represents the substitution in phenyl ring as depicted in figure 4.1) has been studied to understand the electronic effects during oxygenation reaction by their higher oxidized analogs. All the starting iron(III) complexes were characterized by XRD,[19c] HRMS,[19c] UV-Vis, Electrochemistry[19c] and EPR spectroscopy (see appendix D1). When the equimolar amount of aqueous sodium hypochlorite was added into **1a**-**1f**, initially a dark violet colored species (having a broad absorption around 890-950nm) was formed which subsequently decayed to a green colored species (nitro substituted complex shows amber color). UV-Vis spectral changes show that after addition of an equimolar amount of oxidant, it first formed a EPR silent dimeric μ-oxodiiron(IV) species similar to the unsubstituted one.[17] Then the dimeric iron complex decayed to a green colored oxoiron(V) species as has been observed from UV-Vis (characteristic peak at 445nm and 610nm)[17] and EPR (characteristic of published EPR of **1a**).
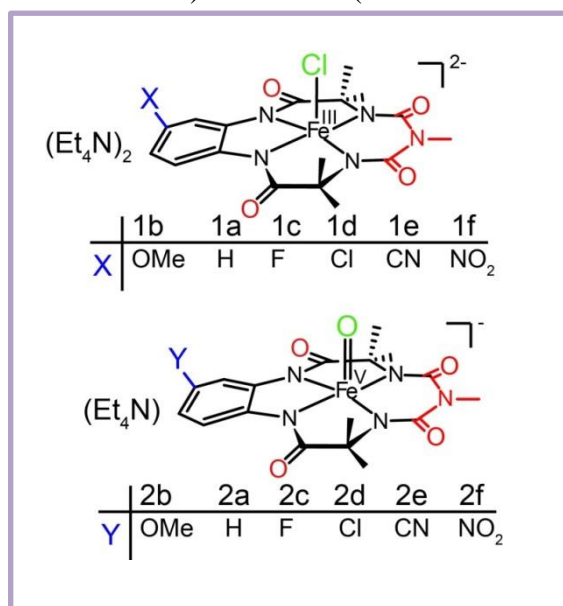
Figure 4.1: Schematic representation of biuret modified tetraamido macrocyclic iron(III)-chloro complexes ([(X-bTAML)Fe^{III}-Cl]; X- OMe, H, F, Cl, CN, and NO$_2$) and ([(Y-bTAML)Fe^V-O]; Y- OMe, H, F, Cl, CN, and NO$_2$ synthesised by previous published procedure.[17,18]
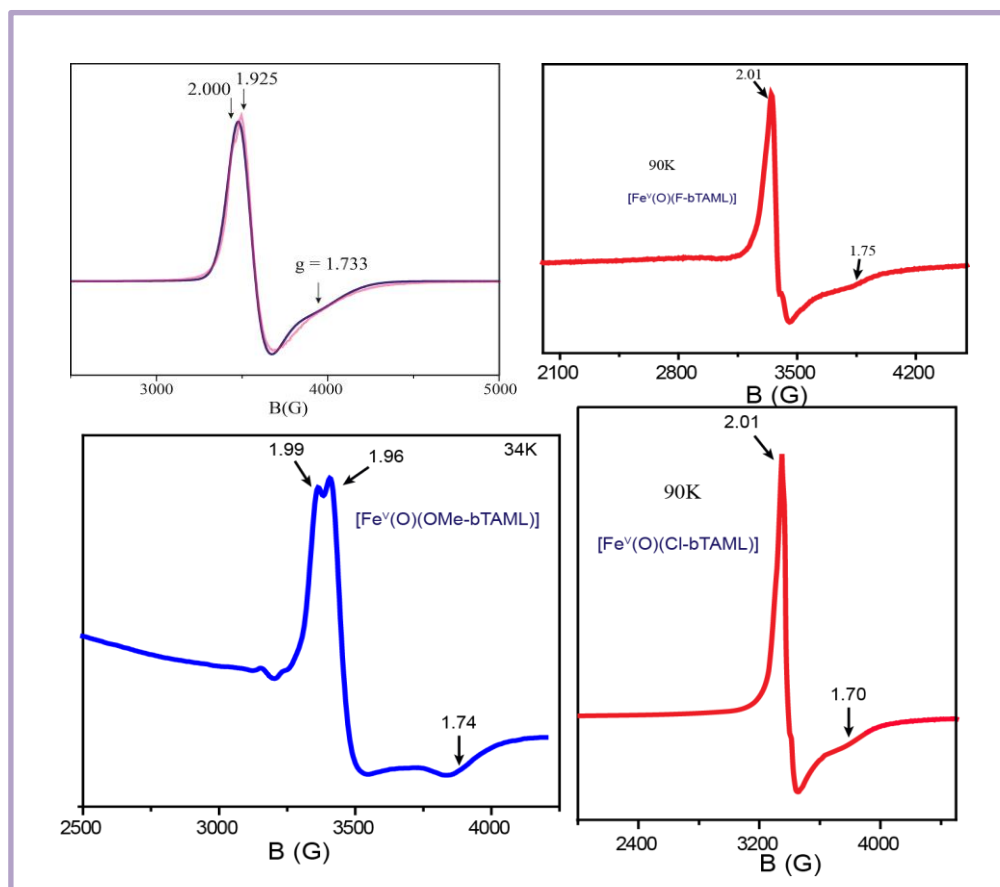
Figure 4.2: X-band EPR spectra of **2a**, **2c**, **2d** and **2e** complex (for details of EPR spectra see experimental section).

The EPR spectroscopy for all substituted oxoiron(V)bTAML complex shows a g_x, g_y and g_z tensor similar to that of $S = ½$ **1a**[17, 22] which indicates that **2b**-**2f** are $S = ½$ oxoiron(V) species (Figure 4.2, EPR spectra of **2a** and **2f** published elewhere[17, 22]). The electronic effect on the iron center is reflected from the UV-Vis spectra; upon increasing electron density (from –NO$_2$ to -OMe substituted oxoiron(V)) absorption band at 600 nm shows a red shift (540 nm for –NO$_2$ to 662 nm for –OMe, Figure 4.3, Table 4.1).
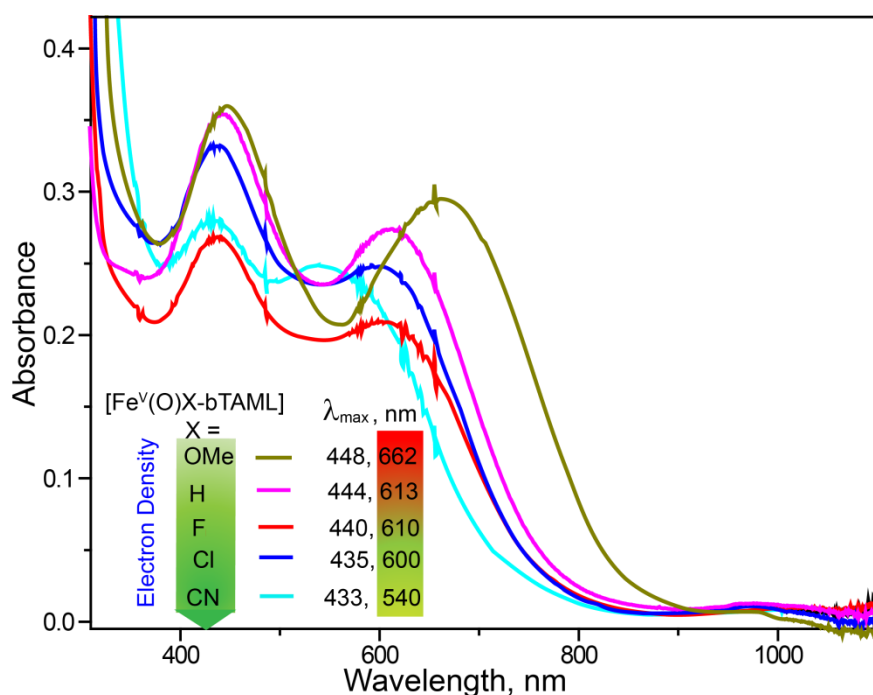
Figure 4.3: UV-Vis absorption spectra of oxoiron(V) for **2a-2f**, synthesized by oxidizing their iron(III) analog with sodium hypochlorite in acetonitrile at room temperature.

Table 4.1: Spectroscopic and kinetic properties of iron(III) and oxoiron(V) complexes.

Complexes	λ_{max} (nm) of Fe(III) (ε, M^{-1} cm^{-1})	λ_{max} (nm) of $[Fe^{V}O]^{-}$ (ε, M^{-1} cm^{-1})	Decay rate of $[Fe^{V}O]^{-}$ $k_{5/4,3}$ s^{-1}
[(OMe-bTAML)Fe]	381(5500)	448(5300), 662(4800)	3.1×10^{-4}
[(H-bTAML)Fe][17,22]	381, (3800)	441 (4350), 613 (3420)	4.45×10^{-5}
[(F-bTAML)Fe]	377, (4150)	435 (3858) 609(2900)	4.8×10^{-4}
[(Cl-bTAML)Fe]	372, (4400)	436(5000), 598(3920)	4.3×10^{-4}
[(NC-bTAML)Fe]	386, (6350)	433(6200), 532(5240)	4.1×10^{-4}
[(O_2N-bTAML)Fe][19b]	380(9000)	540(6500)	3.75×10^{-4}

Footnote: All the λ_{max} values have been determined in acetonitrile solution at room temperature. The decay rate constants ($k_{5/4,3}$ s^{-1}) of all $[Fe^{V}O]^{-}$ experimentally determined similarly to the published literature.[17]

4.4.2 Electronic effect on HAT and OAT reactivity

To understand the electronic effects on the reactivity of hydrogen atom transfer (HAT) and oxygen atom transfer (OAT) by oxoiron(V), toluene and cyclooctene were chosen as a substrate respectively. Hydrogen atom abstraction rate by **2b-2f** was measured under single TON condition under argon atmosphere following methods published by us earlier.[17] To measure KIE, the rate constant for hydrogen atom (k_H) and the rate constant for deuterium (k_D) was measured in the presence of toluene and toluene-d8 respectively at room temperature using substituted oxoiron(V). The non-classical KIE values for **2b-2f** indicate that the rate determining step is hydrogen atom abstraction similar to **2a** (Table 4.2). The HAT rate for electron withdrawing group increases linearly with the increasing electron deficiency on ironoxo center (Figure 4.4). Interestingly, with electron donating substituent the HAT rate was also increased (Figure 4.4). Increase in HAT rate for nitro substitution is twice than that of methoxy substitution compared to **2a**.

Table 4.2 The kinetic isotope effect (KIE) for C-H abstraction of toluene and toluene-d8 at room temperature by different substituted oxoiron.

Complex	2b	2a	2c	2d	2e	2f
k_H/k_D	5	8	12	26	39	46

Further, OAT from **2a-2f** to cyclooctene was studied to understand the effect of electron donating and withdrawing groups on the equatorial plane of ironoxo complex. The rate of OAT was measured according to the previously published method by us (see appendix D for details about kinetic study).[24] The OAT rate increased with decreasing electron density on ironoxo center but surprisingly, the OAT rate for electron rich oxoiron center is also increased (Figure 4.6).
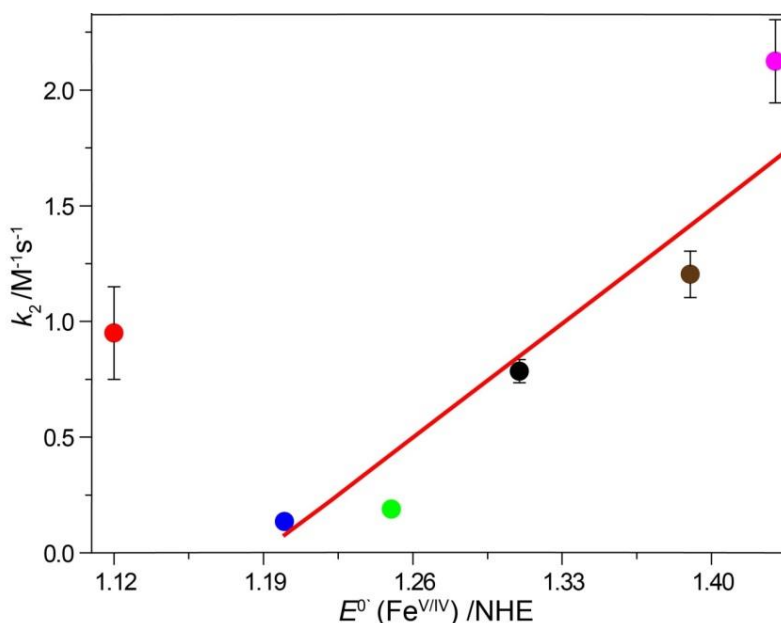
Figure 4.4: Plot of second order rate constants (k_2) for C-H abstraction of Toluene by **2b** (red), **2a** (blue), **2c** (green), **2d** (black), **2e** (brown), and **2f** (pink) versus formal redox potential ($E^{0`}$) of $Fe^{V/IV}$.

The increased reactivity of both HAT and OAT for electron deficient oxoiron(V) (**2a** to **2f**) can be rationalized by considering the thermodynamic affinity (BDE of Fe^{IV}_{O-H}, Figure 4.5) of the metal oxo species.[25] The Thermodynamic affinity (BDE Fe-OH) can be calculated form the figure shown below.
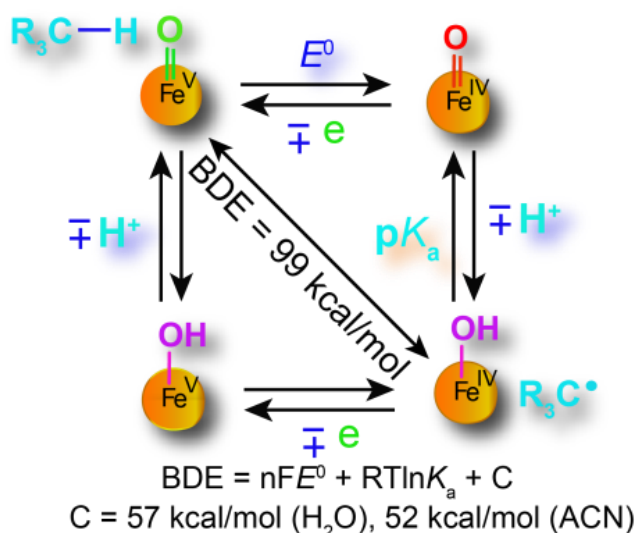
Figure 4.5: The thermochemical cycle of C-H abstraction to calculate BDE(Fe^{IV}_{O-H}).

The increased rate of HAT for the electron deficient oxoiron(V) is predominantly controlled by the redox potential of $Fe^V(O)/Fe^{IV}(O)$ couple which is similar to that observed in heme systems. According to BDE equation, the extent of HAT depends on both the redox potential of the $Fe^V(O)/Fe^{IV}(O)$ couple and the pK_a of $Fe^{IV}(O\text{-}H)$:

$$BDE(O\text{-}H) = 23.06E^o{}_{Fe^V(O)} + 1.37pK_{aFe^{IV}\text{-}OH} + C$$

It is worth noting that although the redox potential increases with decreasing the electron density on the central metal ion but the decreasing trend in pK_a of the reduced metal will have opposite effect on the HAT rates. The BDE equation shows that changes in pKa effect reaction rates more significantly than changes in redox potentials (23 times). Therefore, the HAT rate in case of electron deficient oxoiron(V) species increased with increasing the redox potential of $Fe^V(O)/Fe^{IV}(O)$ couple. Therefore, the experimentally calculated activation energy ($\Delta G^{\#}$) for HAT linearly varies with electron affinity of metal oxo species and $BDE(Fe^{IV}\text{-}OH)$ (see appendix D5 for plots).
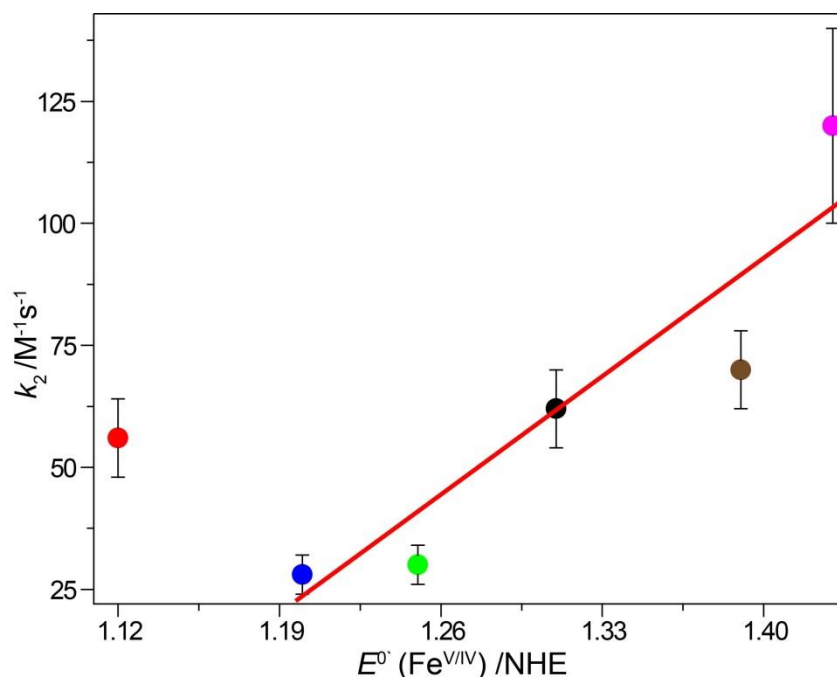
Figure 4.6: Plot of second order rate constants (k_2) for epoxidation of cyclooctene by **2b** (red), **2a** (blue), **2c** (green), **2d** (black), **2e** (brown), and **2f** (pink) versus formal redox potential ($E^{0`}$) of $Fe^{V/IV}$.

On the other hand, the high HAT rate of electron rich oxoiron(V) (**2b**) can be explained on the basis of elevated pK_a of $Fe^{IV}O$-H (11.3, Table 4.3, for details of pK_a calculations, see Appendix D) as has been observed for natural heme enzyme where the elevated pK_a increased the HAT rate by suppressing the non-productive oxidation pathways.[26] However, to obtain a better understanding as to how the frontier MO's control the HAT reactivity by these electron rich oxoiron(V), DFT calculations are currently being carried out.

For the OAT process, on the other hand, two electrons need to be transferred simultaneously to the antibonding orbitals of the M=O core and a similar ferryl basicity approach, as in the HAT process, will not be applicable. A detailed OAT mechanism for the reaction of electrophilic oxoiron(V) with electron rich olefins has been reported by us. Therefore, increasing the electrophilicity will enhance the OAT rate as has been demonstrated for most of the metal oxo mediated OAT process. A plot of second order rate of OAT *vs* redox potential of $Fe^V(O)/Fe^{IV}(O)$ indicates that OAT rate increases with increasing the electrophilicity of ironoxo species (Figure 4.6, Table 4.3). However, for an electron rich oxoiron(V), increase in the HAT rates were observed. This is however counterintuitive when the reactivity trends essentially electrophilic species are discussed. Similarly, the increased OAT (e.g., the oxidation of sulfides and phosphines) rate for the axial ligand effect in heme enzyme is not clear because how increased ferryl basicity would account oxo-transfer reactions.

Table 4.3: Summary of the effect of redox potential and pK_a on the oxygenation reaction by various $[(bTAML)Fe^VO]^-$ complexes.

Catalyst	$E^o_{(Fe^{IV/III})}$	$E^o_{(Fe^{V/IV})}$	σ_{m+p}	pK_a of $Fe^{IV}O*$	$k_2/ M^{-1}s^{-1}$ (Toluene)	$k_2/ M^{-1}s^{-1}$ (Cyclooctene)	$BDE_{Fe(IV)-OH}$ (kcal/mol)
2b-OMe	0.73	1.12	-0.15	11.3	0.95 ± 0.20	56 ± 8	98.3
2a-H	0.85	1.20	0.00	10.1	0.135 ± 0.010	28 ± 4	98.6
2c-F	0.89	1.25	0.40	10.03	0.189 ± 0.020	30 ± 4	99.5
2d-Cl	0.93	1.31	0.60	9.9	0.785 ± 0.050	62 ± 8	100.7
2e-CN	0.99	1.39	1.22	9.4	1.204 ± 0.100	70 ± 8	101.9
2f-NO$_2$	1.11	1.43	1.48	8.8	2.124 ± 0.180	140 ± 20	102.03

* $\pm$ 0.2 Error in pK_a determination

These questions are addressed by a combination of experimental and theoretical approaches in case of model Cpd I complexes. In heme analog, the DFT calculation showed that as the ligand becomes a better electron donor, the Fe=O bond becomes weaker thereby encouraging oxo-transfer reactivity.[27] We believe that for electron rich systems, the weakening of the Fe=O bond occurs which thereby facilitates the ease of O atom transfer onto the olefin. However, detailed spectroscopic and theoretical studies are needed to support this hypothesis.

4.5 Summary and Conclusions

In summary, we have synthesized a wide variety of oxoiron(III)bTAML complexes (**1b-1f**) having electron donating and electron withdrawing groups on the benzene ring of the head part of the complex. These complexes have been characterised by single crystal X-ray diffraction, HR-Ms, UV-Vis, electrochemistry and EPR spectroscopy. Then a series of oxoiron(V) complex (**2b-2f**) have been synthesize by using the equimolar amount of aqueous sodium hypochlorite solution in acetonitrile at room temperature. All the oxoiron(V) species have been characterised by HR-Ms, UV-Vis, electrochemistry and EPR spectroscopy. One electron reduced species (Fe^{IV}O) of **2a-2f** also have been synthesized at higher pH to calculate the pK_a values of Fe^{IV}(O-H) species. The iron(V)oxo complexes, containing an equatorial electron donating and withdrawing group have been used to understand the electronic effect on HAT and OAT reactions. The HAT rate for toluene increases linearly with increasing the redox potential of iron(V) oxo species. On the other hand, the elevated pK_a of one electron reduced Fe^{IV}(O-H) species is found to be responsible for the enhancement of HAT rate by electron rich oxoiron(V) species in line with the natural heme enzyme. The OAT rate enhancement for electron deficient oxoiron(V) is solely responsible for the increase in redox potential of the electron deficient metal oxo species. However, the increase in OAT rate for electron rich oxoiron(V) species is a counterintuitive reactivity trend for an essentially electrophilic species.

4.6 References

(1) A.E. Shilov, G. B. S. p., *Activation and Catalytic Reactions of Saturated Hydrocarbons in the Presence of Metal Complexes* Springer Netherlands: **2002**; Vol. 21.

(2) Arndtsen, B. A.; Bergman, R. G.; Mobley, T. A.; Peterson, T. H., *Acc Chem Res.,* **1995,** 28, (3), 154-162.

(3) Bergman, R. G., *Nature* **2007,** 446, (7134), 391-393.

(4) Cornell, C. N.; Sigman, M. S., Molecular Oxygen Binding and Activation: Oxidation Catalysis. In *Activation of Small Molecules*, Wiley-VCH Verlag GmbH & Co. KGaA: **2006**; pp 159-186.

(5) Labinger, J. A.; Bercaw, J. E., *Nature* **2002,** 417, (6888), 507-514.

(6) Olah, G. A.; Molnar, A., *Hydrocarbon chemistry*. John Wiley & Sons: 2003.

(7) R.A. Sheldon, J. A. K., Metal-Catalyzed Oxidations of Organic Compounds. **1981,** Academic Press, New York.

(8) a) Denisov, I. G.; Makris, T. M.; Sligar, S. G.; Schlichting, I. *Chem. Rev.* **2005**, *105*, 2253-2278. (b) Ortiz de Montellano, P. R. *Chem. Rev.* **2010**, *110*, 932−948. (c) Groves, J. T. Models and Mechanisms of Cytochrome P450 Action. *In Cytochrome P450: Structure, Mechanism and Biochemistry*, 3rd ed.; Ortiz de Montellano, P. R., Ed.; Kluwer Academic/Plenum Publishers: New York, **2005**.

(9) a) Sono, M.; Roach, M. P.; Coulter, E. D.; Dawson, J. H. *Chem. Rev.* **1996**, *96*, 2841−2888. (b) Nam, W. *Acc. Chem. Res.* **2007**, 40, 522−531. (c) Rittle, J.; Green, M. T. *Science,* **2010**, *330*, 933−937. (d) Meunier, B.; de Visser, S. l. P.; Shaik, S. *Chem. Rev.* **2004**, *104*, 3947-3980. (e) Costas, M.; Mehn, M. P.; Jensen, M. P.; Que, L., Jr. *Chem. Rev.* **2004**, *104*, 939-986. (f) Abu-Omar, M. M.; Loaiza, A.; Hontzeas, N. *Chem. Rev.* **2005,** *105*, 2227-2252.

(10) a) van Eldik, R. Coord. *Chem. Rev.* **2007**, *251*, 1649 −1662; b) Shaik, S.; Hirao, H.; Kumar, D. *Acc. Chem. Res*. **2007**, *40*, 532 − 542.

(11) a) Gross, Z.; Nimri, S. *Inorg. Chem.* **1994**, *33*, 1731 −1732; b) Song, W. J.; Ryu, Y. O.; Song, R.; Nam, W. *J. Biol. Inorg. Chem*. **2005**, *10*, 294 − 304; c) Takahashi, A.; Kurahashi, T.; Fujii, H. *Inorg. Chem*. **2009**, *48*, 2614 − 2625; d) Kamachi, T.; Kouno, T.; Nam, W.; Yoshizawa, K. *J. Inorg. Biochem.* **2006**, *100,* 751 − 754; e) de Visser, S. P.; *J. Biol. Inorg. Chem.* **2006**, *11*, 168 − 178; f) Wang, R.; de Visser, S. P. *J. Inorg. Biochem*. **2007**, *101*, 1464 −1472.

(12) a) Hessenauer-Ilicheva, N.; Franke, A.; Meyer, D.; Woggon, W.-D.; van Eldik, R. *Chem. Eur. J.* **2009**, *15*, 2941 − 2959; b) Hessenauer-Ilicheva, N.; Franke, A.; Meyer, D.; Woggon, W.-D.; van Eldik, R. *J. Am. Chem. Soc*. **2007**, *129*, 12473 −12479; c) Franke, A.; Stochel, G.; Suzuki, N.; Higuchi, T.; Okuzono, K.; van Eldik, R. *J. Am. Chem. Soc*. **2005**, *127*, 5360 − 5375; d) Suzuki, N.; Higuchi, T.; Nagano, T. *J. Am. Chem. Soc*. **2002**, *124*, 9622 − 9628; e) Ohno, T.; Suzuki, N.; Dokoh, T.; Urano, Y.; Kikuchi, K.; Hirobe,

M.; Higuchi, T.; Nagano, T. *J. Inorg. Biochem.* **2000**, *82*, 123 –125; f) Higuchi, T.; Shimada, K.; Maruyama, M.; Hirobe, M. *J. Am. Chem. Soc*. **1993**, *115*, 7551 –7552.

(13)   a) Solomon, E. I.; Decker, A.; Lehnert, N. *Proc Nat Acad Sci.,* **2003,** 100, (7), 3589-3594.; b) Kim, J.; Harrison, R. G.; Kim, C.; Que, L. *J Am Chem Soc.,***1996,** 118, (18), 4373-4379.; c) Leising, R. A.; Norman, R. E.; Que, L. *Inorg Chem.,* **1990,** 29, (14), 2553-2555.; d) Walling, C., *Acc Chem Res.,* **1975,** 8, (4), 125-131.; e) Chen, K.; Costas, M.; Que, J. L. *J Chem Soc, Dalton Trans.,* **2002**, (5), 672-679.; f) Ho, R. Y. N.; Roelfes, G.; Feringa, B. L.; Que, L. *J Am Chem Soc.,* **1999,** *121*, (1), 264-265.; g) Roelfes, G.; Vrajmasu, V.; Chen, K.; Ho, R. Y. N.; Rohde, J.-U.; Zondervan, C.; la Crois, R. M.; Schudde, E. P.; Lutz, M.; Spek, A. L.; Hage, R.; Feringa, B. L.; Münck, E.; Que, L. *Inorg Chem.,* **2003,** *42*, 2639-2653.; h) Mekmouche, Y.; Ménage, S.; Toia-Duboc, C.; Fontecave, M.; Galey, J.-B.; Lebrun, C.; Pécaut, J. *Angew Chem Int Ed.,* **2001,** *40*, 949-952.; i) Mekmouche, Y.; Ménage, S.; Pécaut, J.; Lebrun, C.; Reilly, L.; Schuenemann, V.; Trautwein, A.; Fontecave, M. *Eu J Inorg Chem.,* **2004**, *15*, 3163-3171.; j) Britovsek, G. J. P.; England, J.; White, A. J. P. *Inorg Chem.,* **2005,** *44*, (22), 8125-8134.; k) Hitomi, Y.; Arakawa, K.; Kodera, M. *Chem–Eu J.,* **2013***,19*, (43), 14697-14701.; l) Company, A.; Gömez, L.; Güell, M.; Ribas, X.; Luis, J. M.; Que, L.; Costas, M. *J Am Chem Soc.,* **2007,** *129*, (51), 15766-15767.; m) Salomo, G. C.; Olsen, M. H. N.; Drago, V.; Fernandes, C.; Cardozo Filho, L.; Antunes, O. A. C. *Catal Commun.,* **2007,** *8*, (1), 69-72.; n) Foster, T. L.; Caradonna, J. P., *J Am Chem Soc.,* **2003,** *125*, (13), 3678-3679.

(14)   a) Meunier, B.; de Visser S. P.; Shaik, S. *Chem. Rev.*, **2004**, *104*, 3947-3980.; b) Hirao, H.; Kumar, D.; Que, Jr. L.; Shaik, S. *J. Am. Chem. Soc.*, **2006**, *128*, 8590-8606.; c) Hirao, H.; Que, Jr., L.; Nam, W.; Shaik, S. *Chem. Eur. J.*, **2008**, *14*, 1740-1756.; d) Shaik, S.; Hirao, H.; Kumar, D. *Acc. Chem. Res.*, **2007**, *40*, 532-542.; e) Shaik, S.; Kumar, D.; de Visser, S. P. *J. Am. Chem. Soc.*, **2008**, *130*, 10128-10140.

(15)   Sun, X.; Geng, C.; Huo, R.; Ryde, U.; Bu, Y.; Li, J. *J. Phy. Chem. B* **2014**, *118*, (6), 1493-1500.

(16)   a) Costas, M. *Coord. Chem. Rev.* **2011***,255*, 2912-2932.; b) Bell, S. R.; Groves, J. T. *J. Am. Chem. Soc.* **2009**, *131*, 9640–9641.

(17)   Ghosh, M.; Singh, K. K.; Panda, C.; Weitz, A.; Hendrich, M. P.; Collins, T. J.; Dhar, B. B.; Gupta, S. S., *J. Am. Chem. Soc*. **2014**, *136*, 9524–9527.

(18)   Pattanayak, S.; Jasniewski, A. J.; Rana, A.; Draksharapu, A.; Singh, K. K.; Weitz, A.; Hendrich, M.; Que, L., Jr.; Dey, A.; Sen Gupta, S. *Inorg. Chem.* **2017**, *56*, 6352.

(19)   a) Panda, C.; Ghosh, M.; Panda, T.; Banerjee, R.; Gupta, S. S. *Chem. Commun.* **2011**, *47*, 8016-8018.; b) Panda. C.; Debgupta. J.; Díaz. D. D.; Singh. K. K.; Gupta S. S. Dhar. B. B. *J. Am. Chem. Soc.* **2014**, 136, 12273; c) Pattanayak, S.; Chowdhury, R. D.; Garai, B.; Sing, K. K.; Paul, A.; Dhar, B. B.; Gupta, S. S. *Chem.-Eur. J.* **2017**, DOI: 10.1002/chem.201605061.

(20)   Armarego, W. L. F.; Perrin, D. D., Purification of Laboratory Chemicals; 4th ed.; Elsevier Science, USA, 1997.

(21)   Cho, K.; Leeladee, P.; McGown, A. J.; DeBeer, S.; Goldberg, D. P. *J. Am. Chem. Soc*. **2012**, *134*, 7392- 7399.

(22)   Singh, K. K.; Tiwari, M. k.; Ghosh, M.; Panda, C.; Weitz, A.; Hendrich, M. P.; Dhar, B. B.; Vanka, K.; Gupta, S. S. *Inorg. Chem.* **2015**, *54*, 1535-1542.

(23)   Espenson, J. H., Chemical Kinetics and Reaction Mechanisms; 2nd ed.; McGraw-Hill, Inc.: New York, **1995**.

(24)   Singh, K. K.; Tiwari, M. k.; Dhar, B. B.; Vanka, K.; Sen Gupta, S. *Inorg. Chem.* **2015**, *54*, 6112.

(25)   a) Bordwell, F. G.; Cheng, J.-P.; Ji, G.-Z.; Satish, A. V.; Zhang, X. J. Am. Chem. Soc. **1991**, *113*, 9790–9795; b) Bordwell, F. G.; Bausch, M. J. J. Am. Chem. Soc. **1986**, *108*, 1979–1985.

(26)   a) R. K. Behan, M. T. Green, *J. Inorg. Biochem*., **2006**, *100*, 448 –459; b) M. T. Green, J. H. Dawson, H. B. Gray, *Science*, **2004**, *304*, 1653–1656; c) J. H. Dawson, *Science*, **1988**, *240*, 433 –439; d) F. Ogliaro, S. P. de Visser, S. Shaik, *J. Inorg. Biochem*., **2002**, *91*, 554 –567.

(27)   Kang, Y.; Chen, H.; Jeong, Y. J.; Lai, W.; Bae, E. H.; Shaik, S.; Nam, W. *Chem. – A Eur. J.* **2009,** 15, (39), 10039-10046.

Chapter V

Synthesis of a new generation tetrauret tetraamido macrocyclic iron complex [(tTAML)Fe^{III}-Cl](PPh$_4$)$_2$ for Oxidation reactions

5.1 Abstract

A major research effort has evolved which focuses on biologically inspired metal complexes mimicking the structures and function of H_2O_2 or oxygen (O_2) activating metalloenzymes. In recent years various metal complexes have been investigated, each employing a myriad of donor ligands to effectively catalyse either O_2 or peroxide-dependent oxidation reactions. The major challenge in the design of peroxide-activating catalysts is selecting a suitable metal ligand which can stabilize high-valent metal oxidation states while simultaneously remaining resistant to self-oxidation. Recently, a highly stable oxoiron(V) in bTAML ligand framework indicates that the highly electron rich deprotonated amide plays a key role in formation and stabilization of such reactive species. We hypothesize that a π electron cloud around the metal center along with the deprotonated amide would drastically affect the formation and stability of high-valent species. This work presents the synthesis and spectroscopic characterizations of a $[Fe^{III}\text{-Cl}(tTAML)](PPh_4)_2$ complex of a tetrauret modified tetraamido macrocyclic ligand. The complex was characterized primarily by means of EPR and single crystal X-ray diffraction. The EPR spectroscopy of $[Fe^{III}\text{-Cl}(tTAML)](PPh_4)_2$ complex shows signals consistent with $S = 3/2$ intermediate-spin ferric-iron. Besides EPR, HR-MS and UV/vis spectroscopy were used to further characterize it.

5.2 Introduction

One of the most significant challenges in the field of synthetic organic chemistry has been the development of methodology which allows synthesis of complex natural molecules by selective oxidation of C–H bonds under mild conditions.[1-15] An approach pursued by many chemists to achieve this goal has been to mimic enzymes that function as oxidation catalysts. Several efforts have been made to develop catalyst systems that can catalyze this transformation, especially with cheap and available metals like iron.[16-18] Both heme[19-21] and its related systems (e.g. Corroles and Phthalocyanines)[22-26] as well as non-heme iron complexes[21, 27-37] have been studied in detail. Designing metal complexes that activate H_2O_2 or O_2 but are themselves inert to oxidation is the key to the synthesis of efficient transition metal oxidation catalysts.[38] Nature has evolved enzymes that are very efficient as oxidation catalysts. These include cytochrome P450 and peroxidases; enzymes that use an iron(IV) oxoporphyrin radical cation intermediate to catalyze the oxidation of various organic substrates selectively and efficiently.[39,40] Major research efforts have been directed towards

the synthesis of biologically inspired metal complexes that mimic the structure and function of these oxidases.[41-50] Among these, non-heme iron complexes bearing tetradentate N-donor ligands have shown great potential as catalysts for effective C–H bond oxidations with high levels of regio and chemo-selectivity. The first non-heme iron complex reported to catalyse oxidation of alkanes using H_2O_2 as the oxidant was high valent Fe-TPA complex.[33, 51-58] However, the discovery of PDP,[17, 59-62] BPMEN[63-70] and [Me,H/Me]PyTACN[34, 62] ligand based iron complex allowed oxidation of unactivated C–H bonds in aliphatic compounds with predictable selectivity, even in complex molecular scaffolds in a catalytic manner.

In the last few years, significant developments have been made in characterizing the non-heme iron(IV)–oxo species intermediates and understanding their reactivity in a variety of oxygenation reactions. In contrast, although non-heme iron(V)–oxo intermediate was discovered in 2007,[71] Fe-bTAML represents the only system till date in which the $Fe^V(O)$ is fully characterized by Mössbauer, EPR, XAFS, HR-MS and Resonance Raman.[71, 72] The inability of the $Fe^V(O)$(TAML) to oxidize unactivated C-H bonds is due to its instability above -40 °C. Hence, if a robust ligand system can be developed that stabilizes Fe(V)-oxo between 0 °C and RT, we believe it would be very reactive towards unactivated C-H bonds.

The biuret modified Fe-bTAML reported previously, forms the corresponding $Fe^V(O)$ quantitatively using *m*CPBA or NaOCl at room temperature.[73,74] It has been shown to catalyze the hydroxylation of unactivated C–H bonds,[73, 74] epoxidation of electron rich/deficient C=C bonds[75] and oxidation of alcohols to aldehydes/ketones[76] under single turnover conditions. For epoxidation reactions, Fe-bTAML catalyzed epoxidation of alkenes with NaOCl as the oxidant gives modest turnover numbers.[75]

The intriguing stability of oxoiron(V) in bTAML ligand framework indicates that the highly electron rich deprotonated amide plays a key role in formation and stabilization of such reactive species. We hypothesize that a π electron cloud around the metal center along with the deprotonated amide would drastically affect the formation and stability of high-valent species. Therefore, we designed a tetrauret modified tetraamido macrocyclic ligand (tTAML) according to figure 5.1.
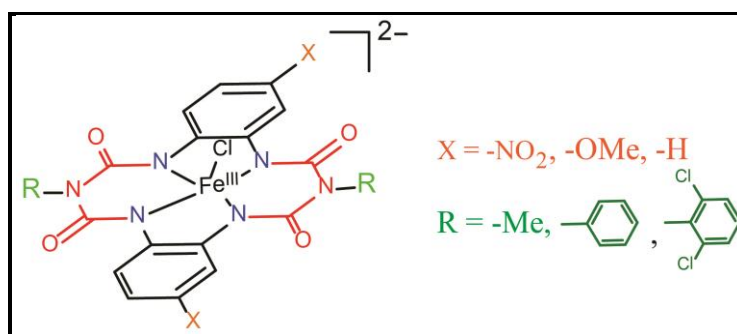
Figure 5.1: Proposed tetrauret modified tetraamido macrocyclic iron complex [Fe^{III}(tTAML)]$^{2-}$ complex.

5.3 Experimental section

5.3.1 General Methods

All the chemicals and solvents were obtained either from Aldrich Chemical Co. USA or Fisher Scientific Company, USA and used as obtained without further purifications unless otherwise stated. Tetrahydrofuran (THF) was purified using sodium and benzoephenone. ^{1}H-NMR spectra were obtained using a 600 MHz Brüker Avance instrument equipped with a 5 mm triple resonance inverse probe. Infrared (IR) spectra were obtained using a Nicolet Magna IR 500 spectrometer. Electrospray ionization mass spectra (ESI-MS) were obtained using an Applied Biosystem API-4000 spectrometer or using an Agilent 100 series MSD VL spectrometer. Electrochemical studies were performed using a Pine Instrument Company Biopotentiostat (model No. AFCBP1). When acetonitrile was used as organic solvent, tetrabutylammonium hexafluorophosphate ([NBu$_4$]PF$_6$) was added in a concentration of 0.1M to act as supporting electrolyte.

5.3.2 Electron paramagnetic resonance (EPR) spectroscopy

X-band (9 GHz) EPR spectra were recorded on a Bruker EMX Plus spectrometer equipped with a bimodal resonator (Bruker model 4116DM). Low-temperature measurements were made using an Oxford ESR900 cryostat and an Oxford ITC 503 tempera- ture controller. A modulation frequency of 100 kHz was used for EPR spectra.

5.3.3 Crystallographic Details

For the single Crystal X-ray diffraction experiment, as synthesized crystals of the respective materials were taken out of the solution and coated with Paratone-N oil. It was then placed in a nylon cryoloop (Hampton research) and then mounted in the diffractometer.

The data collection was done at 298 K. The crystals were mounted on a Super Nova Dual source X-ray Diffractometer system (Agilent Technologies) equipped with a CCD area detector and operated at 250 W power (50 kV, 0.8 mA) to generate Mo Kα radiation (λ = 0.71073 Å) and Cu Kα radiation (λ = 1.54178 Å) at 298(2) K. Initial scans of each specimen were performed to obtain preliminary unit cell parameters and to assess the mosaicity (breadth of spots between frames) of the crystal to select the required frame width for data collection. CrysAlisPro program software was used suite to carry out overlapping φ and ω scans at detector (2θ) settings (2θ = 28). Following data collection, reflections were sampled from all regions of the Ewald sphere to redetermine unit cell parameters for data integration. Following exhaustive review of collected frames, the resolution of the data set was judged. Data were integrated using CrysAlisPro software with a narrow frame algorithm. Data were subsequently corrected for absorption by the program SCALE3 ABSPACK1 scaling algorithm. These structures were solved by direct method and refined using the SHELXTL 972 software suite. Atoms were located from iterative examination of difference F-maps following least squares refinements of the earlier models. Final model was refined anisotropically (if the number of data permitted) until full convergence was achieved. Hydrogen atoms were placed in calculated positions (C-H = 0.93 Å) and included as riding atoms with isotropic displacement parameters 1.2-1.5 times U_{eq} of the attached C atoms. In some cases modelling of electron density within the voids of the frameworks did not lead to identification of recognizable solvent molecules in these structures, probably due to the highly disordered contents of the large pores in the frameworks. Highly porous crystals that contain solvent-filled pores often yield raw data where observed strong (high intensity) scattering becomes limited to ~1.0 Å at best, with higher resolution data present at low intensity. Additionally, diffused scattering from the highly disordered solvent within the void spaces of the framework and from the capillary to mount the crystal contributes to the background and the 'washing out' of the weaker data. Electron density within void spaces has not been assigned to any guest entity but has been modeled as isolated oxygen and/or carbon atoms. The foremost errors in all the models are thought to lie in the assignment of guest electron density. The structure was examined using the *ADSYM* subroutine of PLATON[3] to assure that no additional symmetry could be applied to the models. The ellipsoids in ORTEP diagrams are displayed at the 50% probability level unless noted otherwise.

5.3.4 Synthesis of the complex
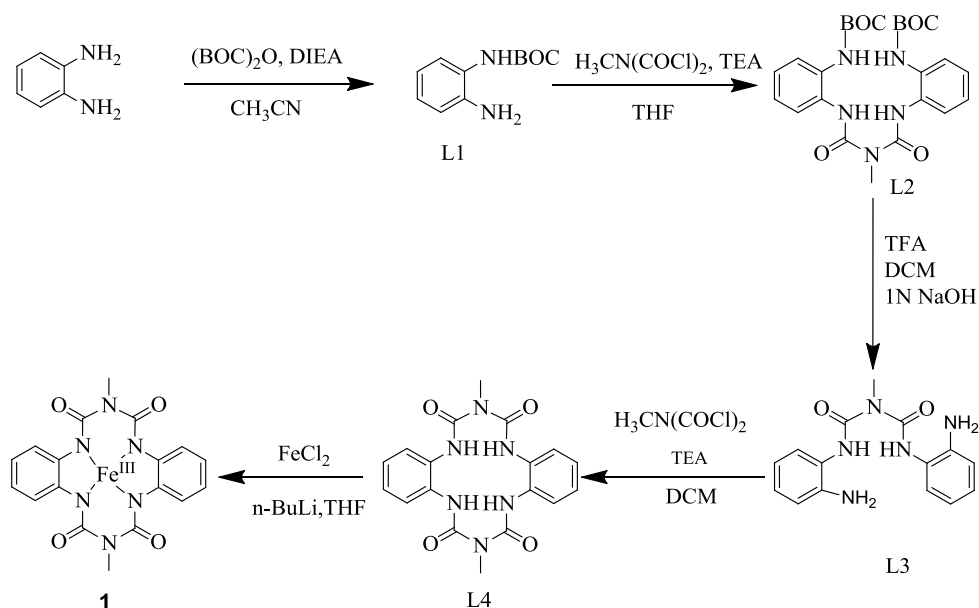
Scheme 5.1: The general scheme for the synthesis of ligand (**L4**) and its iron (III) complex (**1**)

Synthesis of (2-Amino-phenyl)-carbamic acid tert-butyl ester (3)

O-phenylenediamine (3 gm, 27.8 mmol) and triethylamine (27.8 mmol, 3.8 mL) were dissolved

in 47 mL of dry THF (dried over sodium and benzophenone). Di-tert-butyl-carbonate (6.05 gm, 27.8 mmol) was dissolved in 50 mL of THF. Both the solutions were combined in two gas tight syringes separately and added in a three neck round bottom flask containing 50 mL THF via a syringe pump at 0 °C. The addition was completed within 16 h. The reaction mixture was then further stirred at room temperature for another 4 h. After the reaction, solvent was removed using a rotoevaporator. The residue was dissolved in 200 mL dichloromethane and washed with 5% Na_2CO_3 (3 x 100 mL). The organic layer was collected and dried using anhydrous sodium sulphate. After filtration, the organic layer was concentrated using a rotary evaporator to yield the slightly yellow product **L1**. The compound was further purified by recrystallizing from benzene. Yield (4.68, 81%). ^{1}H-NMR δ_H (DMSO-d6, 200MHz): 1.48 (s, 9H for k), 4.84 (s, 2H for a), 6.55 (m, broad, 1H for e), 6.59 (m, 1H for c), 6.72 (m, 1H for d), 7.20 (d, 1H for f). ^{13}C-NMR δ_c (CDCl$_3$, 200MHz): 28.29(k), 80.15(j), 117.58(c), 119.60(e), 124.37(d), 126.12(f),
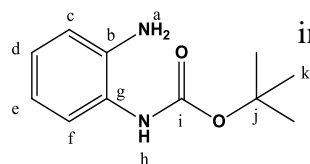
139.90(b), 153.82(i); IR (solution, v_{max}/cm^{-1}), N-H 3443 and 3476 (**CONH**), 1681 (C=O, carbonate), 1683, (**CONH**).

*Synthesis of (**L2**)*

L1 (2.08 gm, 10 mmol,) was dissolved in 50 mL dry THF. To this solution was added

triethylamine (1.4 mL, 10 mmol). The mixture was transferred to a 100 mL two neck round bottom flask and cooled to 0 ºC. N-Me acid chloride (1.45 mL, 11 mmol) dissolved in 50 mL dry THF was added into a dropping funnel and the solution was combined slowly for 60 min to the other solution drop-wise under nitrogen atmosphere. During the addition, a white precipitate was noted to be formed. After addition of N-Me acid chloride, the reaction
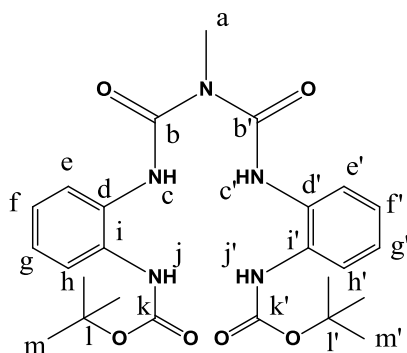
mixture was brought to room temperature and stirred overnight under inert atmosphere. After the reaction the solution was filtered to remove insoluble and filtrate was collected. The residue was dissolved in 200 mL dichloromethane and washed with 5% Na$_2$CO$_3$ (3 x 100 mL). The organic layer was collected and dried using anhydrous sodium sulphate. After filtration the organic layer was concentrated using a rotary evaporator to yield an off-white crude product, **L2**. Following evaporation of the solvent, the product was washed with diethyl ether and dried in vacuum. The compound **L2** was further purified by recrystallizing from benzene. Yield (4.09 g, 80%). ^{1}H-NMR (DMSO-d6, 200MHz): 1.41 (s, 18H for m, m´), 3.38(s, 3H for a), 7.16 (m, 4H for f, f´, g, g´), 7.41 (m, 2H for h, h´), 7.66 (m, 2H for e, e´), 8.78 (s, 2NH for c, c´), 10.17 (s, 2NH for j, j´). ^{13}C-NMR δ_c(DMSO-d6, 200MHz): 27.85(m, m´), 79.10(k, k´), 124.49(f, f´, g, g´), 130.73(e, e´, h, h´), 131.45(i, i´), 153.56(k, k´), 154.14(b, b´). IR (KBr, v_{max}/cm^{-1}), 3498 and 3524 (**CONH**), 1742 (C=O, carbonate) 1631 (C=O, amide), 1200 (C-O, ester), 1295 (C-N, amide).

*Synthesis of (**L3**)*

L2 (1.5 gm, 3.18 mmol) was dissolved in 10 mL dichloromethane and cooled to 0 ℃. To this solution was added a mixture of trifluoroacetic acid (10 mL) and dichloromethane (20 mL) drop-wise over a period of 30 min under inert atmosphere. After the addition, the reaction mixture was brought to room temperature and stirred for another 2 h. The reaction mixture then was concentrated using a rota evaporator to obtain a slightly yellow viscous liquid. This solution was diluted with 75 mL of water and the pH was adjusted with enough 1 M sodium hydroxide solution to bring the pH of the solution to 10 and then extracted with 20mL of dichloromethane (3 x 20mL). The organic layer was dried using anhydrous sodium sulphate. After filtration the organic layer was concentrated using rotary evaporator to yield the white product. Yield (0.72 g, 79%). ^{1}H-NMR (DMSO-d6, 200MHz), 3.93 (s, 3H for a), 4.90 (br, 4H for i, i′), 6.75 (m, 2H for e, e′), 6.79 (m, 2H for g, g′), 6.96 (m, 2H for f, f′), 7.22 (dd, 2H for d, d′), 7.79 (s, 2H for j, j′). ^{13}C-NMR δ_c(DMSO-d6, 200MHz): 31.86(a), 117.18(g, g′), 119.60(d, d′), 124.37(e, e′), 126.12(c, c′), 139.90(h, h′), 153.82(b, b′). IR (KBr, v_{max}/cm^{-1}), 3263 (N-H, amine), 1642 (C=O, amide), 1320 (C-N, amide).
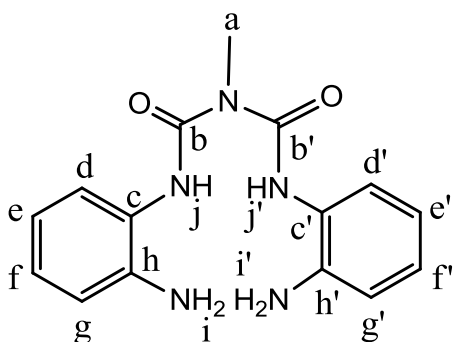
*Synthesis of (**L4**)*

L3 (0.408 g, 1.31 mmol) was dissolved in 30 mL dry THF and to the solution was added triethylamine (0.38 mL). The solution was collected in a gas tight syringe. N-Me acid chloride (0.11 mL, 1.31 mmol) was dissolved in 30 mL dry THF and collected in another gas tight syringe. Both solutions were added drop-wise via syringe pump, into a round bottom flask containing 30 mL dry THF that had been cooled to 0 ℃ and maintained under inert atmosphere. The addition was completed in 16 h. The mixture was allowed to continue stirring for an additional 4 h at room temperature. Precipitate from the reaction mixture was collected by filtration and washed with copious amount of distilled water. The resulting product was transferred to a round bottom flask and 200mL of diethyl ether added. The mixture was sonicated for 15
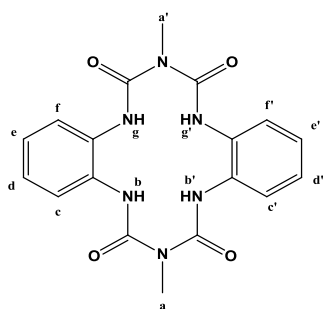
minutes and then filtered. The precipitate was collected and rinsed with additional ether to further purify the material. The resulting product was dried for 12 h under vacuum at 80 ℃ to yield the desired macrocyclic ligand (**L4**). Yield (0.36 g, 72%). ^{1}H-NMR (d^6-DMSO, 200MHz), 3.26 (s, 6H fo a, a′), 7.14 (dd, 4H for c, c′, e, e′), 7.59 (dd, 4H for d, d′, f, f′), 10.13 (s, 4H for b, b′, g, g′); ESI-MS (negative ion mode): m/z, 381.139(M-H$^+$, 100%). IR (KBr, v $_{max}$/cm^{-1}), 1642, 1663, 1602 (C=O, amide), 1298 (C-N, amide).

Synthesis of 1 (with Li$^+$ as counter cation of the Fe-complex)

L4 (200 mg, 0.52 mmol) was dissolved in 30 mL dry THF in a 100 mL Schlenk flask containing a magnetic stir bar and fitted with an N$_2$ gas line. The mixture was cooled to 0 ℃ using an ice bath. To this mixture was added n-butyllithium (2.56 mmol, 1 mL) and the reaction mixture was stirred for 15 min. After stirring for an additional 15 min at room temperature, ferrous chloride (72.6 mg, 0.57 mmol), was added and the solution was allowed to stir overnight under N$_2$ atmosphere. During the reaction the mixture turned deep brown. The solution was opened to air and the red precipitate was collected by filtration and washed with dichloromethane for several times. Yield (0.19 g, 79%). HR-MS (negative ion mode): m/z, 434.0420 (434.0420 calculated for C$_{18}$H$_{14}$FeN$_6$O$_4$ (without axial Cl ligand), 100%). IR (KBr, v $_{max}$ cm^{-1}), 1640 (C=O amide), 1300 (C-N amide).

Synthesis of [PPh$_4$]$_2$ ((with PPh$_4^+$ as counter cation of the Fe-complex)

Lithium salt of **1** (0.4 g, 0.87 mmol) was dissolved in deionized water (3 mL) and the solution was filtered. A solution of [PPh$_4$]Cl (2.1 g, 5.6 mmol) in water (5 mL) was added drop-wise to the solution of **2** on stirring. A light red precipitate formed was collected and dried in vacuum. Yield (0.48 g, 72%). X-ray diffraction quality crystal was obtained by vapour diffusion method.
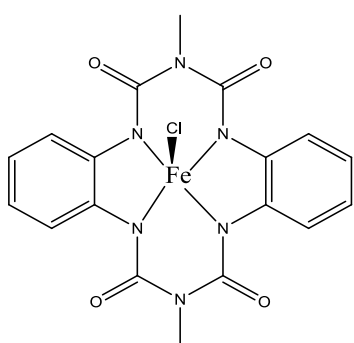
5.4 Results and discussion

The complex $(PPh_4)_2[Fe^{III}(tTAML)]$ (**1**; Figure 5.1) was obtained by the base-assisted insertion of $FeCl_2$ into the tetrauret tetraamido macrocyclic ligand (tTAML) L**4** which gets
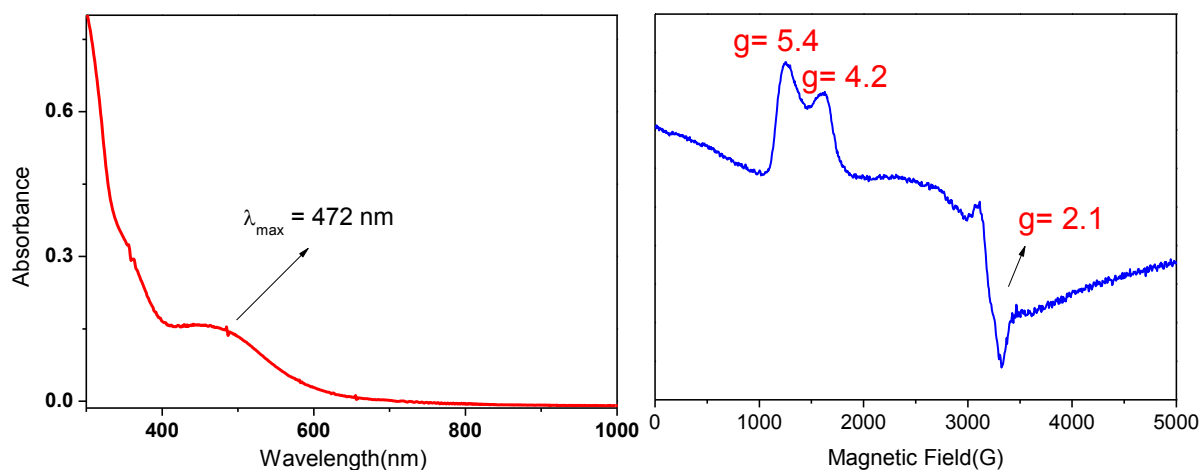
Figure 5.2: UV-Vis of 5 x 10^{-4} mM of $(PPh_4)_2[Fe^{III}(tTAML)]$ in acetonitrile (left). X-band (operating at a field modulation of 100 kHz, modulation amplitude of 10 G and microwave radiation power of 10 mW at 90K) EPR spectra of $(PPh_4)_2[Fe^{III}(tTAML)]$ in acetonitrile.

oxidized to corresponding Fe(III) complex only after exposure to air during the synthesis. The X-band EPR spectroscopy at 90K temperature shows g values at 5.4, 4.2 and 2.1. This g values indicate that in $(PPh_4)_2[Fe^{III}(tTAML)]$ complex central metal ion spin state is $S = 3/2$. The UV-Vis of $(PPh_4)_2[Fe^{III}(tTAML)]$ in acetonitrile shows very weak absorbance at 472 nm. But in case of $(PPh_4)_2[Fe^{III}(bTAML)]$ complex this value is at 380 nm. The complex crystallizes in tetragonal crystal system (space group, I 2/a). The crystal structure shows that the complex is highly puckered. The phenyl ring goes out of the molecular plane which results in butterfly kind of geometry. This puckered geometry is probably due contraction in metal binding pocket compared to the bTAML iron complex.
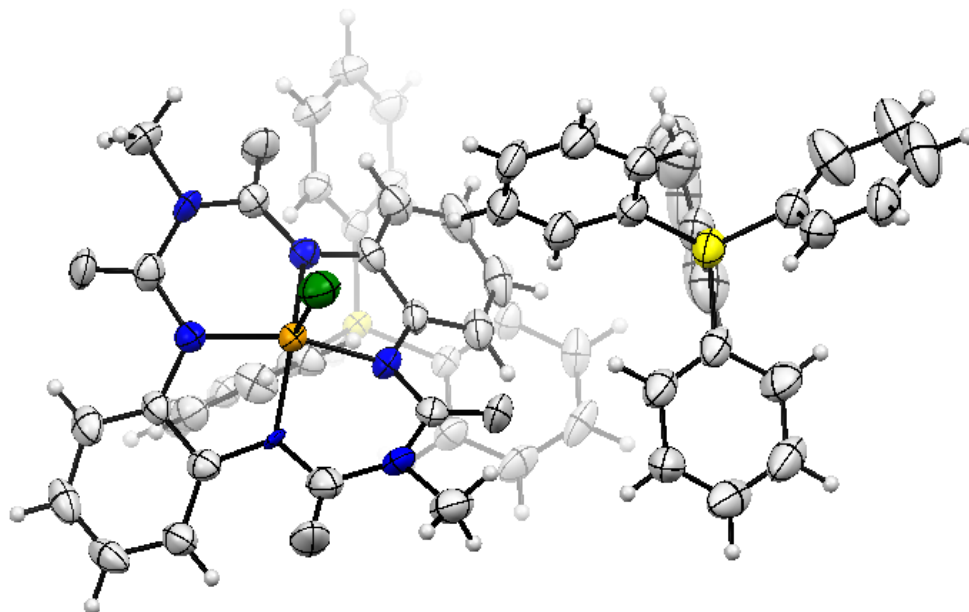
Figure 5.3: ORTEP diagram of $(PPh_4)_2[Fe^{III}(tTAML)]$ complex.

The X-ray crystal structure of $(PPh_4)_2[Fe^{III}(tTAML)]$ indicates a square-pyramidal Fe(III) with an axial Cl atom (Figure 5.3). There are two type of Fe-N bond in this molecule. The one Fe–N bond length is 1.88(2) Å and the other one is 1.90 Å. The Fe(III) lies 0.248 Å above the plane formed by the four donor nitrogens (NA, NB, NC, ND). The N5 atom of the Me-biuret ring is 3.09 Å away from the Fe(III) indicating that this N-atom is not involved in bonding with the Fe(III) center. The Me-biuret ring is close to planarity and the torsion angle between the C(N-Me) –N(N-Me) and C(nearest C of amide) -N planes is around −175.13°. Therefore the N5 atom in the six-membered ring is strictly sp^2 hybridized and the nitrogen lone pair, residing in the p orbital of N5 atom, is conjugated extensively to the carbonyl C-atom on both sides.

5.5 Summary and Conclusions

The $(PPh_4)_2[Fe^{III}(tTAML)]$ complex has been synthesised and characterised by various spectroscopic technique. The stability and reactivity will be studied separately.

5.6 References

(1) *Handbook of Chemistry and Physics*. 77th ed. ed.; CRC Press, Boca Raton, FL: 1988.

(2) In *Activation of Small Molecules*, Wiley-VCH Verlag GmbH & Co. KGaA: 2006; pp I-XVII.

(3) In *Handbook of C–H Transformations*, Wiley-VCH Verlag GmbH: 2008; pp I-XXVI.

(4) A.E. Shilov, G. B. S. p., *Activation and Catalytic Reactions of Saturated Hydrocarbons in the Presence of Metal Complexes* Springer Netherlands: **2002**; Vol. *21*.

(5) Arndtsen, B. A.; Bergman, R. G.; Mobley, T. A.; Peterson, T. H., *Acc. Chem. Res.* **1995,** *28*, (3), 154-162.

(6) Ball, P., Why Synthesis. *Nature* **2015**.

(7) Bergman, R. G., Organometallic chemistry: C-H activation. *Nature* **2007,** *446*, (7134), 391-393.

(8) Christmann, M., *Angew Chem Int Ed.* **2008,** *47*, (15), 2740-2742.

(9) Labinger, J. A.; Bercaw, J. E., *Nature* **2002,** *417*, (6888), 507-514.

(10) Newhouse, T.; Baran, P. S., *Angew Chem Int Ed* **2011,** *50*, (15), 3362-3374.

(11). Olah, G. A.; Molnar, A., *Hydrocarbon chemistry*. John Wiley & Sons: 2003.

(12) Ortiz de Montellano, P. R., *Chem Rev.,* **2010,** *110*, (2), 932.

(13) R.A. Sheldon, J. A. K., Metal-Catalyzed Oxidations of Organic Compounds. **1981,** Academic Press, New York.

(14) Sawyer, D. T.; Sobkowiak, A.; Matsushita, T., *Acc Chem Res* **1996,** *29*, (9), 409-416.

(15) Shilov, A. E.; Shul'pin, G. B., *Chem Rev.* **1997,** *97*, (8), 2879-2932.

(16) Barton, D. H. R.; Beck, A. H.; Taylor, D. *Tetrahedron* **1995,** *51*, (18), 5245-5254.

(17) Gormisky, P. E.; White, M. C., *J Am Chem Soc.,* **2013,** *135*, (38), 14052-14055.

(18) Lindhorst, A. C.; Haslinger, S.; Kuhn, F. E. *Chem. Comm., 51*, (97), 17193-17212.

(19). Bell, S. R.; Groves, J. T. *J. Am. Chem. Soc.* **2009,** *131*, (28), 9640-9641.

(20). Cho, K.; Leeladee, P.; McGown, A. J.; DeBeer, S.; Goldberg, D. P., *J Am Chem Soc.* **2012,** *134*, (17), 7392-7399.

(21) Nam, W. *Acc. Chem. Res.* **2007,** *40*, (7), 522-531.

(22) Biswas, A. N.; Das, P.; Agarwala, A.; Bandyopadhyay, D.; Bandyopadhyay, P., *J Mol Cat A:Chem.* **2010,** *326*, 94-98.

(23) Biswas, A. N.; Pariyar, A.; Bose, S.; Das, P.; Bandyopadhyay, P., *Catal Comm.11*, (12), 1008-1011.

(24) Brown, E. S.; Robinson, J. R.; McCoy, A. M.; McGaff, R. W., *Dalton Trans.,* **2011,** *40*, (22), 5921-5925.

(25) Sorokin, A. B., *Chem Rev.,* **2013,** *113*, (10), 8152-8191.

(26) Sorokin, A. B.; Kudrik, E. V.; Bouchu, D., *Chem Comm* **2008**, (22), 2562-2564.

(27) Que, L., *Acc Chem Res* **2007,** *40*, (7), 493-500.

(28 Oloo, W. N.; Que, L., *Acc Chem Res.,* **2015** *48*, (9), 2612-2621.

(29) Costas, M.; Mehn, M. P.; Jensen, M. P.; Que, L., *Chem Rev.* **2004,** *104*, (2), 939-986.

(30) Bilis, G.; Christoforidis, K. C.; Deligiannakis, Y.; Louloudi, M., *Catal Today* **2010** *157*, 101-106.

(31) Bigi, J. P.; Harman, W. H.; Lassalle-Kaiser, B.; Robles, D. M.; Stich, T. A.; Yano, J.; Britt, R. D.; Chang, C. J., *J. Am. Chem. Soc.* **2012,** *134*, (3), 1536-1542.

(32) Bukowski, M. R.; Koehntop, K. D.; Stubna, A.; Bominaar, E. L.; Halfen, J. A.; Münck, E.; Nam,W.; Que, L., *Science* **2005,** *310*, (5750), 1000-1002.

(33) Chen, K.; Que, L., *J Am Chem Soc.* **2001,** *123*, (26), 6327-6337.

(34) Company, A.; Gömez, L.; Güell, M.; Ribas, X.; Luis, J. M.; Que, L.; Costas, M., *J Am Chem Soc.***2007**, *129*, (51), 15766-15767.

(35) Kaizer, J. z.; Klinker, E. J.; Oh, N. Y.; Rohde, J.-U.; Song, W. J.; Stubna, A.; Kim, J.; Münck, E.; Nam, W.; Que, L., *J Am Chem Soc.* **2003,** *126*, (2), 472-473.

(36) Krebs, C.; Galoni-Fujimori, D. P.; Walsh, C. T.; Bollinger, J. M., *Acc Chem Res.,* **2007,** *40*, (7), DOI: 10.1021/ar700066p.

(37) Lim, M. H.; Rohde, J.-U.; Stubna, A.; *Proc. Natl. Acad. Sci.* **2003,** *100*, (7), 3665-3670.

(38) Collins, T. J. *Acc. Chem. Res*. **1994**, *27*, 279-285.

(39) Peterson, J. A.; Deisenhofer, J. *Structure (Cambridge, MA, United States)*, **1995**, *3*, 41

(40) Dunford, H. B. *Heme Peroxidases*, Wiley-VCH, New York, **1999**.

(41) Chavez, F. A.; Mascharak, P. K. *Acc. Chem. Res*. **2000**, *33*, 539-545.

(42) Costas, M.; Mehn, M. P.; Jensen, M. P.; Que, L. *Chem. Rev*. **2004**, *104*, 939-986.

(43) MacBeth, C. E.; Golombek, A. P.; Young, V. G.; Yang, C.; Kuczera, K.; Hendrich, M. P.; Borovik, A. S. *Science* **2000**, *289*, 938-941.

(44) Meunier, B.; Bernadou, J. in *Metal-Oxo and Metal-Peroxo Species in Catalytic Oxidations*, Springer Berlin / Heidelberg, **2000**, pp. 1-35.

(45) Nam, W. *Acc. Chem. Res*., **2007**, *40*, 522-531.

(46) Roelfes, G.; Lubben, M.; Hage, R.; Que, J. L.; Feringa, B. L. *Chem. Eur. J.* **2000**, *6*, 2152-2159.

(47) Tshuva, E. Y.; Lippard, S. J. *Chem. Rev.* **2004**, *104*, 987-1012.

(48) White, M. C.; Doyle, A. G.; Jacobsen, E. N. *J. Am. Chem. Soc.* **2001**, *123*, 7194-7195.

(49) Wieghardt, K.; Bossek, U.; Nuber, B.; Weiss, J.; Bonvoisin, J.; Corbella, M.; Vitols, S. E.; Girerd, J. J. *J. Am. Chem. Soc.* **1988**, *110*, 7398-7411.

(50) G. Yin, M. Buchalova, A. M. Danby, C. M. Perkins, D. Kitko, J. D. Carter, W. M. Scheper and D. H. Busch, *J. Am. Chem. Soc.*, **2005**, *127*, 17170-17171.

(51) Hitomi, Y.; Furukawa, S.; Higuchi, M.; Shishido, T.; Tanaka, T., *J Mol Cat A: Chem* **2008**, *288*, 83-86.

(52) Chen, K.; Costas, M.; Que, J. L., *J. Chem. Soc. Dalton Trans* **2002**, (5), 672-679.

(53) Leising, R. A.; Norman, R. E.; Que, L. *Inorg Chem.* **1990**, *29*, (14), 2553-2555.

(54) Arends, I. W. C. E.; Ingold, K. U.; Wayner, D. D. M. *J. Am. Chem. Soc.* **1995**, *117*, (16), 4710-4711.

(55) Kim, J.; Harrison, R. G.; Kim, C.; Que, L. *J. Am. Chem. Soc.* **1996**, *118*, (18), 4373-4379.

(56) Kim, C.; Chen, K.; Kim, J.; Que, L. *J. Am. Chem. Soc.* **1997**, *119*, (25), 5964-5965.

(57) Jensen, M. P.; Lange, S. J.; Mehn, M. P.; Que, E. L.; Que, L., *J Am Chem Soc.* **2003**, 125, (8), 2113-2128.

(58) Kaizer, J.; Costas, M.; Que, L. *Angew Chem. Int. Ed,* **2003**, *42*, (31), 3671-3673.

(59) Chen, M. S.; White, M. C. *Science* **2007**, *318*, (5851), 783-787.

(60) Chen, M. S.; White, M. C. *Science* **2010**, *327*, (5965), 566-571.

(61) Vermeulen, N. A.; Chen, M. S.; Christina White, M. *Tetrahedron* **2009**, *65*, (16), 3078-3084.

(62) Bigi, M. A.; Reed, S. A.; White, M. C. *J. Am. Chem. Soc.* **2012**, *134*, (23), 9721-9726.

(63) Okuno, T.; Ito, S.; Ohba, S.; Nishida, Y. *J. Chem. Soc. Dalton Trans* **1997**, (19), 3547-3551.

(64) Mekmouche, Y.; Ménage, S.; Pécaut, J.; Lebrun, C.; Reilly, L.; Schuenemann, V.; Trautwein, A.; Fontecave, M. *Eur. J. Inorg. Chem.* **2004**, *2004*, (15), 3163-3171.

(65) Mekmouche, Y.; Ménage, S.; Toia-Duboc, C.; Fontecave, M.; Galey, J.-B.; Lebrun, C.; Pécaut, J. *Angew Chem. Int. Ed.* **2001**, *40*, (5), 949-952.

(66) England, J.; Davies, C. R.; Banaru, M.; White, A. J. P.; Britovsek, G. J. P. *Adv. Synth. Catal.* **2008,** *350*, (6), 883-897.

(67) Britovsek, G. J. P.; England, J.; White, A. J. P. *Dalton Trans.* **2006**, (11), 1399-1408.

(68) Britovsek, G. J. P.; England, J.; White, A. J. P., *Inorg Chem.,* **2005,** *44*, (22), 8125-8134.

(69) England, J.; Britovsek, G. J. P.; Rabadia, N.; White, A. J. P. *Inorg. Chem.* **2007,** *46*, (9), 3752-3767.

(70) England, J.; Gondhia, R.; Bigorra-Lopez, L.; Petersen, A. R.; White, A. J. P.; Britovsek, G. J. P. *Dalton Trans.* **2009**, (27), 5319-5334.

(71) de Oliveira, F. T.; Chanda, A.; Banerjee, D.; Shan, X.; Mondal, S.; Que, L.; Bominaar, E. L.; Münck, E.; Collins, T. J., *Science* **2007,** *315*, (5813), 835-838.

(72) Kundu, S.; Thompson, J. V. K.; Ryabov, A. D.; Collins, T. J. *J. Am. Chem. Soc.* **2011,** *133*, (46), 18546-18549.

(73) Ghosh, M.; Singh, K. K.; Panda, C.; Weitz, A.; Hendrich, M. P.; Collins, T. J.; Dhar, B. B.; Sen Gupta, S. *J. Am. Chem. Soc.* **2014,** *136*, (27), 9524-9527.

(74) Singh, K. K.; Tiwari, M. k.; Ghosh, M.; Panda, C.; Weitz, A.; Hendrich, M. P.; Dhar, B. B.; Vanka, K.; Sen Gupta, S. *Inorg. Chem.* **2015***, 54*, (4), 1535-1542.

(75) Singh, K. K.; Tiwari, M. k.; Dhar, B. B.; Vanka, K.; Sen Gupta, S. *Inorg. Chem.* **2015,** *54*, (13), 6112-6121.

(76) Ghosh, M.; Nikhil, Y. L. K.; Dhar, B. B.; Sen Gupta, S. *Inorg. Chem.* **2015,** *54*, (24), 11792-11798.

Chapter VI

Conclusions and Future Direction

6.1 Conclusions

The selective oxidation of water and C–H bonds, which are ubiquitous, represent the most challenging chemical transformation. Nature performs this selective functionalization very efficiently and selectively with different enzymes including the Fe-containing CytP450 and methane monooxygenase. In photosystem II (PS II), a manganese oxo complex has been proposed to be an active intermediate for O-O bond formation step which is a crucial step during oxygen evolution. Detailed study of the natural enzymes and synthetic mimics of natural enzyme demonstrate that the high valent iron-oxo is the reactive intermediate during the enzymatic oxidations. Several efforts have been directed towards the synthesis of biologically inspired metal complexes that mimic the structure and function of these oxidases. For monomeric non-heme iron-catalysed oxidations, $Fe^{IV}(O)$ active intermediates have been isolated and structurally characterized and their reactivity toward C–H bond hydroxylation studied in detail. Functional models of both heme and non-heme iron-dependent monooxygenase enzymes results in formation of weakly reactive $Fe^{IV}(O)$. To achieve higher reactivity, the one electron oxidised $Fe^{V}(O)$ have been synthesised by Collins *et al.* by the oxidation of Fe^{III}-TAML complex at −40 °C using *meta*-chloroperbenzoic acid (*m*CPBA). Study of the reactivity of the $Fe^{V}(O)$ towards strong C–H bonds could not be performed convincingly due to the instability of this species at elevated temperatures. Recently a biuret modified TAML (bTAML) iron complex have been synthesised at room temperature with a half-life of 4hrs. These complexes can react with unactivated C-H bonds and olefins to afford oxidized products but their reactivity has not been correlated to their spectroscopic properties.

Further, the proximal axial ligand in natural enzymes are thought to play an important role in tuning the reactivity of the iron(IV)-oxo porphyrin p-cation radicals (compound I; Cpd I). Interestingly, in the case of thiolate-ligated enzymes (CytP450), it has been observed that the electron donation from the axial ligand to the iron center increases the basicity of the iron-oxo group, thereby allowing a hydrogen atom to be abstracted from C-H bonds by Cpd I under mild conditions. In case of synthetic iron porphyrin complex, the axial electron donating ligand increases the basicity of ferryl species thereby increase the hydrogen atom abstraction rate. For epoxidation reaction, the higher rate has been explained on the basis of ease of oxo transfer from the iron oxo species to olefins. Significant progress in understanding of the electronic and spectroscopic properties of these compounds, and how

they react with C−H bonds in these enzymatic reactions has been performed via both experimental and theoretical investigations.

The thesis describes the comparison of the geometric and electronic structures and reactivities of $[Fe^V(O)]^-$ and $[Fe^{IV}(O)]^{2-}$ species supported by the same ancillary nonheme biuret tetraamido macrocyclic ligand (bTAML). The reactivity difference for HAT from benzyl alcohol by $[Fe^V(O)]^-$ and $[Fe^{IV}(O)]^{2-}$ species has been explained with the help of resonance Raman, EXAFS, electrochemistry, thermodynamic parameter analysis and DFT analysis. We have also studied the detailed mechanism of O-O bond formation reaction which is a crucial step in water oxidation. Electrochemical kinetics analysis and spectroelectrochemical study were performed to understand the active species responsible for O-O bond formation reaction. We also showed the effect of ligand electronics on hydrogen atom transfer (HAT) and oxygen atom transfer (OAT). It was found out that electron rich oxoiron(V) show higher reactivity towards HAT in comparison to some of electron deficient intermediates. Finally, a new iron complex has been synthesized and characterized. The reactivity of this complex will be reported in a separate study.

The key achievement of this thesis work entitled "Spectroscopic and Electrochemical Studies Towards Understanding the Activation of C-H and O-H Bonds by High-valent Metal Oxo Intermediates" can be summarized as follows:

Chapter I:

❖ This chapter presents an overview of the existing literature on the importance of high-valent Fe-oxo intermediate in bio-inspired oxygenation and water oxidation reaction

❖ It describes the mechanism of various metal catalyzed C-H bond hydroxylation and C=C bond epoxidation reaction

❖ A provides a brief outline of synthetic heme and non-heme ligand systems which form both $Fe^{IV}(O)$ and $Fe^V(O)$ complexes. DFT studies were performed to understand the difference in their reactivity

❖ This chapter explained the effect of axial and equatorial ligand on oxygenation reaction by heme and non-heme analog

Chapter II:

❖ This chapter demonstrates the comparison of the geometric and electronic structures and reactivities of $[Fe^{V}(O)]^{-}$ and $[Fe^{IV}(O)]^{2-}$ species supported by the same ancillary nonheme ligand framework

❖ It demonstrates that significant strengthening and shortening of the Fe=O bond upon oxidation from Fe^{IV} to Fe^{V} occurs due to an increase in π bond order and this phenomenon is well supported by resonance Raman, DFT and EXAFS analysis

❖ It illustrates that structural change translates into a significant difference in redox potential between $Fe^{IV}(O)$ and $Fe^{V}(O)$ and a 2500-fold greater reactivity of $Fe^{V}(O)$ over its one-electron analogue $Fe^{IV}(O)$ towards oxidation of benzyl alcohol. DFT calculations provide a computational basis for rationalizing the observed differences in properties

Chapter III:

❖ In this chapter, we demonstrate that $[Fe^{III}\text{-bTAML}]^{1-}$ catalyst can act as a homogeneous electrocatalyst for WO. A CPET process was assigned for $Fe^{IV}(O)$ formation from $Fe^{III}\text{-OH}_2$ and the further oxidation results into $Fe^{V}(O)$, which is responsible for WO

❖ This chapter provides a spectroscopic characterization of the $Fe^{V}(O)$ synthesised by CPE, indicates that oxoiron(V) is solely responsible for WO. KIE of 3.2 and effect of buffer base suggest the APT(Atom Proton Transfer) mechanism. Water oxidation rate is first order with respect to both water and catalyst

❖ Here, FOWA analysis was used to get a 1.2 $M^{-1}s^{-1}$ second order rate constant for water oxidation

❖ This chapter also showed synthesis, characterization, and electrochemical properties of a square planer cobalt complex, capable of catalyzing electrochemical WO at pH = 9.2

❖ Here, we demonstrate that the O–O bond formation step occurs due to the attack of H_2O on a high valent intermediate (probably $[Co(O)bTAML]^{1-})$

Chapter IV:

❖ This chapter illustrates the synthesis and characterization of series of Oxoiron(V) complex having electron rich and electron deficient iron metal

❖ Here we showed the enhanced HAT and OAT reactivity for electron deficient oxoiron(V) due to increase in redox potential of the oxidizing metal ion

❖ This chapter also demonstrates that the higher HAT rate for electron-rich oxoiron(V) is due to the high basicity of ferryl species as has been observed for CytP450. However, the OAT rate enhancement is probably due to the weakening of metal oxo bond due to equatorial donation

Chapter V:

❖ This chapter shows the synthesis and characterization of a new generation iron complex based on a tetrauret modified tetraamido macrocyclic ligand $(PPh_4)[(tTAML)Fe^{III}(Cl)]$. This $[(tTAML)Fe^{III}Cl]^{2-}$ complex was characterized by UV-Vis, HR-MS, EPR and single crystal X-ray diffraction.

6.2 Future Direction

This thesis investigates the reasons underlying the higher reactivity of high valent oxoiron(V) towards C-H abstraction reaction in comparison to its one electron reduced species oxoiron(IV). These oxoiron species is very good hydroxylating intermediate due to fast rebound of ferryl species into carbon-based radical. Recently, carbon-halogen bond formation reactions by several mononuclear non-heme iron enzyme draw the attention of several bioinorganic chemists. In nature, selective arene halogenation is catalyzed by flavin-dependent halogenases,[1] which employ halide salts and air as the halogen source terminal oxidant respectively to form a high spin halo ferric hydroxo intermediate. The very efficient halogenation of C-H bonds by mononuclear nonheme iron (NHFe) enzymes[2] wonder chemists that how it controls the rebound selectivity between hydroxo and chloro group. There has been some effort to obtain synthetic models for the oxoiron(IV)–halide intermediates of the halogenases, but all the synthetic models show very low selectivity towards halogenation over hydroxylation probably due to fast rebound of hydroxo group.[3] The mechanism of halogenation reaction by non-heme halogenase enzyme indicates the necessity of a TBP geometry with *cis* vacant position (Figure 6.1). After careful observation of the halogenation mechanism, we designed a mimic of this halogenase

for carbon-halogen bond formation. The design scheme is depicted in below scheme (Scheme 6.1).
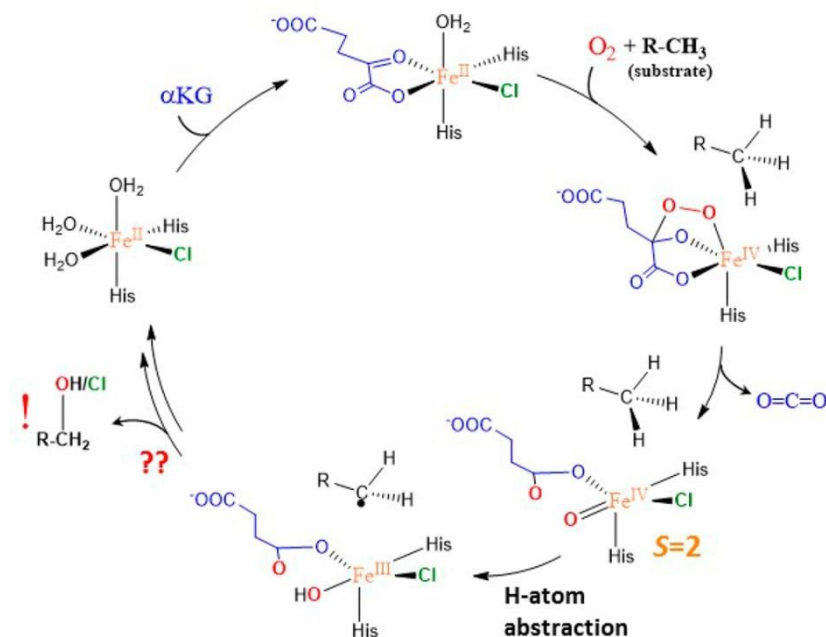
Figure 6.1: Proposed mechanism of halogenation of organic substrate by the SyrB2 halogenase[4] enzyme. This figure has been adapted with permission from ref 5.
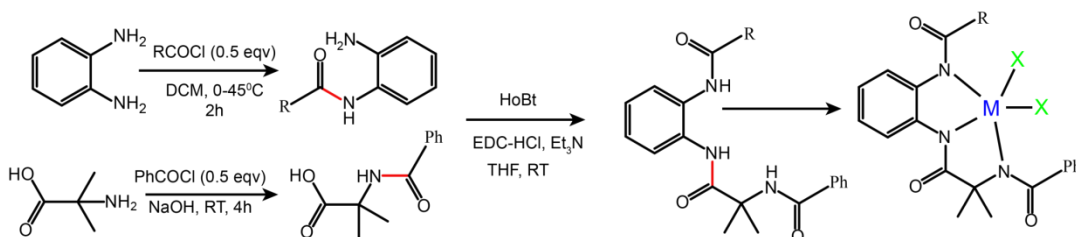
Scheme 6.1: Synthesis route for the acyclic iron complex

6.3 References

(1) van Pée, K. H.; Patallo, E. P. *Appl Microbiol Biotechnol*. **2006**, *70*, 631–641

(2) a). Solomon, E. I.; Brunold, T. C.; Davis, M. I.; Kemsley, J. N.; Lee, S. K.; Lehnert, N.; Neese, F.; Skulan, A. J.; Yang, Y. S.; Zhou, J. *Chem. Rev*. **2000**, *100*, 235– 350; b). Blasiak, L. C.; Vaillancourt, F. H.; Walsh, C. T.; Drennan, C. L. *Nature* **2006**, *440*, 368– 371.

(3) Puri, M.; Biswas, N. A.; Fan, R.; Guo, Y.; Que, L. Jr. *J. Am. Chem. Soc.* **2016**, *138*, 2484–2487.

(4) Vaillancourt, F. H.; Yin, J.; Walsh, C. T. *Proc. Natl. Acad. Sci. U. S. A.* **2005**, *102*, 10111– 10116.

(5) Wong, S. D.; Srnec, M.; Matthews, M. L.; Liu, L. V.; Kwak, Y.; Park, K.; Bell Iii, C. B.; Alp, E. E.; Zhao, J.; Yoda, Y.; Kitao, S.; Seto, M.; Krebs, C.; Bollinger, J. M.; Solomon, E. I. *Nature*, **2013**, *499*, 320.

Appendix A
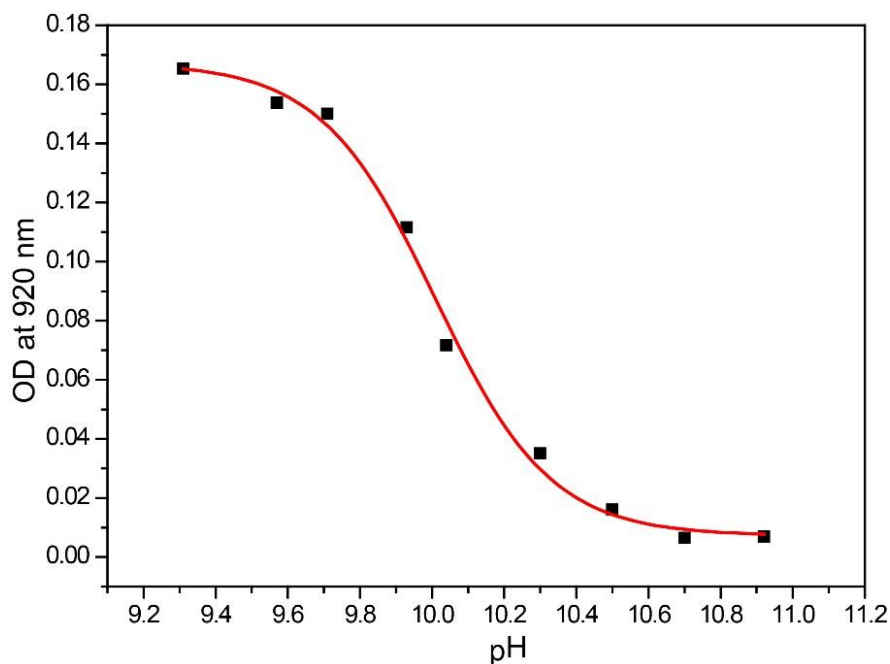
Appendix A1. pK$_a$ determination of **2** in water. The pK$_a$ was determined by monitoring the increase in absorbance at 920 nm due to the formation of μ-O-Fe$^{IV}_2$ upon addition of acid. The following equilibrium takes place:

$$2\ Fe^{IV}(O)^{2-} + 2\ H^+ \rightleftharpoons Fe^{IV}(OH)^{1-} \xrightarrow{\ -H_2O\ } [Fe^{IV}_2O]^{1-}$$
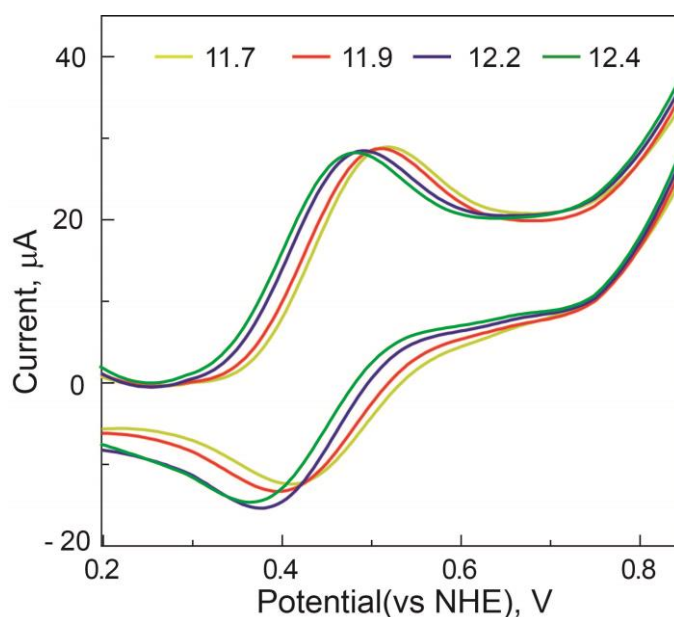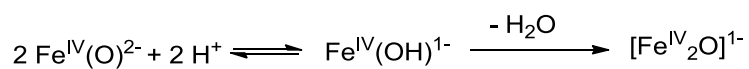
Appendix A2. CVs of 2 mM of [(bTAML)Fe^{III}(Cl)]$^{2-}$ (scan rate 100 mV/s, 0.1 M KNO$_3$ as supporting electrolyte) in between pH 11.7 and 12.4. Scan window of 0.2 to 0.9 V.
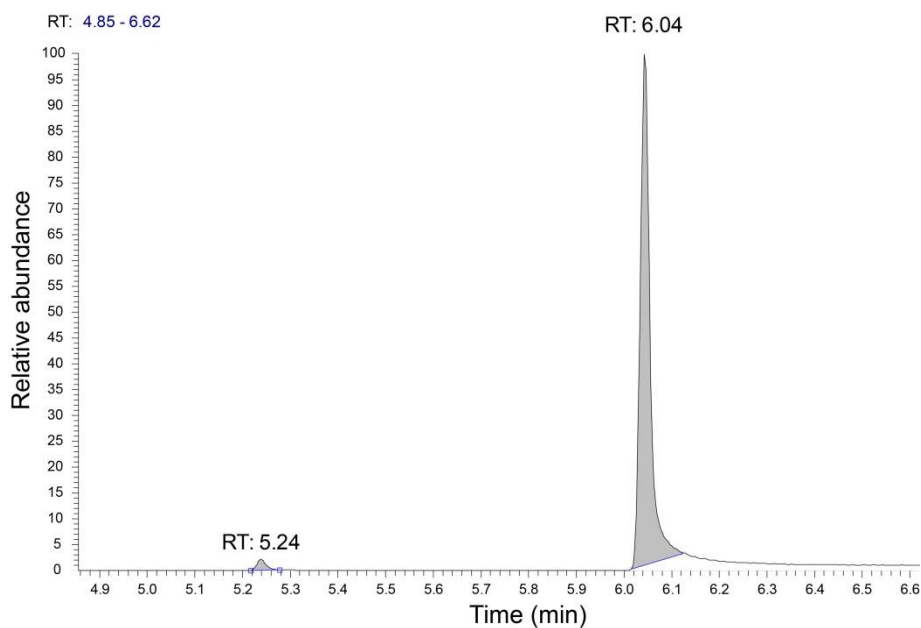
Appendix A3. Gas chromatography traces for the reaction of benzyl alcohol with $[Fe^{IV}(O)]^{2-}$. Chromatogram at 5.24 min and 6.04 min retention time correspond to benzaldehyde and benzyl alcohol respectively.
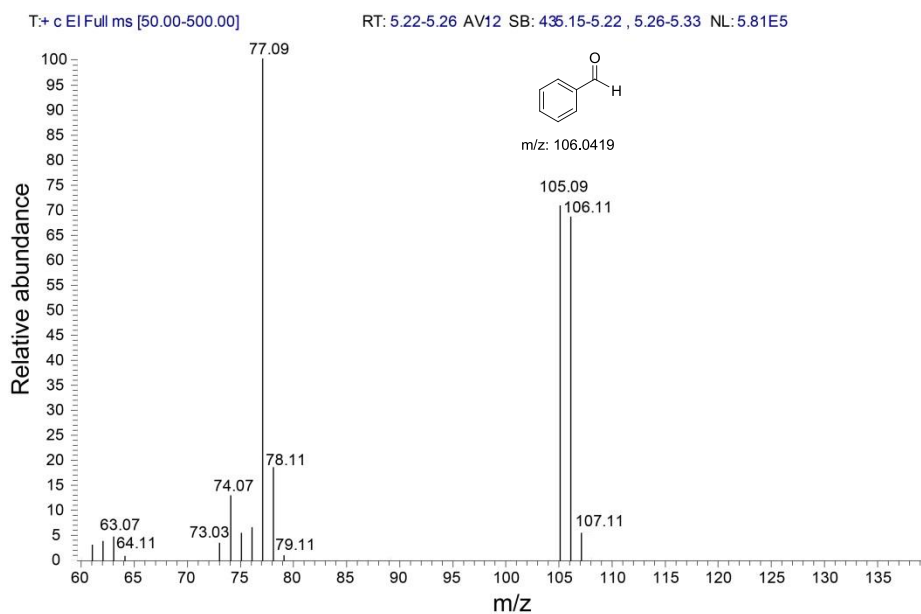
Appendix A4. Mass spectra for benzaldehyde from the reaction of benzyl alcohol with $[Fe^{IV}(O)]^{2-}$

Appendix A5. Fit Parameters of unfiltered XAS data for 1 from k = 2 – 15 Å⁻¹. Fit 8 is the most reasonable fit.

	Fe-N			Fe-Cl			Fe•••C			GOF	
Fit	N	R(Å)	$\sigma^2(10^{-3})$	N	R(Å)	$\sigma^2(10^{-3})$	N	R(Å)	$\sigma^2(10^{-3})$	E_o	F	F'
1	6	1.86	3.17							-1.36	1722	675
2	5	1.86	2.31							-0.95	1579	647
3	4	1.87	1.43							-0.10	1516	633
4	3	1.87	0.46							0.63	1566	644
5	4	1.87	1.45	1	2.38	3.54				-0.62	1224	569
6	4	1.87	1.34	1	2.37	3.10	6	2.83	1.00	-0.03	761	449
7	4	1.87	1.26	1	2.37	3.00	6	2.83	1.21	0.11	620	405
							4	3.99	0.00			
8	**4**	**1.87**	**1.29**	**1**	**2.37**	**3.06**	**6**	**2.83**	**1.15**	**0.06**	**641**	**411**
							5	**3.99**	**1.19**			
9	4	1.87	1.32	1	2.37	3.07	6	2.83	1.02	1.69	673	422
							6	3.83	1.44			

Scale Factor S_0^2=0.9. GOF= Goodness-of-fit calculated as $F = \sqrt{\sum k^6 \left(\chi_{\exp} - \chi_{calc} \right)^2}$

$$F' = \sqrt{\sum k^6 \left(\chi_{\exp} - \chi_{calc} \right)^2 / \sum k^6 \chi_{\exp}^2}$$

Fit 8 gives the most reasonable fit of the experimental data

Appendix A6. Fit Parameters of unfiltered XAS data for 2 from k = 2 – 15 Å⁻¹

	Fe-N			Fe-O			Fe•••C			GOF	
Fit	N	R(Å)	$\sigma^2(10^{-3})$	N	R(Å)	$\sigma^2(10^{-3})$	N	R(Å)	$\sigma^2(10^{-3})$	E_o	F	F'
1	6	1.86	6.04							5.00	1051	702
2	5	1.86	4.48							5.38	903	650
3	4	1.87	3.15							6.70	795	610
4	3	1.87	1.87							8.01	768	599

5	4	1.87	3.06				6	2.83	2.78	5.77	519	493
6	4	1.86	2.69	1	1.64	6.19	6	2.82	2.66	3.39	409	437
7	**4**	**1.86**	**2.67**	**1**	**1.64**	**5.95**	**6**	**2.82**	**2.67**	**3.22**	**345**	**402**
							5	**4.01**	**5.14**			

Scale Factor S_0^2=0.9. GOF= Goodness-of-fit calculated as $F = \sqrt{\sum k^6 (\chi_{exp} - \chi_{calc})^2}$

$$F' = \sqrt{\sum k^6 (\chi_{exp} - \chi_{calc})^2 / \sum k^6 \chi_{exp}^2}$$

Fit 7 gives the most reasonable fit of the experimental data

Appendix A7. Fit Parameters of unfiltered XAS data for 3 from $k = 2 - 15$ Å^{-1}.

		Fe-N			Fe-O			Fe•••C			GOF	
Fit	**N**	**R(Å)**	**$\sigma^2(10^{-3})$**	**N**	**R(Å)**	**$\sigma^2(10^{-3})$**	**N**	**R(Å)**	**$\sigma^2(10^{-3})$**	**E_o**	**F**	**F'**
1	6	1.87	4.85							0.31	1796	853
2	5	1.87	3.06							0.56	1457	769
3	4	1.87	1.82							1.61	1163	687
4	3	1.87	0.58							2.64	957	623
5	4	1.86	2.11	1	1.59	1.56				-0.40	677	524
6	5	1.86	3.41	1	1.60	0.93				-0.95	789	565
7	**4**	**1.86**	**2.19**	**1**	**1.59**	**1.34**	**6**	**2.82**	**2.18**	**-1.63**	**295**	**346**
8	4	1.86	2.17	1	1.59	1.33	5	2.82	1.42	-1.52	291	343
9	4	1.86	2.15	1	1.59	1.32	4	2.83	0.66	-1.25	298	347

Scale Factor S_0^2=0.9. GOF= Goodness-of-fit calculated as $F = \sqrt{\sum k^6 (\chi_{exp} - \chi_{calc})^2}$

$$F' = \sqrt{\sum k^6 (\chi_{exp} - \chi_{calc})^2 / \sum k^6 \chi_{exp}^2}$$

Fit 7 gives the most reasonable fit of the experimental data

XYZ Coordinates for the optimized geometries in Gas Phase

Fe^V(O)_(S = ½) (BP86)

Fe	0.03811100	0.07370500	-0.00044800
O	-0.00935100	-0.00176800	3.97117600
O	4.04984600	0.14101500	0.71339300
O	2.05855000	1.39252600	-3.20596200
O	-3.00301000	1.60191000	-2.14596600
N	-0.60797300	0.25567000	1.73388300
N	1.73443500	0.27503400	0.81852100
N	0.52352100	1.00968800	-1.51227100
N	-1.71383900	0.67542400	-0.43369100
C	-2.00427400	0.39776700	1.86927600
C	0.29181600	0.08415900	2.77019800
C	1.74867200	-0.02902800	2.26994200
C	2.93549900	0.33514400	0.17879400
C	1.80937100	1.04831000	-2.03084300
C	-0.59035200	1.30433700	-2.46880400
C	-1.91930300	1.21409500	-1.67371500
C	-2.64001000	0.63693600	0.61330300
C	-4.03227100	0.84630800	0.54990600
H	-4.48885900	1.04701800	-0.42110600
C	-4.78108300	0.80126100	1.73717900
H	-5.86658200	0.95453100	1.69304000
C	-4.15585900	0.55930000	2.97402500
H	-4.75429800	0.52053000	3.89257600
C	-2.76671400	0.36231500	3.05402600
H	-2.26060500	0.18046300	4.00311500
C	2.58453300	0.97989400	3.09214700
H	3.65467300	0.84979300	2.87869200
H	2.37766600	0.81643400	4.16381400
H	2.29251500	2.01433400	2.83531400
C	2.20810500	-1.48619300	2.53034800
H	3.26981400	-1.58561000	2.25509100

H	1.60877500	-2.17744800	1.91203600
H	2.06505800	-1.73894800	3.59585000
C	4.19357300	0.73047500	-1.90188300
H	4.39732300	1.75359200	-2.26242800
H	4.18777300	0.06031700	-2.77788800
H	4.95235000	0.41985800	-1.17227700
C	-0.66557000	0.23227000	-3.58373400
H	0.21240600	0.30882700	-4.24335500
H	-1.59218200	0.38239100	-4.16555200
H	-0.69260600	-0.77329100	-3.12717500
C	-0.51046800	2.73346500	-3.04834600
H	0.32368400	2.81621800	-3.75850900
H	-0.36177800	3.46512900	-2.23368700
H	-1.47174100	2.95797700	-3.54174200
O	-0.01536700	-1.47477800	-0.37488700
N	2.89705800	0.67660300	-1.21375900

$Fe^V(O)$ (S = 3/2) (BP86)

Fe	0.09085700	0.23822200	0.02084100
O	-0.01233600	-0.06292300	4.02006300
O	4.04445900	0.22336700	0.71805600
O	2.10163000	1.30066800	-3.28059700
O	-3.00606000	1.63046800	-2.11710800
N	-0.63169800	0.14389600	1.77430100
N	1.73939500	0.41573400	0.88070100
N	0.53720400	1.09421400	-1.57521500
N	-1.69151200	0.74268400	-0.39789500
C	-2.01441600	0.32786100	1.89547200
C	0.26971700	0.02346700	2.81340600
C	1.74738300	0.03229800	2.32024100
C	2.92365300	0.37892500	0.18687400
C	1.80170000	1.00158900	-2.10480900
C	-0.60324800	1.35065500	-2.49804000
C	-1.91313400	1.25570000	-1.66108200

C	-2.62530600	0.67373900	0.64298900
C	-4.01439600	0.91359500	0.57556600
H	-4.45339900	1.19003000	-0.38468900
C	-4.78199300	0.79986900	1.74428800
H	-5.86265200	0.98240900	1.69597500
C	-4.18219700	0.45995900	2.97413000
H	-4.79841700	0.37916700	3.87814800
C	-2.80164900	0.22654100	3.06236400
H	-2.31296800	-0.02280600	4.00590100
C	2.52280200	1.05171900	3.18102100
H	3.59431700	1.00634600	2.93644000
H	2.35636900	0.81964600	4.24689900
H	2.15402300	2.07477400	2.98546600
C	2.28786800	-1.40787500	2.51454200
H	3.35851800	-1.44159500	2.26115200
H	1.73743000	-2.09571100	1.84886000
H	2.13712800	-1.71904500	3.56311200
C	4.16349300	0.52431900	-1.91624900
H	4.55655800	1.53602600	-2.12916500
H	4.03806500	0.00325300	-2.87700200
H	4.85907700	-0.00302000	-1.25163100
C	-0.69573000	0.25653600	-3.59285900
H	0.17376200	0.32771400	-4.26424100
H	-1.62951200	0.38815100	-4.16719400
H	-0.70133200	-0.73793800	-3.11318100
C	-0.53415900	2.76438500	-3.11203100
H	0.32860600	2.83046000	-3.79141600
H	-0.42162000	3.52154900	-2.31526700
H	-1.47382000	2.96634400	-3.65412400
O	0.28503700	-1.30854000	-0.50167400
N	2.86353600	0.59112700	-1.23372300

Fe^{IV}(O)_(S = 1) (BP86)

| Fe | 0.06225900 | 0.24826400 | 0.03785000 |
| O | 0.03211900 | -0.04473700 | 4.05282400 |

O	4.07726200	0.24381200	0.72601700
O	2.13182600	1.35498400	-3.28427600
O	-3.00162700	1.65514300	-2.16221700
N	-0.62073700	0.23291400	1.81486900
N	1.75686200	0.41587800	0.86182000
N	0.55974200	1.09142700	-1.57411100
N	-1.69711500	0.83510800	-0.39004000
C	-2.00812800	0.40035800	1.91687000
C	0.27502300	0.05982500	2.82588000
C	1.74605900	-0.03043400	2.28385500
C	2.94588700	0.45534400	0.20696600
C	1.81697900	1.09250400	-2.09109400
C	-0.58955500	1.28700100	-2.50022800
C	-1.91332900	1.28686300	-1.65715700
C	-2.62259700	0.74397600	0.65785400
C	-4.01350300	0.97345000	0.59913800
H	-4.44597900	1.24684000	-0.36692000
C	-4.79195000	0.85880400	1.76796000
H	-5.87629900	1.03489700	1.71396800
C	-4.19297900	0.52369900	2.99556100
H	-4.80816500	0.43719500	3.90320500
C	-2.80459200	0.29725100	3.07695600
H	-2.30737100	0.05040000	4.01871000
C	2.62355700	0.84902200	3.20166100
H	3.68759600	0.70099400	2.96478400
H	2.40418900	0.59031700	4.25320700
H	2.37382800	1.91627300	3.04929100
C	2.15150500	-1.52395500	2.37425200
H	3.21165600	-1.63568400	2.08965400
H	1.51975000	-2.08977200	1.66610900
H	1.99075900	-1.90197100	3.40178900
C	4.21284000	0.87069700	-1.85861500
H	4.38552500	1.87566500	-2.28807900
H	4.26916300	0.14929700	-2.69501000

H	4.96432900	0.63799900	-1.09096800
C	-0.68981700	0.08944700	-3.47994300
H	0.18125300	0.09784900	-4.15730300
H	-1.62798200	0.14812600	-4.06408100
H	-0.68049900	-0.84033600	-2.88308900
C	-0.52805000	2.63019600	-3.25977400
H	0.31456700	2.62168400	-3.96736900
H	-0.37898500	3.46054600	-2.54363900
H	-1.49069900	2.79008700	-3.77806500
O	-0.00255300	-1.34302100	-0.36381700
N	2.90901100	0.80372800	-1.19763900

Fe^{IV}(O)_(S = 2) (BP86)

Fe	0.06761200	-0.17136700	-0.09604900		H	-4.82910500	0.00439800	3.81787400
O	-0.01010600	-0.01384000	3.99242200		C	-2.83543300	-0.15143200	2.96468100
O	4.07696300	0.36610600	0.70509300		H	-2.38107200	-0.61446300	3.84451800
O	2.15972400	1.21949100	-3.33985600		C	2.34314100	1.29874700	2.99796600
O	-2.92475100	1.86103900	-2.07461400		H	3.41498300	1.37355800	2.75500000
N	-0.64032900	-0.17941100	1.74091700		H	2.18740100	1.20092500	4.08671200
N	1.74255700	0.23434900	0.80571100		H	1.83418700	2.21801100	2.65452400
N	0.57761800	0.83119800	-1.67050900		C	2.47167100	-1.22444200	2.71089800
N	-1.63101200	1.01900400	-0.30144800		H	3.53949200	-1.14816900	2.44889000
C	-2.01537300	0.10906500	1.85079400		H	2.03358300	-2.09345600	2.18554500
C	0.25111400	-0.05329600	2.76673900		H	2.34646300	-1.37353200	3.79962400
C	1.73619200	0.07012800	2.27872000		C	4.23693500	0.46045000	-1.87710100
C	2.93553000	0.36825000	0.16650300		H	4.82063300	1.37466000	-1.64458100
C	1.83424500	0.87594400	-2.17100800		H	4.09423200	0.39455300	-2.96484300
C	-0.56827000	1.31823700	-2.47952900		H	4.80769300	-0.39837900	-1.48560900
C	-1.85563300	1.43061900	-1.56843700		C	-0.89324100	0.30024500	-3.59904900
C	-2.56704800	0.77400400	0.69051400		H	-0.05373000	0.26417700	-4.31550200
C	-3.94089800	1.11496600	0.68483900		H	-1.82685800	0.58864200	-4.11611700
H	-4.33524000	1.60490400	-0.20999300		H	-1.02348900	-0.69041600	-3.12781100
C	-4.74464200	0.83128000	1.80406900		C	-0.32216000	2.73105800	-3.05832100
H	-5.81024300	1.10548200	1.78715000		H	0.47340100	2.70564800	-3.81850300
C	-4.19766600	0.21051700	2.94145200		H	-0.01513500	3.42046500	-2.24910400

H	-1.27287600	3.09701500	-3.48552300
O	-0.68612100	-1.50223900	-0.74887500
N	2.90609200	0.48526200	-1.27115700

Fe^V(O)_(S = ½) (B3LYP)

Fe	0.02380000	-0.06578700	-0.01563400
O	0.00800400	0.20511000	3.92521500
O	4.03573500	-0.07048900	0.71407700
O	2.04556000	1.40262200	-3.15583400
O	-2.99619700	1.42523400	-2.17741000
N	-0.59046600	0.25387100	1.70106200
N	1.75635900	0.09501000	0.79222400
N	0.51459600	0.79470500	-1.58748900
N	-1.70931900	0.57586400	-0.45930300
C	-1.98578100	0.38511100	1.83712800
C	0.30633100	0.16996900	2.74087000
C	1.75555100	0.01106900	2.26834800
C	2.94234700	0.03833200	0.14872300
C	2.92900000	0.05821800	-1.39853000
C	1.79252300	0.83948900	-2.09294100
C	-0.59805600	1.26445400	-2.46667700
C	-1.92061000	1.08334300	-1.69903700
C	-2.62737900	0.55781700	0.58837300
C	-4.01295700	0.73275000	0.52434800
H	-4.48046000	0.88030100	-0.43841100
C	-4.74996500	0.72188900	1.70728800
H	-5.82802700	0.84974200	1.66330700
C	-4.11872000	0.54690800	2.93871700
H	-4.70479200	0.53703800	3.85337500
C	-2.73586300	0.38289800	3.01747600
H	-2.23513900	0.25743600	3.96514400
C	2.56203200	1.15277100	2.92025900
H	3.62083600	1.03618800	2.70414600
H	2.39245100	1.14196300	3.99880300

H	2.22933000	2.11882000	2.52922500
C	2.24600300	-1.36727200	2.76063200
H	3.29722700	-1.49266300	2.50689500
H	1.66982400	-2.16351500	2.28187700
H	2.11321400	-1.44359900	3.84223000
C	4.27228600	0.63020000	-1.88522600
H	4.38065000	1.67997300	-1.60166500
H	4.33480300	0.57072400	-2.97104000
H	5.08997700	0.07503700	-1.42935300
C	2.82063900	-1.41718100	-1.87426100
H	1.89648500	-1.88825500	-1.53955300
H	3.66307900	-1.98573600	-1.47184600
H	2.86348600	-1.46118700	-2.96630600
C	-0.68717000	0.43042000	-3.75750300
H	0.17278000	0.61794100	-4.39782300
H	-1.60500200	0.69379600	-4.28737200
H	-0.72471500	-0.63530300	-3.51508400
C	-0.49076000	2.77224400	-2.77394200
H	0.36163200	2.97230300	-3.41765800
H	-0.36990900	3.33659400	-1.84479600
H	-1.41440500	3.09974800	-3.25521900
O	-0.11401200	-1.60857900	-0.28057500

Fe^V(O) (S = 3/2) (B3LYP)

Fe	0.08621500	0.20425900	0.01281100
O	0.00310800	0.08648000	4.00150300
O	4.02303600	0.19883000	0.68083900
O	2.09620300	1.26813400	-3.26693000
O	-2.95750900	1.74076000	-2.06134400
N	-0.62156300	0.18517500	1.77531700
N	1.74253400	0.41932600	0.85806200
N	0.55572500	1.08560400	-1.57031000
N	-1.67929100	0.77728200	-0.38988800
C	-2.01719400	0.30638800	1.88122000

C	0.27787700	0.12482000	2.80245100
C	1.74694600	0.10164500	2.30988900
C	2.91290000	0.35156800	0.15775700
C	1.80791200	0.96660100	-2.10278000
C	-0.58658700	1.39925200	-2.46824600
C	-1.88305500	1.33141600	-1.62251200
C	-2.62185300	0.64516100	0.64334600
C	-4.00714900	0.82431100	0.56110600
H	-4.44807700	1.09645700	-0.38853000
C	-4.78039700	0.66194300	1.71464300
H	-5.85792100	0.79923700	1.65532900
C	-4.18493000	0.32822600	2.93370700
H	-4.79888900	0.20567000	3.82335100
C	-2.80159500	0.14872100	3.02913300
H	-2.32060000	-0.09555800	3.96682700
C	2.53053300	1.15490700	3.11226300
H	3.59294400	1.09559900	2.87259700
H	2.36929500	0.97885700	4.18005000
H	2.16796900	2.16048600	2.87008800
C	2.27605700	-1.32581900	2.57546800
H	3.33544100	-1.38655400	2.32082200
H	1.72020900	-2.04334600	1.96186700
H	2.13044600	-1.57554300	3.63161000
C	4.14659500	0.36210500	-1.93303100
H	4.67682300	1.32098100	-1.98959200
H	3.97038500	0.00695500	-2.94696000
H	4.75514000	-0.33889700	-1.36564000
C	-0.73635900	0.34185700	-3.58502200
H	0.11625100	0.39035200	-4.26446500
H	-1.66433100	0.52627000	-4.13631900
H	-0.78135300	-0.65804600	-3.13961000
C	-0.47118500	2.82093600	-3.04479000
H	0.37379600	2.87917000	-3.73203900
H	-0.32105400	3.54491800	-2.23572700

H	-1.40255300	3.07076800	-3.56179600
O	0.18746300	-1.34253600	-0.46279200
N	2.85267600	0.50282800	-1.25612000

$Fe^{IV}(O)\_(S = 1)$ (B3LYP)

Fe	0.05803100	0.20579800	0.02887600
O	0.03488700	-0.03150600	4.02844500
O	4.05569200	0.24155400	0.71536900
O	2.12593200	1.33352900	-3.26474300
O	-2.97566900	1.66465100	-2.14490000
N	-0.62080400	0.22337700	1.81049600
N	1.75649400	0.39316800	0.85470900
N	0.56200000	1.06756100	-1.57904800
N	-1.69521700	0.82516600	-0.39205700
C	-2.00500600	0.38609200	1.90627300
C	0.27175200	0.06485200	2.81114300
C	1.74192300	-0.01530400	2.28096300
C	2.93258300	0.43515000	0.19927300
C	1.81157900	1.06429100	-2.08490300
C	-0.58494100	1.29713400	-2.48930200
C	-1.90127100	1.28753400	-1.64440700
C	-2.61560900	0.72831300	0.65429200
C	-3.99818700	0.94949400	0.59539100
H	-4.43284800	1.22022300	-0.35922700
C	-4.77435100	0.83054600	1.75647600
H	-5.84979100	1.00204800	1.70118500
C	-4.17998200	0.49730300	2.97534300
H	-4.78983800	0.40771300	3.87484300
C	-2.79808600	0.27673900	3.05647000
H	-2.31142900	0.03084800	3.99254300
C	2.59514100	0.90577100	3.17450500
H	3.65316300	0.78866600	2.93670700
H	2.39975800	0.66544800	4.22492500
H	2.31350000	1.95327400	3.00517300
C	2.17525300	-1.49240700	2.42335300

H	3.22849900	-1.59608500	2.14758600
H	1.56411000	-2.09630100	1.74377300
H	2.02201300	-1.83467500	3.45453500
C	4.19583700	0.79625300	-1.87076500
H	4.40035000	1.79786100	-2.26971100
H	4.21655200	0.10381200	-2.71975400
H	4.94671700	0.52280900	-1.13274000
C	-0.70753300	0.13939400	-3.50675300
H	0.15309800	0.15131800	-4.18160600
H	-1.63701600	0.23555200	-4.08207000
H	-0.71734200	-0.80606100	-2.95357100
C	-0.51119100	2.66005000	-3.20402700
H	0.33032500	2.67362700	-3.89812900
H	-0.36814700	3.46031500	-2.46627000
H	-1.45573200	2.84287400	-3.72733500
O	-0.00167500	-1.36391500	-0.37035700
N	2.89750900	0.75410500	-1.20335300

Fe^{IV}(O)_(S = 2) (B3LYP)

Fe	0.05413700	-0.19599800	-0.10599900
O	0.00447700	-0.02011900	3.97960400
O	4.05869600	0.37820200	0.68652300
O	2.16308400	1.23357700	-3.30857500
O	-2.91040100	1.85480000	-2.06360200
N	-0.64540600	-0.16633100	1.75257100
N	1.74994500	0.19988600	0.80393600
N	0.57529300	0.83713400	-1.67199300
N	-1.65141100	0.94126900	-0.32731700
C	-2.01583300	0.11690100	1.85553700

C	0.24869800	-0.05800700	2.76083500
C	1.73292400	0.06435000	2.27377300
C	2.92515100	0.35299200	0.15996500
C	1.82623600	0.87189200	-2.16134200
C	-0.56726700	1.33285400	-2.46998500
C	-1.85811800	1.40226500	-1.56961300
C	-2.57547000	0.73253700	0.68188400
C	-3.94044500	1.06705400	0.67128300
H	-4.34134600	1.52782400	-0.22396900
C	-4.73543500	0.81697300	1.79588900
H	-5.79254900	1.08538200	1.77425100
C	-4.18541900	0.23592500	2.94069300
H	-4.80753100	0.05350600	3.81737300
C	-2.82850400	-0.11481200	2.97056400
H	-2.37573400	-0.54525600	3.85587500
C	2.32209700	1.30954300	2.97099000
H	3.38272400	1.40132700	2.72735800
H	2.17713800	1.22942900	4.05294800
H	1.80150300	2.20881800	2.61949400
C	2.47443400	-1.21095200	2.73369400
H	3.53566700	-1.13500400	2.48426900
H	2.05359100	-2.08684000	2.22411400
H	2.34455600	-1.34345100	3.81448500
C	4.20472900	0.40479600	-1.89782200
H	4.74020200	1.36293200	-1.81834900
H	4.07277700	0.17423100	-2.95409300
H	4.80949300	-0.35274800	-1.39654600
C	-0.87186600	0.35787300	-3.62714800
H	-0.03197400	0.34861600	-4.32920000
H	-1.79151800	0.65677000	-4.14352500
H	-1.00263500	-0.64557900	-3.20758900
C	-0.32881200	2.76377100	-2.99458000
H	0.47747000	2.77364000	-3.72981600

| H | -0.05071400 | 3.42298500 | -2.16217200 |
H	-1.26129500	3.13601600	-3.43148800
O	-0.53951900	-1.58321000	-0.73036400
N	2.88520900	0.45019400	-1.27520700

Appendix B
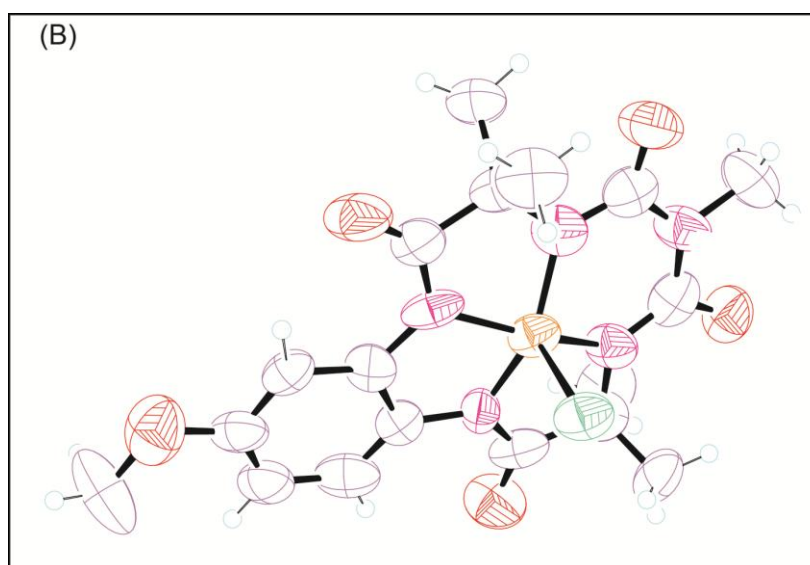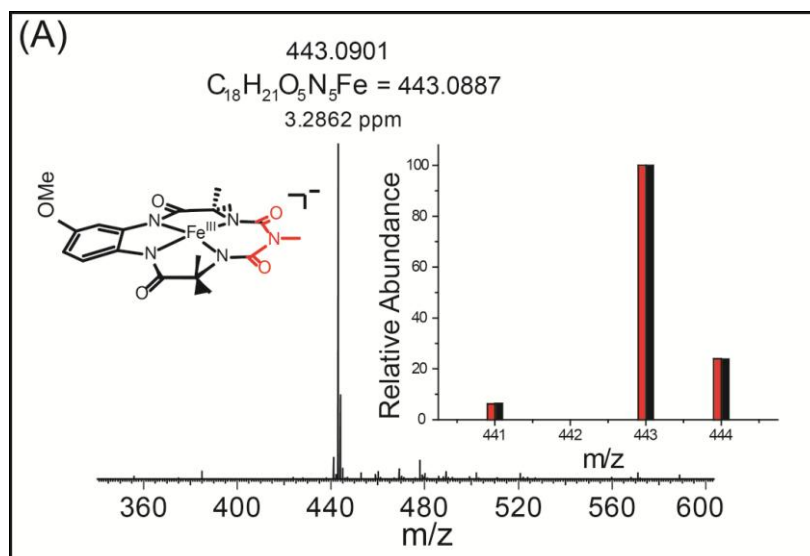
Appendix B1: High resolution mass spectrum of **1b** in CH$_3$CN (*m/z* 443.0887). Inset shows comparison of simulated (red bars) and observed (black bars) isotopic distribution pattern for ion of interest ("3.2862 ppm" represents resolution and the number refers to the error associated with the experiment). The axial ligand was not observed as this ligand is labile and gets dissociated under the conditions of the mass spectrometry experiment. (B) Thermal ellipsoid (50%) structure of **1b**(counter cations and other solvent molecules are omitted for clarity).
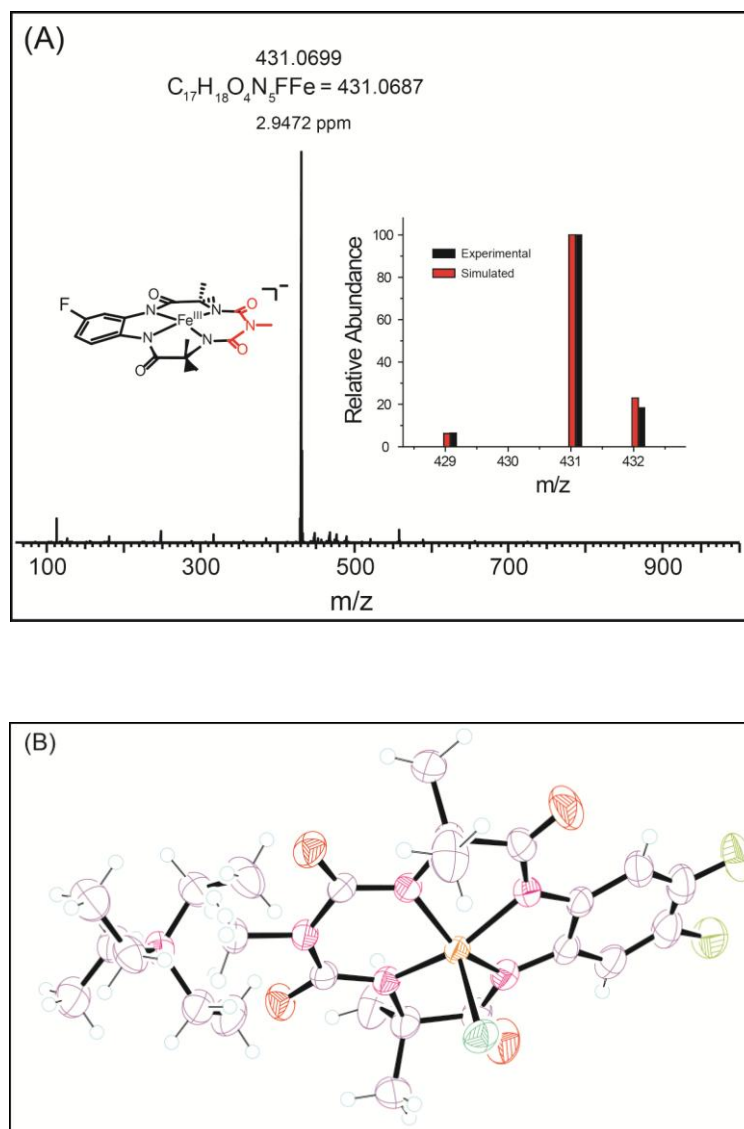
Appendix B2: (A) High resolution mass spectrum of **1c** in CH₃CN (*m/z* 431.0687). Inset shows comparison of simulated (red bars) and observed (black bars) isotopic distribution pattern for ion of interest ("2.9472 ppm" represents resolution and the number refers to the error associated with the experiment). The axial ligand was not observed as this ligand is labile and gets dissociated under the conditions of the mass spectrometry experiment. (B) Thermal ellipsoid structure of **1c** with disorder (counter cations and other solvent molecules omitted for clarity). The chemical occupancy of the substituent (-F) in each of the positions was 50%, indicating the equal probability of finding the substituent on both the positions, and the overall chemical composition is one per macrocycle.
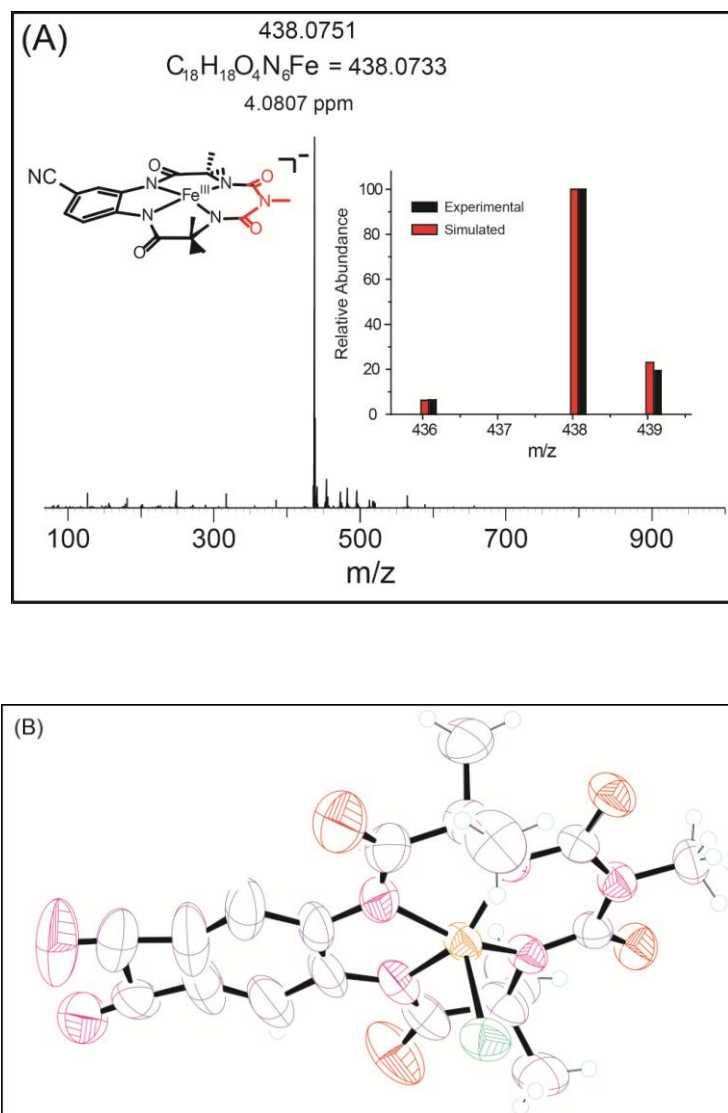
Appendix B3: (A) High resolution mass spectrum of **1e**in CH$_3$CN (*m/z* 438.0733). Inset shows comparison of simulated (red bars) and observed (black bars) isotopic distribution pattern for ion of interest ("4.0807 ppm" represents resolution and the number refers to the error associated with the experiment). The axial ligand was not observed as this ligand is labile and gets dissociated under the conditions of the mass spectrometry experiment. (B) Thermal ellipsoid structure of **1e** with disorder (counter cations and other solvent molecules omitted for clarity).The chemical occupancy of the substituent (-CN) in each of the positions was 50%, indicating the equal probability of finding the substituent on both the positions, and the overall chemical composition is one per macrocycle.

(A)

447.0410
$C_{17}H_{18}O_4N_5ClFe = 447.0391$
4.2284 ppm

(B)
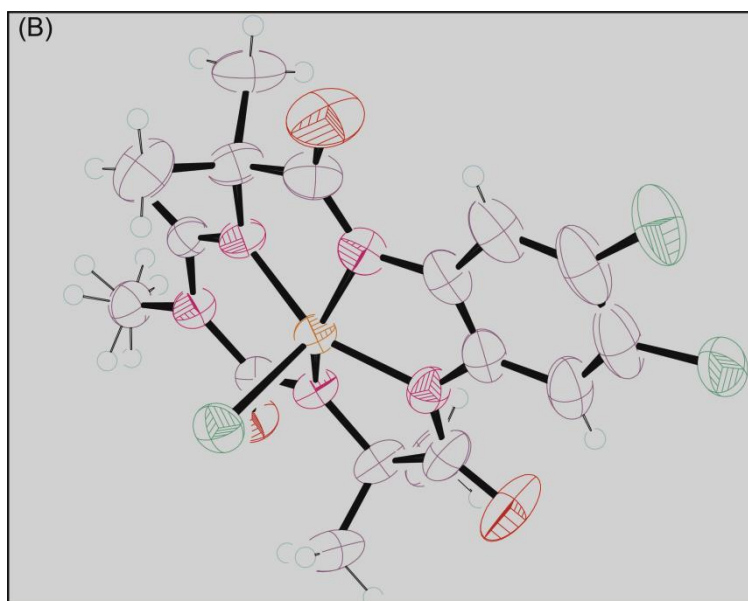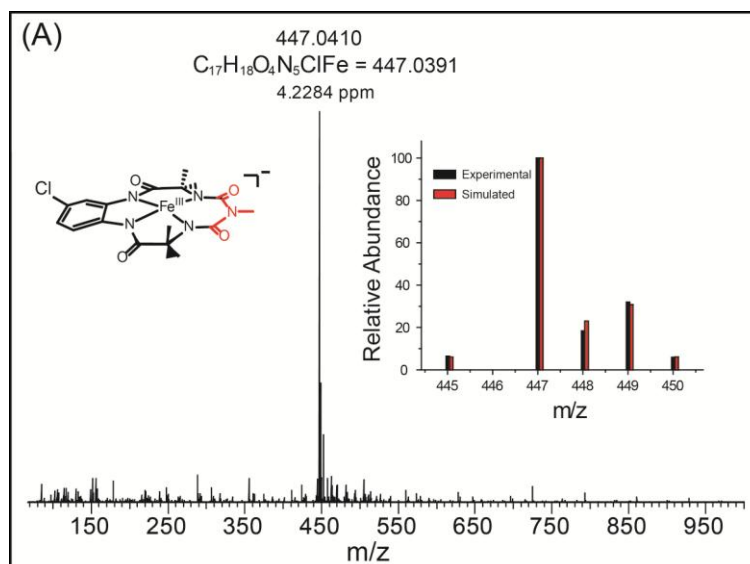
Appendix B4: High resolution mass spectrum of **1d** in CH$_3$CN (*m/z* 447.0391). Inset shows comparison of simulated (red bars) and observed (black bars) isotopic distribution pattern for ion of interest ("4.2284 ppm" represents resolution and the number refers to the error associated with the experiment). The axial ligand was not observed as this ligand is labile and gets dissociated under the conditions of the mass spectrometry experiment. (B) Thermal ellipsoid structure of **1d** with disorder (counter cations and other solvent molecules omitted for clarity). The chemical occupancy of the substituent (-Cl) in each of the positions was 50%, indicating the equal probability of finding the substituent on both the positions, and the overall chemical composition is one per macrocycle.
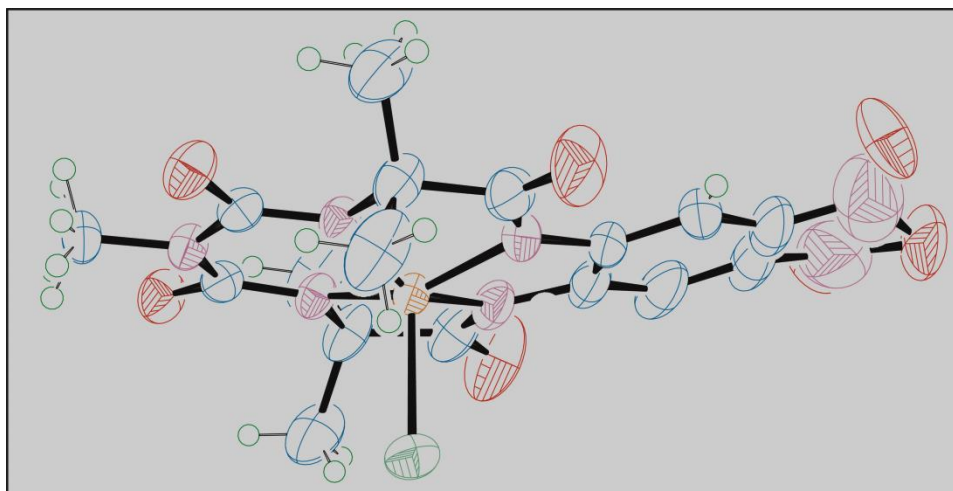
Appendix B5a: Thermal ellipsoid structure of **1f** with disorder (counter cations omitted for clarity). The chemical occupancy of the substituent (-NO$_2$) in each of the positions was 50%, indicating the equal probability of finding the substituent on both the positions, and the overall chemical composition is one per macrocycle.
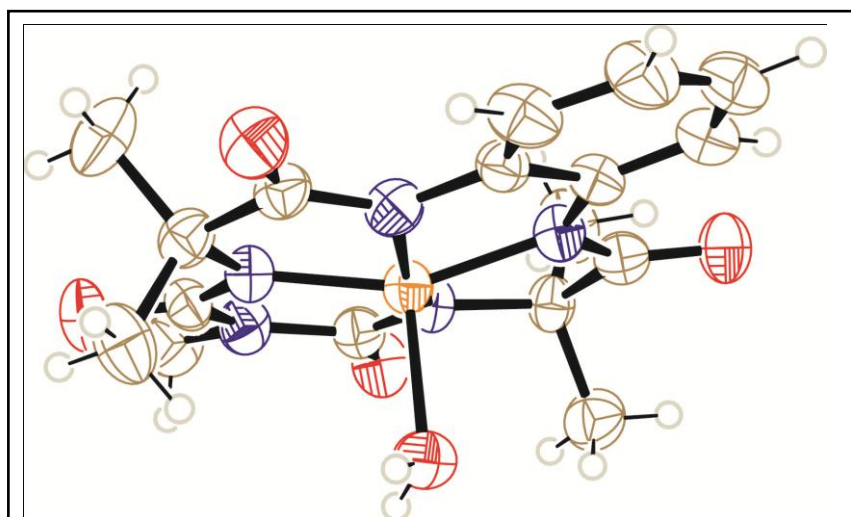
Appendix B5b: Thermal ellipsoid structure of **1a**-H$_2$Owith disorder (counter cations omitted for clarity).

Appendix B6: Crystal data and structure refinement for**1b.**

Identification code	OMe-Fe(III)-bTAML(**1b**)
Empirical formula	$C_{34} H_{59} Cl Fe N_7 O_6$
Formula weight	753.18
Temperature/K	298
Crystal system	monoclinic
Space group	$P2_1/c$
a/Å	13.229(2)
b/Å	15.5311(15)
c/Å	22.979(4)
α/°	90.00
β/°	123.558(12)
γ/°	90.00
Volume/Å^3	3934.4(10)
Z	4
ρ_{calc}mg/mm^3	1.272
m/mm^{-1}	0.501
F(000)	1612
Crystal size/mm^3	$0.5 \times 0.2 \times 0.2$
2Θ range for data collection	5.94 to 58.36°
Index ranges	$-18 \le h \le 16, -19 \le k \le 19, -28 \le l \le 30$
Reflections collected	19907
Independent reflections	9134[R(int) = 0.2636]
Data/restraints/parameters	9134/0/452
Goodness-of-fit on F^2	0.915
Final R indexes [I>=2σ (I)]	$R_1 = 0.1493$, w$R_2 = 0.3352$
Final R indexes [all data]	$R_1 = 0.3448$, w$R_2 = 0.4560$
Largest diff. peak/hole / e Å^{-3}	0.69/-0.70

Appendix B7: Crystal data and structure refinement for **1c**

Identification code	F-Fe(III)-bTAML (**1c**)
Empirical formula	$C_{66}H_{70}Cl_2F_2Fe_2N_{14}O_{10}$
Formula weight	1438.34
Temperature/K	298
Crystal system	tetragonal
Space group	$P4_2/mbc$
a/Å	22.1471(6)
b/Å	22.1471(6)
c/Å	15.1435(7)
α/°	90.00
β/°	90.00
γ/°	90.00
Volume/Å^3	7427.8(5)
Z	4
ρ_{calc}mg/mm^3	1.288
m/mm^{-1}	0.530
F(000)	2992
Crystal size/mm^3	$0.5 \times 0.2 \times 0.2$
2Θ range for data collection	5.82 to 58.32°
Index ranges	$-29 \leq h \leq 27$, $-26 \leq k \leq 24$, $-20 \leq l \leq 14$
Reflections collected	23756
Independent reflections	4755[R(int) = 0.0397]
Data/restraints/parameters	4755/0/275
Goodness-of-fit on F^2	1.059
Final R indexes [I>=2σ (I)]	$R_1 = 0.0611$, $wR_2 = 0.1682$
Final R indexes [all data]	$R_1 = 0.0844$, $wR_2 = 0.1888$
Largest diff. peak/hole / e Å^{-3}	0.73/-0.44

Appendix B8:Crystal data and structure refinement for **1d**

Identification code	Cl-Fe(III)-bTAML(**1d**)
Empirical formula	$C_{64} H_{60} Cl_4 Fe_2 N_{14} O_{10}$
Formula weight	1438.76
Temperature/K	298
Crystal system	tetragonal
Space group	$P4_2/mbc$
a/Å	22.3720(5)
b/Å	22.3720(5)
c/Å	15.1613(5)
α/°	90.00
β/°	90.00
γ/°	90.00
Volume/Å^3	7588.3(3)
Z	4
ρ_{calc}mg/mm^3	1.259
m/mm^{-1}	0.583
F(000)	2968.0
Crystal size/mm^3	$0.5 \times 0.2 \times 0.2$
2Θ range for data collection	5.8 to 58.1°
Index ranges	$-25 \leq h \leq 26, -17 \leq k \leq 30, -11 \leq l \leq 20$
Reflections collected	23535
Independent reflections	4695[R(int) = 0.0531]
Data/restraints/parameters	4695/0/268
Goodness-of-fit on F^2	1.036
Final R indexes [I>=2σ (I)]	$R_1 = 0.0713, wR_2 = 0.2087$
Final R indexes [all data]	$R_1 = 0.0917, wR_2 = 0.2309$
Largest diff. peak/hole / e Å^{-3}	0.76/-0.47

Appendix B9:Crystal data and structure refinement for **1e**

Identification code	CN-Fe(III)-bTAML(**1e**)
Empirical formula	$C_{68} H_{69} Cl_2 Fe_2 N_{16} O_9$
Formula weight	1436.99
Temperature/K	298
Crystal system	tetragonal
Space group	$P4_2/mbc$
a/Å	22.5907(5)
b/Å	22.5907(5)
c/Å	15.1389(5)
α/°	90.00
β/°	90.00
γ/°	90.00
Volume/Å^3	7726.0(3)
Z	4
ρ_{calc}mg/mm^3	1.235
m/mm^{-1}	0.506
F(000)	2988
Crystal size/mm^3	$0.5 \times 0.2 \times 0.2$
2Θ range for data collection	6.3 to 58.02°
Index ranges	$-30 \leq h \leq 19, -26 \leq k \leq 13, -19 \leq l \leq 11$
Reflections collected	18513
Independent reflections	4815[R(int) = 0.0477]
Data/restraints/parameters	4815/0/271
Goodness-of-fit on F^2	1.052
Final R indexes [I>=2σ (I)]	$R_1 = 0.0969$, w$R_2 = 0.2767$
Final R indexes [all data]	$R_1 = 0.1343$, w$R_2 = 0.3139$
Largest diff. peak/hole / e Å^{-3}	0.91/-0.45

Appendix B10:Crystal data and structure refinement for **1f**

Identification code	NO$_2$-Fe(III)-bTAML(**1f**)
Empirical formula	C$_{67}$ H$_{66}$ Cl$_2$ Fe$_2$ N$_{18}$ O$_{12}$
Formula weight	1497.98
Temperature/K	298
Crystal system	tetragonal
Space group	*P*4$_2$/mbc
a/Å	22.3478(4)
b/Å	22.3478(4)
c/Å	15.1619(4)
α/°	90.00
β/°	90.00
γ/°	90.00
Volume/Å^3	7572.2(3)
Z	4
ρ$_{calc}$mg/mm^3	1.314
m/mm^{-1}	0.522
F(000)	3104.0
Crystal size/mm^3	$0.5 \times 0.2 \times 0.2$
2Θ range for data collection	5.96 to 58.32°
Index ranges	-15 ≤ h ≤ 29, -28 ≤ k ≤ 30, -20 ≤ l ≤ 19
Reflections collected	22792
Independent reflections	4825[R(int) = 0.0748]
Data/restraints/parameters	4825/0/274
Goodness-of-fit on F^2	1.066
Final R indexes [I>=2σ (I)]	R$_1$ = 0.1002, wR$_2$ = 0.2942
Final R indexes [all data]	R$_1$ = 0.1331, wR$_2$ = 0.3180
Largest diff. peak/hole / e Å^{-3}	2.15/-0.65

Appendix B11:Crystal data and structure refinement for **2a**

Empirical formula	$C_{41}H_{51}FeN_5O_{10}P$
Formula weight	860.69
Temperature/K	298
Crystal system	triclinic
Space group	P-1
a/Å	13.0126(10)
b/Å	13.0978(6)
c/Å	14.5680(10)
α/°	66.670(6)
β/°	68.921(7)
γ/°	83.126(5)
Volume/Å^3	2126.6(2)
Z	2
ρ_{calc}mg/mm^3	1.344
m/mm^{-1}	0.454
F(000)	906.0
Crystal size/mm^3	$0.5 \times 0.5 \times 0.2$
2Θ range for data collection	5.8 to 58.36°
Index ranges	$-17 \leq h \leq 17$, $-15 \leq k \leq 17$, $-19 \leq l \leq 18$
Reflections collected	16562
Independent reflections	9555[R(int) = 0.0445]
Data/restraints/parameters	9555/0/540
Goodness-of-fit on F^2	1.074
Final R indexes [I>=2σ (I)]	$R_1 = 0.0727$, $wR_2 = 0.2023$
Final R indexes [all data]	$R_1 = 0.1082$, $wR_2 = 0.2740$
Largest diff. peak/hole / e Å^{-3}	0.90/-0.95

Appendix B12:Details of synthesis and Characterisations of complex 1b-e

	1b	1c	1d	1e
X	OMe	F	Cl	CN
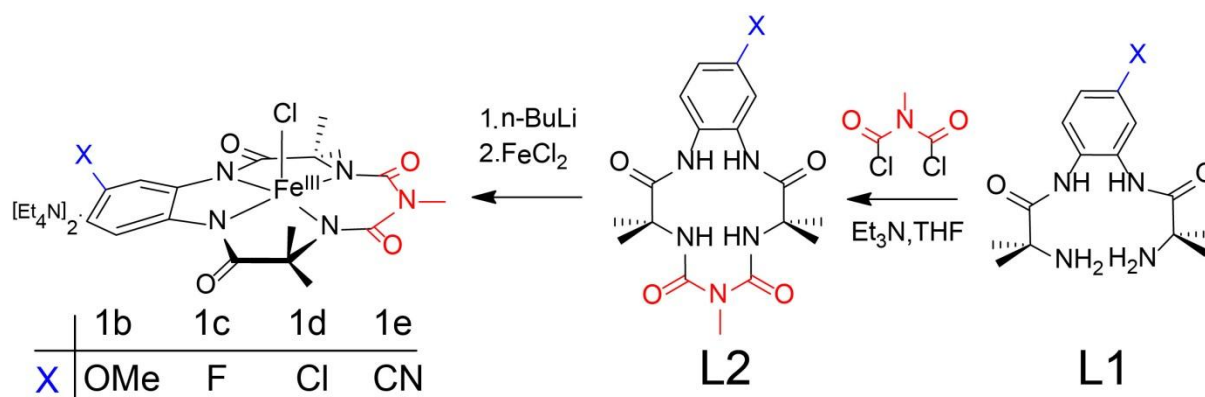
Synthesis scheme for 1a-1e

Synthesis of Diamines (**L1**):   L1 were synthesised according to published method.[8] In a typical reaction, to a dry tetrahydrofuran (THF) solution containing 1gm of 4-substituted benzene-1,2-diamine and 2.05eq (14.62mmol, 2.04mL)   dry triethylamine under inert atmosphere, a dry   THF solution containing 3.73gm (2.05eq, 14.73mmol) of 2-(1,3-dioxoisoindolin-2-yl)-2-methylpropanoyl chloride under inert atmosphere was added dropwise at 0ºC for 2hrs. Reaction was monitored by thin layer chromatography. THF was evaporated by rotary evaporator and dichloromethane was added to the crude product. Excess propanoyl chloride was removed by three times bicarbonate wash then dichloromethane was evaporated. Phthalimide protected crude product was refluxed with excess amount of 60% aqueous hydrazine hydrate in ethanol for 8hrs. A white precipitate of dihydrophthalazine was filtered off and diamine (L1) was isolated from basic solution of water by work up with dichloromethane. For **L1e** having nitrile group in aromatic head part, base workup was done using ice cold aqueous sodium hydroxide (2M) solution during diamine synthesis. Diamine was obtained by crystallization from hot ethyl acetate.

NMR and Mass Spectroscopic characterisation of related compounds

Methoxy Diamine (L1b): 1.74gm(5.51mmol, 84.6% yield) ^{1}H NMR δ_H(200 MHz; DMSO-d_6): 1.29 (d, 12 H, J=3.66Hz, for b, p´), 3.37 (s, 3H, OMe, for i), 3.43 (b, 4H, 2NH$_2$, for a), 6.69 (dd, 1 H, J$_d$= 4.49Hz, J$_{dd}$= 2.91Hz, Ph, for j), 7.26 (d, 1 H, J=8.84, Ph, for g), 7.48 (d, 1 H, J=2.91Hz, Ph, for k). ^{13}C NMR; δ_C(400 MHz; DMSO-d_6): 176.37(d), 176.23(n´), 157.00(h), 133.54(f), 126.71(l), 122.36(k), 109.55(j), 107.55(g), 55.32(i), 55.08(o´), 54.85(c), 28.68(p´), and 28.75(b). ESI-MS (positive ion mode): m/z 309.19 (M+H$^+$, 100%)

Fluoro Diamine(L1c):1.64gm (5.53mmol, 77.6% yield) ^{1}H NMR

δ_H(200 MHz; DMSO-d_6): 1.28(s, 6H, CH$_3$,for b), 1.30(s, 6H, CH$_3$,for

p′), 4.71(b, 4H, 2NH$_2$,for a), 6.96(td, 1H, J$_t$= 9.18Hz, J$_{dt}$= 8.80Hz, Ph,

for g), 7.39(dd, 1H, J$_d$ = 10.26Hz, J$_{dd}$ = 2.93Hz, Ph, for g), 7.72(dd,

1H, Ph, for k). ^{13}C NMR; δ_C(400 MHz; DMSO-d_6); 28.60(b),

28.70(p′), 54.93(c), 55.12(o′), 108.69(d, J = 26.20Hz, for g),

110.48(d, J = 22.35Hz, for j), 125.62(for k), 127.62(d, J = 10.02Hz, for l), 133.55(d, J =

12.33Hz, for f), 176.87(d), 177.41(n′);

DEPT δ_C(400 MHz; DMSO-d_6): 28.47, 28.59, 108.57(d, J = 26.20Hz, for g), 110.38(d, J =

22.35Hz, for j), 127.14(d, J = 9.25Hz, for k);ESI-MS(positive ion mode): m/z 297.17 (M+H^{+},

100%).

Chloro Diamine(L1d):1.76gm (5.63mmol, 89% yield) ^{1}H NMR δ_H(200 MHz; DMSO-d_6):

1.297(s, 6H, CH$_3$, for b), 1.299(s, 6H, CH$_3$, for p′), 7.19(dd, 1H, J$_d$=

8.65Hz, J$_{dd}$= 2.40Hz, Ph, for j), 7.55(d, 1H, J$_d$= 8.59Hz, Ph, for k),

7.79(d, 1H, J$_d$= 2.53Hz, Ph, for g);^{13}C NMR; δ_C(200 MHz; DMSO-d_6):

28.59(b), 28.65(p′), 54.98(c), 55.06(o′), 122.79(for j), 124.28(for k),

126.05(for g), 128.77(for h), 129.36(for l), 132.88(for f), 177.01(for d),

and 177.13(for n′); DEPT δ_C(400 MHz; DMSO-d_6): 28.50, 28.55,

122.70, 124.20, and 125.97; ESI-MS(positive ion mode): m/z 313.14 (M+H^{+}, 100%).

Cyano Diamine(L1e):1.2gm (3.96mmol, 58.5% yield) ^{1}H NMR δ_H(200 MHz; DMSO-d_6):

1.29(s, 6H, CH$_3$, for b), 1.31(s, 6H, CH$_3$, for p′),), 4.97(s, 4H, NH$_2$,

for a),), 7.62(dd, 1H, J$_d$= 8.63Hz, J$_{dd}$= 1.89Hz, Ph, for j), 7.92(d, 1H,

J$_d$= 1.89Hz, Ph, for k), 8.03(d, 1H, J$_d$= 8.46Hz, Ph, for g); ^{13}C NMR;

δ_C(200 MHz; DMSO-d_6): 28.52(for b), 28.60(for p′), 55.18(for c),

55.41(for o′), 79.26(for i), 106.11(for h), 123.07(for k), 128.63(for

g), 129.60(for j), 130.61(for f), 136.94(for l), 177.66(for d), and 177.26(for n´);   DEPT δ_C(400 MHz; DMSO-d$_6$): 28.29(for b), 28.37(for p´),   122.83 (for k), 128.40(for g) and 129.36 (for j); ESI-MS (positive ion mode): m/z 304.17 (M+H$^+$, 100%).

Synthesis of Ligands (L2): All the ligands (L2) were synthesised according to previous report.[8] In an oven dried two-neck round bottom flask, 500mg of L1 was taken and dried under high vacuum for 2-hrs and backfill several times with nitrogen gas in schlenk line. Then 50 mL dry dichloromethane was added to L2 under nitrogen atmosphere followed by addition of dry trimethylamine (two equivalents). This solution was transferred into an addition funnel under inert atmosphere. N,N-dichloroformylmethylamine (one equivalent) was diluted with 50 mL dry dichloromethane and was also transferred into another addition funnel. Both the solution was added dropwise over a period of 3-hrs in to a 500 mL two neck round bottom flask containing 300 mL dry dichloromethane under inert atmosphere at ice bath. After completion of addition reaction mixture was warmed to room temperature and stirred for overnight. Then the reaction mixture was dried by rotary evaporator and purified by column chromatography using (8:2) ethyl acetate/petroleum ether as an eluent. Isolated yield was measured and L2 of different substitution were characterised by NMR and ESI-MS spectroscopy.

Methoxy Ligand (L2b):1.86gm (0.5mmol, 44% yield) ^{1}H NMR δ_H(200 MHz; DMSO-d$_6$): 1.48(s, 6H, CH3, for c), 1.52(s, 6H, CH3, for n), 2.97(s, 3H, OMe, for i), 3.37(s, 3H, NMe, for a), 6.75(dd, 1H, J$_d$= 4.41Hz, J$_{dd}$= 2.91Hz, for j), 7.29(d, 1H, J$_d$= 8.68Hz, for g), 7.42(d, 1H, J$_d$= 2.85, for k), 7.73(s, 1H, NH, for r), 8.18(s, 1H, NH, for q), 8.91(s, 1H, NH, for t), 9.08(s, 1H, NH, for s).^{13}C NMR; δ_C(400 MHz; DMSO-d$_6$): 25.13(for o), 25.81(for c), 31.62(for a), 55.40(for i), 58.71(for n), 59.12(for d), 108.65(for g), 110.14(for j), 121.79(for l), 128.21(for k), 133.38(for f), 155.71(for h),

157.16(for m), 157.31(for e), 173.57(for p), 173.70(for b); DEPT δ_C(400 MHz; DMSO-d_6):

25.49(for o), 26.17(for c), 31.99(for a), 55.75(for i), 109.02(for g), 110.50(for j), 128.57(for

k);ESI-MS (negative ion mode): m/z 390.17 (M-H+, 100%).

Fluoro Ligand(L2c):210mg (0.55mmol, 49% yield) ^{1}H NMR δ_H(200 MHz; DMSO-d_6):

1.49(s, 6H, CH3, for c), 1.52(s, 6H, CH3, for o), 2.97(s, 3H, NMe, for a), 7.03(dt, 1H, J_d=

2.93Hz, J_t= 8.64Hz, for j), 7.42(dd, 1H, J_d= 9.18Hz, J_{dd}=

8.80Hz, for g), 7.64(dd, 1H, J_d= 10.26Hz, J_{dd}= 2.93Hz, for

k), 7.79(s, 1H, NH, for r), 8.17(s, 1H, NH, for q), 9.05(s,

1H, NH, for t), 9.19(s, 1H, NH, for s);^{13}C NMR; δ_C(200

MHz; DMSO-d_6): 25.09(for c), 25.74(for o), 31.64(for a),

58.72(for d), 59.10(for n), 110.14(d, J_d= 26.20Hz, for g), 111.44(d, J_d= 22.35Hz, for j),

125.31(d, J_d= 2.31Hz, for l), 128.78(d, J_d= 10.02Hz, for k), 133.71(d, J_d= 12.33Hz, for f),

155.76(for p), 157.28(for b),159.48(d, J = 241.98Hz, for h), 173.72(for m), 173.78(for e);

DEPT δ_C(400 MHz; DMSO-d6): 25.47(for c), 26.12(for o), 32.02(for a), 110.52(d, J =

26.20Hz, for g), 111.82(d, J = 22.35Hz, for j), 129.17(d, J = 9.25Hz, for k);ESI-MS (negative

ion mode): *m/z* 364.14 (M-H+, 100%).

Chloro Ligand (L2d): 220mg (0.55mmol, 52% yield)^{1}H NMR δ_H (200 MHz; DMSO-d_6):

1.50(s,6H, CH3, for c), 1.51(s,6H, CH3, for o), 2.97(s, 3H,

NCH3, for a), 7.26(dd, 1H, J_d= 4.65Hz, J_{dd}= 2.40Hz, for j),

7.56(d, 1H, J_d= 8.59Hz, for k), 7.73(d, 1H, J_d= 2.40Hz, for

g), 7.91(s, 1H, NH, for r), 8.03(s, 1H, NH, for q), 9.14(s,

1H, NH, for e), 9.16(s, 1H, NH, for m). ^{13}C NMR; δ_C(500 MHz; DMSO-d_6): 25.37(for c),

25.57(for o), 31.75(for a), 58.95(for d), 59.06(for n), 124.38(for j), 125.24(for k), 127.55(for

l), 129.18(for h), 129.46(for l), 132.53(for f), 156.39(for b), 156.87(for p), 173.83(for e),

173.92(for m); DEPT δ_C(500 MHz; DMSO-d_6): 25.11(for c), 25.31(for o), 31.50(for a),

124.13(for j), 124.98(for k), 127.29(for l).ESI-MS (negative ion mode): *m/z* 394.13 (M-H+, 100%).

Cyano Ligand(L2e):172mg(0.44mmol, 40% yield)^{1}H NMR δ_H(500 MHz; DMSO-d_6): 1.49(s, 6H, CH3, for c), 1.51(s, 6H, CH3, for o), 2.96(s, 3H, NCH3, for a), 7.69(d, 1H, J_d= 8.54Hz, for j), 7.89(s, 2H, for g, k), 7.95(1H, NH, for r), 8.16(s, 1H, NH, for q), 9.23(s, 1H, NH, for s), 9.40(s, 1H, NH, for t); ^{13}C NMR; δ_C(500 MHz; DMSO-d_6): 25.17(for c), 25.69(for o), 31.08(for a), 58.85(for d), 59.25(for n), 107.06 (for h), 118.54(for i), 124.49(for k), 129.94(for g), 130.28(for j), 130.81(for f), 136.68(for l), 155.93(for b), 157.30(for p), 173.96(for e), 174.05(for m);DEPT δ_C(500 MHz; DMSO-d6): 24.91, 25.44, 31.55, 124.22, 130.03, 130.56.ESI-MS (negative ion mode): *m/z* 385.16 (M-H+, 100%).
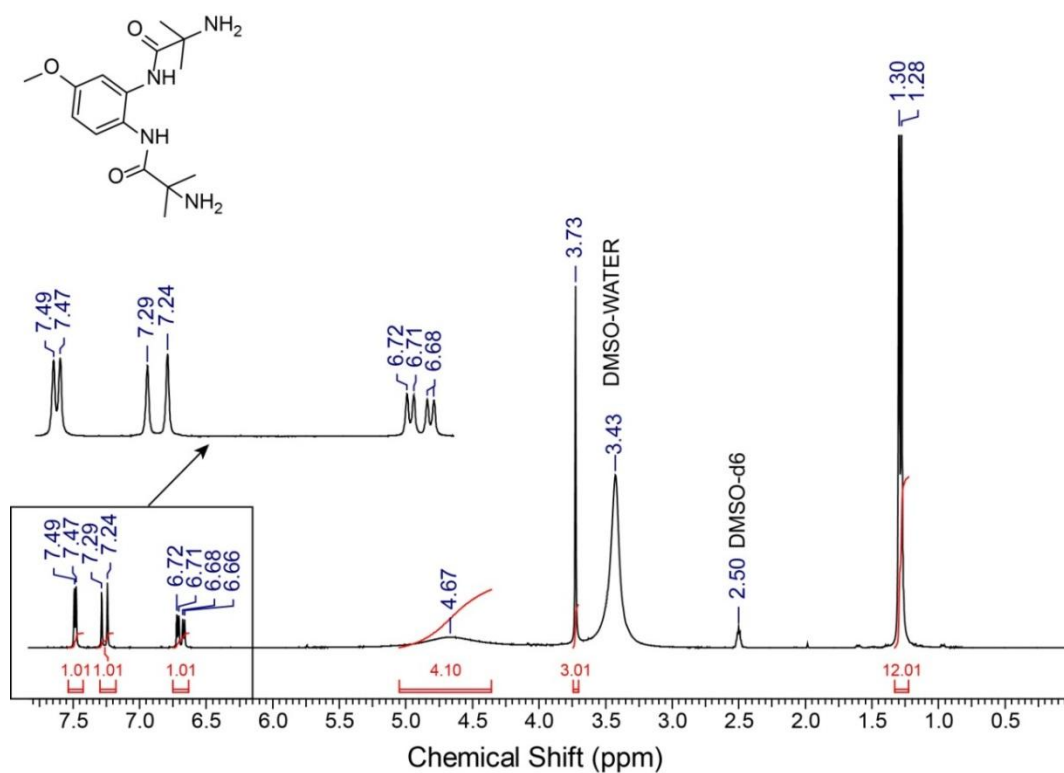
^{1}H NMR Spectra of methoxy Diamine (L1b) in DMSO-d$_6$.
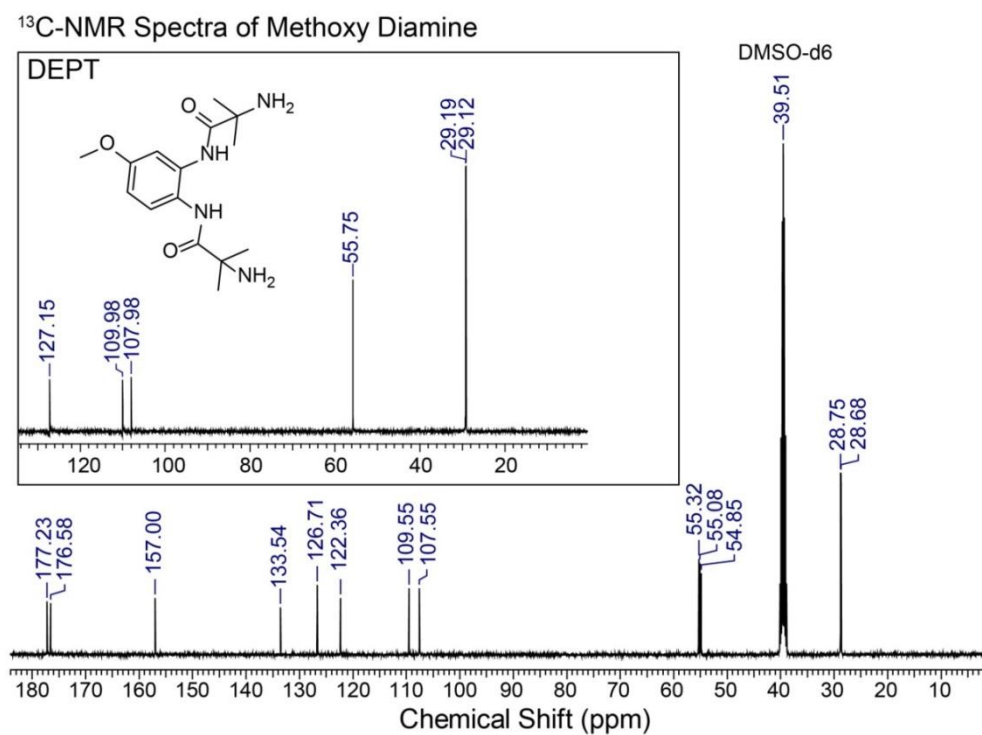
^{13}C NMR (insetDEPT of L1b) Spectra of methoxy diamine (L1b) in DMSO-d$_6$.

¹H-NMR Spectra of Methoxy Ligand
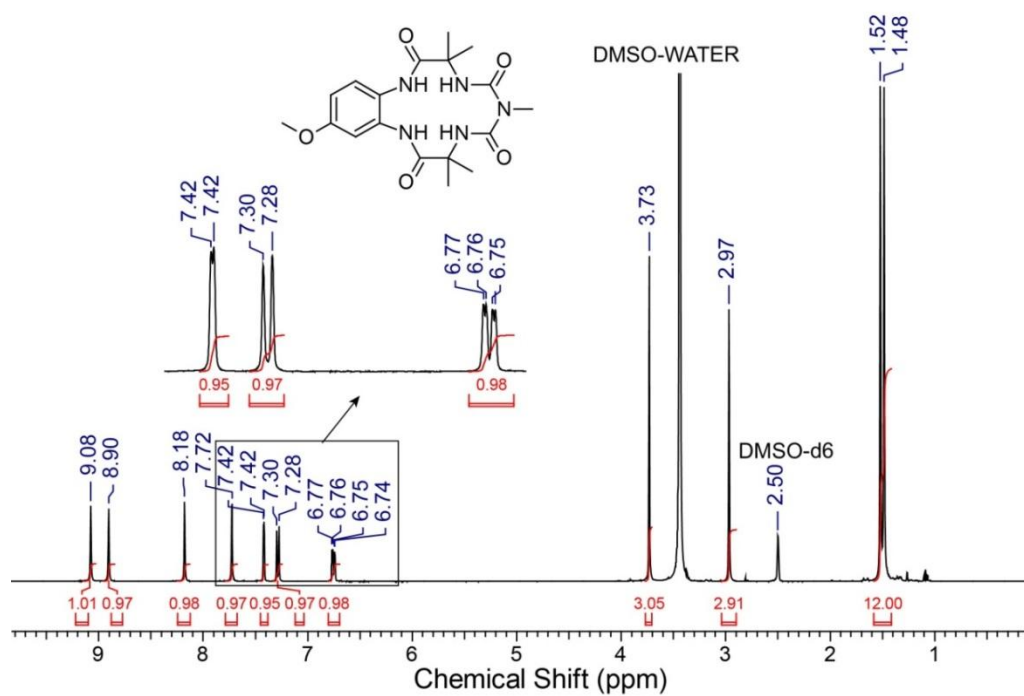
¹H NMR of methoxy ligand (L2b) in DMSO-d₆.

¹³C-NMR Spectra of Methoxy Diamine
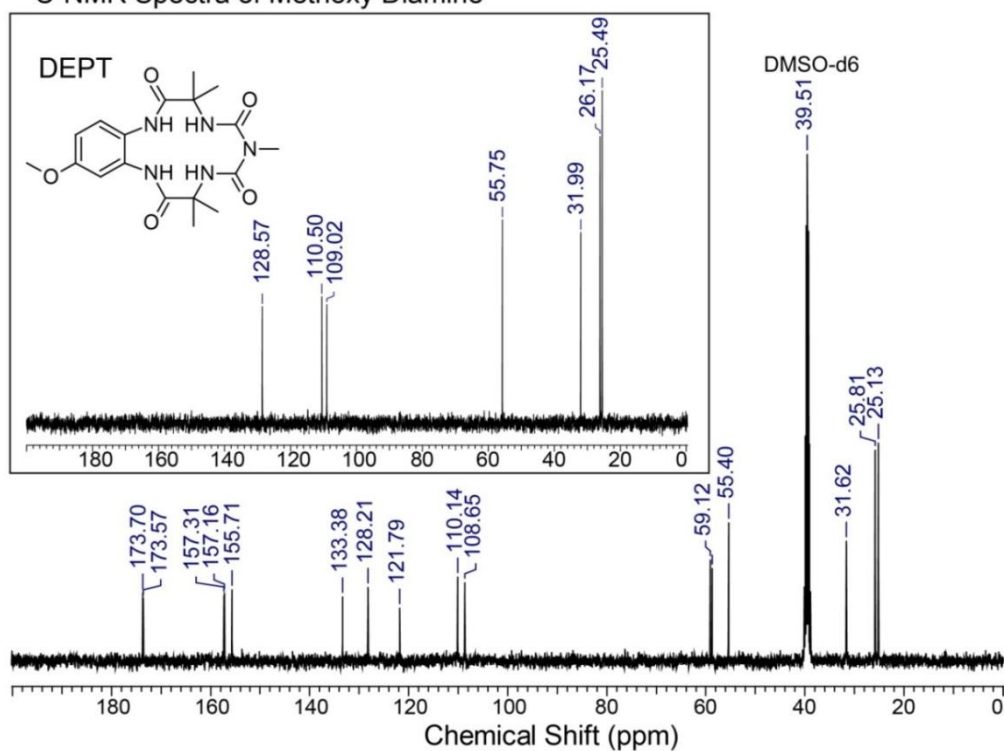
¹³C NMR (inset DEPT of the L2b) of methoxy ligand (L2b) in DMSO-d₆.
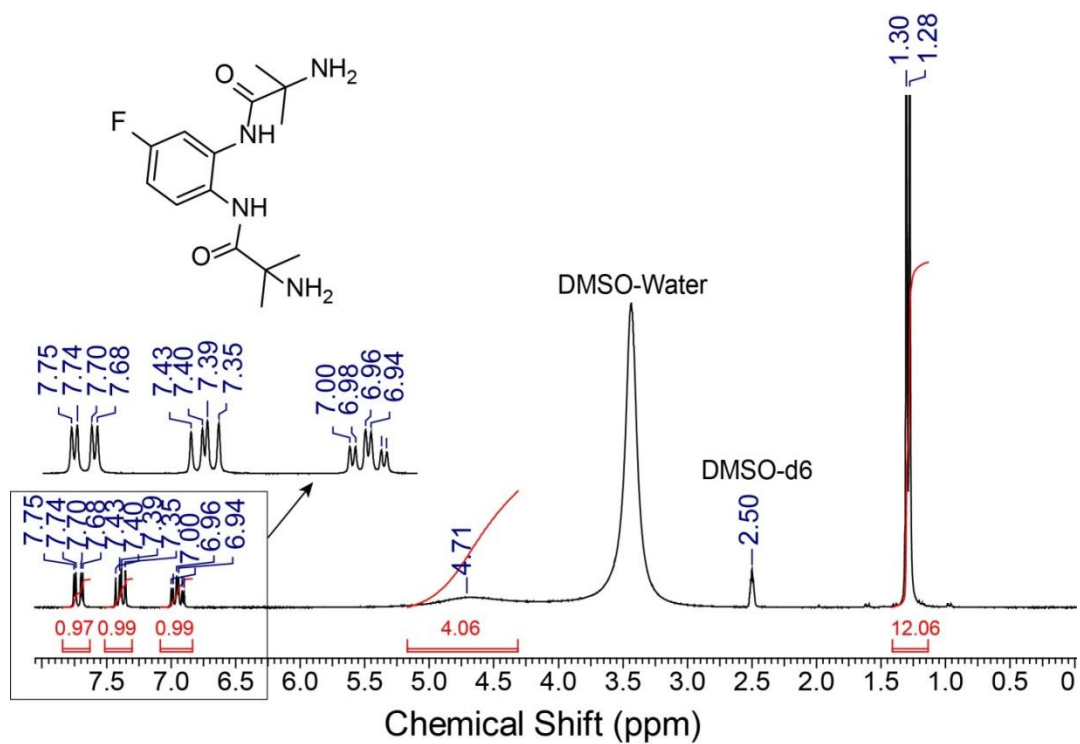
^{1}H NMR of fluoro diamine (L1c) in DMSO-d$_6$.

^{13}C-NMR Spectra of Fluoro Diamine
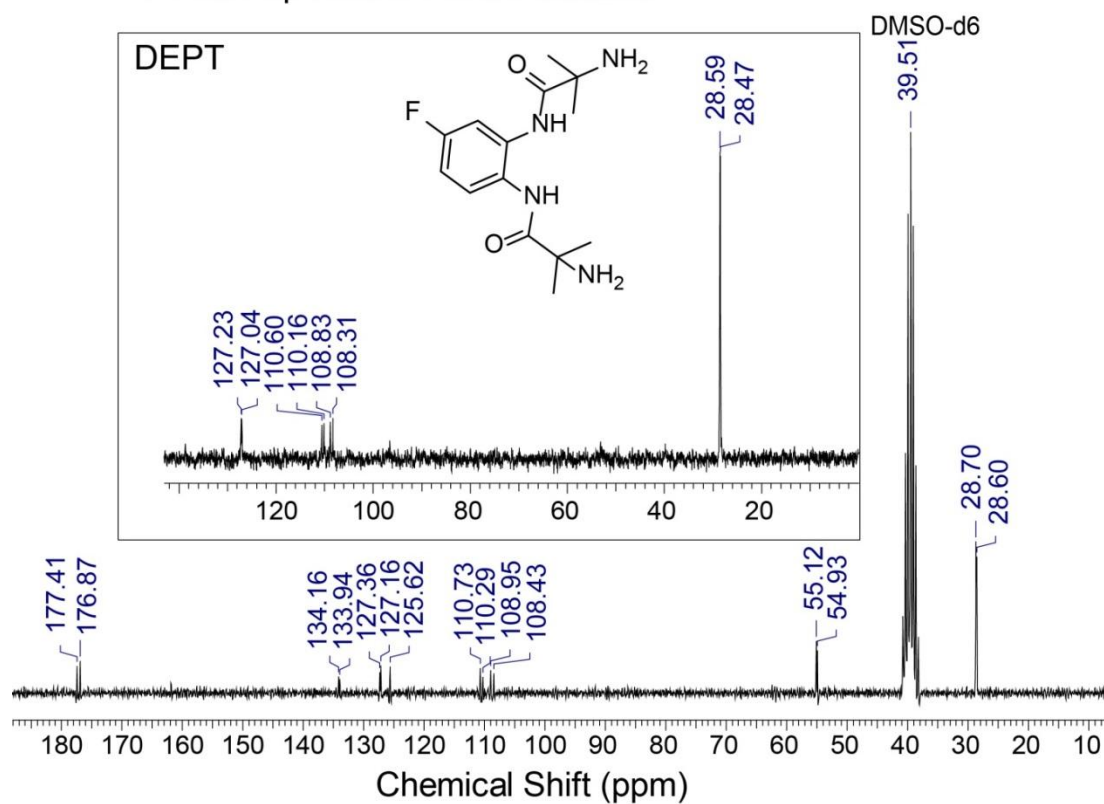
^{13}C NMR (inset DEPT of L1c) of fluoro diamine (L1c) in DMSO-d$_6$.
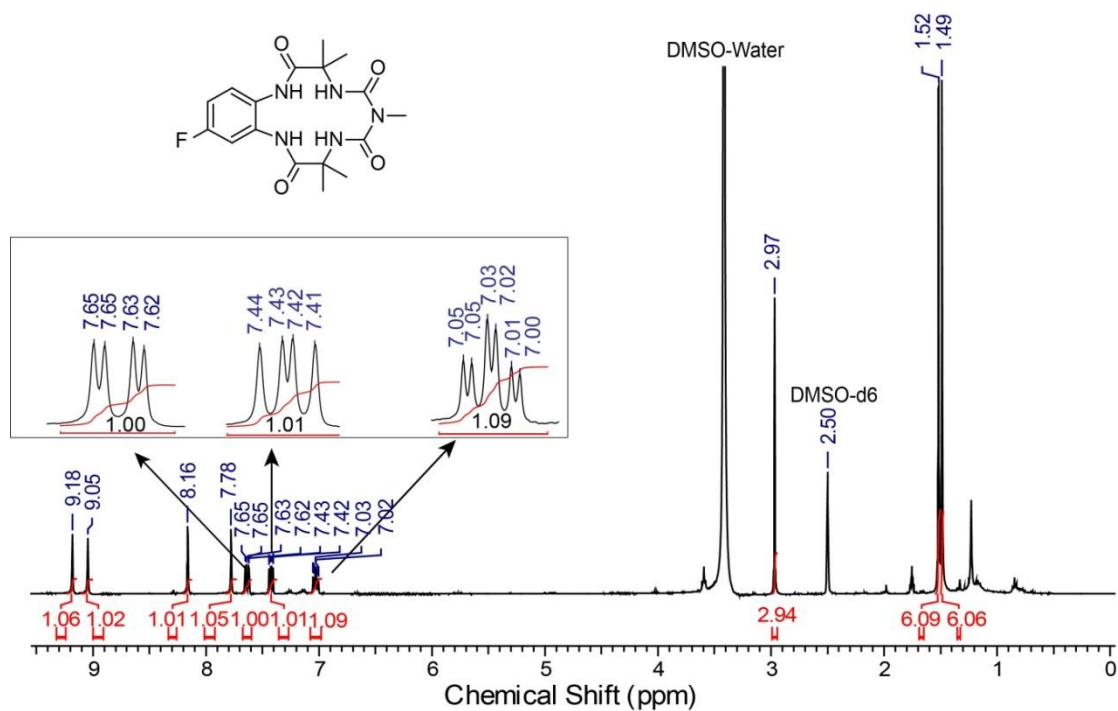
^{1}H NMR of fluoro ligand (L2c) in DMSO-d$_6$.
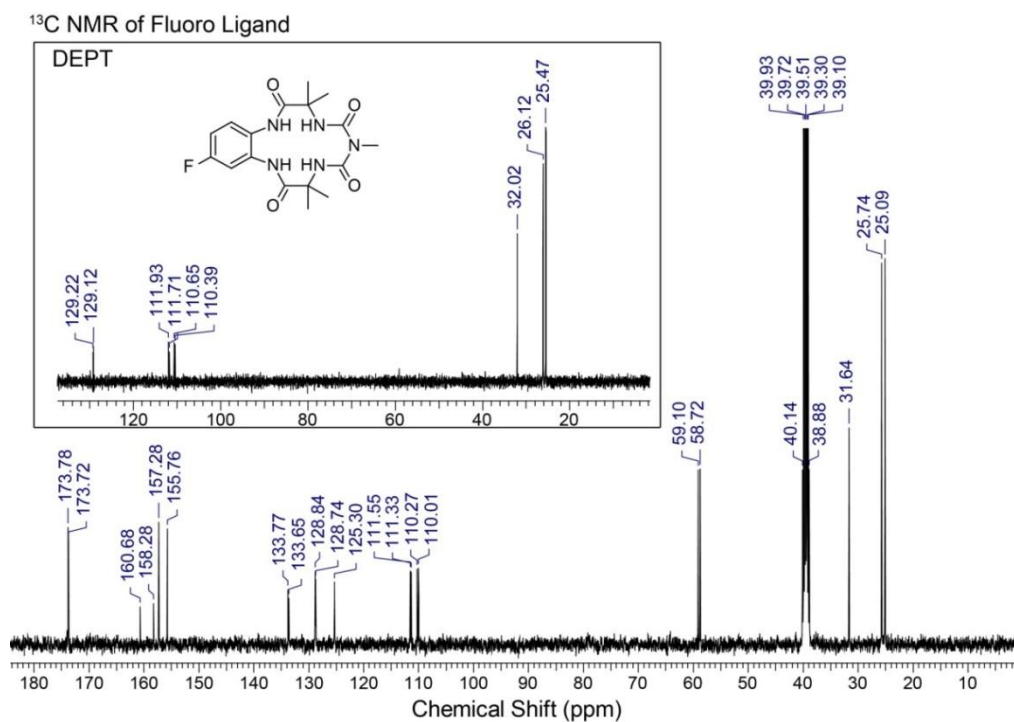
^{13}C NMR (inset DEPT of L2c) of fluoro ligand (L2c) in DMSO-d$_6$.
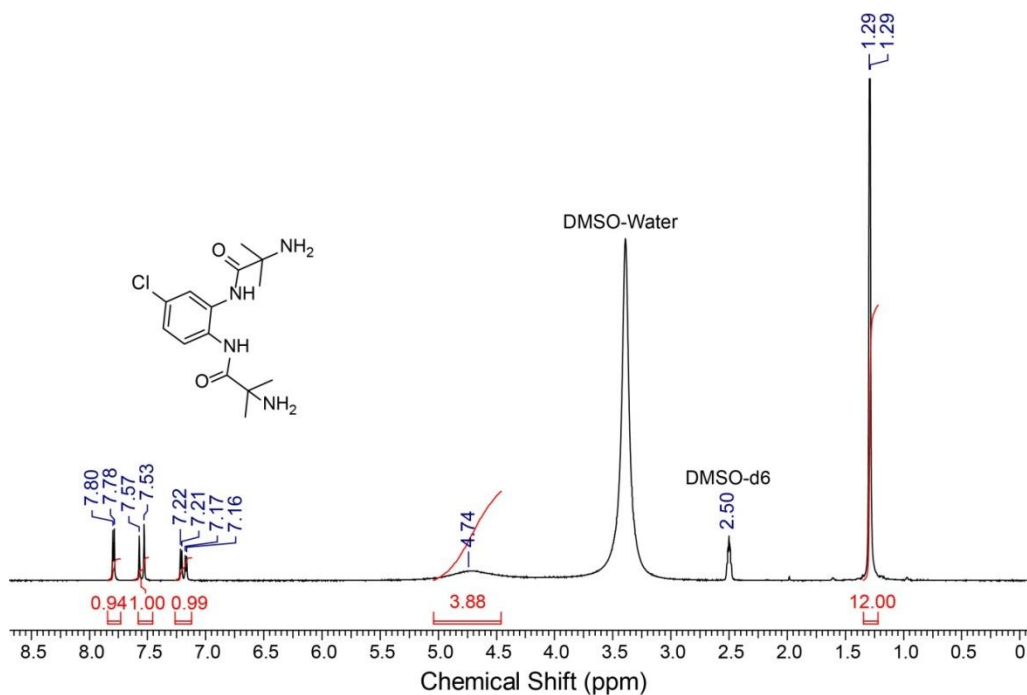
^{1}H NMR spectra of chloro diamine (L1d) in DMSO-d$_6$.
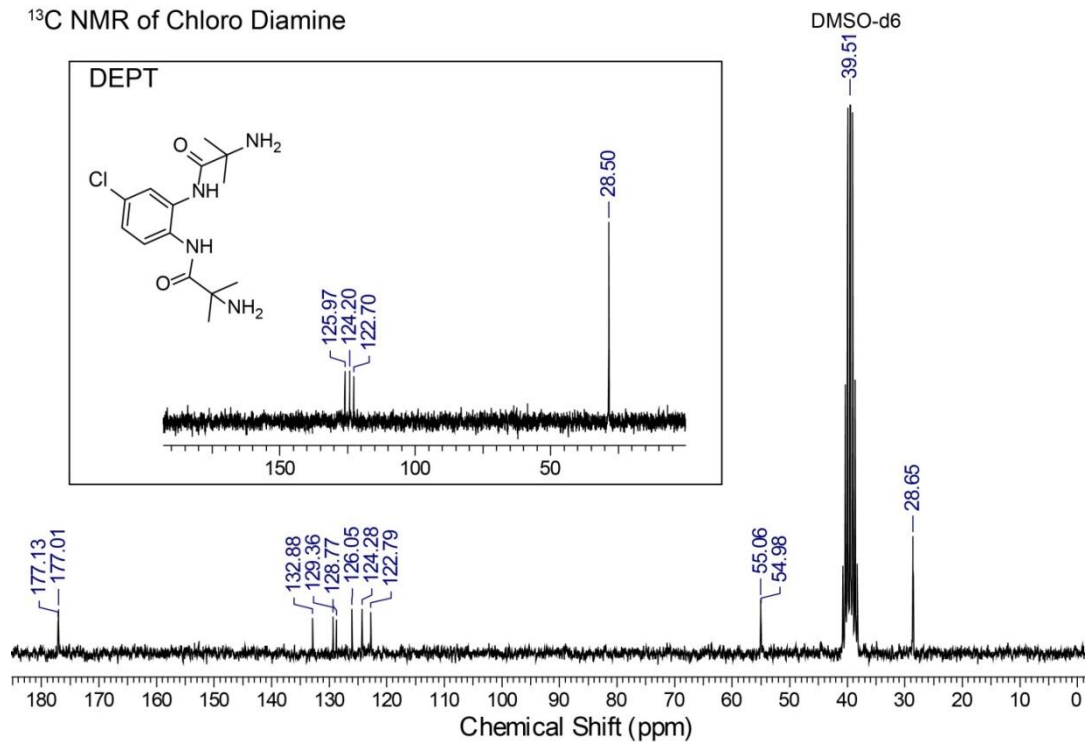
^{13}C NMR spectra (inset DEPT of L1d) of chloro diamine (L1d) in DMSO-d$_6$.
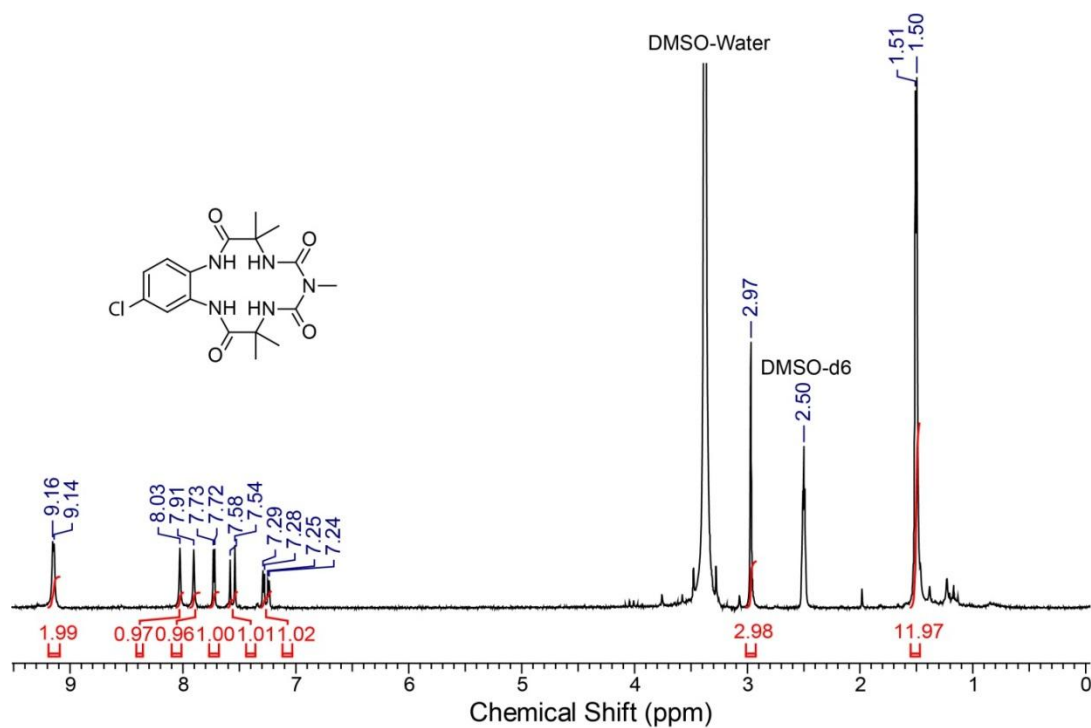
^{1}H NMR spectra of chloro ligand (L2d) in DMSO-d$_6$.
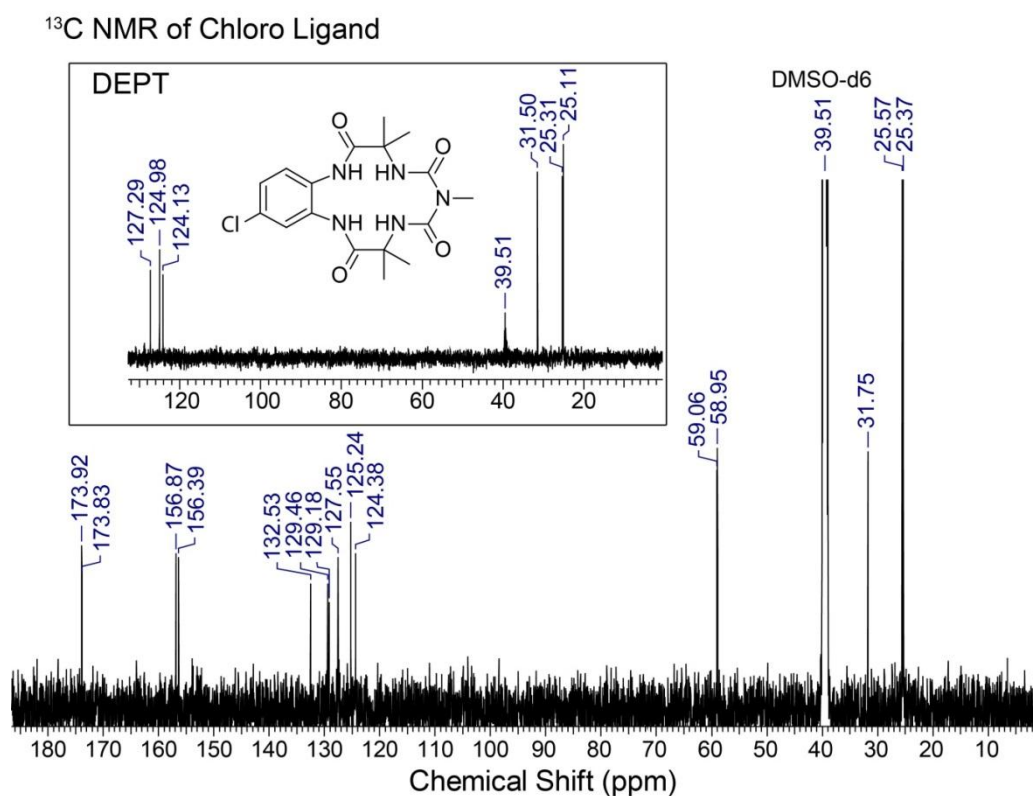
^{13}C NMR spectroscopy (inset DEPT of L2d) of chloro ligand (L2d) in DMSO-d$_6$.
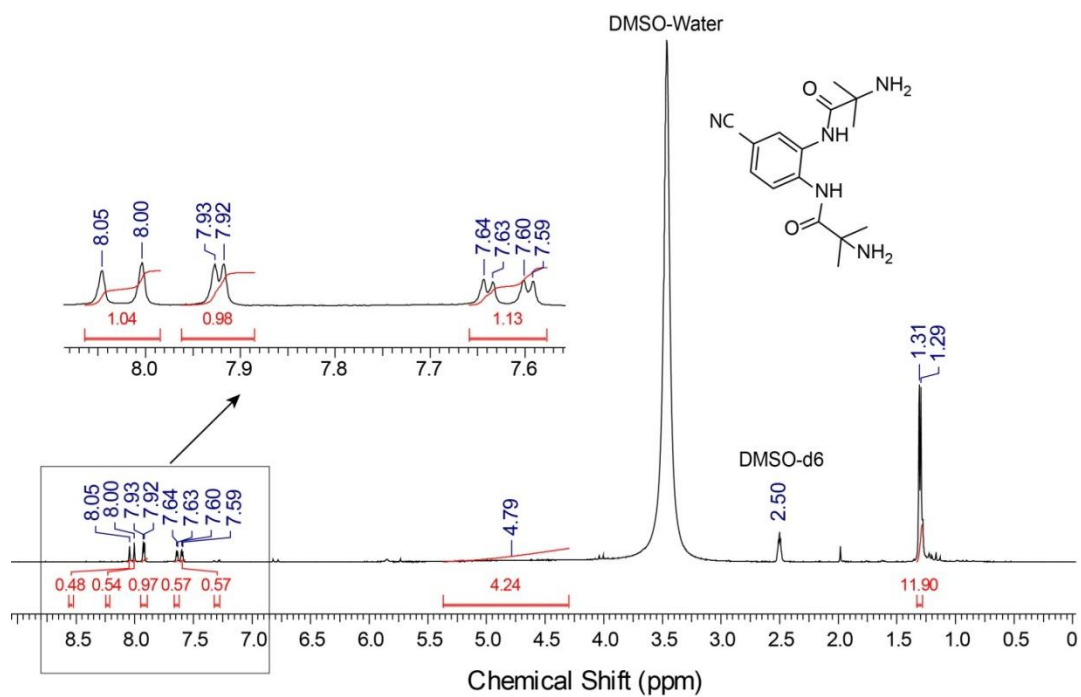
^{1}H NMR spectra of cyano ligand (L1e) in DMSO-d$_6$.
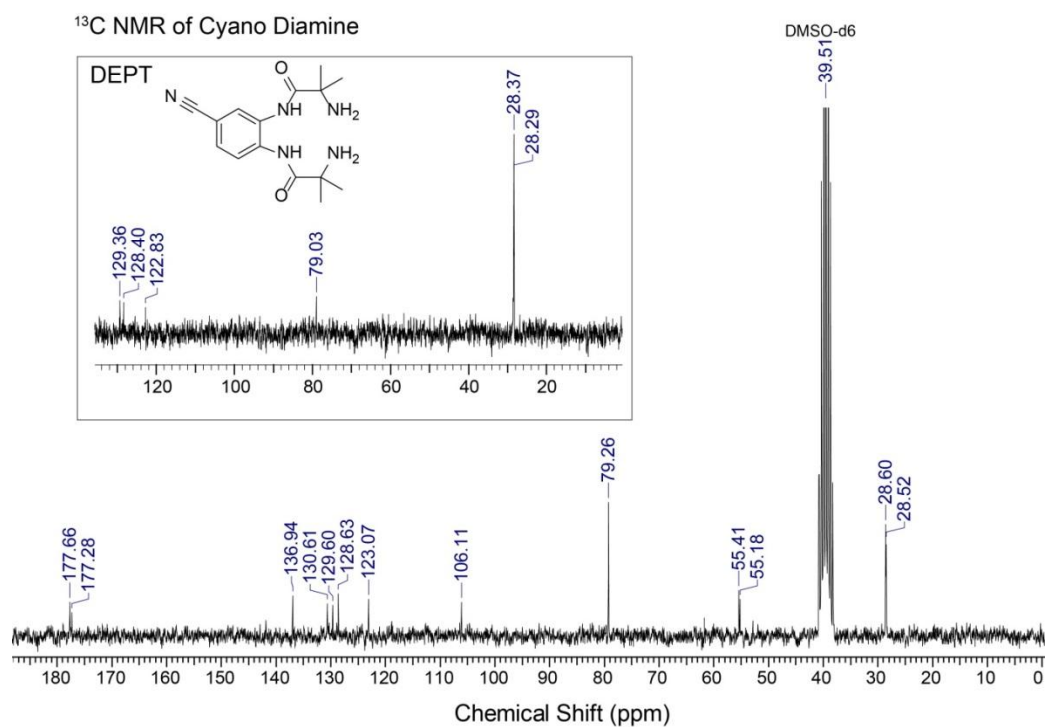
^{13}C NMR spectra (inset DEPT of L1e) of cyano diamine (L1e) in DMSO-d$_6$.
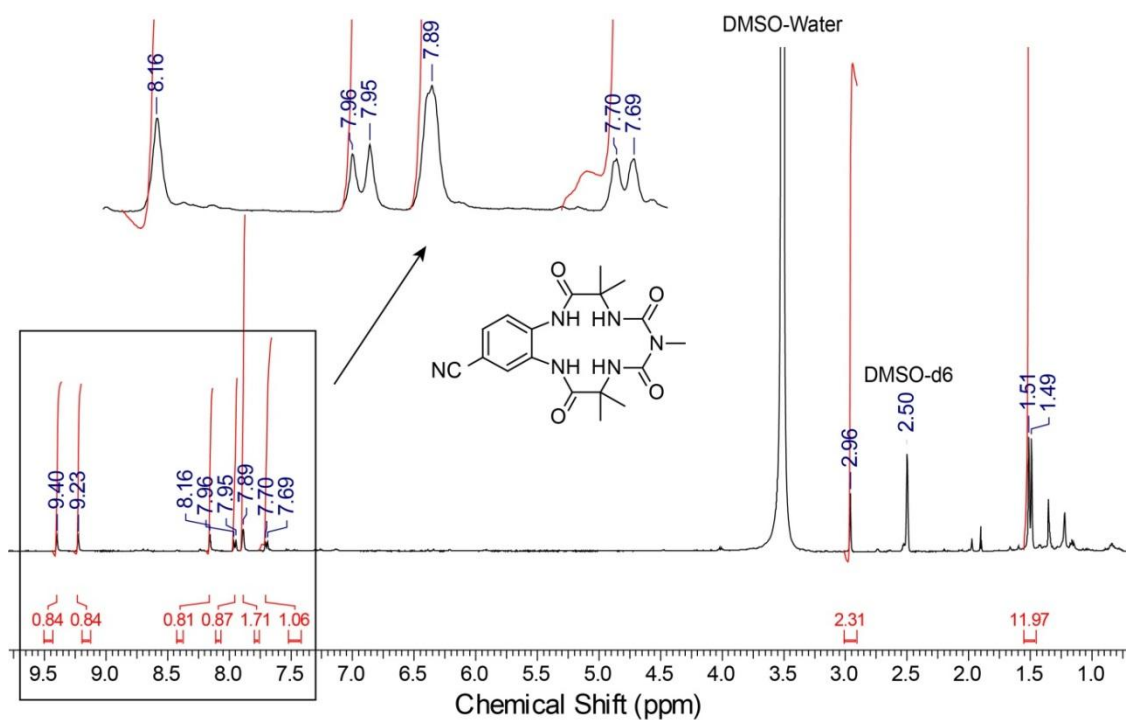
^{1}H NMR spectra of Cyano ligand (L2e) in DMSO-d$_6$.
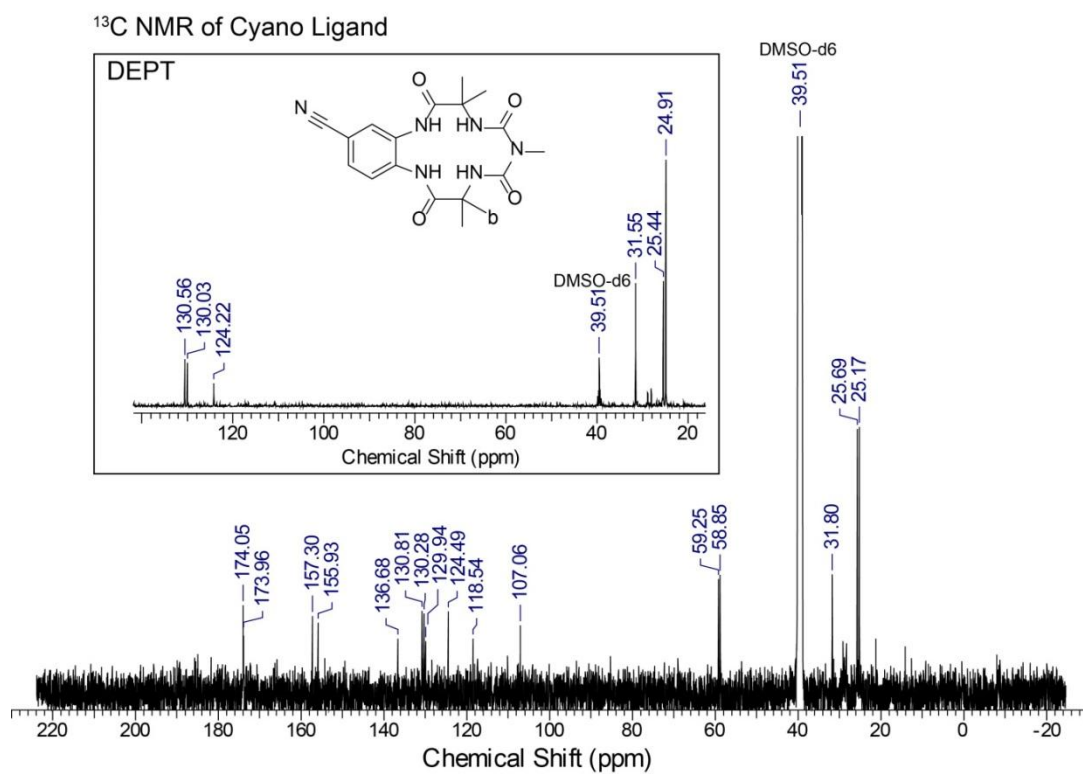
^{13}C NMR spectra (inset DEPT of L2e) of cyano ligand (L2e) in DMSO-d$_6$.
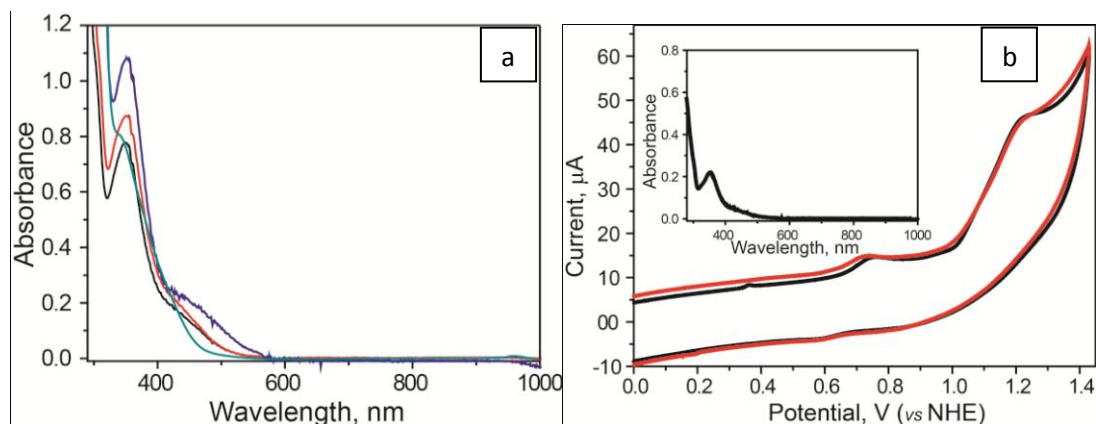
Appendix B13: (a) UV-Vis spectra of 0.2 mM of **1b** (violet), **1c** (black), **1d** (red), and 0.12 mM of **1e** (green) in water. (b) CVs of 5×10^{-4} M **1a** (black) in water and **1a**-H_2O(red) in 2% CH_3CN-98% water (glassy carbon as working and platinum wire used as counter electrode, scan rate 100 mVs^{-1}, 0.1 M $NaNO_3$ as electrolyte); inset UV-Vis of **1a**-H_2O in 2% CH_3CN-98% water.

Appendix B14:Characteristic charge transfer band for $(Et_4N)_2[Fe^{III}(bTAML)(Cl)]$ (**1a-f**) in water and $(PPh_4)[Fe^{III}(bTAML)(OH_2)]$ (**1a**-H_2O)

Catalyst	Substituent	λ_{max}/ nm, ε / $M^{-1}cm^{-1}$
1b	-OMe	352, 5500
1a	-H	356, 3990[5]
1c	-F	350, 4300
1d	-Cl	351, 4450
1e	-CN	350,6500
1f	-NO$_2$	356, 9028[5]
1a-H_2O	-H	356
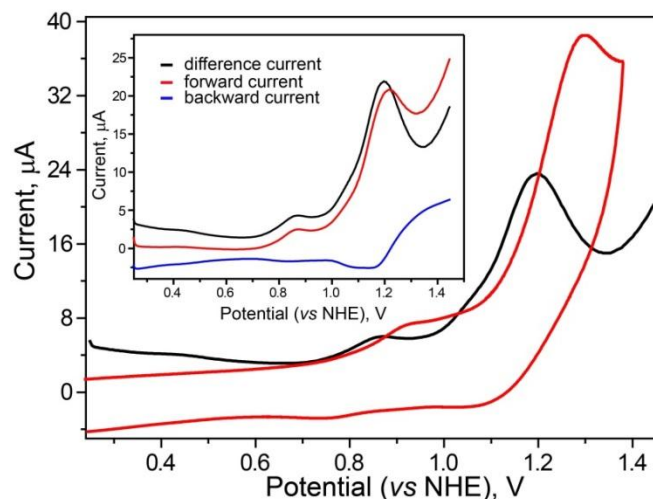
Appendix B15:CVs (red) and SQWV (black) of **1a**(0.3mM) in pH 7.2, 15 mM phosphate buffer; (inset) forward, backward and difference SQWVs (glassy carbon as working and platinum wire used as counter electrode, scan rate 100 mVs^{-1}, 0.1 M NaNO$_3$ as electrolyte).
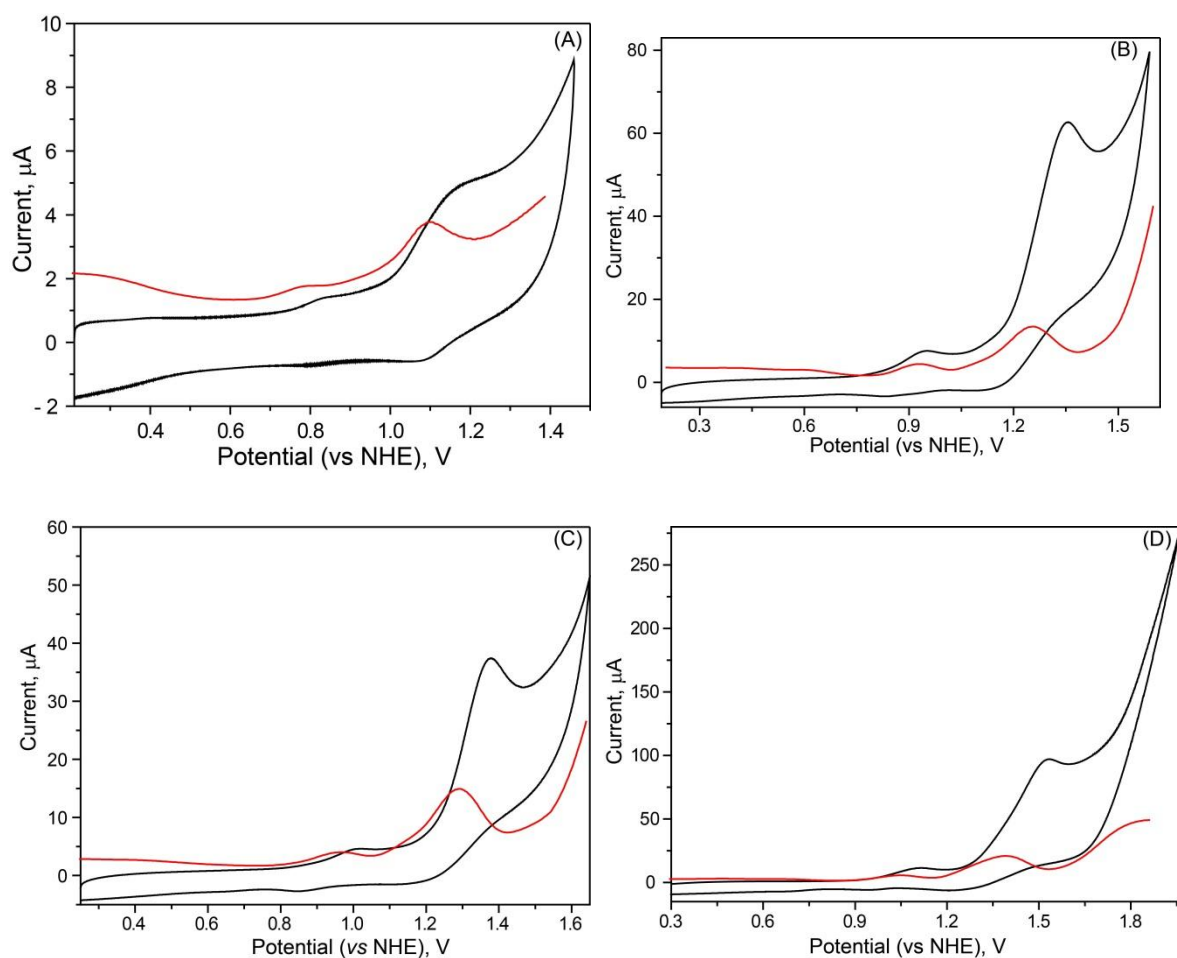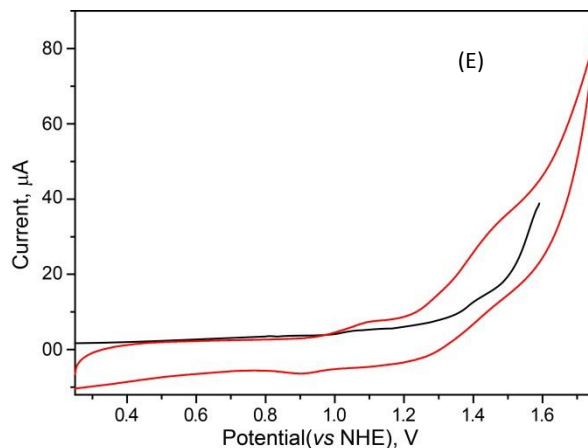
Appendix B16: CVs of 0.5 mM **1b**(black-3A), 0.5 mM **1c**(black-3B), 0.5 mM **1d**(black-3C) and (B) 0.5 mM **1e**(black-3D), 0.2 mM **1f** (black-3E) and SQWV's of 0.3 mM **1b**(black-3A), 0.5 mM **1c**(black-3B), 0.5 mM **1d**(black-3C) and (B) 0.5 mM **1e**(black-3D), 0.2 mM **1f** (black-3E) in pH 7.2 phosphate buffer (glassy carbon as working and platinum wire used as counter electrode, scan rate 100mVs^{-1}, I = 0.1M NaNO$_3$). The pink trace represents blank scan.
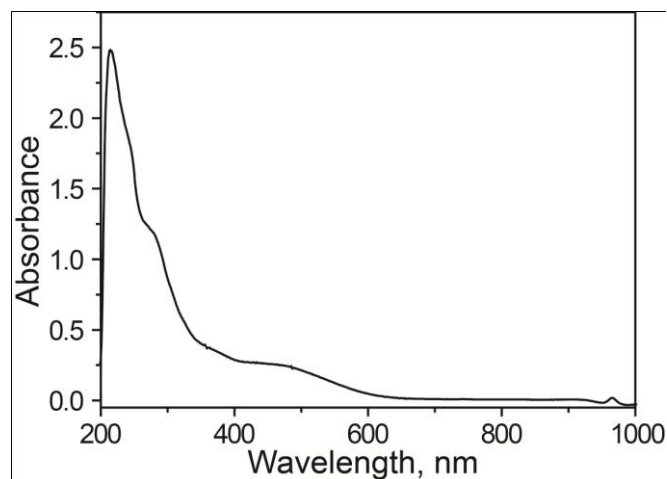
Appendix B17: UV-Vis spectra of $[Fe^{IV}(O)]^{2-}$ in pH 12, 10 mM phosphate buffer in presences of 0.1M $NaNO_3$ as supporting electrolyte.
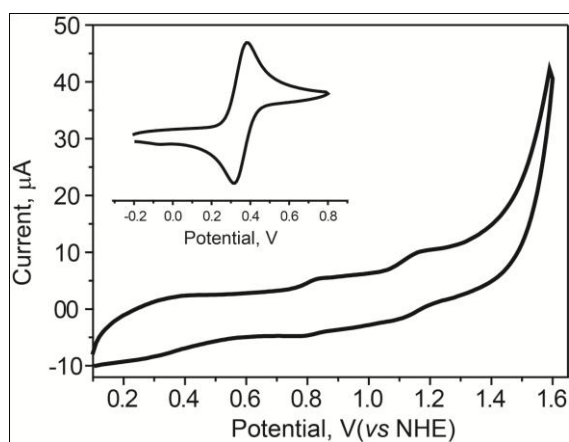
Appendix B18: CV of 0.3 mM **1a** in 90% $CH_3CN:H_2O$ (glassy carbon as working and platinum wire used as counter electrode: scan window 0.1 to 1.6 V, scan rate 100 mVs^{-1}, 0.1 M KPF_6 as electrolyte); (inset) CV of ferrocene under similar condition.
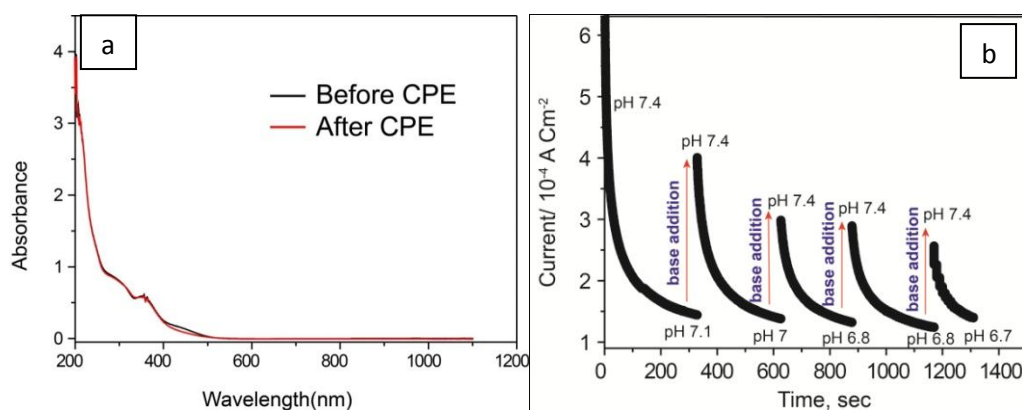
Appendix B19: (a) UV-Visible spectra of **1a** in water (0.1M $NaNO_3$) before (black) and after (red) 2 hrs of CPE. (b) The pH maintaining during WO by addition of NaOH solution after every 300 sec interval.
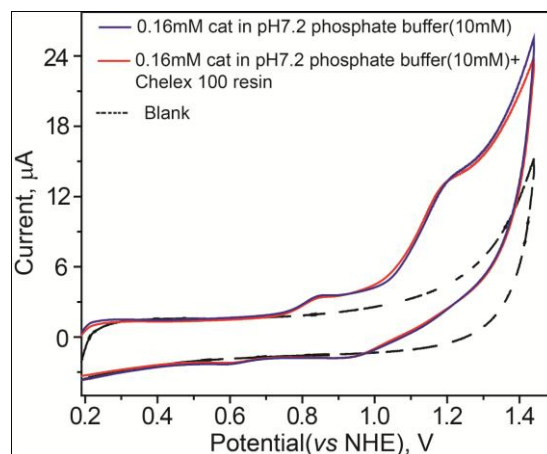
Appendix B20: CV of **1a** in presence of Chelex 100 sodium form resin in pH 7.2 phosphate buffer (15 mM).
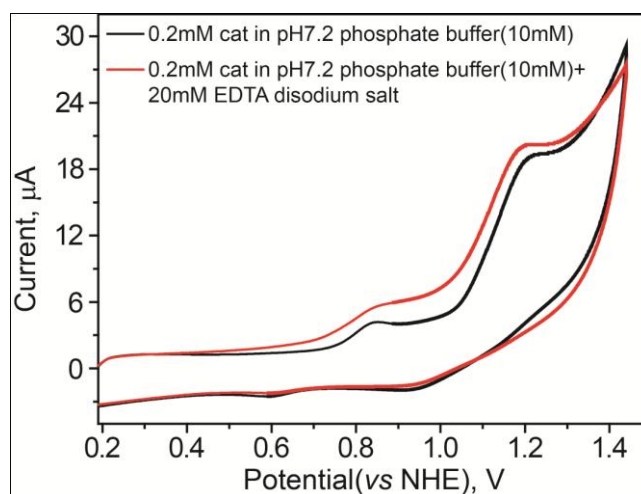
Appendix B21: CVs of **1a** in presence of disodium EDTA salt at 15 mM phosphate buffer (pH=7.2, *I*= 0.1 MNaNO₃).
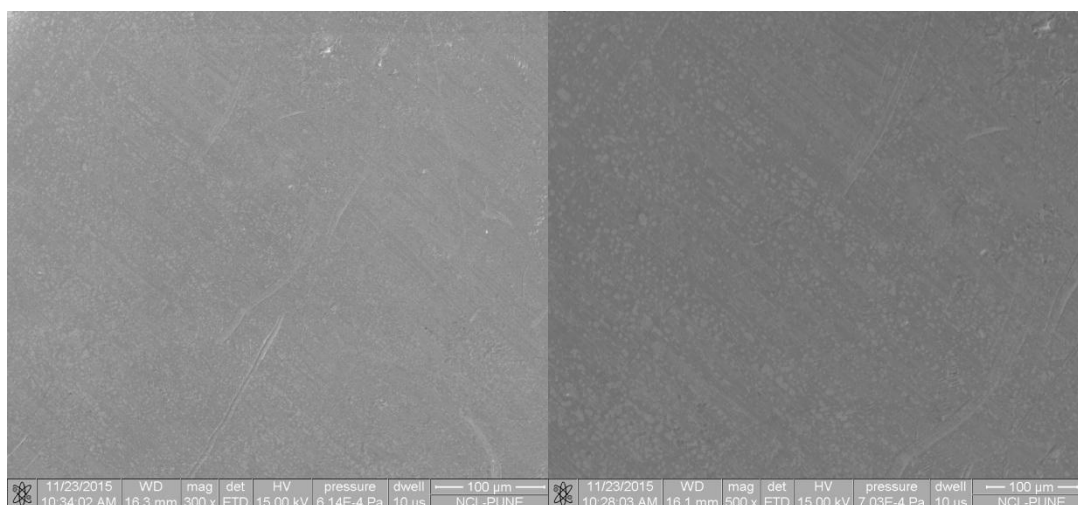
Appendix B22a:. SEM images of the platinum foil working electrode before (left) and after (right) 2 hrsof CPE.
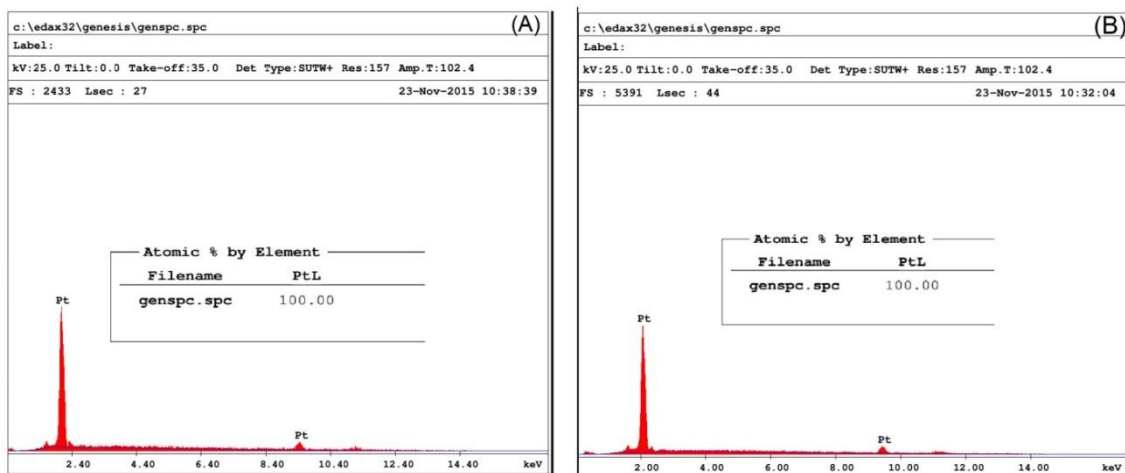
Appendix B22b:EDX analysis of the Platinum foil working electrode before (left) and after (right)2hrs CPE (inset: atomic % by element of platinum).
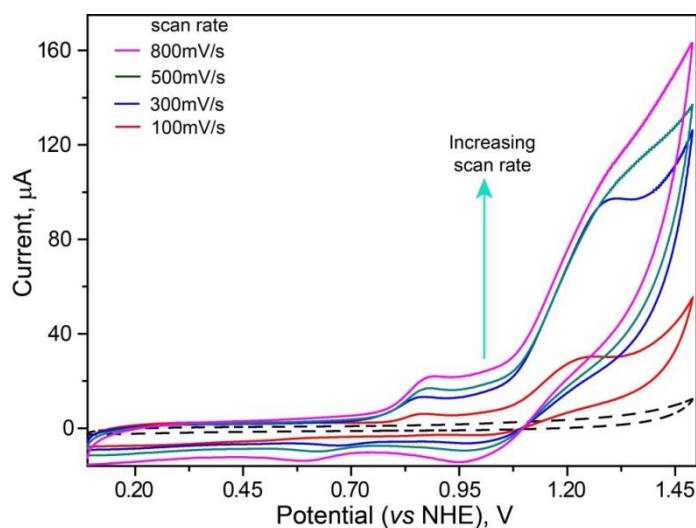
Appendix B23:CV of **1a**(0.5 mM) in 15 mM phosphate buffer (pH=7.2, I= 0.1 MNaNO$_3$) at different scan rates on a glassy carbon working electrode.
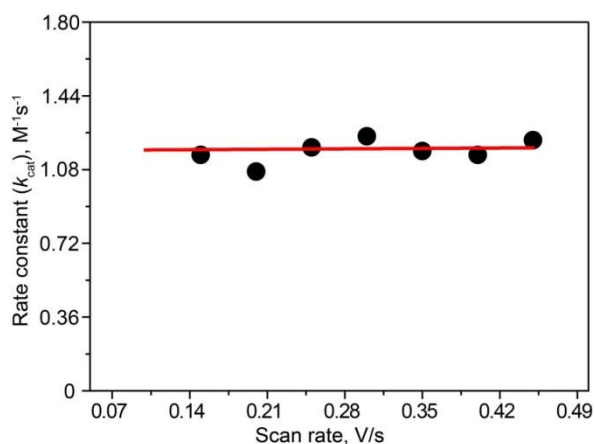
Appendix B24:A plot of rate constant (k_{cat}) versus scan rates (V/s)for electrocatalytic WO by **1a** in water showing scan rates independence of the rate constant.
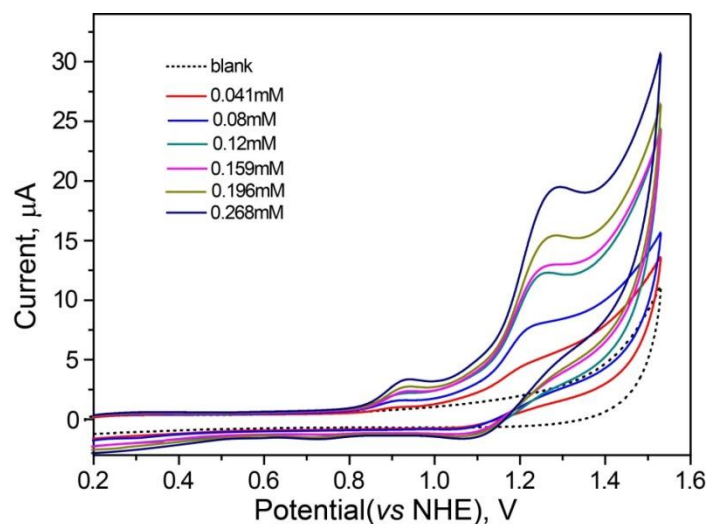
Appendix B25:CVs of **1a** in 15 mM phosphate (pH=7.2, I= 0.1 MNaNO$_3$) with increasing concentration of **1a** at a scan rate of 100 mV/s.
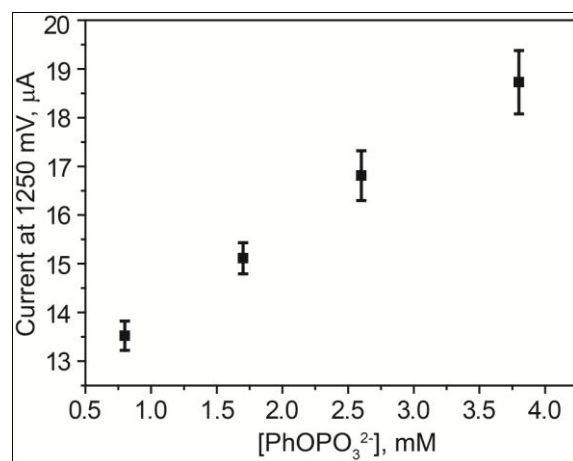
Appendix B26:Plot of catalytic current at 1250 mV as a function of disodium phenyl phosphate buffer anion concentration (pH 7.2).
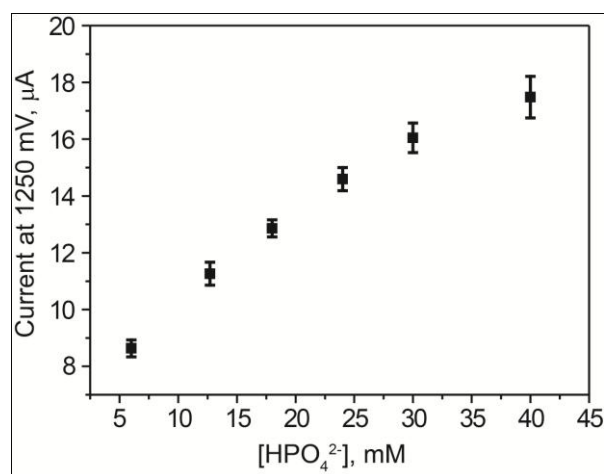
Appendix B27: Plot of catalytic current at 1250 mV as a function of disodium phosphate buffer anion concentration (pH 7.2)
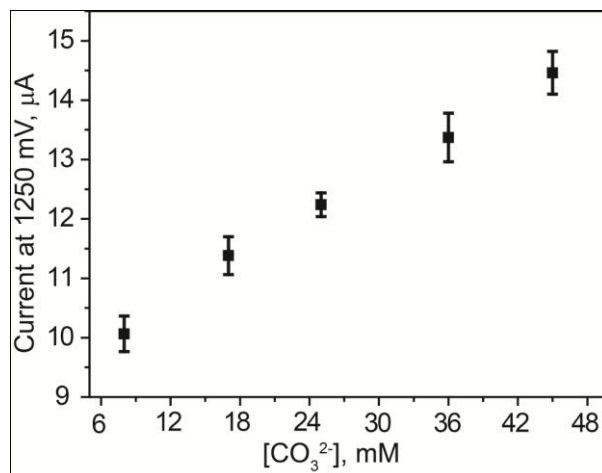
Appendix B28:Plot of catalytic current at 1250 mV as a function of bicarbonate buffer anion concentration (pH 7.2). Please note that the pH if slightly inaccurate due to coupled equilibrium for the decomposition of carbonic acid to dissolved CO_2.
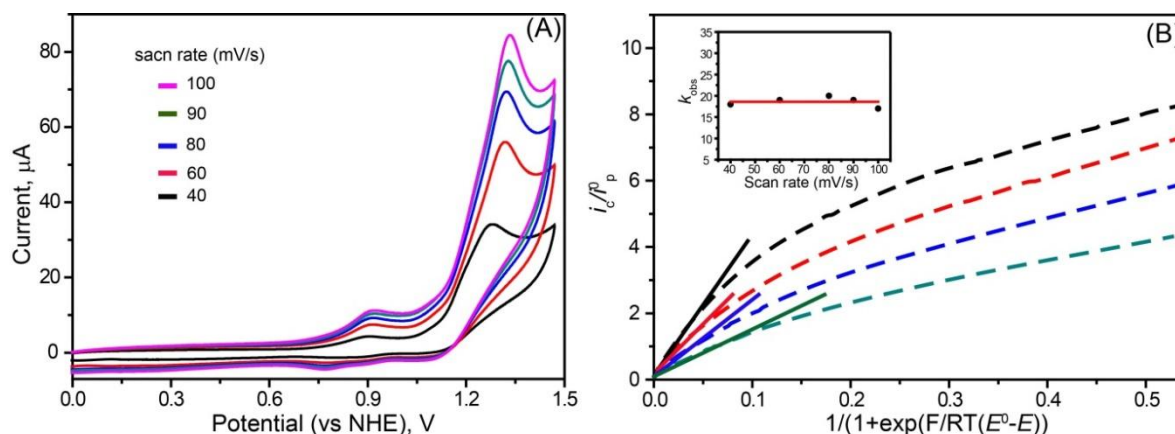
Appendix B29: (A) CVs at different scan rates of **1a**(1mM) in water (0.5 M NaNO$_3$ used as supporting electrolyte, glassy carbon used as working electrode). (B) The linear portion of i_{cat}/i_p^0 *vs* $1/(1+\exp(F/RT(E^{0'}-E))$ plot for **1a** in water at different scan rates (black- 40 mV/s, red- 60 mV/s, 80 mV/s green- 90 mV/s) use to obtain rate constant (k_{obs}) (inset) Plot of scan rates *vs*$k_{obs}$to obtain scan rate independent k_{obs}value of 18.9 ± 3 s^{-1}.
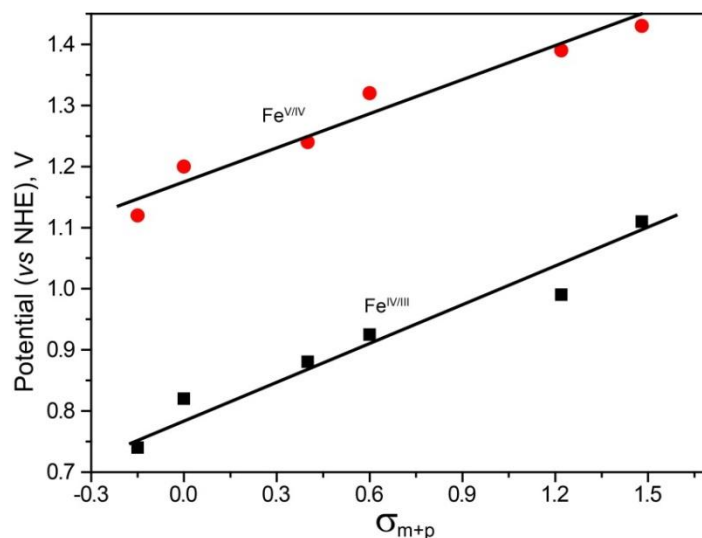
Appendix B30: Hammett plot for catalyst **1a**-**f** with formal potential of Fe$^{V/IV}$ and Fe$^{IV/III}$ redox couples.
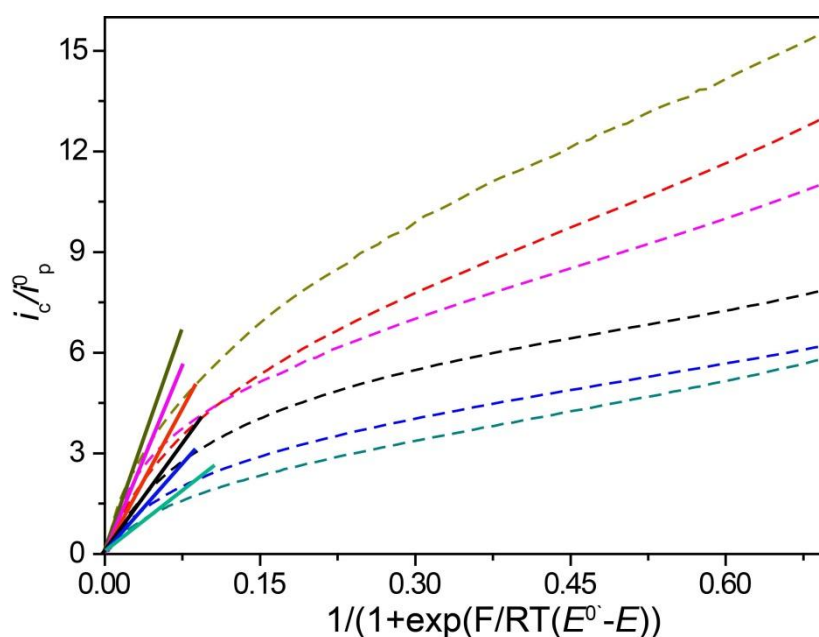
Appendix B31: Plots of i_{cat}/i^0_p as a function of $1/(1+\exp(F/RT(E^{0'}-E))$ for various Fe^{III}-bTAML complex used in this study **1b**(turquoise dottedline, solid line indicate y = mx fit at linear i_c/i^0_p), **1a** (blue dotted line, solid line indicate y = mx fit at linear i_c/i^0_p), **1c** (black dotted line, solid line indicate y = mx fit at linear i_c/i^0_p), **1d** (pink dotted line, solid line indicate y = mx fit at linear i_c/i^0_p), **1e** (red dotted line, solid line indicatey = mx fit at linear i_c/i^0_p) and **1f**(yellow green dotted line,solid line indicate y = mx fit at linear i_c/i^0_p). The k_{cat} values were determined from the initial linear portion of i_c/i^0_p (solid lines indicate linear fit with intercept close to zero). $i_{cat}/i^0_p$for various catalyst were obtained for CVs of 400 mV/s scan rates.

Appendix B32:**Calculations of O-O bond formation Rate Constant at zero over potential**

Catalytic Tafel plot based on foot-of-the-wave analysis i.e. Turnover frequency-overpotential (TOF-η)relationship for homogeneous water oxidation catalyst has been used to obtain the O-O bond formation rate constant (TOF^0) at zero over potential during water oxidation by [Fe^{III}-bTAML] complex. Following equations (equation I-III) has been used to calculate the TOF^0 as follows.

$$\text{TOF} = \frac{k_{obs}}{1 + \exp(\frac{F}{RT}(E^{0'}-E^{0}_{H_2O/O_2,\,pH\,7}- \eta))} \tag{I}$$

$$\log(\text{TOF}) = \log(k_{obs}) - \frac{F}{(\ln10)RT}(E^{0'}-E^{0}_{H_2O/O_2,\,pH\,7}) + \frac{\eta F}{(\ln10)RT} \tag{II}$$

At zero over potential $\eta = 0$ and TOF = TOF^0

$$\log(\text{TOF}^0) = \log(k_{obs}) - \frac{F}{(\ln10)RT}(E^{0'}-E^{0}_{H_2O/O_2,\,pH\,7}) \tag{III}$$

Using equation III TOF^0 for all catalyst (**1a**-**f**) was determined and compared with Hammett parameter (see below figure).
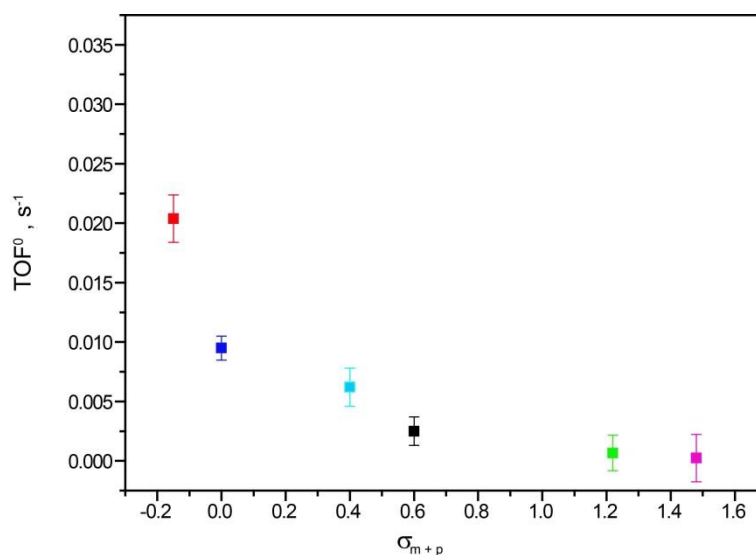
Plot of rate constants at zero overpotential (TOF) *vs* Hammett parameter (σ_{m+p}) of substituted group on catalyst (**1b**-red, **1a**-blue, **1c**-cayan, **1d**-black, **1e**-green and **1f**-pink).

Appendix C
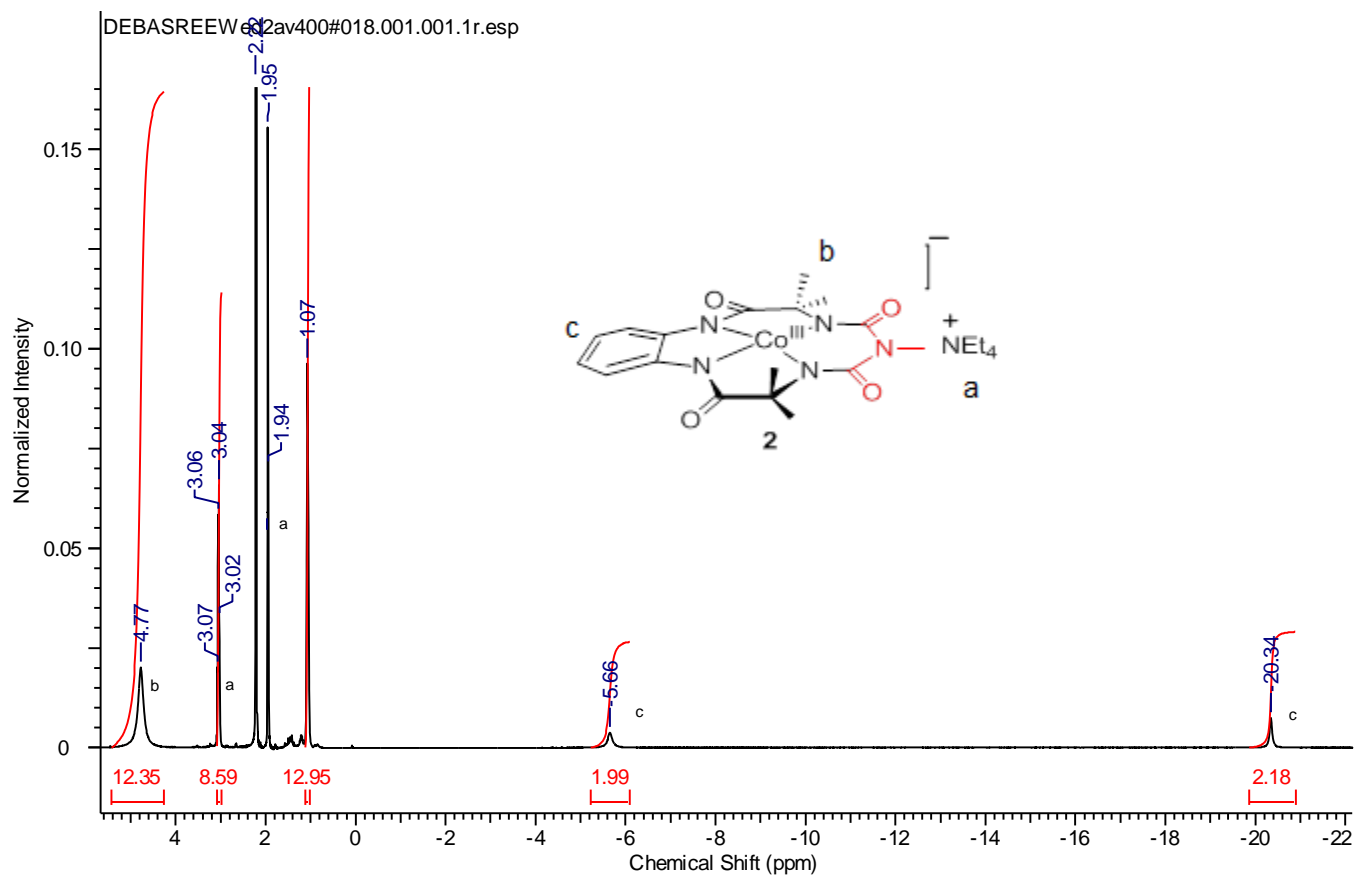
Appendix C1: ^{1}H NMR of (Et$_4$N)[Co^{III}(biuret-modified-TAML)] complex (**2**) in CD$_3$CN (400MHz, 25^{0}C).
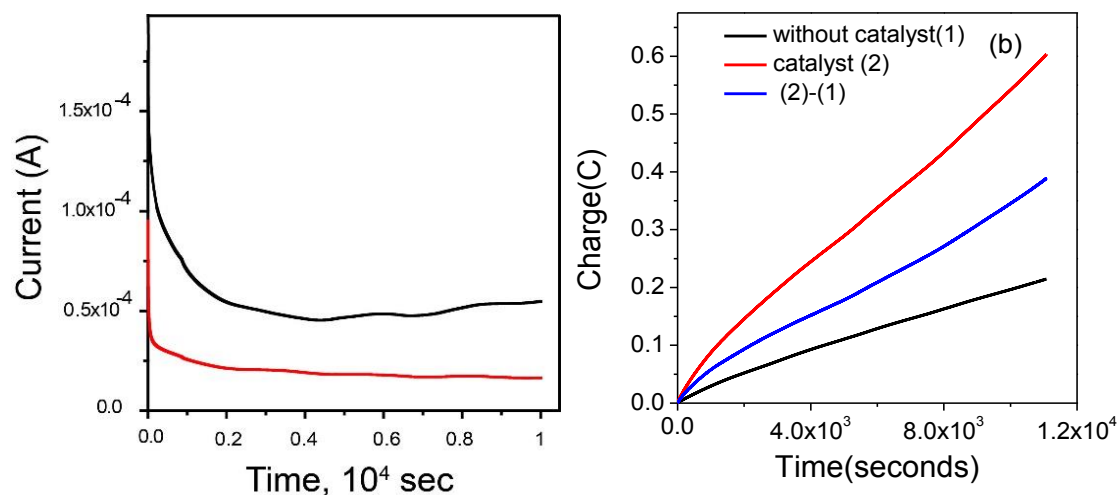
Appendix C2: (a) Current obtained and (b) charge passed in 3 h with (red line) and without the catalyst (black line) during CPE at 1.5 V (*vs* NHE) of 1 mM **2** in pH 9.2 phosphate buffer (0.1 M) for 3 h on 1 cm^2 clean ITO surface (condition: platinum wire as counter electrode and Ag/AgCl (satured KCl) as reference electrode).
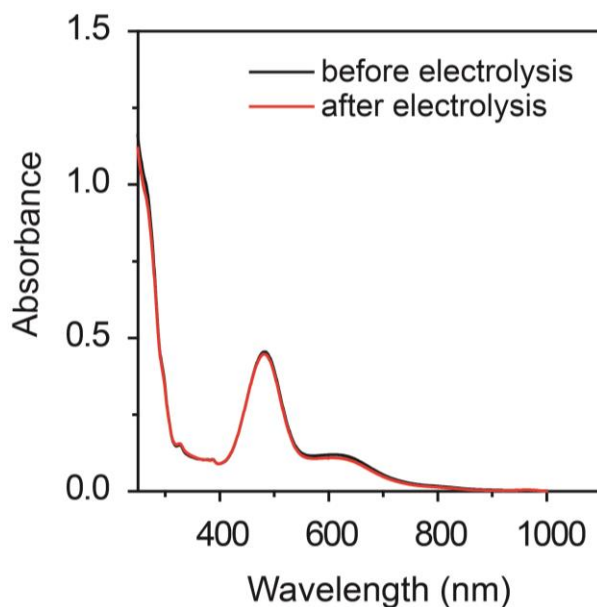
Appendix C3: The UV-Visible spectra of **2** in water (0.1M pH 9.2 phosphate buffer) before (black) and after (red) 3 hrs of CPE.
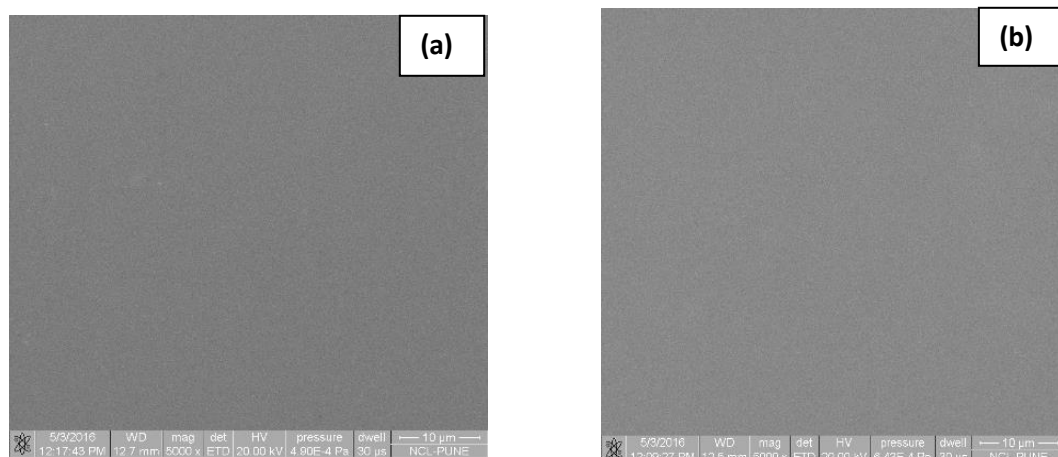
Appendix C4: Scanning electron microscopy (SEM) images of a ITO working electrode before (A) and after (B) 3 hrs of CPE at pH 9.2 phosphate buffer.
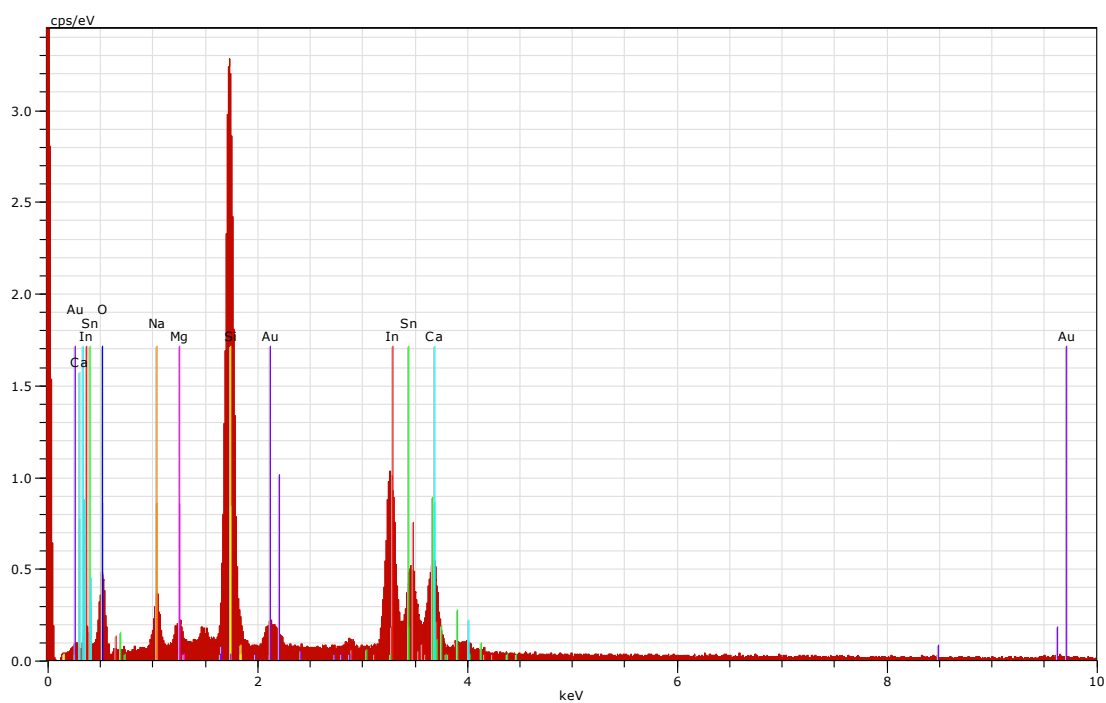
```
                                        Spectrum: S-1

        El AN  Series  unn. C norm. C Atom. C Error
                        [wt.%]  [wt.%]  [at.%]   [%]
        -------------------------------------------
        O  8  K-series  22.52   30.77   57.90   3.7
        In 49 L-series  22.15   30.26    7.93   1.9
        Si 14 K-series  16.92   23.12   24.79   0.9
        Ca 20 K-series   3.78    5.17    3.88   1.1
        Sn 50 L-series   3.68    5.03    1.28   0.6
        Au 79 M-series   1.98    2.71    0.41   0.1
        Na 11 K-series   1.65    2.26    2.96   0.1
        Mg 12 K-series   0.50    0.68    0.84   0.1
        -------------------------------------------
                 Total:  73.20  100.00  100.00
```

Appendix C5a: Energy dispersive X-ray analysis (EDX) of a clean ITO electrode before CPE (the above table indicates the composition ITO electrode surface).
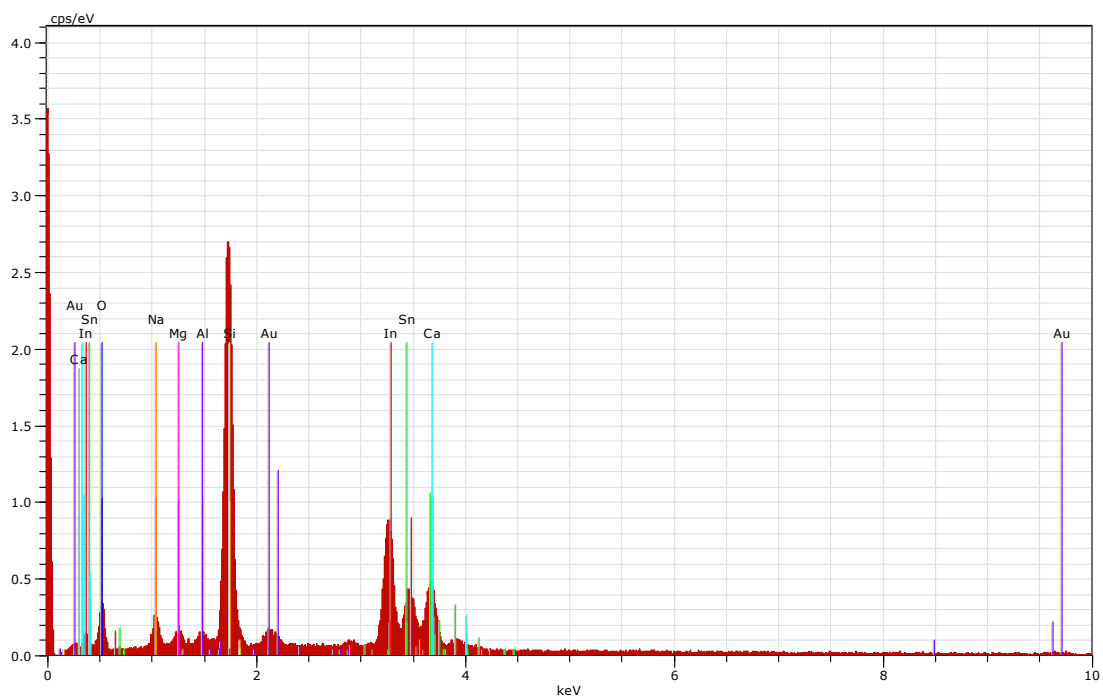
```
                    Spectrum: S-2

    El AN  Series  unn. C norm. C Atom. C Error
                   [wt.%]  [wt.%]  [at.%]   [%]
    ------------------------------------------
    In 49 L-series  23.41   32.35    8.76   2.0
    O  8  K-series  20.70   28.60   55.58   3.6
    Si 14 K-series  17.11   23.65   26.17   1.0
    Ca 20 K-series   4.08    5.64    4.37   1.2
    Sn 50 L-series   3.59    4.95    1.30   0.6
    Au 79 M-series   1.57    2.17    0.34   0.1
    Na 11 K-series   1.35    1.86    2.52   0.1
    Mg 12 K-series   0.40    0.56    0.72   0.1
    Al 13 K-series   0.15    0.21    0.25   0.0
    ------------------------------------------

      Total:  72.36  100.00  100.00
```

Appendix C5b: Energy dispersive X-ray analysis (EDX) of an ITO electrode after CPE (the above table indicates the composition ITO electrode surface).

```
------------------------------------------
Initialisation
------------------------------------------

Setting temperature to 25.0°C...

Equilibrating sample for 120 seconds...

------------------------------------------
Size measurement
------------------------------------------

Starting measurement 1

90 degree measurement

------------------------------------------
Optimisation
------------------------------------------

Checking preset position

Seeking best attenuator at position 4.65mm...
Set attenuator: 11
Count rate: 0.88 kcps
Unable to find a suitable attenuator. Count rate is too low for acceptable measurement.

[ATTENTION]: Unable to find an optimum attenuator and measurement position.
[ATTENTION]: Low count rate
Measurement aborted

Setting temperature to 25.0°C...
```

Appendix C6: Report of dynamic light scattering (DLS) spectroscopy for catalyst **2** in 0.1M phosphate buffer (pH = 9.2) after 3 hours of CPE.
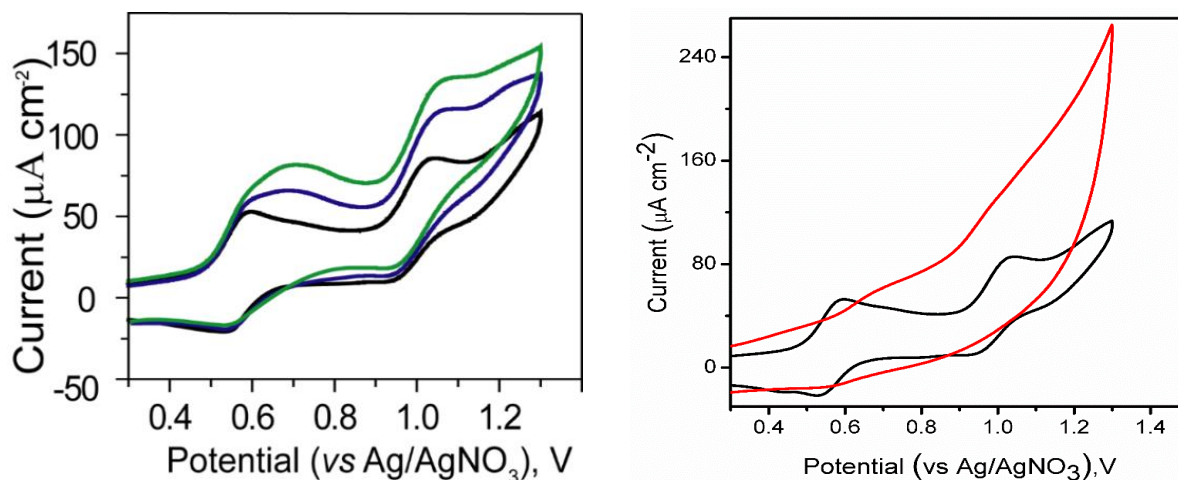
Appendix C7: CVs (left) of **2**(0.5mM) in (black) acetonitrile, 0.4 % pH 9.2 (0.4 mM phosphate buffer) in acetonitrile (blue) and 0.5 % pH =9.2 0.5mM buffer in acetonitrile (green). CVs (right) of **2** in acetonitrile (black), 1.75 % pH 9.2 (0.1M phosphate buffer) acetonitrile (red).Conditions: Scan rate 50mVs^{-1}, Glassy carbon as working electrode, platinum wire as counter electrode, Ag/AgNO$_3$ as reference electrode and 0.1 M potassium hexafluoro phosphate as supporting electrolyte.
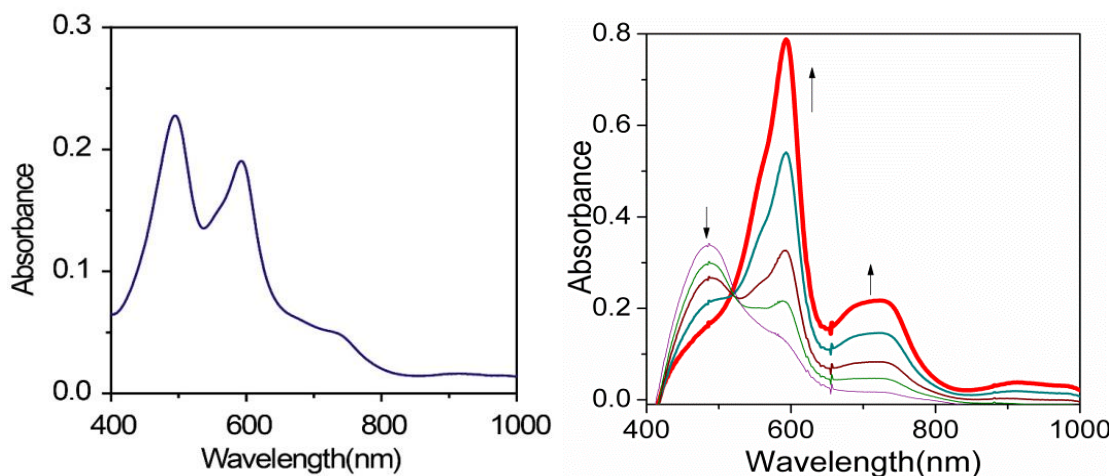

Appendix C8: UV-Vis spectrum (left) of mixture of [Co^{IV}(O)bTAML] and (Co^{III}-bTAML) generated by controlled potential electrolysis (1.2V *vs* NHE) in acetonitrile at -15^{0}C. Conversion of **2** to one electrons higher oxidized species [Co^{IV}(O)bTAML] through isosbestic point at 510nm by CPE at -15^{0}C (right). Condition: 9 cm^2 clean ITO as working, platinum foil as counter, Ag/AgNO$_3$ as reference electrode and 0.1 M potassium hexafluoro phosphate as supporting electrolyte.
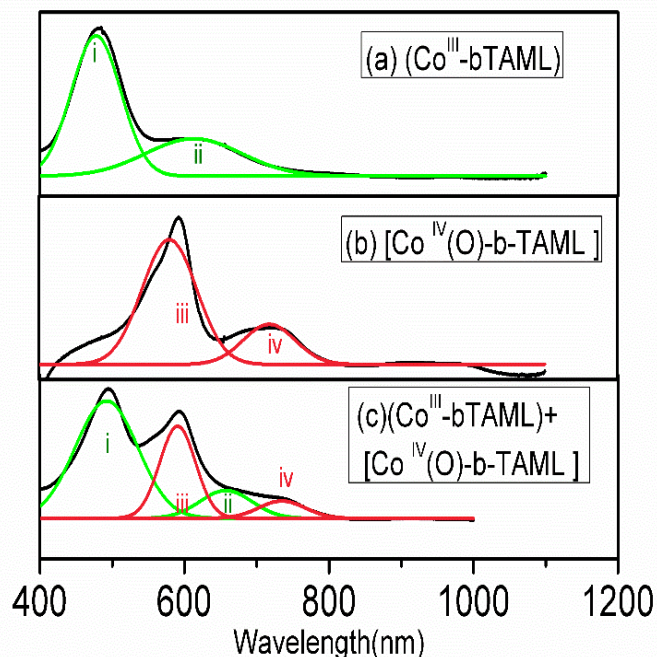
Appendix C9: Absorption spectra of (a) [Co^{III}-bTAML], (b) mixture of [Co^{IV}(O)bTAML] and (Co^{III}-bTAML), (c) [Co^{IV}(O)bTAML]. The spectra in (a) to (c) have been fitted to sums of Gaussian functions, and the component bands are assigned as i , ii, iii, iv.
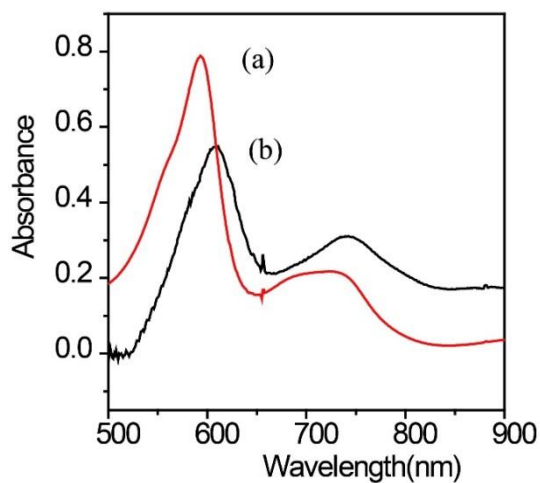
Appendix C10: UV-Vis spectra of complex [Co^{IV}(O)bTAML] in (a) acetonitrile and (b) dichloromethane generated from **2** by addition of chemical oxidant (ceric ammonium nitrate) at -40^{0}C.
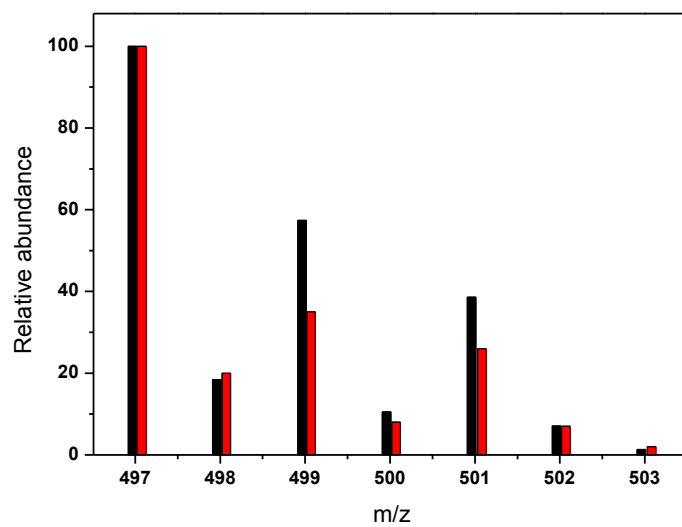
Appendix C11: Comparison of simulated (black bars) and observed (red bars) isotopic distribution pattern of $[Co(O)(Zn)(bTAML)]^-[H]^+$

Appendix D
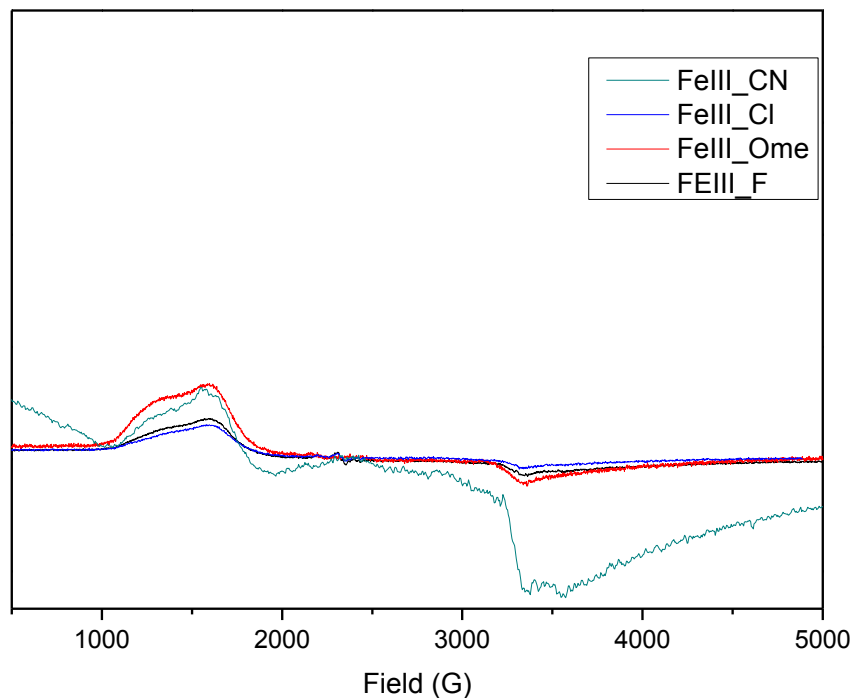
Appendix D1. X-band EPR spectra of $S = 3/2$ $[(\text{X-bTAML})\text{Fe}^{\text{III}}(\text{Cl})]^{2-}$ complex in acetonitrile at 90K (X = F, black; Cl, violet; CN, green, OMe, red).
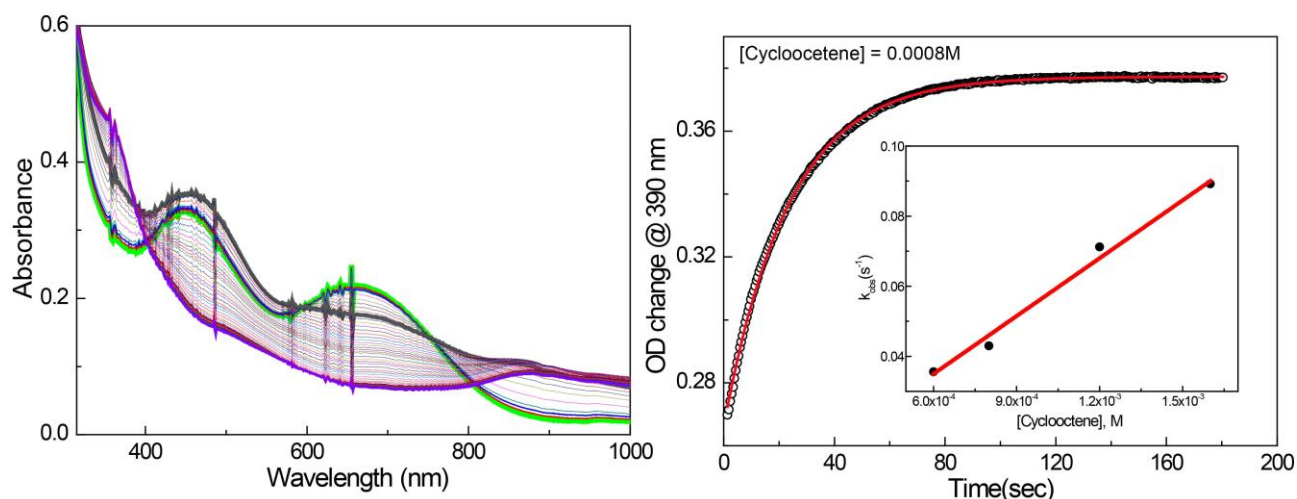
Appendix D2. Kinetic traces for cyclooctene oxidation by **2b** (left). Calculation of first order rate constant for cyclooctene (0.0008 M) oxidation; inset: second order rate constant calculation from different cyclooctene concentration (right).
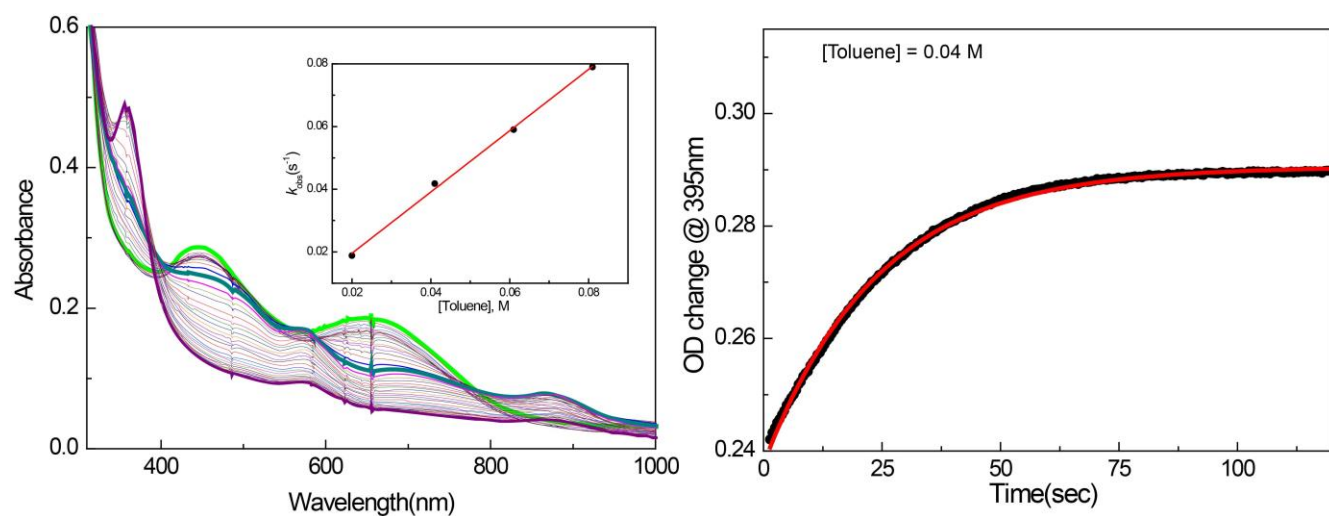
Appendix D3. Kinetic traces for toluene oxidation by **2b**; inset: second order rate constant calculation from different toluene concentration (left). Calculation of first order rate constants for tolene (0.04 M) oxidation (right).
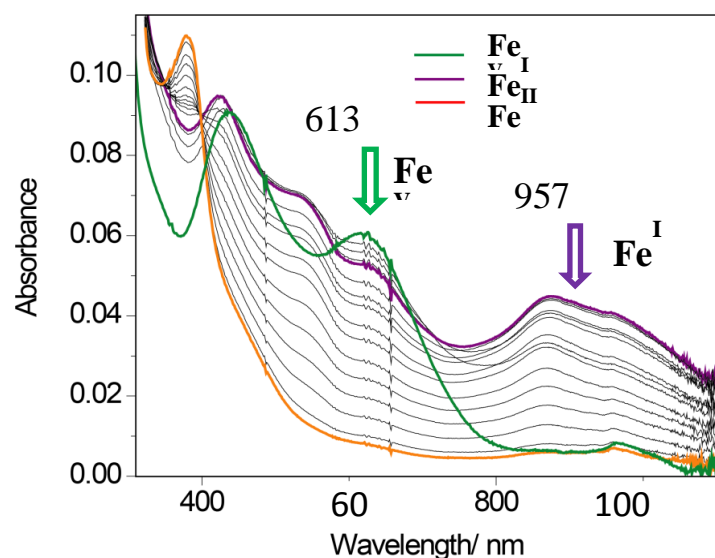
Appendix D3. Spectral change upon addition of equimolar aqueous sodium hypochlorite solution to [Fe(III)(X-bTAML)] solution in acetonitrile at room temperature.
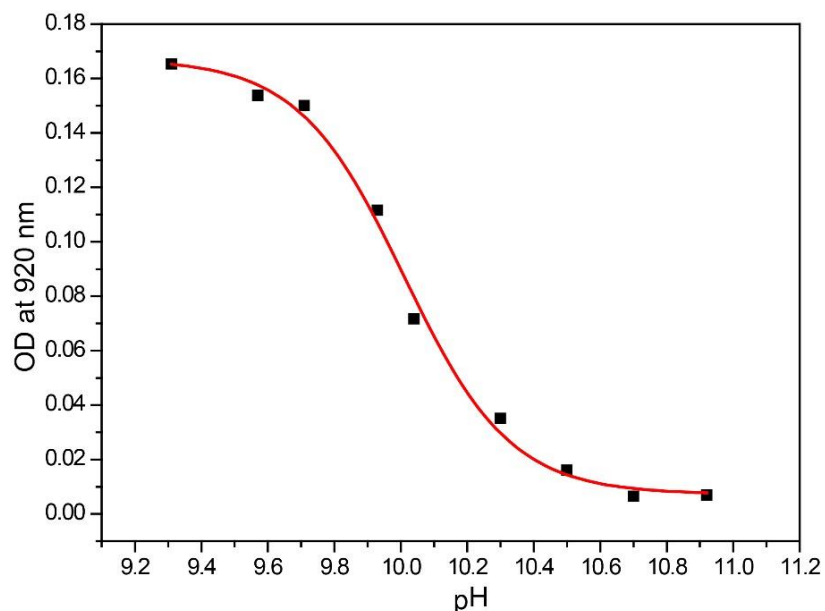
Appendix D4. pK$_a$ determination of Fe^{IV}(O).

The pK$_a$ was determined by monitoring the increase in absorbance at 920 nm due to the formation of μ-O-Fe$^{IV}_2$upon addition of acid. For all catalyst the pKa of FeIV(O) was detrmined using same method.
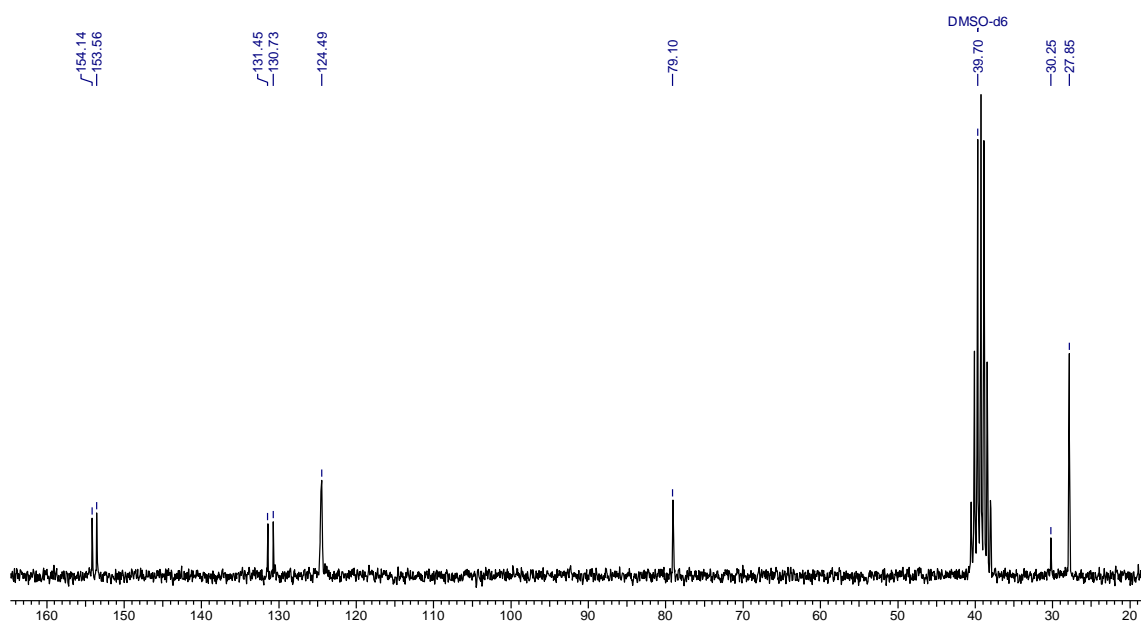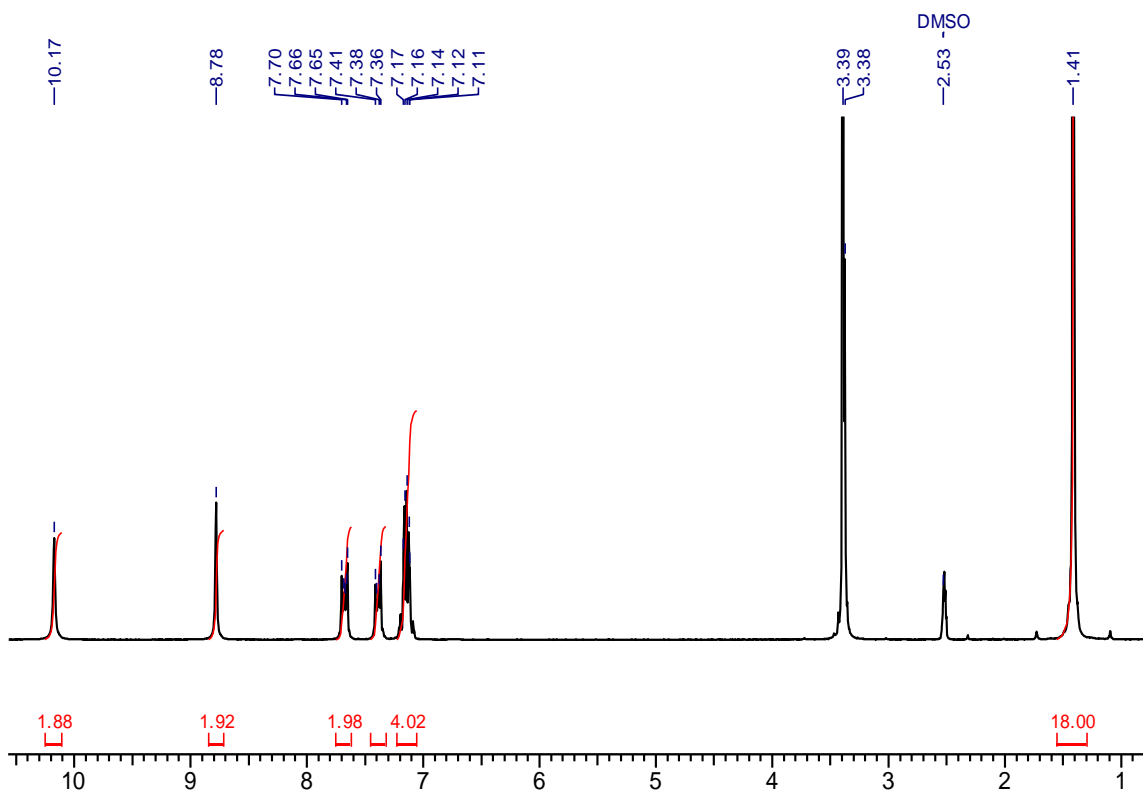
The following equilibrium takes place:

$$2\ Fe^{IV}(O)^{2-} + 2\ H^+ \rightleftharpoons Fe^{IV}(OH)^{1-} \xrightarrow{\ -\ H_2O\ } [Fe^{IV}_2O]^{1-}$$
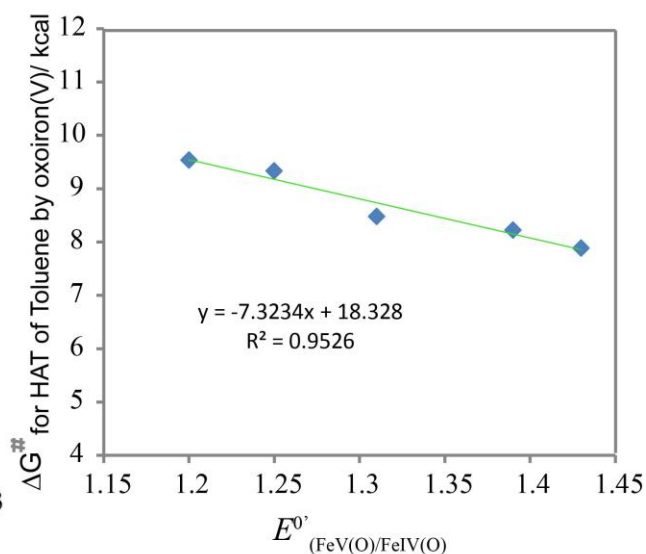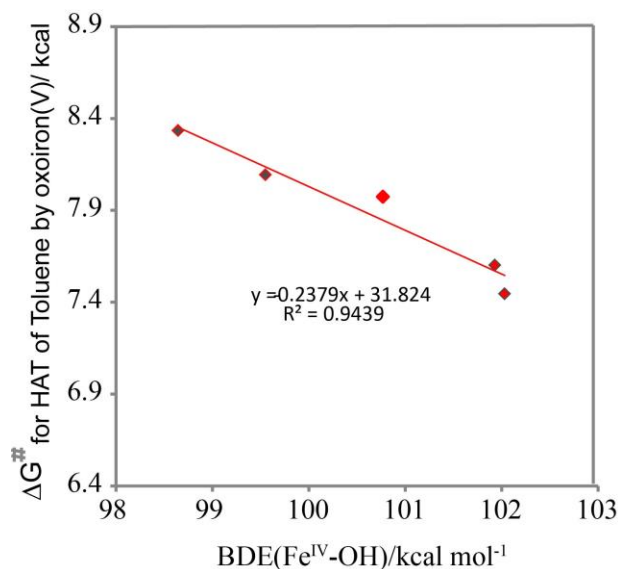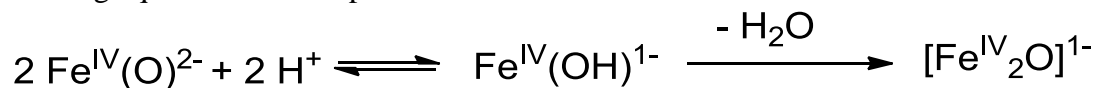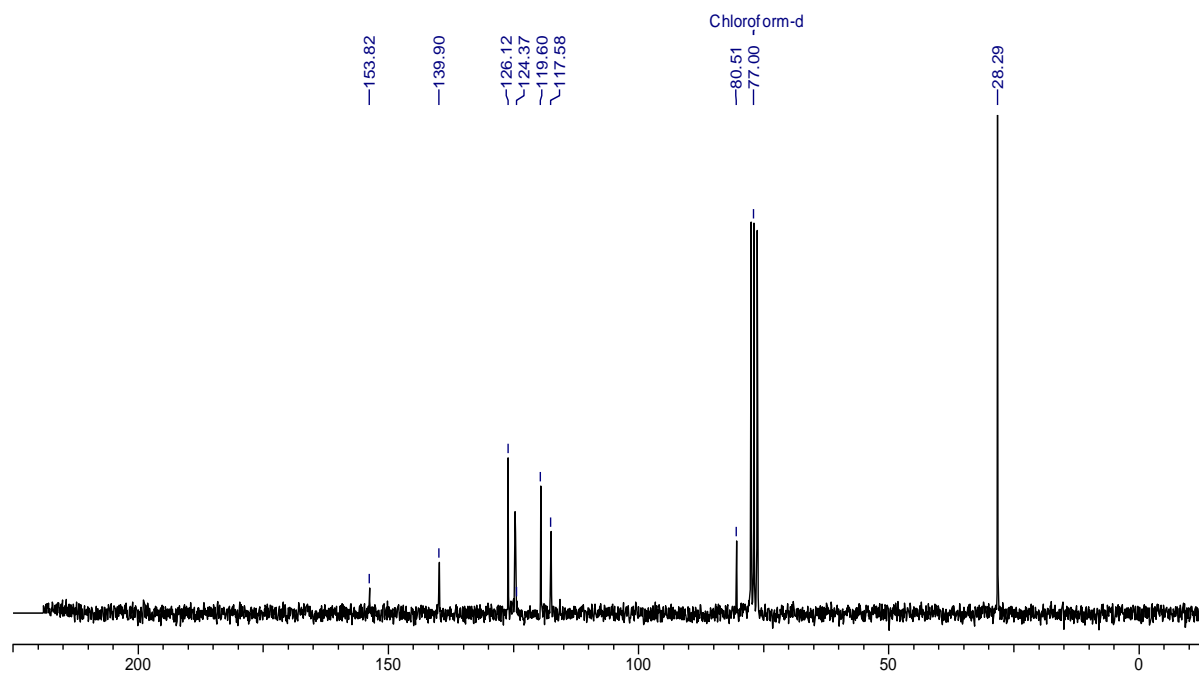

Appendix D5: Correlation of free energy of activation with BDE(Fe^{IV}-OH) (left) and The electron affinity of oxoiron(V).

Appendix E
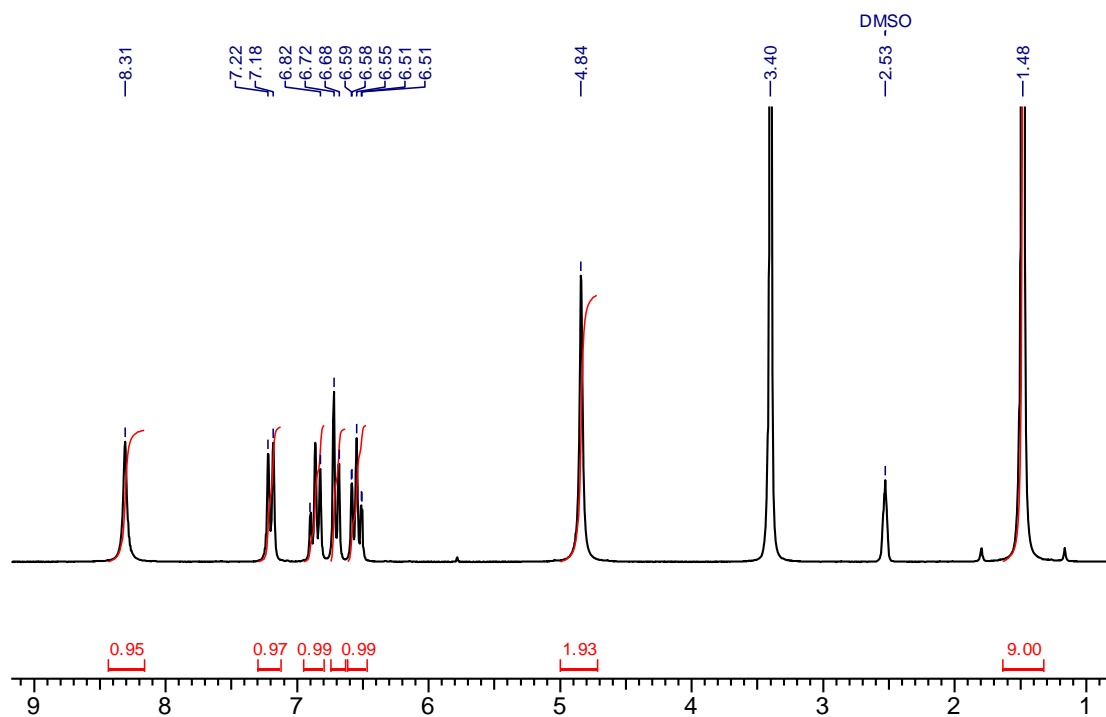
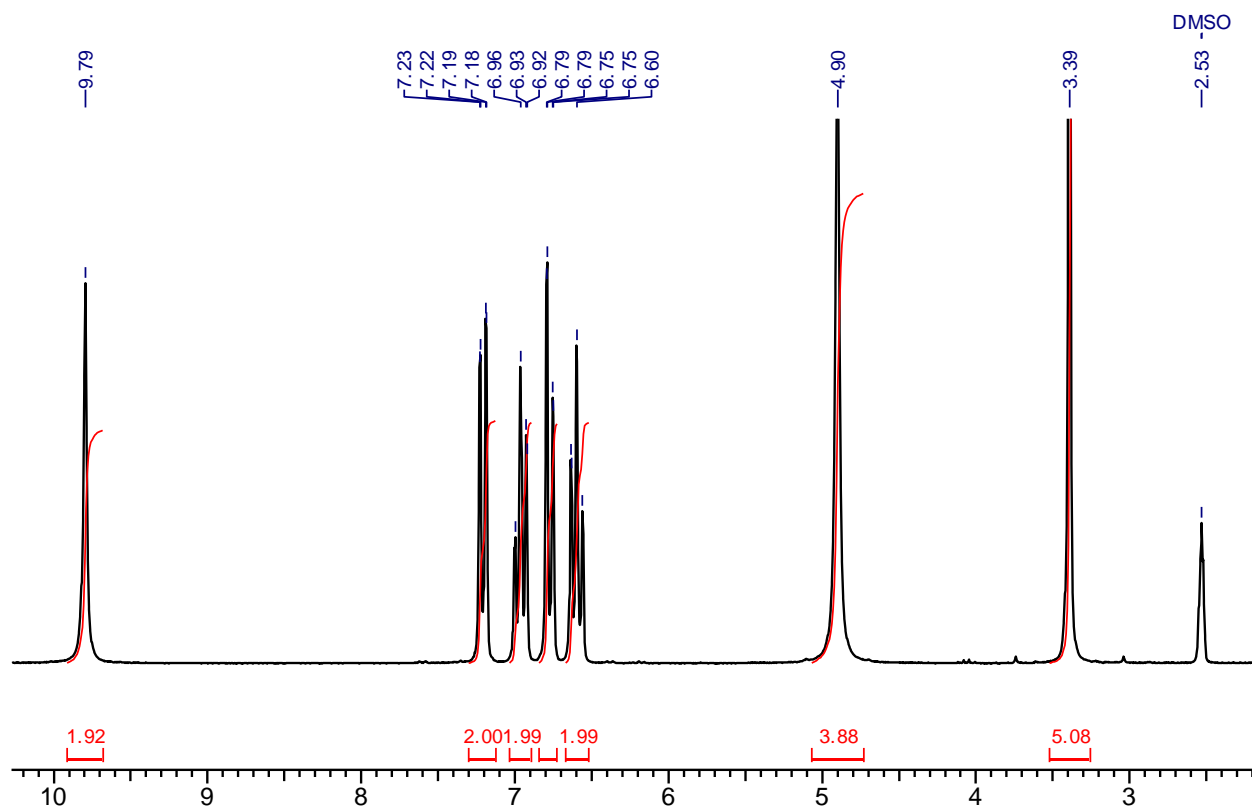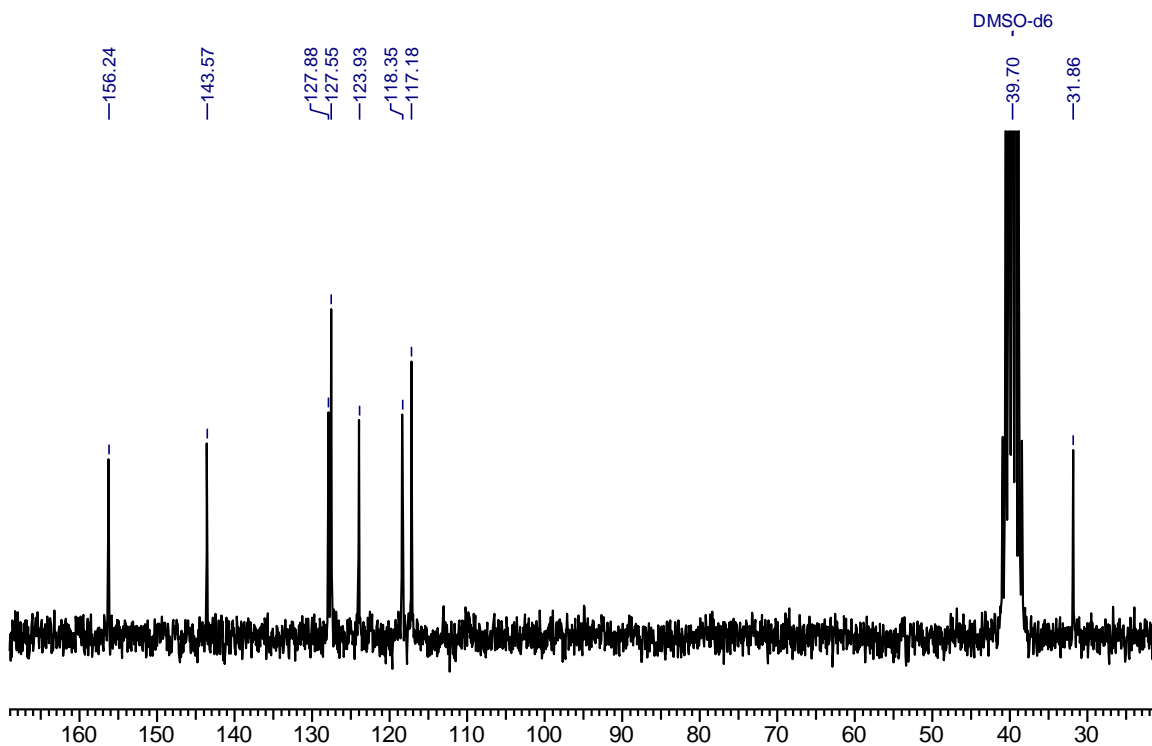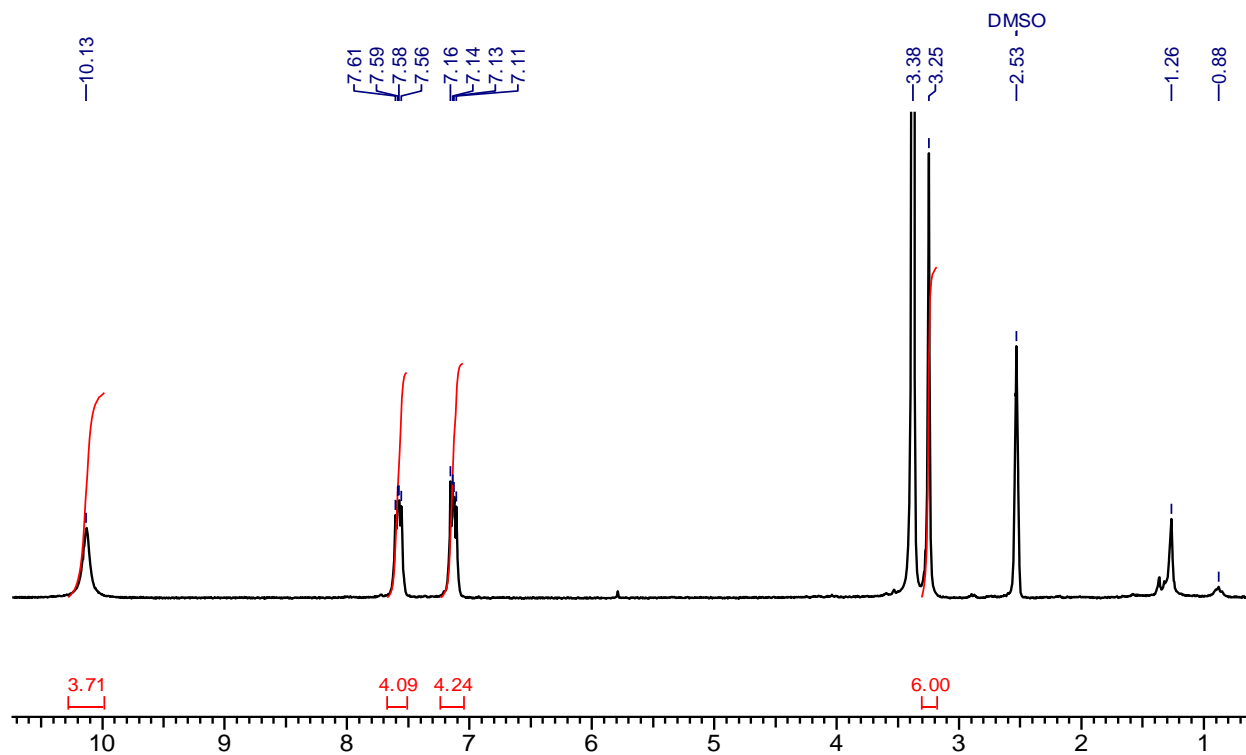**Appendix E1**. ^{1}H –NMR of **L1** in DMSO-d6

10 Jun 2011

Appendix E2. ^{13}C –NMR of **L1** in CDCl$_3$

Appendix E3. ¹H –NMR of **L2** in DMSO-d6

Appendix E4. ¹³C –NMR of **L2** in DMSO-d6

Appendix E5. ^{1}H –NMR of **L3** in DMSO-d6

Appendix E6. ^{13}C –NMR of **L3** in DMSO-d6

Appendix E7. ^{1}H –NMR of **L4** in DMSO-d6

S2-FE #96 RT: 0.43 AV: 1 SB: 66 0.26-0.39 , 0.25-0.40 NL: 1.59E7
T: FTMS - p ESI Full ms [100.00-1500.00]
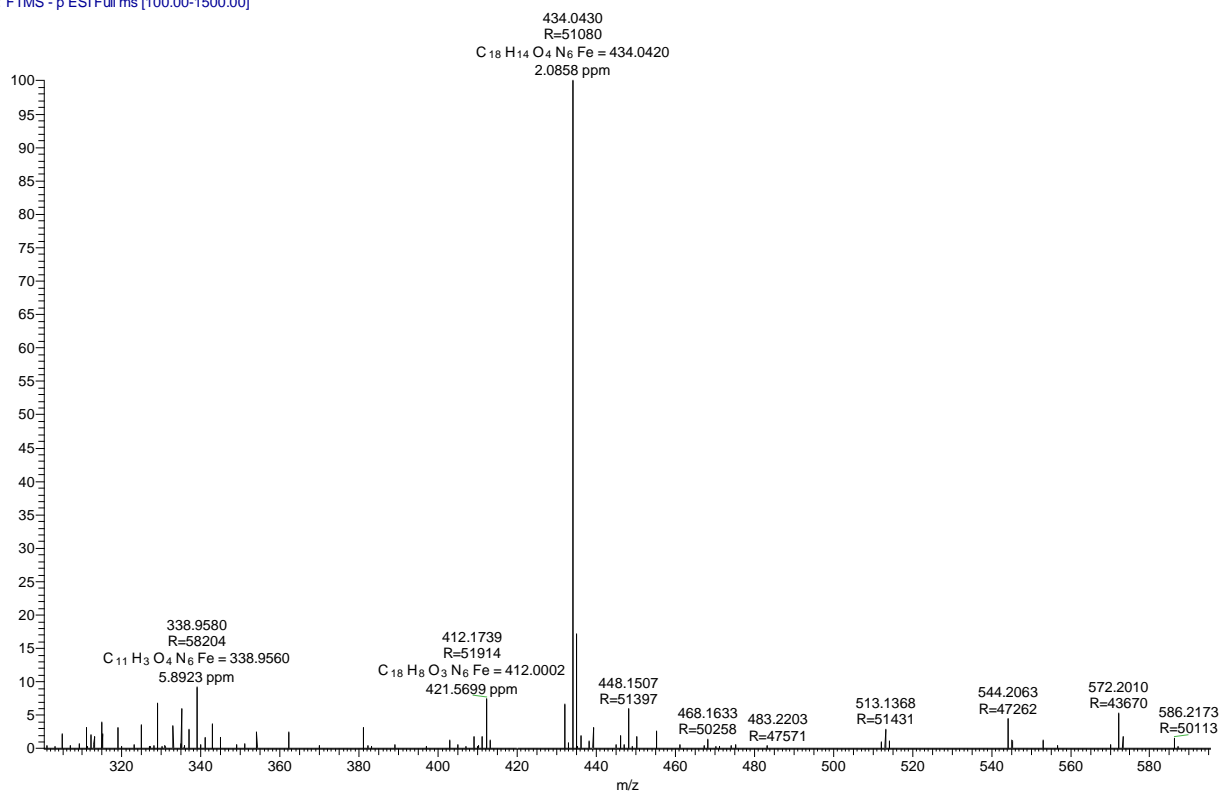
Appendix E8. HR-Ms of 1a (isotope pattern matches perfectly with theoretical pattern)

List of Research Credentials, Awards and Conferences

List of Publications

1. Spectroscopic and Reactivity Comparisons of a Pair of bTAML Complexes with $Fe^V=O$ and $Fe^{IV}=O$ Units; **Santanu Pattanayak**, Andrew J. Jasniewski, Atanu Rana, Apparao Draksharapu, Kundan K. Singh, Andrew Weitz, Michael Hendrich, Lawrence Que, Abhishek Dey and Sayam Sen Gupta. *Inorg. Chem.*, **2017**, 56 (11), 6352-6361

2. Electrochemical formation of $Fe^V(O)$ and mechanism of its reaction with water during $O-O$ bond formation; **Santanu Pattanayak**, Debarati Roy Chowdhury, Bikash Garai, Kundan K Singh, Amit Paul, Basab B Dhar, and Sayam Sen Gupta. *Chem.-Eur. J.*, **2017**, 23 (14), 3414-3424.

3. Electrocatalytic water oxidation by a molecular cobalt complex through a high valent cobalt oxo intermediate" Debasree Das, **Santanu Pattanayak**, Kundan K Singh, Bikash Garai, Sayam Sen Gupta. *Chem. Commun.*, **2016**, *52* (79), 11787-11790.

4. Reactivity and Operational Stability of N-Tailed TAMLs through Kinetic Studies of the Catalyzed Oxidation of Orange II by H_2O_2: Synthesis and X-ray Structure of an N-Phenyl TAML; Genoa R Warner, Matthew R Mills, Clarissa Enslin, **Santanu Pattanayak**, Chakadola Panda, Tamas Kumar Panda, Sayam Sen Gupta, Alexander D. Ryabov, Terrence J. Collins. *Chem. -Eur. J.*, **2015**, *21* (16), 6226-6233.

5. Selective C–H Bond Oxidation Catalyzed by the Fe-bTAML Complex: Mechanistic Implications; Munmun Ghosh, **Santanu Pattanayak**, Basab B Dhar, Kundan K Singh, Chakadola Panda, Sayam Sen Gupta. Inorg. Chem., **2017**, *56* (18), 10852-10860.

Awards

1. CSIR-UGC National Eligibility Test (NET) for Lectureship and Junior Research Fellowship (India) in Chemical Sciences for the period July 2012 to July 2017.

Conferences/Symposia attended

1. "International Conference on Structural and Inorganic Chemistry" during December 4-5, 2014. Hosted by CSIR-NCL, IISER-Pune and SP Pune University, India. "17th

CESI National Symposium in Chemistry" organized by CSIR-NCL Pune during 6-8th February, 2015 in Pune.

2. Poster presentation in "5th Symposium on Advanced Biological Inorganic Chemistry (SABIC)" held in Kolkata during January 7-11, 2017. Hosted by TIFR Mumbai and IACS-Kolkata, India.

About the Author

Santanu Pattanayak, son of Mr. Shyamsundar Pattanayak and Mrs. Snehalata Pattanayak was born in Purba Medinipur, West Bengal, India. He received his secondary education from Gobardhanpur Pramathanath Vidyayatan, West Bengal. He completed his B.Sc. in Chemistry (Hons.) from Vidyasagar University in 2010. After completion of his B.Sc. degree, he joined Department of Chemistry; University of Pune to pursue M.Sc. in Chemistry. He was awarded junior research fellowship (JRF) for 2012-2017. Then, He joined Department of Chemical Engineering and Process Development division, CSIR-NCL, Pune to pursue his Ph.D. degree in July 2012 under Dr. Sayam Sen Gupta. After that he moved to Dr. Kumar Vanka in Physical Chemistry Division, CSIR-NCL, Pune to complete his Ph.D degree.